Massive black holes in dwarf galaxies : off-center binary formation through gravitational capture

Thibaut François

Université de Strasbourg

UNIVERSITÉ DE STRASBOURG

École doctorale Physique, chimie-physique ED 182 Université de Strasbourg

ÉCOLE DOCTORALE DE PHYSIQUE ET CHIMIE-PHYSIQUE

Observatoire Astronomique de Strasbourg

THÈSE présentée par

Thibaut François

soutenue le : **03 octobre 2024**

pour obtenir le grade de : **Docteur de l'Université de Strasbourg**
Discipline/Spécialité : Astrophysique

Trous noirs massifs dans les galaxies naines

Formation de binaires excentrées par capture gravitationnelle

THÈSE dirigée par :

M. BOILY Christian	Professeur, Observatoire de Strasbourg
M. FREUNDLICH Jonathan	Maître de conférences, Observatoire de Strasbourg

RAPPORTEURS :

M. JOHANSSON Peter	Professeur, University of Helsinki
M. PEÑARRUBIA Jorge	Professeur, Royal Observatory Edinburgh

AUTRES MEMBRES DU JURY :

Mme DI MATEO Paola	Astronome, Observatoire de Paris, GEPI
M. FAMAEY Benoit	Directeur de recherches, Observatoire de Strasbourg

— · ● · —

— · ● · —

À mon père.

Remerciements

Je tiens tout d'abord à remercier chaleureusement Peter, Jorge, Paola et Benoit d'avoir accepté de faire partie du jury. C'était un honneur de vous présenter mon travail, et j'espère sincèrement que nos chemins se croiseront de nouveau.

Merci ensuite à Christian de m'avoir offert l'opportunité de réaliser cette thèse, en me laissant un formidable terrain d'exploration sans trop de contraintes. Cela m'a permis de développer une indépendance précieuse, que j'emporte avec moi pour la suite de ma carrière. Un grand merci également à Jonathan. Cela fait maintenant un moment que nous travaillons ensemble, et ce fut un immense plaisir d'explorer l'univers à tes côtés. Tu as trouvé les mots justes dans les moments difficiles, et ton soutien m'a toujours été d'une grande aide.

L'observatoire de Strasbourg a été un lieu formidable pour mener à bien cette thèse, et je voudrais remercier toutes les personnes qui ont veillé à son bon fonctionnement pendant ces trois dernières années. Un merci particulier à Véronique, Sandrine, l'équipe logistique, et l'équipe informatique. Merci également à tous les chercheurs, étudiants, et ingénieurs de l'observatoire, qui, par leur simple présence, ont rendu cet endroit convivial et chaleureux. Je tiens également à remercier les chercheurs qui m'ont aidé au cours de ces trois années et durant la préparation de cette thèse : Ada, Clément, Florent, Karina, Katarina, Lorenzo, Nicolas et Rodrigo.

Les travaux présentés dans cette thèse ont été fortement influencés par trois personnes qui m'ont guidé et soutenu tout au long de cette dernière, et je tiens à leur adresser un remerciement tout particulier. First of all, thank you Rapha: you have always been there to help me, and I've learned so much through our stimulating discussions. Merci aussi à toi Simon, pour ton aide précieuse et cette semaine passée à Édimbourg, où j'ai énormément appris et gagné en confiance dans mon travail. Enfin, merci à Paolo, dont les conseils ont été de véritables repères tout au long de mon parcours. Tu as toujours pris le temps de répondre à mes questions, qu'elles soient scientifiques ou liées à ma carrière, et au-delà du travail, tu es une personne formidable avec qui j'ai partagé des moments inoubliables.

Je pense maintenant à mes acolytes doctorants, avec qui j'ai partagé tant d'éclats de rire. Merci à vous tous pour ces instants que je ne suis pas près d'oublier. Un merci particulier à Amandine, Elisabeth, Émilie, Julien, Lucie, Samuel, Srikanth et Thomas (c'est Thomas), qui ont fait partie de mon quotidien. Nos interactions ont illuminé les moments les plus difficiles, et nos déjeuners au RU (départ à 11h23) resteront parmi mes souvenirs les plus savoureux (culinairement parlant).

Merci mes PAWT (□ ◯ △) pour tous les moments extraordinaires qu'on a partagés. Merci pour la virée à Besac, les matchs de ping-pong, le mur des mèmes, les soirées foot, Halloween 2023 (la plus modérée des soirées), les verres après le boulot, les pauses thé, les discussions à l'orangerie, les king spots et les soirées Minecraft. Merci pour ces moments de joie et merci d'avoir été présent pour les moments les plus compliqués, je ne l'oublierai jamais. Notre amitié est très précieuse et j'espère qu'elle se poursuivra encore bien au-delà de cette thèse. Merci aussi à tous les amis que j'ai rencontrés au fil de ces huit années. Merci Paul et Hugo pour cette amitié qui prend de l'âge et reste naturelle, ponctuée par les après-midis jeux de société. Merci Aurélien, Boris, Clara et Clément, mes compagnons d'infortune du master, pour votre soutien durant cette période tourmentée. Thank you Clare for our weekly discussions, which greatly helped me build confidence. You've done me a great favour, and I am sincerely grateful to you.

Achever une thèse est un défi de taille, mais le soutien de sa famille le rend bien plus léger. J'ai eu la chance d'avoir une famille qui m'a accompagné tout au long de ce parcours. Merci à Laure, Aurélie, Mamie, Lulu, Papi et Marie. Merci Loïs d'avoir supporté d'être mon frère aussi longtemps, hâte de notre prochaine bataille de radiateur. Merci Papa et Maman de m'avoir toujours soutenu dans tout ce que j'entreprenais, merci pour la manière dont vous m'avez éduqué, pour votre amour, et pour mille autres raisons, c'est grâce à vous que je suis là aujourd'hui. Papa, tu attendais avec impatience cette soutenance, et je sais que de là où tu es, tu y as assisté aux premières loges. Enfin, un merci infini à celle qui a été là, chaque jour, de manière inconditionnelle durant ces huit dernières années : Lévana. J'ai eu une chance inouïe de t'avoir à mes côtés, et je t'en serai toujours reconnaissant. Tu m'as fait grandir, tu m'as aidé à devenir une meilleure personne, et tu m'as apporté bien plus que des mots ne peuvent exprimer. Sans toi, cette thèse n'aurait jamais vu le jour, et tu le sais, elle est tout autant le fruit de ton soutien que de mes efforts.

Merci à vous tous de faire partie de ma vie, je suis le plus chanceux des docteurs.

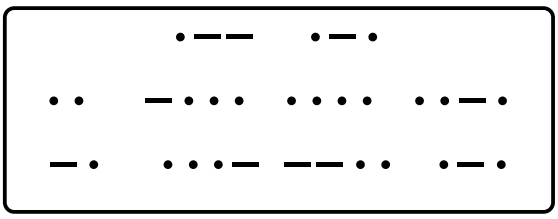

Contents

Massive Black Holes in Dwarf Galaxies

Off-center binary formation through gravitational capture

Thibaut François

Galaxies and black holes | 1

Overview

In this chapter, we dive into the universe of galaxies, discussing their classifications, features, and compositions. We will also introduce the main focus of this manuscript, massive black holes, and delve into their relationship with their host galaxies.

1.1 Galaxies, a variety of floating worlds

Galaxies are fundamental constituents of the Universe, serving not only as stellar and metal nurseries but also as cosmic milestones that help us explore the fabric of space-time. It is remarkable to consider that until Hubble discerned Cepheid variables in the Andromeda Nebula in the 1920s (Hubble, 1929), the notion that the myriad 'nebulous' entities chronicled in John Dreyer's catalogues (Dreyer, 1888, 1910) were separate galaxies was not widely accepted. Consequently, the field of extragalactic astronomy has emerged quite recently in our history. Yet, the strides made since then have been substantial: meticulous surveys of local galaxies have been conducted across the full electromagnetic spectrum, vast redshift surveys have mapped out the large-scale structure of the Universe, and we are gradually revealing the galaxies of the distant past.

1.1.1 The Classification of Galaxies

A galaxy is a vast collection of gas, dust, billions of stars, and their solar systems, all bound together by gravity. When we look up at the sky in search of galaxies, the first thing we notice is the diversity of their characteristics. Some are uniform, elliptical, and emit smooth light, while others, more complex, feature central bulges surrounded by spiral arms, and still others have more irregular shapes. Fig. 1.1 shows some examples of galaxy images. To obtain these, different observational techniques are used by

astronomers to reveal various aspects of galaxies: starlight is prominent in optical and near-infrared views, dust emissions stand out in the far-infrared, and the high-energy processes unfold at the far ends of the wavelength spectrum.

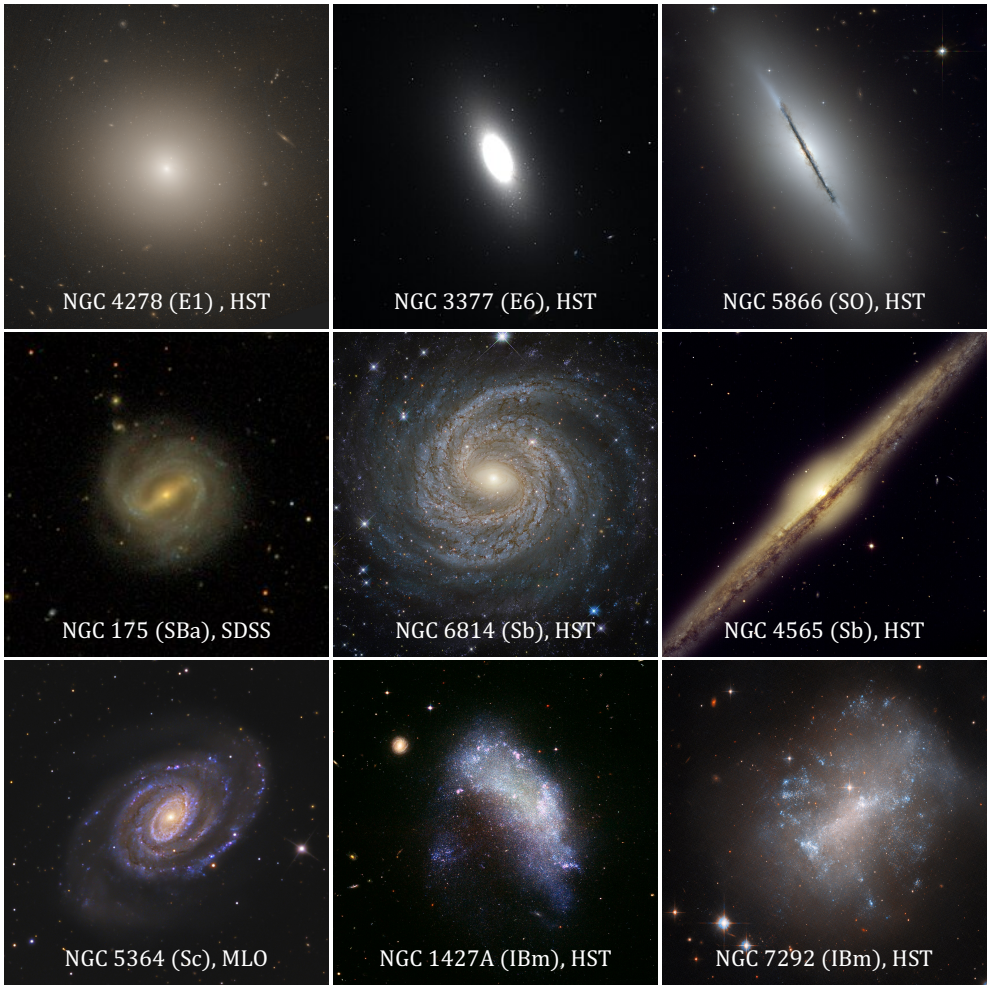

Figure 1.1: Examples of different types of galaxies.

To better organize the diverse range of morphologies, American astronomer Edwin Hubble developed a classification system known as the Hubble sequence or the Hubble tuning-fork diagram (Hubble, 1926), detailed in Fig. 1.2. Hubble's classification encompasses four main categories:

1. Elliptical Galaxies: Characterized by their smooth, elliptical light profiles, these galaxies are categorized into subtypes from E0 to E7, where a galaxy of type En has axis ratio $b/a = 1 - n/10$, with a and b the lengths of the semimajor and semiminor axes, respectively.

2. Spiral Galaxies: Identified by their distinct disk shapes and spiral arms, these galaxies are further divided into barred and normal spirals based on the presence of a central bar. Each type is then classified into subclasses (a, b, c) based on three factors: the proportion of light in the central bulge, how tightly the spiral arms are wound, and the clarity of features such as stars, ionized hydrogen (HII) regions, and dust lanes within the arms. These criteria are correlated, with galaxies like Sa having prominent bulges and tightly wound arms, while Sc galaxies feature weak or absent bulges and open arms with bright HII regions. When these criteria conflict, the openness of the spiral arms is the deciding factor.

3. Lenticular (S0) Galaxies: Serving as a bridge between elliptical and spiral galaxies, lenticulars combine features of both. They have a smooth light profile without spiral arms or HII regions, akin to ellipticals, yet possess a thin disk and a bulge, with the bulge being more pronounced than in spirals. Barred lenticulars are labeled SB0.

4. Irregular Galaxies: These galaxies lack a dominant bulge or symmetric disk, showing no clear structure but rather a patchy appearance with notable HII regions. Hubble initially excluded irregulars from his sequence, uncertain of their classification. Today, they are often considered an extension of the spiral category.

Elliptical and lenticular galaxies are frequently grouped as early-type galaxies, whereas spirals and irregulars are categorized as late-type galaxies. Moving from left to right across the Hubble sequence, galaxy morphologies transition from early-type to late-type. It is important to note that these terms are historical designations and do not refer to an evolutionary property of galaxies. They should not be interpreted as a chronological sequence.

Following Hubble's original framework, various classification systems have emerged, with de Vaucouleurs' scheme being notably influential (de Vaucouleurs, 1974). He refined the categorization of spiral galaxies within the Hubble sequence by introducing additional types like SOa, Sab, Sbc, as well as their barred counterparts. Recognizing that several galaxies labeled as irregular by Hubble actually possessed faint spiral arms, de Vaucouleurs expanded the spiral category to include irregular galaxies, introducing classifications such as Scd, Sd, Sdm, Sm, Im, and I0 based on a scale of decreasing regularity.

Beyond morphology, galaxies are also classified by other characteristics. These include their luminosity (bright vs. faint), surface brightness (high vs. low), color (red vs. blue), gas content (gas-rich vs. gas-poor), level of star formation activity (quiescent vs.

starburst), and whether or not they host an active galactic nucleus (normal vs. active). A key insight from the Hubble sequence and its extensions is the systematic variation of these attributes along the sequence, suggesting it mirrors underlying physical differences among galaxies.

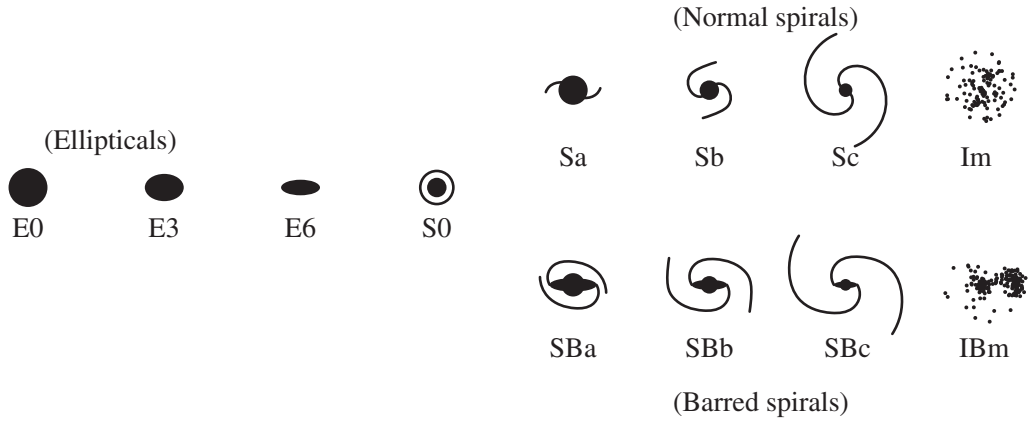

Figure 1.2: The "tuning fork" of the Hubble classification of galaxy morphologies (schematic from Abraham, 1998; Mo et al., 2010).

1.1.2 Relaxation time

Given that galaxies are primarily made of billions of stars bound together by gravity, a logical initial question to ask is: **Is it a mess in there?** In other words, can a star move freely among this crowd of other stars, or is it constantly perturbed by its peers? We will answer this question by following the derivation presented in Binney & Tremaine (2008). We track a single star on a circular orbit as it moves through a galaxy composed of N other stars of the same mass m, and we will estimate the magnitude of velocity perturbation caused by interactions with other stars. For now, let's consider the perturbation caused by a single close encounter with another star. Figure 1.3 illustrates this scenario, showing the subject star approaching a field star with an impact parameter b.

We aim to calculate the change in the velocity δv of the subject star as a result of the encounter. First, we assume that the velocity perturbation is small $\mid \delta v \mid /v \ll 1$, and that the field star remains stationary throughout the encounter such that the velocity change parallel to the trajectory averages to zero and the subject star has, to a first approximation, a straight-line trajectory. The perpendicular force is given by

$$F_\perp = \frac{Gm^2}{b^2+x^2}\cos\theta = \frac{Gm^2 b}{(b^2+x^2)^{3/2}} = \frac{Gm^2}{b^2}\left[1+\left(\frac{vt}{b}\right)^2\right]^{-3/2}. \tag{1.1}$$

Using Newton's second law

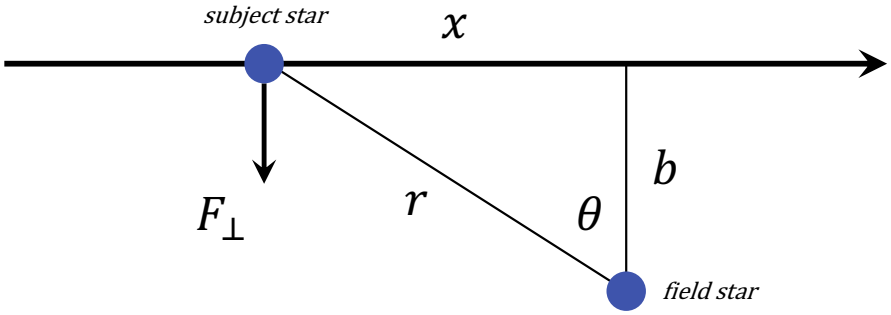

Figure 1.3: Close encounter with impact parameter b between a subject star and a field star.

$$m\frac{d\mathbf{v}}{dt} = \mathbf{F} \tag{1.2}$$

and projecting it onto the perpendicular direction, we obtain :

$$\delta v = \frac{1}{m}\int_{-\infty}^{\infty} F_{\perp}\, dt \tag{1.3}$$

where we choose the origin of time at the moment of the closest approach between the stars. With (1.1) this gives :

$$\delta v = \frac{Gm}{b^2}\int_{-\infty}^{\infty}\frac{dt}{[1+(vt/b)^2]^{3/2}} = \frac{Gm}{bv}\int_{-\infty}^{\infty}\frac{ds}{(1+s^2)^{3/2}} = \frac{2Gm}{bv}. \tag{1.4}$$

We see that our approximation $\mid \delta v \mid /v \ll 1$ holds only if

$$b \gg \frac{2Gm}{v^2} \equiv b_{\min}. \tag{1.5}$$

The equation (1.4) quantifies the velocity perturbation resulting from an encounter. To calculate the total perturbation, we need to sum up all such encounters. In the galaxy, the surface density is of order $N/\pi R^2$, where N is the total number of stars and R is the radius of the galaxy. The number of encounters with an impact parameter between b and $b + db$ during a passage through the galaxy is therefore:

$$\delta n = \frac{N}{\pi R^2} 2\pi b\, db = \frac{2N}{R^2} b\, db. \tag{1.6}$$

As encounters are a random process, the mean velocity perturbation is zero. However, the mean-square change $(\delta v)^2$ is not. For a passage through the galaxy, it is :

$$(\delta v)^2\, \delta n = \left(\frac{2Gm}{bv}\right)^2 \frac{2N}{R^2} b\, db. \tag{1.7}$$

Integrating over the impact parameters gives the mean-square velocity change per crossing [1] :

$$\Delta v^2 = \int_{b_{\min}}^{b_{\max}} \left(\frac{2Gm}{bv}\right)^2 \frac{2N}{R^2} b\, db = 8N \left(\frac{Gm}{vR}\right)^2 \ln\left(\frac{b_{\max}}{b_{\min}}\right). \tag{1.8}$$

This expression can be simplified by noting that the velocity of the subject star is of the order of magnitude of that of a star in circular orbit at the edge of the galaxy, so that we can substitute

$$v^2 \simeq \frac{GNm}{R}, \tag{1.9}$$

which allows to write, by setting $b_{\max} = R$,

$$\frac{b_{\max}}{b_{\min}} = \frac{Rv^2}{2Gm} \simeq \frac{N}{2}. \tag{1.10}$$

The relative velocity change is

$$\frac{\Delta v^2}{v^2} \approx \frac{8}{N} \ln\left(\frac{N}{2}\right). \tag{1.11}$$

It becomes significant after n_{relax} passages if

$$\frac{\Delta v^2}{v^2}\, n_{\text{relax}} \approx 1 \quad \Leftrightarrow \quad n_{\text{relax}} = \frac{N}{8 \ln\left(\frac{N}{2}\right)}. \tag{1.12}$$

Encounters with other stars thus become non-negligible after a time

$$t_{\text{relax}} = n_{\text{relax}} \times t_{\text{cross}} \tag{1.13}$$

where t_{cross} is the typical crossing time.

We can now answer our initial question. A typical galaxy consists of $\sim 10^{11}$ stars, yielding a relaxation time of about 5×10^8 crossing times. Considering that galaxies are aged by several hundred crossing times, we conclude that stellar **collisions within them are negligible**. This result allows to model galaxies using smooth potentials rather than as an assembly of billions of point masses.

1.1.3 Globular clusters: collisional islands in a collisionless sea

Although collisions are rare, galaxies contain clumps of denser stellar systems where collisions are prevalent. The first type of star cluster is the open clusters, which are

[1] A more accurate estimation of this quantity can be obtained by using equation (A.43).

young systems, loosely bound, and rarely exceed a few billion years in age. They are composed of $10^2 - 10^4$ stars that originated together from a recent star-formation event.

The second type of clusters is called globular clusters. These are much denser than the open clusters. A typical globular cluster consists of $10^4 - 10^6$ stars distributed spherically and has a short crossing time $t_{\rm cross} \approx 1$Myr. Using equation (1.13), it is deduced that the relaxation time is very short, meaning that collisions significantly influence the structure of these systems, making them unique laboratories for studying the gravitational N-body problem. The center of these clusters is so dense that their size is generally described by three characteristic radii: (i) the core radius, where the brightness drops to half its center value; (ii) the median or half-light radius, encompassing half the cluster's total luminosity; (iii) and the tidal radius, marking the cluster's outer edge where the density drops to zero.

Their highly collisional environment makes globular clusters a factory for the formation of stellar mass black hole binaries with high eccentricity and peak gravitational wave frequencies within the LIGO band (Samsing et al., 2014, 2018a). Moreover, although a clear consensus has yet to emerge due to limitations in observed kinematics and dynamical modeling, studies are revealing indications of intermediate-mass black holes at the centers of some globular clusters (see Noyola et al., 2008; van der Marel & Anderson, 2010; McNamara et al., 2012; Lützgendorf et al., 2013a,b; Lanzoni et al., 2013; Häberle et al., 2024).

Globular clusters are found in almost all galaxies. Our Galaxy houses about 150 globular clusters, though larger elliptical galaxies, like M87, may have up to 10 000. Unlike open clusters, they are ancient and considered remnants from the galaxy's early formation stages. They can also get disrupted by tidal forces from their host galaxies, resulting in the creation of narrow stellar streams (see Murali & Dubinski, 1999; Odenkirchen et al., 2003; Grillmair, 2009; Ibata et al., 2019; Jensen et al., 2021).

1.1.4 Observational properties in a nutshell

To conclude this introductory section on galaxies, we will discuss some observational properties of elliptical and disk galaxies, drawing on insights summarized in Mo et al. (2010).

Elliptical galaxies. On the left side of the Hubble sequence, Elliptical galaxies are characterized by their smooth, elliptical surface brightness distribution, with isophotes often approximated by ellipses, defined by their minor-to-major axis ratios b/a (or ellipticities $\varepsilon = 1 - b/a$) and position angles. However, detailed modeling of their surface brightness reveals that these isophotes generally don't strictly conform to elliptical shapes, but rather exhibit "disky" or "boxy" configurations, as illustrated in Fig. 1.4.

This distinction between disky and boxy ellipticals is crucial because it corresponds to notable differences in their properties. Boxy ellipticals tend to be brighter, exhibit slower rotation, and display pronounced radio and X-ray emissions. On the other hand, disky ellipticals are generally fainter, show more significant rotation, and have minimal to no radio and X-ray emissions (Bender et al., 1989; Pasquali et al., 2007). Furthermore, the shape of the isophotes correlates with the nuclear features; disky ellipticals usually possess steep cusps, whereas boxy ones often feature central cores (Faber et al., 1997).

Elliptical galaxies have red photometric colors, indicative of an old, metal-rich stellar population. These galaxies also exhibit a color gradient, with the outer regions appearing bluer than the core (Peletier et al., 1990).

Contrary to early beliefs that elliptical galaxies were devoid of gas and dust, research has shown they possess a considerable interstellar medium, different from that in spiral galaxies (Roberts et al., 1991; Buson et al., 1993; Welch et al., 2010). Dominated by hot ($\sim 10^7$ K) X-ray emitting gas, this medium can account for a significant portion of an elliptical's mass. Additionally, ellipticals contain smaller quantities of warm ionized gas, cold gas and dust, but these components don't correlate with galaxy luminosity like in spirals. Often, dust and gas form a central disk or exhibit complex distributions (van Dokkum & Franx, 1995; Tran et al., 2001), originating from internal stellar mass loss or external accretion, evidenced by their kinematics occasionally diverging from the stars' motion (Braun et al., 1992; Temi et al., 2007).

Finally, in terms of kinematics, they generally have low rotation velocities (Fried & Illingworth, 1994).

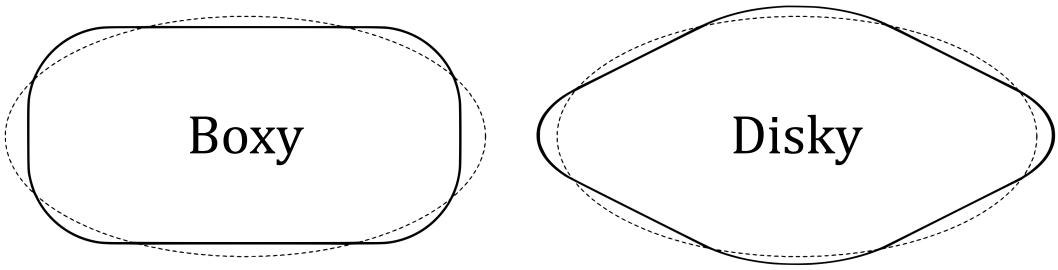

Figure 1.4: Illustration of boxy and disky isophotes shown by solid lines, with their respective best-fit ellipses represented by dashed lines.

Disk galaxies. Disk galaxies display a more intricate morphology than ellipticals, typically featuring a rotationally supported disk characterized by spiral arms and often a bar, alongside a central bulge. Surrounding this structure, a spheroidal stellar halo

stretches across large radii.

• The disk itself usually comprises both a thin and a thick component. The thick disk is notable for its excess surface brightness at considerable distances from the mid-plane and has a scale height about three times that of the thin disk, though their radial scale lengths are quite similar (Yoachim & Dalcanton, 2006).

• Bulges vary significantly across disk galaxies; they are prominent in earlier types and may be absent in later ones. Studies have explored bulge-disk decompositions across large samples of disk galaxies, finding the ratio between the bulges effective radius and the disk scale length to be relatively consistent regardless of Hubble type (see de Jong, 1996; MacArthur et al., 2003a). While most bulges have nearly elliptical isophotes, some faint bulges in edge-on, late-type disk galaxies, display boxy or even peanut-shaped isophotes. These latter bulges are typically bars that have thickened vertically.

• Over half of all spiral galaxies exhibit bar-like structures in their central areas, a characteristic not significantly influenced by spiral type, with S0 galaxies frequently featuring bars as well. These bars often have squarish isophotes and are generally elongated.

• The spiral structure is delineated by young stars, HII regions, molecular gas, and dust absorption. Galaxy disks exhibit diverse spiral formations: 'Grand-design' systems with well-defined arms, often connected to a strong bar or an interacting neighbor, and 'flocculent' systems that lack a clear large-scale pattern and consist of numerous arm segments (Peek, 1932; Reid et al., 2019; Poggio et al., 2021; Chugunov et al., 2024). The orientation of these spiral arms is typically trailing, aligning with the galaxy's rotational direction (leading being the opposite).

• Disk galaxies finally possess a stellar halo composed of old, metal-poor stars (Zibetti et al., 2004) with a large amount of substructure in the form of stellar streams (e.g. Helmi et al., 1999; Ferguson et al., 2002; Yanny et al., 2003; Bell et al., 2008; Tenachi et al., 2022; Oria et al., 2022). These streams originate from satellite dwarf galaxies and globular clusters that have been tidally stripped by tidal forces from the host galaxies. In certain instances, they can be linked back to their original stellar structures (e.g. Ibata et al., 1994; Odenkirchen et al., 2002), which allows us to learn a great deal about the history of galaxy assembly.

In contrast to elliptical galaxies, where the gas is mostly in a hot, highly ionized state, the gas in spiral galaxies primarily consist of neutral and molecular hydrogen forms, namely HI and HII (Young & Scoville, 1991). The fraction of gas mass varies significantly in the local Universe, ranging from about 5% in larger, early-type spiral galaxies (Sa/SBa) to as much as 80% in some smaller, low surface brightness disk galaxies (McGaugh & de Blok, 1997). Disk galaxies tend to appear bluer than ellipticals

with similar luminosity due to ongoing star formation, which predominantly involves younger, bluer stars.

Rotation curve. Thanks to the conservation of angular momentum along the vertical axis imposed by axisymmetry, the stars and gas in disk galaxies follow nearly circular orbits. Consequently, the dynamics of these galaxies can be well described by the circular velocity of their constituents as a function of the orbital radius. Assuming for simplicity a spherical symmetry (this is also valid for the simple model of a Mestel disk, Mestel 1963), the circular velocity is given by:

$$v_c^2 = \frac{GM(< R)}{R}, \tag{1.14}$$

with R the orbital radius, G the universal gravitational constant, and $M(< R)$ the galactic mass enclosed within radius R. Equation (1.14) thus allows us to estimate the mass content of a galaxy from measurements of the circular velocity of its constituents. Figure 1.5 shows rotation curves for the spiral galaxy NGC 2998. The data come from the SPARC database, which includes 175 late-type galaxies (spirals and irregulars). The HI+Hα rotation curves [2] , tracing the gravitational potential out to large radii, are measured using Spitzer photometry with wavelength bands at $3.6\mu m$.

There is an intriguing discrepancy in these curves, isn't there? The solid blue curve, representing the theoretical rotation curve derived from the observable matter (gas and stars), fails to match the actual measured rotation curve (black points). More strikingly, the curves diverge at larger radii. Contrary to expectations of a decrease in circular velocity with increasing distance from the galactic center, the observed velocity remains surprisingly constant!

1.2 Something more than the observable

1.2.1 Field or matter?

Changing the law of gravity. To address the issue we have just highlighted, two different approaches have emerged [3] . The first involves changing the law of gravitational attraction. For example, Modified Newtonian Dynamics (MOND) proposes

[2] The Hα line corresponds to a transition of the electron in a hydrogen atom ($n = 3 \rightarrow 2$), emitting a photon with a specific wavelength in the red part of the visible spectrum. It is a key indicator of HII regions, which are clouds of ionized hydrogen around young, hot stars. The presence of strong Hα emission indicates intense star formation activity. Therefore, this emission is used to map star-forming regions in galaxies. HI neutral gas, on the other hand, typically extends further than the ionized gas found in HII regions, allowing rotation curves to be measured at larger galactocentric radii.

[3] Are they fundamentally different? In quantum field theory, matter is merely the manifestation of a field after all...

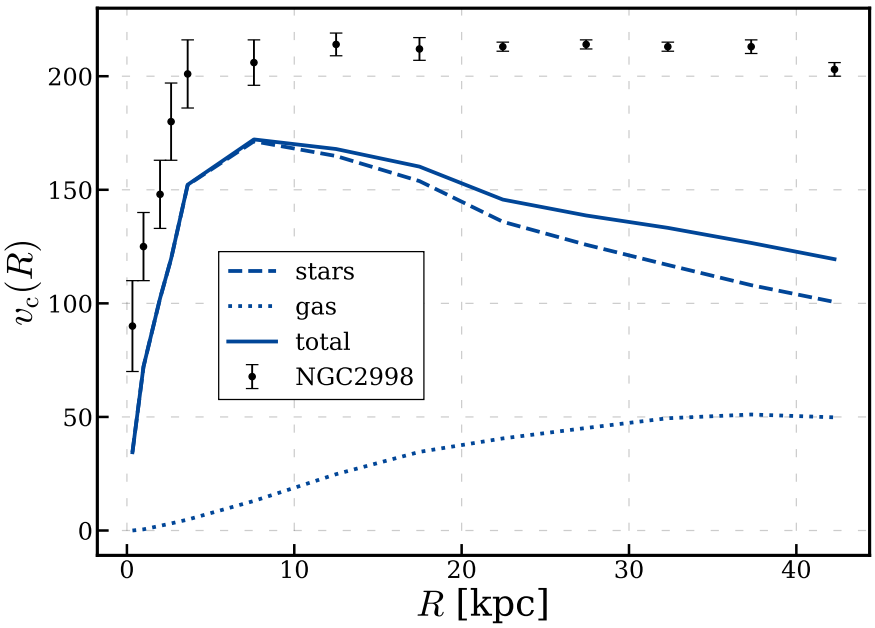

Figure 1.5: The rotation curves of the spiral galaxy NGC 2998. The blue solid curve shows the theoretical rotation curve obtained from the contribution of visible mass (gas and stars), assuming a mass-to-light ratio of $0.6\,M_\odot/L_\odot$ (from McGaugh & Schombert, 2014). The black points are the actual measurements of the rotation speed obtained using Spitzer photometry.

modifying Newton's law (Milgrom, 1983; Famaey & McGaugh, 2012) in the regime of very low accelerations (this regime is precisely what we find at large radii of galaxies, where the curves diverge in Fig. 1.5).

This modification is defined by a constant: $a_0 \simeq 10^{-10}$ ms^{-2}. In cases where $F/m = g \gg a_0$, the dynamic is described by the usual Newtonian law, i.e., $g = g_N$ (with g_N the Newtonian acceleration). Conversely, when $F/m = g \ll a_0$, a modification applies: $g = \sqrt{g_N\, a_0}$. For a test particle in circular motion around a point mass M, the balance between the radial component of the force and the centripetal acceleration yields equation (1.14):

$$\frac{v_c^2}{R} = g_N = \frac{GM}{R^2}. \tag{1.15}$$

In the regime of low acceleration, this relationship becomes:

$$\frac{v_c^2}{R} = g = \sqrt{\frac{GMa_0}{R^2}} \quad \Rightarrow \quad v_c^4(R) = v_c^4 = a_0 GM, \tag{1.16}$$

the circular velocity no longer depends on the radius; it asymptotically approaches a constant that depends only on the mass of the central object and fundamental constants. This allows to match the observed constant behavior of the rotation curve in Fig. 1.5.

ΛCDM model. The second approach is to assume that galaxies possess more mass than what can be observed with our telescopes (Faber & Gallagher, 1979; Peebles, 1980). This view is supported by the observation that the flatness of the rotation curves can be explained if the enclosed mass is proportional to the orbital radius, $M(< R) \propto R$. Therefore, this theory includes an additional component known as "dark matter" which, although invisible, significantly influences the dynamics of baryonic matter. Consequently, Equation (1.14) becomes:

$$v_c^2 = \frac{G}{R}\left(M_b(< R) + \underbrace{M_{DM}(< R)}_{\propto R}\right), \tag{1.17}$$

with $M_b(< R)$ the usual baryonic galactic mass and $M_{DM}(< R)$ the enclosed mass of invisible dark matter.

Dark matter has proven to be profoundly successful in both astrophysics and general physics, offering explanations that extend to cosmological scales. It forms a cornerstone of the ΛCDM model, which relies on three foundational assumptions to describe the Universe:

1. The cosmological principle: the Universe is homogeneous and isotropic on large scales.
2. The universality principle: gravitation is consistently described by general relativity across all scales.
3. The matter composition: the Universe primarily consists of cold dark matter [4] (CDM), baryons and radiation.

Additionally, the Universe contains dark energy, which drives the acceleration of its expansion. The cosmological constant, denoted by Λ, represents the simplest form of dark energy.

A prime example of the effectiveness of dark matter at cosmological scales can be seen in the power spectrum of the Cosmic Microwave Background (CMB) fluctuations. This background is radiation from about 300 000 years post-Big Bang, first predicted in the 1940s (Gamow, 1948a,b; Alpher & Herman, 1948a,b) and discovered by Penzias & Wilson (1965). It is linked to the era when the dense, hot plasma of subatomic particles that composed the Universe cooled sufficiently for protons and electrons to combine to form mostly hydrogen atoms. This transition from plasma to neutral atoms, known

[4] Cold because the particles move slowly compared to the speed of light.

as the recombination epoch, rendered the Universe transparent, as these atoms did not scatter thermal radiation like plasma. Consequently, this allowed photons to move freely through space, marking the emergence of the Universe's first diffuse radiation.

The CMB is crucial for understanding cosmological structures because matter perturbations left imprints on this radiation, observed as small temperature anisotropies against an otherwise isotropic background (Zeldovich & Sunyaev, 1969; Peebles, 1982a,b). These anisotropies were confirmed by the COBE and WMAP satellites and the Planck space observatory (Smoot et al., 1992; Bennett et al., 2013; Planck Collaboration et al., 2020), supporting the inflationary flat ΛCDM model.

The detailed structure of the CMB, especially its acoustic peaks, is highly sensitive to the parameters of the cosmological model that depicts the Universe, influencing the understanding of its matter content. The ΛCDM model enables the description of the CMB using six independent parameters (Planck Collaboration et al., 2020). To align with observations, the Universe must contain non-interacting, non-relativistic dark matter, which accounts for over 84% of all matter at the time of recombination and plays a crucial role in the formation and evolution of the Universe.

1.2.2 The radial distribution of dark matter

Upon considering the existence of dark matter, the critical question arises concerning its distribution around galaxies, specifically how to determine $M_{\rm DM}(< R)$ from equation (1.17). Note that for convenience, the distribution of dark matter is also described using its density profile, noted ρ. The flat rotation curves of spiral galaxies suggest that $M_{\rm DM}(< R)$ is proportional to R. If we assume the simplest scenario where dark matter is distributed in spherical halos encompassing galaxies (we will now use the notation for radius in spherical coordinates r), this linear dependence of $M_{\rm DM}(< r)$ implies that $\rho \propto r^{-2}$ because:

$$M(< r) = \int_0^r 4\pi\tilde{r}^2\rho(\tilde{r})d\tilde{r}. \tag{1.18}$$

The simplest density model satisfying this dependence on r is the isothermal sphere, given by the following expression:

$$\rho(r) = \frac{\sigma^2}{2\pi G r^2} \tag{1.19}$$

where σ is the velocity dispersion and G is the gravitational constant. This model was initially used to describe dark matter halos and was supported by observations at the time. Initially at the galactic scale, with White et al. (1983) demonstrating with galaxy binaries that the relative velocity dispersion does not depend on the separation between each pair, which is a characteristic of the isothermal sphere model [5] . Then, at the scale

[5] Their observations on how velocity differences depend on the luminosity and separation resulted in estimated parameters of $\alpha = 0.25, \beta = 0$ for the scaling relation $\Delta v^2 \sim L^\alpha r_{\rm p}^{-2\beta}$ (where $r_{\rm p}$ represents

of galaxy clusters, Tully (1982) showed that the number density of luminous galaxies in the Virgo Cluster falls off as r^{-2} (after averaging over angles to account for the non-spherical shape of the Virgo supercluster). Thus, across the range from individual or binary galaxies to superclusters, the mass (or mass excess) density profile consistently seems to follow an r^{-2} distribution.

A few years later, however, studies using numerical simulations showed that dark matter halos are not perfectly described by the simple isothermal sphere profile, but rather have gently changing logarithmic slopes (Dubinski & Carlberg, 1991; Navarro et al., 1995). Navarro et al. (1996) showed that the density profiles of cold dark matter (CDM) halos across all masses could be uniformly described by scaling an empirical universal profile:

$$\rho(r) = \rho_0 \left(\frac{r}{r_\mathrm{s}}\right)^{-1} \left[1 + \frac{r}{r_\mathrm{s}}\right]^{-2}. \tag{1.20}$$

This formula is a specific instance of the broader Zhao profile (Zhao, 1996), expressed as:

$$\rho(r) = \rho_0 \left(\frac{r}{r_\mathrm{s}}\right)^{-\gamma} \left[1 + \left(\frac{r}{r_\mathrm{s}}\right)^{\alpha}\right]^{\frac{\gamma-\beta}{\alpha}}, \tag{1.21}$$

where $\alpha = 1$, $\beta = 3$ and $\gamma = 1$ define the outer, transitional, and inner logarithmic slopes of the density profile, respectively. The scale radius r_s indicates where the profiles shape transitions, and:

$$\rho_0 = \rho_\mathrm{crit}\delta_\mathrm{c} \quad \text{with} \quad \rho_\mathrm{crit} = \frac{3H^2}{8\pi G} \quad \text{and} \quad \delta_\mathrm{c} = \frac{200}{3}\frac{c^3}{[\ln(1+c) - c/(1+c)]} \tag{1.22}$$

where ρ_crit is the critical density of the Universe, H is the Hubble constant, and $c = r_{200}/r_\mathrm{s}$ is a dimensionless parameter known as the halo concentration. Here, r_{200} is defined as the radius within which the mean enclosed density is $200 \times \rho_\mathrm{crit}$. In the remainder of this manuscript, we will associate this radius with the virial radius, used to characterize the size of a dark matter halo.

The NFW profile exhibits a shallower slope than the isothermal profile near the center of a halo and a steeper one in the outer regions. It remains the predominant model for characterizing dark matter halo distributions, despite its limitations in accounting for density cores, which will be discussed further in Chapter 2.

1.2.3 Stellar-to-halo mass relation

In the ΛCDM model, the dark matter halos are fundamental to galaxy formation, acting as gravitational wells that attract baryonic matter after the Big Bang (White &

the projected distance). A β value of 0 indicates an isothermal interaction potential. Within such a potential, the relationship $\Delta v^2 \sim L^\alpha$ is scale-independent.

Rees, 1978; Blumenthal et al., 1984; Springel et al., 2005). This process begins with the rapid growth of baryonic fluctuations matching that of dark matter, following recombination at $z_{\rm rec} \approx 1\ 100$ [6] . The fluctuations in smaller masses evolve into nonlinear and virialized states, organizing into progressively larger systems through hierarchical clustering. Subsequently, ordinary matter in systems with masses ranging from 10^8 to $10^{12} M_\odot$ cools efficiently within these dark matter halos, leading to galaxy formation. In contrast, larger mass fluctuations result in the formation of galaxy clusters. Thus, the inner regions of galaxies show a strong correlation between the baryon-to-dark matter ratio and their stellar and total mass, as well as the environment and hydrodynamical processes (e.g., stellar and/or active galactic nuclei feedback).

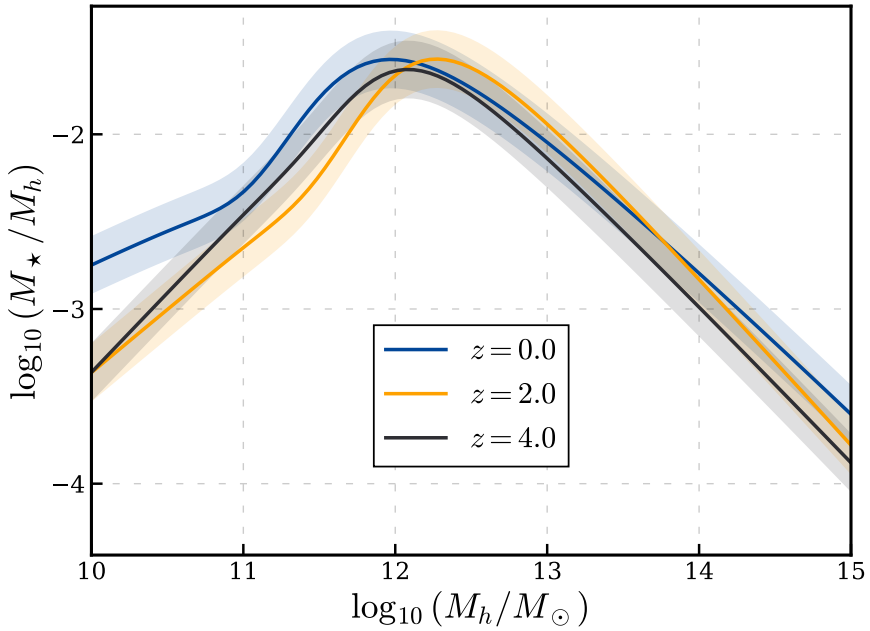

Figure 1.6: Stellar mass fraction relative to the dark matter halo mass across different redshifts. Halos around $\sim 10^{12} M_\odot$ consistently show higher star formation efficiency across all epochs. In contrast, halos with higher or lower masses display drastically reduced efficiency. This curves are based on the five-parameter fit function from Behroozi et al. (2013).

Figure 1.6 illustrates the correlation between the stellar mass of a galaxy and its dark matter halo mass across various redshifts. This correlation is modeled based on the five-parameter fit function proposed by Behroozi et al. (2013), with comparable findings reported in several other studies (see Yang et al., 2009; Conroy & Wechsler, 2009; Behroozi et al., 2010; Moster et al., 2010; Yang et al., 2012; Leauthaud et al., 2012; Moster et al., 2013). To achieve this, they start with dark matter simulations, which

[6] The redshift z measures the expansion of the universe, reflecting the shift in wavelengths of light from distant objects. The higher the redshift, the older and more distant the observed object is.

provide the properties of halos over time and their assembly history as they grow and merge. On top of that, they add a galaxy formation model, SFR $= f(M_h, \dot{M}_h, z)$, where SFR is the star formation rate, M_h the halo mass, $\dot{M}_h$ the rate of mass change, and z the redshift. This formulation, while speculative, assigns a star formation rate to each halo, allowing for the calculation of the stellar mass (as well as color and luminosity) by integrating the halo's mass accretion and merger history. Each model variation generates a mock Universe which is then compared against actual observational data. Through this comparison, a likelihood function is derived and then fit using Markov Chain Monte Carlo (MCMC) methods to identify the allowed range of physical models that reproduce observations.

We observe in Fig. 1.6 that halos with a mass around $\sim 10^{12} M_\odot$ are notably more efficient at forming stars compared to those larger or smaller, where star formation efficiency drops off dramatically. This difference in efficiency is interpreted as a consequence of feedback processes in galaxies, where energy, momentum, and mass are transferred from stars, supernovae, and Active Galactic Nuclei (AGN) back into the interstellar medium. These processes play a crucial role in shaping galactic properties such as star formation rates (Baldry et al., 2006; Wilman et al., 2010; Fossati et al., 2015; Arora et al., 2019), gas content (Shangguan et al., 2018), stellar and gas kinematics (Frosst et al., 2022; Waterval et al., 2022), and chemical compositions (Planelles et al., 2014). At the low mass end of the stellar mass function, stellar winds and supernova explosions limit star formation in smaller halos (Dekel & Silk, 1986), while in larger halos, AGN feedback from supermassive black holes prevents further star formation by expelling vast quantities of material from the galaxy's core (Silk & Rees, 1998; Silk & Mamon, 2012). Furthermore, these feedback processes may also influence the dark matter distribution within galaxies, providing an explanation for the creation of density cores as discussed in Chapter 2.

1.3 Dwarf galaxies, unique laboratories for studying the Universe

The low mass end of Fig. 1.6 is the realm of dwarf galaxies, the most dark matter-dominated objects in the Universe. By number, these are the most abundant galaxies, yet they stand out due to their unique characteristics which make them crucial for testing theoretical models. Despite their prevalence, dwarf galaxies do not fit neatly into the traditional Hubble sequence, highlighting their distinct nature from larger galaxies not only in scale but also in intrinsic properties and evolutionary paths. Their key difference from larger galaxies often lies in their capacity to retain baryonic matter during evolutionary processes. While larger late-type galaxies tend to maintain a constant central surface brightness indicating the retention of initial baryonic components, dwarf

galaxies frequently lose a significant portion of their baryons, likely due to supernova-driven winds (Dekel & Silk, 1986) or tidal interactions (Peñarrubia et al., 2008; Wetzel & White, 2010) which are more disruptive in galaxies with shallower gravitational wells (Sales et al., 2022).

Types of dwarf galaxies. Dwarf galaxies are generally characterized by certain mass or luminosity thresholds: (i) a virial mass (mass within r_{200}) less than or equal to $10^{11} M_{\odot}$ (Saifollahi, 2022), (ii) an absolute magnitude in the V-band fainter than $\mathcal{M}_V \sim -18$ (Grebel et al., 2003; McConnachie, 2012). Despite these parameters, dwarf galaxies do not form a homogeneous group; they include various types (Saifollahi, 2022):

1. **Early-type dwarf spheroidals.** Dwarf spheroidals (**dSphs**) and dwarf ellipticals (**dEs**) are the predominant dwarf galaxy types found in galaxy groups and clusters. They are characterized by their red color and lack of gas. Both dSphs and dEs exhibit low luminosity and surface brightness, with light profiles that typically follow an exponential profile. They generally possess a V-band absolute magnitude ranging from-16 to -8 and an effective radius between 0.1 and 2 kiloparsecs (kpc). The main distinction between dSphs and dEs lies in their brightness and surface brightness, with dSphs being the dimmer and less luminous counterparts of dEs. Some early-type dwarfs host a nuclear star cluster at their center (Neumayer et al., 2020).

2. **Late-type dwarf irregulars.** Dwarf irregulars (**dIs**), found primarily in the low-density regions and peripheries of galaxy groups and clusters, are characterized by their blue color, abundant gas, and ongoing star formation. These low-mass galaxies exhibit an irregular morphology and share similar attributes such as luminosity, effective radius, and surface brightness with their early-type dwarf counterparts.

3. **Blue compact dwarfs (BCDs)** are a more compact form of dIs. These galaxies, characterized by their blue hue, feature several bright knots and active star-forming regions, all set within a low surface brightness envelope. Despite sharing similar luminosity levels with late-type dwarf irregulars, BCDs have significantly smaller effective radii.

4. **Ultra faint dwarfs (UFDs)** are the faintest category of dwarf galaxies currently identified, exhibiting luminosities comparable to or even lower than those of typical Milky Way globular clusters (GCs), with absolute magnitudes $\mathcal{M}_V > -8$. Unlike GCs that generally have radii around $2-3$ parsecs (pc), UFDs are more extended, with effective radii around 100 pc. These galaxies are not only the most dark matter-dominated but also the most metal-poor objects in the Universe (Simon, 2019).

5. **Ultra compact dwarfs (UCDs)** are dense stellar systems that surpass typical Milky Way GCs in size, brightness, and mass. These systems display absolute magnitudes between $\mathcal{M}_V = -13$ and -10 and maintain effective radii less than 100 pc. Commonly located in the dense centers of galaxy clusters or near massive galaxies, UCDs exhibit scaling relations similar to those of nuclear star clusters in dwarf early-type galaxies. This resemblance indicates that many UCDs may be the remnants of nuclear star clusters from dwarf galaxies that were tidally disrupted in high-density environments (Neumayer et al., 2020). Some UCDs are thought to have originated from GCs (Alfaro-Cuello et al., 2019).

Our knowledge primarily stems from dwarf galaxies within the Local Group, around our Milky Way, where approximately sixty such galaxies have been documented. Observations extend to denser environments like galaxy groups and clusters, hosting a greater diversity of morphologies influenced by various physical processes (Gunn & Gott, 1972; Boselli & Gavazzi, 2014).

Simulation of dwarf galaxies. The challenges of representing dwarf galaxies in cosmological simulations are substantial due to their low mass. Typically, these simulations encompass vast volumes, on the order of $100\,\mathrm{Mpc}^3$. This extensive scope often precludes achieving the fine mass resolution necessary to accurately simulate the smallest galaxies, given the current limits of computing capabilities. Nevertheless, recent advancements have led to the development of cosmological simulations that are capable of resolving systems with stellar masses $\gtrsim 10^7 M_\odot$, albeit within significantly smaller volumes. For instance, the NewHorizon simulation (Dubois et al., 2021) operates within a zoom-in region of $16\,\mathrm{Mpc}^3$, embedded within a larger box. This region is re-simulated at a high resolution, achieving a spatial resolution of 34 pc within galaxies. Such precision allows the simulation to capture the multi-phase nature of the interstellar medium. It also boasts a dark matter mass resolution of $M_{\mathrm{DM}} = 1.2 \times 10^6 M_\odot$ for the best-resolved region. Similarly, the Illustris TNG50 simulation (Pillepich et al., 2019) achieves a comparable mass resolution of $M_{\mathrm{DM}} = 4.5 \times 10^5 M_\odot$ and a spatial resolution up to 100 pc.

Given their low luminosity and challenging observability, combined with the difficulty of accurately simulating their low mass, dwarf galaxies remain relatively unexplored despite their abundance. These characteristics position them as critical yet underutilized keys to unlocking deeper insights into the assembly of more massive galaxies and the elusive nature of dark matter. By advancing our understanding of dwarf galaxies, we can significantly enhance our knowledge of cosmic structure formation and evolution.

1.4 Black holes

As discussed in previous sections, galaxies contain stars, gas, dust, and dark matter. They also harbor well-known yet enigmatic objects: black holes. Before delving into the interaction between black holes and galaxies, it is essential to define these objects.

1.4.1 Definition and types of black holes

A black hole is an object with such strong gravity that nothing, not even light or other electromagnetic waves, can escape its pull [7] . Consider an object with mass $M_\bullet$. We can calculate the size this object must have for even light to be unable to escape. This requires its potential energy to be greater than the kinetic energy of light [8] :

$$\frac{GM_\bullet}{r} > \frac{1}{2}c^2 \quad \Leftrightarrow \quad r < r_{\rm Sch} \equiv \frac{2GM_\bullet}{c^2} \tag{1.23}$$

where G is the gravitational constant, c is the speed of light, and $r_{\rm Sch}$ is the critical radius satisfying this condition, known as the Schwarzschild radius. Any object with mass $M_\bullet$ and a size smaller than this radius is a black hole.

To get a sense of the magnitudes involved, consider this example: for Earth (mass $m^{\rm E} = 5.972 \times 10^{24}\,{\rm kg}$) to become a black hole, it would need to be compressed to a size smaller than $r^{\rm E}_{\rm Sch} = 9\,{\rm mm}$, roughly the size of a grape! Notice that the requirement for an object to be a black hole does not constrain its mass, allowing theoretical freedom regarding this property. Today, we distinguish three populations of black holes in the Universe, categorized by their mass [9] :

1. **Stellar-Mass Black Holes:** These black holes form from the gravitational collapse of massive stars. Their masses range from a few solar masses ($M_\odot$) to about $60 - 80\,M_\odot$, with the upper limit for this category set at $100\,M_\odot$.

2. **Intermediate-Mass Black Holes (IMBHs):** This type of black hole is hypothetical, with limited direct evidence of their existence. They are believed to have masses between those of stellar-mass and supermassive black holes, estimated to be around $100 - 10^6\,M_\odot$ [10] .

[7] For simplicity, we refer to it as an object with mass, though it can also be viewed as a region of spacetime with extreme curvature.

[8] Note here that this is a Newtonian derivation to obtain an order of magnitude, which is strictly speaking not correct, as black holes are objects predicted by general relativity.

[9] There are theoretical extensions proposing other mass ranges, such as mini black holes with masses smaller than stellar-mass black holes, but we will not discuss these cases in this manuscript.

[10] The upper limit varies among authors, with some placing it at $10^4 M_\odot$ and others at $10^5 M_\odot$. Since this manuscript focuses particularly on these black holes, it is prudent to adopt the broadest possible mass range to consider the maximum number of scenarios, hence setting the limit at $10^6 M_\odot$. It is important to remember that this is a convention.

3. **Supermassive Black Holes (SMBHs):** These are the most massive black holes, with masses exceeding $10^6 M_\odot$. As we will see in the following subsections, there is still much uncertainty regarding their formation.

1.4.2 Dynamical Friction

After exploring the grandeur of galaxies and the singularity of black holes, we arrive at an intriguing intersection: what happens when a black hole navigates through the sea of stars in a galaxy? The resulting gravitational interactions reveal a fundamental phenomenon in galactic astrophysics, known as dynamical friction. In this section, we will present a concise overview of dynamical friction to facilitate reading. Nevertheless, a complete and pedagogical derivation can be found in Appendix A.

Chandrasekhar's dynamical friction. Consider the case of a black hole with mass M moving within a galaxy composed of stars with mass m. During an encounter with one of these stars, the black hole's velocity is perturbed by the gravitational interaction between the two objects. It can be shown (see Sect. A.1) that this encounter induces a change in the black hole's velocity, both parallel and tangential to its motion, given by [11]

$$|\Delta v_{M\perp}| = \frac{2\,m\,v_0}{M+m}\,\frac{b/b_{90}}{1+b^2/b_{90}^2} \tag{1.24}$$

$$|\Delta v_{M\parallel}| = \frac{2\,m\,v_0}{M+m}\,\frac{1}{1+b^2/b_{90}^2} \tag{1.25}$$

where v_0 is the norm of the relative velocity vector between the two objects, b is the impact parameter of the encounter, and $b_{90} \equiv \frac{G(M+m)}{v_0^2}$.

Let us now consider the cumulative effect of all encounters when the black hole orbits within the galaxy. As we have seen in Section 1.1.2, the perpendicular perturbations cancel out on average due to the stochastic nature of the encounter process. Although the mean of the squared perturbations is not zero, leading to a stochastic alteration of the black hole's trajectory, the time required for this modification to become significant is much greater than the age of the Universe for galaxies. Conversely, the perturbations parallel to the black hole's motion do not cancel out, and their sum generates a force. Assuming a homogeneous medium, we obtain an analytical expression (see Sect. A.2):

$$\frac{d\overrightarrow{v_M}}{dt} = -8\pi^2 G^2 m(M+m)\ln\left(1+\Lambda^2\right)\frac{\overrightarrow{v_M}}{v_M^3}\int_0^{v_M} v_m^2\, f(\overrightarrow{v_m})dv_m \tag{1.26}$$

[11] In the limit of large impact parameters: $|\Delta v_{M\perp}| \simeq \frac{2\,m\,v_0}{M+m}\frac{b_{90}}{b} = \frac{2\,m\,v_0}{M+m}\frac{G(M+m)}{b\,v_0^2} = \frac{2\,G\,m}{b\,v_0}$, which corresponds to the expression obtained in equation (1.4).

with $\Lambda \equiv \frac{b_{\max}}{b_{90}} = \frac{b_{\max} v_0^2}{G(M+m)}$ where $b_{\max}$ is the maximum impact parameter. Equation (1.26) is often referred to as the Chandrasekhar's dynamical friction formula (Chandrasekhar, 1943). If we then assume that the velocities are distributed according to a Maxwellian distribution, we obtain

$$\boxed{\frac{d\overrightarrow{v_M}}{dt} = -2\pi\, G^2\, \rho_0\, (M+m) \ln\Big(1+\Lambda^2\Big) \left[-\frac{2X}{\sqrt{\pi}} \exp\Big(-X^2\Big) + \mathrm{erf}(X)\right] \frac{\overrightarrow{v_M}}{v_M^3}} \tag{1.27}$$

with $X \equiv \frac{v_M}{\sqrt{2}\,\sigma}$ where σ is the velocity dispersion of the stars, and $\mathrm{erf}(x)$ is the error function [12] . In the case of interest for IMBHs or SMBHs where $M \gg m$ and since $\Lambda \gg 1$ typically, we can simplify the expression:

$$\boxed{\frac{d\overrightarrow{v_M}}{dt} = -4\pi\, G^2\, \rho_0\, M \ln(\Lambda) \left[-\frac{2X}{\sqrt{\pi}} \exp\Big(-X^2\Big) + \mathrm{erf}(X)\right] \frac{\overrightarrow{v_M}}{v_M^3}} \tag{1.28}$$

The force generated by the encounters is collinear and opposite to the black hole's velocity, acting as a frictional force that causes it to lose energy and angular momentum during its motion. Consequently, the orbiting black hole will spiral towards the center of the galaxy. It is noted that: (i) the force ($\overrightarrow{F} = M \times d\overrightarrow{v_M}/dt \propto M^2$) is proportional to the square of the black hole's mass, meaning a more massive black hole falls more quickly towards the center of the galaxy; (ii) $\overrightarrow{F}$ depends on the density of stars ρ_0 regardless of their mass m.

The limitations of Chandrasekhar's formula. This derivation has several limitations: (i) we do not account for the response of the medium; indeed, the black hole perturbs the surrounding stars, and this perturbation in turn affects the black hole. Additionally, although we consider the gravitational attraction between the black hole and the stars, we do not take into account the mutual attraction between the stars themselves; (ii) to obtain equation (1.26), we assume that the stars pass by M in Keplerian hyperbolae (cf. Sect. A.1). However, the orbits in the combined gravitational fields of M and the galaxy are more complex. These simplifications are particularly problematic when the black hole is near the galactic center, where the integrated galactic mass is comparable to the black hole's mass. We will discuss this point in the following chapters. For most general cases, however, N-body simulations and linearized response calculations show that Chandrasekhar's formula provides a remarkably accurate description of the drag experienced by a body orbiting in a stellar system (White, 1983; Bontekoe & van Albada, 1987; Zaritsky & White, 1988; Weinberg, 1989; Cora et al., 1997) even for non-spherical distribution if we take into account the correction for velocity anisotropy

[12] $\mathrm{erf}(x) = \frac{2}{\sqrt{\pi}} \int_0^x \exp\big(-t^2\big)\, dt$

(see Binney, 1977; Peñarrubia et al., 2004).

Here, we have focused on dynamical friction in a collisionless medium, and our stars can be replaced by collisionless dark matter particles without changing the results. It is worth noting that dynamical friction also exists in gaseous media where more advanced physics is involved (see Ostriker, 1999).

1.4.3 Chasing Shadows

The detection of black holes. Massive black holes (MBHs) are expected to migrate to the centers of galaxies due to dynamical friction, making these regions prime targets for observation with our telescopes. The galactic centers are typically rich in gas, which MBHs can accrete, leading to significant luminosity, according to:

$$\begin{aligned} L &= \epsilon\, \dot{M}_{\rm in}\, c^2 \\ &= 5 \times 10^{20} L_\odot\, \epsilon\, \frac{\dot{M}_{\rm in}}{M_\odot.{\rm yr}^{-1}}, \end{aligned} \tag{1.29}$$

where $\epsilon \simeq 0.1$ is the average efficiency of converting rest mass into energy, $\dot{M}_{\rm in}$ is the inflow rate of mass towards the MBH [13] , c is the speed of light and $L_\odot$ is the luminosity of the Sun. This high luminosity makes MBHs observable. The energy output from these AGN can be so immense that they outshine their host galaxies. Among AGNs, quasars (quasi-stellar objects) are the most luminous and can be detected at great distances. Quasars emit energy at levels hundreds to thousands of times greater than that of the Milky Way and exhibit high redshifts, indicating their significant distances. Consequently, quasars are crucial for studying MBHs in the early Universe. As of now, the SDSS DR16 quasar catalog has listed 750 414 observed quasars (Lyke et al., 2020). Another method for detecting MBHs involves analyzing the dynamics of stars within their sphere of influence. By resolving the kinematics of these stars, one can infer the presence of a MBH and estimate its mass using Jeans modeling (Voggel et al., 2022). Over the past few decades, these techniques have revealed MBHs at the centers of massive galaxies (Kormendy & Richstone, 1995) and more recent studies, with various probes (e.g., optical, X-ray, Radio or infrared) have brought to light the presence of such black holes within dwarf galaxies (Reines et al., 2013; Pardo et al., 2016; Mezcua et al., 2018, 2019; Zaw et al., 2020; Cann et al., 2020).

A co-evolution between black holes and galaxies. The mass of MBHs correlates with various properties of their host galaxy such as the bulge's velocity dispersion (Ferrarese & Merritt, 2000; Gebhardt et al., 2000; Tremaine et al., 2002; Gültekin et al.,

[13] If $\dot{M}$ is the rate of mass growth of the black hole by accretion, then $dM = (1-\epsilon)\, dM_{\rm in}$.

2009; van den Bosch, 2016, see Fig. 1.7), mass (Magorrian et al., 1998; Häring & Rix, 2004), luminosity (Marconi & Hunt, 2003), concentration (Graham & Driver, 2007) or other host properties such as the number of globular clusters (Burkert & Tremaine, 2010) or their global velocity dispersion (Sadoun & Colin, 2012). These correlations suggest a common past history between MBHs and galaxies: as galaxies increase their mass via accretion and mergers [14] , MBHs correspondingly increase their mass (Malbon et al., 2007; Anglés-Alcázar et al., 2013).

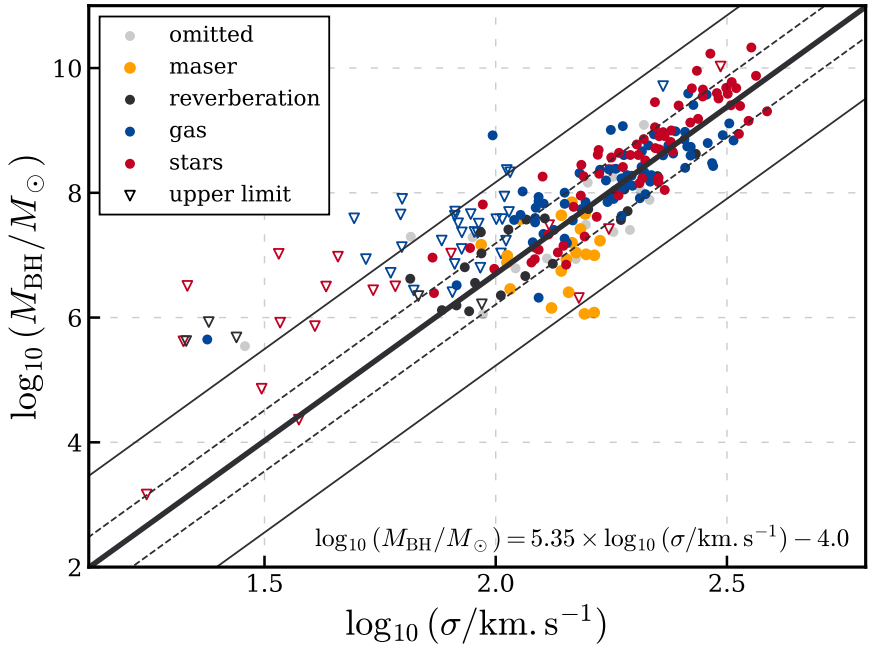

Figure 1.7: Scaling relation between black hole mass and stellar velocity dispersion in the bulge. The $M-\sigma$ relation is represented by the thick solid black line: $\log_{10}(M_{\rm BH}/M_\odot) = \alpha \log_{10}(\sigma/{\rm km.s^{-1}}) + \beta$, with $\alpha = 5.35 \pm 0.23$ and $\beta = -4.0 \pm 0.5$. The gray dashed and solid thin lines denote one and three times the intrinsic scatter of the relation $\epsilon = 0.49 \pm 0.03$. The fit is based on 230 galaxies, ranging from dwarf to elliptical galaxies. The fit and data selection are from van den Bosch (2016). Upper limits are shown as open triangles. Different colors represent different types of black hole mass measurements (see van den Bosch, 2016, Section 2 for more details).

Due to the co-evolution of MBHs and galaxies, it is expected that black holes initially possess small masses in the early Universe, positioned at the lower left of the $M-\sigma$ relation shown in Fig. 1.7. Over time, they would grow through accretion and mergers alongside their host galaxies, ultimately reaching the upper right of the relation. However, recent observations have challenged this scenario. Indeed, very massive quasars,

[14] The correlation between black hole mass and bulge properties indicates that mergers play a crucial role, as classical bulges are typically formed from the merging of disks.

on the order of $10^9\,M_\odot$, have been observed at high redshifts ($z > 6.4$), when the Universe was less than 0.9 Gigayear (Gyr) old (Willott et al., 2003; Mortlock et al., 2011; Venemans et al., 2013, 2015; Bañados et al., 2015, 2018). The most extreme example in mass to date is a SMBH of $(1.6 \pm 0.4) \times 10^9 M_\odot$ at $z = 7.642$, which corresponds to ~ 670 million years after the Big Bang (Wang et al., 2021).

The problem of mass growth. One might think that black holes could achieve these masses rapidly through intense accretion, but under the spherical geometry assumption, accretion is theoretically limited by the Eddington limit, beyond which radiation pressure counteracts gravitational attraction. Above the Eddington limit, radiation pressure exceeds gravitational pull, causing material to be expelled rather than accreted by the black hole. While it is theoretically possible for a black hole starting with $1\,M_\odot$ to grow by 9 orders of magnitude in slightly over 1 Gyr, this would require continuous accretion over its entire lifetime and the feedback produced by the stars and the black hole itself would also have to be negligible, which is highly unlikely.

To address this issue, the initial seed from which black holes grow would need to be more massive. Indeed, it is much easier for a black hole of $100 - 10^5\,M_\odot$ to reach the masses observed at high redshifts (Haiman & Loeb, 2001). Thus, it appears that IMBHs may hold the key to this problem. The question then becomes how they form and whether they truly exist. Regarding their formation, several models have been proposed, such as population III stars and direct collapse (see Volonteri & Bellovary, 2012), with dense environments also potentially providing an answer. Proposed scenarios include stellar-mass black hole mergers (Miller & Hamilton, 2002) and star collisions (Portegies Zwart et al., 2004) in globular clusters, but many uncertainties still surround these processes. As for observations, the situation is not much clearer. There are observations of both nuclear and non-nuclear IMBHs in dwarf galaxies (Mezcua & Lobanov, 2011; Reines et al., 2013; Secrest et al., 2015; Baldassare et al., 2015, 2017; Reines et al., 2020) [15] but their detection is still debated in the low mass regime ($10^3 - 10^4\,M_\odot$). Some studies also suggest the detection of such black holes at the centers of globular clusters (see Noyola et al., 2008; van der Marel & Anderson, 2010; McNamara et al., 2012; Lützgendorf et al., 2013a,b; Lanzoni et al., 2013; Häberle et al., 2024), but due to limitations in observed kinematics and dynamical modeling, a clear consensus has yet to emerge.

1.4.4 Gravitational waves: a new look at the Universe

IMBHs are difficult to observe because, being less massive than SMBHs, they accrete less, if at all, and have a smaller impact on the dynamics of surrounding stars.

[15] See Mezcua (2017) for a review of the observations.

Additionally, they migrate to the centers of galaxies more slowly due to dynamical friction, and as we will see later, this migration time can be so prolonged that they remain in off-center orbits in some galaxies. This off-center positioning exacerbates detection challenges because they are located in regions with lower densities of gas and stars. Furthermore, unlike galactic centers, there is no preferential zone to target with telescopes since they can wander anywhere within the galaxy.

However, since 2015, a revolution has occurred in observational astrophysics with the detection of the first stellar-mass black hole coalescence through gravitational waves. The initial detection of these waves by the LIGO interferometer (Laser Interferometer Gravitational-Wave Observatory; Abbott et al., 2016) marked the beginning of a new era in astrophysics, allowing us to probe cosmic phenomena previously inaccessible through traditional astronomy. These waves are generated when two black holes spiral towards each other before merging. They propagate across the Universe at the speed of light, distorting spacetime as they pass.

Since the first detection in 2015, several observatories have been built and improved to detect these waves with increasing precision. The main detectors currently in operation are LIGO (LIGO Scientific Collaboration et al., 2015) in the United States and Virgo (Accadia et al., 2012; Acernese et al., 2015) in Europe. These detectors can identify black hole mergers ranging from a few solar masses to several tens of solar masses, with the most massive merger detected so far involving black holes of $85\,M_\odot$ and $66\,M_\odot$, forming a remnant of $142\,M_\odot$ (Abbott et al., 2020). To date, over 90 merger events have been observed [16] (Abbott et al., 2023).

The Future of Gravitational Waves. Although we are currently limited to detecting lower-mass black holes, the future of gravitational wave detection is promising with the development of even more sensitive detectors. Among them, the future space interferometer LISA (Laser Interferometer Space Antenna; Amaro-Seoane et al., 2017), scheduled for the 2030s, will be capable of detecting very low-frequency gravitational waves, opening a window to more massive black holes. This instrument will be able to detect mergers involving IMBHs (Amaro-Seoane et al., 2017), bridging the observational gap between stellar-mass and supermassive black holes. The coming years will be crucial for our understanding of these types of black holes, making it essential to develop our theoretical models to best interpret this new data.

[16] Black hole-black hole merger or black hole-neutron star merger.

1.5 Outline of this thesis

In this thesis, I aim to deepen our understanding of the dynamics of IMBHs within the unique setting of dwarf galaxies. In Chapter 2, I first explore the centers of these galaxies to study the formation of density cores. I study the cusp-core discrepancy by examining the interplay between dark matter and baryonic matter through feedback processes. The presence of such cores significantly impacts orbital dynamics, which I will examine in Chapter 3 by analyzing their effect on the structure of Lagrange points and the influence radius of a black hole binary system. I propose a new scenario for IMBH mergers occurring outside the galactic center, initiated by gravitational capture. Chapter 4 delves into the phenomenon of gravitational capture within a galactic context, exploring its behavior, properties, and dependence on initial conditions to build a comprehensive understanding of this process. In Chapter 5, I will derive a capture probability based on specific physical assumptions. Finally, Chapter 6 presents my conclusions and discusses future perspectives for the study of off-center black hole mergers.

A detour to the centers of galaxies: the formation of cores

2

Overview

In this chapter, we explore the core of galaxies to better understand the interplay between dark matter and baryonic matter. We begin by outlining the cusp-core discrepancy problem and then attempt to explain this divergence using a theoretical framework. Next, we present the simulation setup used to test the theoretical model and our results. Finally, we discuss the consequences of the presence of a density core on the orbital dynamics of perturbers, which partly motivates the work presented in the following chapters. A summary of the chapter is available in Section 2.6.

2.1 The cusp-core discrepancy

In the ΛCDM model, large scale structures such as galaxy clusters are governed by dark matter, while baryons come into play later in the history of the Universe. Consequently, simulations using only dark matter are often employed to understand the formation of large structures up to the early stages of galaxy formation. These simulations are particularly useful for deriving the density profile of dark matter halos, indicating that this profile is universal across all scales (Dubinski & Carlberg, 1991; Navarro et al., 1995, 1996; Newman et al., 2013, cf. Eq. 1.20). A notable feature of this profile is the presence of a density divergence at the center of halos, known as the "cusp" ($\rho \propto r^{-\gamma}$ with $\gamma = 1$). However, observations have shown that the centers of some dark matter halos actually exhibit a constant density, i.e., a density core instead

of a divergence (Moore, 1994; de Blok et al., 2008; de Blok, 2010; Oh et al., 2011, 2015). Figure 2.1 shows the density profiles of seven dwarf galaxies taken from the H_I Nearby Galaxy Survey (THINGS). It is observed that the data flattens at the centers of the halos, deviating from the NFW (cusp) profile. This indicates a discrepancy between the predictions of dark matter-only simulations and observational data.

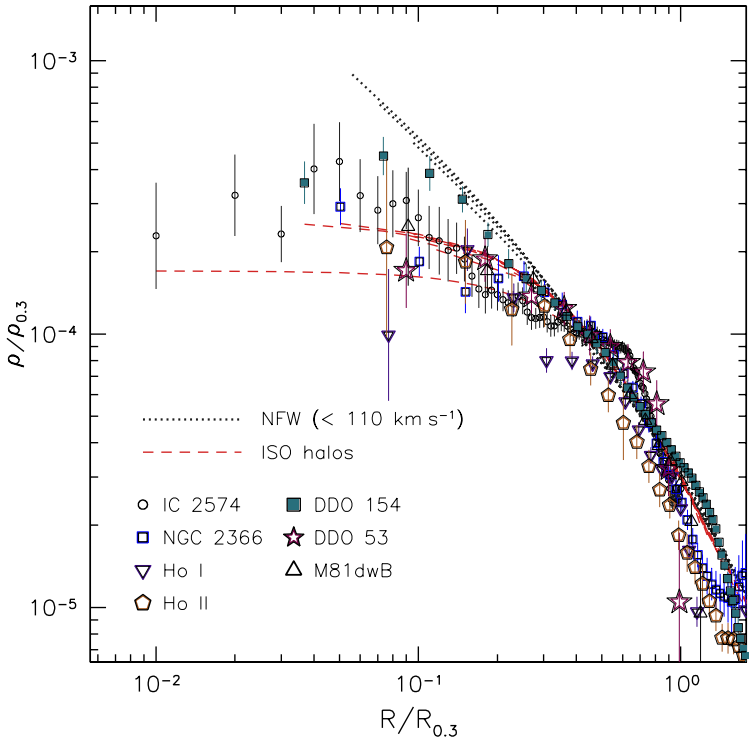

Figure 2.1: Dark matter density profiles of seven dwarf galaxies taken from the H_I Nearby Galaxy Survey (THINGS). The black dotted curves represent the NFW density profiles (with an inner logarithmic slope $\gamma = 1$), and the red dashed curves represent the best fits with pseudo-isothermal halo models (inner logarithmic slope $\gamma = 0$). It is evident that the data flattens and deviates from the black dotted curves at the centers of the halos, indicating the presence of density cores. This figure is from Oh et al. (2011).

Alternatives to cold dark matter. To explain this cusp-core discrepancy, one approach is to modify dark matter to create density cores. Spergel & Steinhardt (2000) proposed a model in which dark matter particles experience weak self-interaction on kilo- to megaparsec scales. This interaction creates cores similar to those observed in dwarf galaxies (Burkert, 2000). Another popular model is Warm Dark Matter, which posits that dark matter is composed of particles with masses around the keV scale [1], resulting in significant thermal motion that erases small-scale perturbations (Colín et al.,

[1] $1\,\mathrm{keV}/c^2 \simeq 1.783 \times 10^{-30}$ grams.

2000; Bode et al., 2001). However, this model faces challenges because the particle mass required to reproduce the observed cores does not allow for the formation of dwarf galaxies in the first place (Hannestad & Scherrer, 2000; Macciò et al., 2012). Other models include self-interacting warm dark matter (Hannestad & Scherrer, 2000), fuzzy dark matter (Hu et al., 2000), repulsive dark matter (Goodman, 2000), fluid dark matter (Peebles, 2000), ultralight axions (Marsh & Silk, 2014), or the MOND phenomenology (Gentile et al., 2011), which fundamentally changes the gravitational law.

Baryonic processes. A second approach is to retain cold dark matter but focus more on baryonic processes. Since the cusp-core discrepancy arises from simulations that only include dark matter and occur at the scale at which baryons start to play an important role, it might be wise to examine the interplay between dark matter and baryonic matter. One significant baryonic process is that massive objects such as satellite galaxies or gas clumps can transfer some of their kinetic energy to the dark matter background through dynamical friction. This process can "heat" the halo, thereby helping to suppress the central cusp (El-Zant et al., 2001, 2004; Tonini et al., 2006; Romano-Díaz et al., 2008; Goerdt et al., 2010; Cole et al., 2011; Nipoti & Binney, 2015). A second important process is the phenomenon of feedback. As we saw in Section 1.2.3, feedback processes are crucial in shaping the galactic properties. Powerful stellar feedback processes, such as stellar winds, supernova explosions, and AGNs, cause significant gas movements. These variations in the baryonic mass distribution induce strong potential fluctuations that can push dark matter particles away from the center of the halo, eventually forming a core (Dekel & Silk, 1986; Pontzen & Governato, 2012, 2014; El-Zant et al., 2016; Freundlich et al., 2020a). Hydrodynamical simulations with different feedback implementations are able to reproduce dark matter cores (Read & Gilmore, 2005; Mashchenko et al., 2006, 2008; Governato et al., 2010, 2012; Macciò et al., 2012; Zolotov et al., 2012; Martizzi et al., 2013; Teyssier et al., 2013; Madau et al., 2014; Di Cintio et al., 2014; Chan et al., 2015; Dutton et al., 2016; Peirani et al., 2017; Macciò et al., 2020; Arora et al., 2024), but the feedback recipes used are often ad hoc, with finely tuned parameters to match observables rather than physics-motivated ones. Therefore, it is crucial to develop a physical intuition for the interplay between feedback processes and dark matter using theoretical models. While we have mentioned some of the existing models, we will focus on the CuspCore model developed by Freundlich et al. (2020a).

2.2 Theoretical framework

In this section, we present the CuspCore model for dark matter core formation (Freundlich et al., 2020a). Initially, we derive the velocity dispersion of a dark matter

halo, grounded in the fundamental principles of collisionless systems theory introduced in Section 2.2.1. This derivation will be instrumental in our later discussions. Following this, we detail the CuspCore model's principles in Section 2.2.2 and outline its implementation in the subsequent Sections 2.2.3, 2.2.4 and 2.2.5.

2.2.1 Describing a collisionless halo

A halo is composed of a very large number of dark matter particles interacting gravitationally. To describe it, it is impractical to track the movement of each individual particle; instead, the problem must be approached statistically. Similar to a galaxy, a halo is a system where collisions are negligible (cf. Section 1.1.2), making it a good approximation to ignore them. Following Binney & Tremaine (2008) chapter 4, let's consider a collection of N identical point masses (in our example, these point masses represent dark matter, but they could also be stars). The probability of finding a particle at time t within an infinitesimal phase space volume $\mathrm{d}^3\mathbf{x}\mathrm{d}^3\mathbf{v}$ around position $\mathbf{x}$ and velocity $\mathbf{v}$ is given by $f(\mathbf{x},\mathbf{v},t)\,\mathrm{d}^3\mathbf{x}\mathrm{d}^3\mathbf{v}$, where f is the probability density function (PDF, also known as the distribution function DF) of the system. This probability is the same for all particles since we have assumed they are identical. By definition, f is normalized such that:

$$\int f(\mathbf{x},\mathbf{v},t)\,\mathrm{d}^3\mathbf{x}\,\mathrm{d}^3\mathbf{v} = 1. \tag{2.1}$$

If we follow a star during its movement in phase space, the probability must be conserved in the absence of collisions [2] , which translates to a zero Lagrangian derivative:

$$\begin{aligned}
\frac{\mathrm{d}f}{\mathrm{d}t} = 0 \quad &\Leftrightarrow \quad \frac{\partial f}{\partial t} + \frac{\partial}{\partial \mathbf{q}}\cdot(f\dot{\mathbf{q}}) + \frac{\partial}{\partial \mathbf{p}}\cdot(f\dot{\mathbf{p}}) = 0 \\
&\Leftrightarrow \quad \frac{\partial f}{\partial t} + \frac{\partial}{\partial \mathbf{q}}\cdot\left(f\frac{\partial H}{\partial \mathbf{p}}\right) - \frac{\partial}{\partial \mathbf{p}}\cdot\left(f\frac{\partial H}{\partial \mathbf{q}}\right) = 0 \\
&\Leftrightarrow \quad \frac{\partial f}{\partial t} + \frac{\partial f}{\partial \mathbf{q}}\cdot\frac{\partial H}{\partial \mathbf{p}} - \frac{\partial f}{\partial \mathbf{p}}\cdot\frac{\partial H}{\partial \mathbf{q}} = 0
\end{aligned}$$

where to transition to the second and third lines, we used Hamilton's equations $\dot{\mathbf{q}} = \partial H/\partial \mathbf{p}$ and $\dot{\mathbf{p}} = \partial H/\partial \mathbf{q}$ with H being the Hamiltonian of the system, as well as Schwarz's theorem $\partial^2 H/\partial\mathbf{q}\partial\mathbf{p} = \partial^2 H/\partial\mathbf{p}\partial\mathbf{q}$. By using these equations once more, we obtain the **collisionless Boltzmann equation**:

$$\boxed{\frac{\partial f}{\partial t} + \dot{\mathbf{q}}\cdot\frac{\partial f}{\partial \mathbf{q}} + \dot{\mathbf{p}}\cdot\frac{\partial f}{\partial \mathbf{p}} = 0.} \tag{2.2}$$

[2] A perhaps more intuitive way to think about this is to talk in terms of the number of stars rather than probability. The reasoning is the same, provided we change the normalization of Eq. 2.1 to: $\int f(\mathbf{x},\mathbf{v},t)\,\mathrm{d}^3\mathbf{x}\,\mathrm{d}^3\mathbf{v} = N$. In this case, it is clear that if we follow a particle or a group of particles during their movement in phase space, the number of particles must be conserved.

For studying a spherically symmetric dark matter halo, spherical coordinates are used with the corresponding Hamiltonian:

$$H = \frac{1}{2}\left(p_r^2 + \frac{p_\theta^2}{r^2} + \frac{p_\phi^2}{r^2 \sin^2\theta}\right) + \Phi, \tag{2.3}$$

allowing us to rewrite equation (2.2) :

$$\begin{aligned}\frac{\partial f}{\partial t} + p_r \frac{\partial f}{\partial r} + \frac{p_\theta}{r^2}\frac{\partial f}{\partial \theta} + \frac{p_\phi}{r^2 \sin^2\theta}\frac{\partial f}{\partial \phi} - \left(\frac{\partial \Phi}{\partial r} - \frac{p_\theta^2}{r^3} - \frac{p_\phi^2}{r^3 \sin^2\theta}\right)\frac{\partial f}{\partial p_r} \\ - \left(\frac{\partial \Phi}{\partial \theta} - \frac{p_\phi^2 \cos\theta}{r^2 \sin^3\theta}\right)\frac{\partial f}{\partial p_\theta} - \frac{\partial \Phi}{\partial \phi}\frac{\partial f}{\partial p_\phi} = 0.\end{aligned} \tag{2.4}$$

The Boltzmann equation deals with the probability density function, which is not an observable quantity. However, it is possible to derive observable and more intuitive quantities by integrating the PDF. For example, integrating over the velocities yields the probability per unit volume $\nu(\mathbf{x})$ of finding a particular star at position $\mathbf{x}$, regardless of its velocity:

$$\nu(\mathbf{x}) \equiv \int f(\mathbf{x}, \mathbf{v})\, \mathrm{d}^3\mathbf{v}. \tag{2.5}$$

This quantity is directly related to the number density and mass density of the system. By multiplying it by the total number of stars and the total mass of the system, respectively, we obtain these densities:

$$\begin{aligned} n(\mathbf{x}) &\equiv N\nu(\mathbf{x}) \\ \rho(\mathbf{x}) &\equiv M\nu(\mathbf{x}). \end{aligned} \tag{2.6}$$

R

Note that the second equation (2.6) links the density ρ to the distribution function, and the density is also related to the gravitational potential Φ from (2.3) through the Poisson equation:

$$\nabla^2\Phi = 4\pi G\rho.$$

Thus, it is evident that integrating the Boltzmann equation (2.4) over velocities will be fruitful in deriving equations that relate observable quantities. By multiplying Eq. (2.4) by p_r and integrating over the momenta, we obtain a new equation:

$$\boxed{\frac{\mathrm{d}(\nu\overline{v_r^2})}{\mathrm{d}r} + 2\frac{\beta}{r}\nu\overline{v_r^2} = -\nu\frac{\mathrm{d}\Phi}{\mathrm{d}r}} \tag{2.7}$$

where the anisotropy parameter β is defined as:

$$\beta \equiv 1 - \frac{\overline{v_\theta^2} + \overline{v_\phi^2}}{2\overline{v_r^2}} = 1 - \frac{\sigma_\theta^2 + \sigma_\phi^2}{2\sigma_r^2}, \tag{2.8}$$

with $\overline{v_i^2} \equiv \sigma_i^2$ the velocity dispersion. The complete derivation of this equation is detailed in Appendix B. Eq. (2.7) is the **Jeans equation**, which relates velocity dispersions to the gravitational potential. The β parameter quantifies the degree of radial anisotropy in the system. If all orbits are circular, $\sigma_r = 0$ and $\beta = -\infty$; conversely, if all orbits are perfectly radial, $\sigma_\theta = \sigma_\phi = 0$ and $\beta = 1$. Finally, if the system is isotropic at all points, $\sigma_r = \sigma_\theta = \sigma_\phi$ and $\beta = 0$.

If we assume the halo is isotropic, the second term in Eq. (2.7) vanishes, and integrating over the radii yields the velocity dispersion of the dark matter (see Appendix B for more details):

$$\boxed{\overline{v_r^2}(r) = \frac{1}{\rho(r)} \int_r^{r_{\rm max}} \rho(r') \frac{G\, m(r')}{r'^2} \mathrm{d}r'} \tag{2.9}$$

where $r_{\rm max}$ is the maximum radius of the halo, satisfying the boundary condition: $\lim_{r \to r_{\rm max}} \overline{v_r^2} = 0$. In our case, for dark matter, $r_{\rm max} = r_{200}$ where r_{200} is the radius within which the mean enclosed density is $200 \times \rho_{\rm crit}$, the critical density of the Universe (see Eq. 1.22). The density profile $\rho(r)$ refers to the population for which we want to determine the dispersion (here the dark matter halo), and $m(r)$ is the total enclosed mass.

2.2.2 The CuspCore model

Let's now focus on the CuspCore model of dark matter core formation. According to this model, core formation results from fluctuations in the central potential caused by feedback processes. The general framework of this model was first introduced by Pontzen & Governato (2012, 2014), who showed that the impulsive nature of feedback processes produces an irreversible transfer of energy to the collisionless particles of the dark matter halo, thereby creating cores. This idea was then taken up by Dutton et al. (2016), who developed a toy model consisting of cycles of adiabatic inflow and impulsive gas outflow, and compared it to NIHAO simulations (hydrodynamical zoom-in simulations conducted using the GASOLINE code). Finally, Freundlich et al. (2020a) generalized the model and also tested it with NIHAO. This is the version we will present here.

A three-step process. We aim to describe the response of a collisionless spherical halo with an initial mass profile $M_{\rm i}(r)$ when mass is instantaneously added or removed around the center with a profile $m(r)$. We seek to determine the final mass profile of the collisionless halo $M_{\rm f}(r)$. Positive values of m correspond to inflows, while negative values correspond to outflows. To achieve this, we follow the evolution of isolated spherical shells that initially enclose a mass M of dark matter at radius $r_{\rm i}$ and, after relaxation,

are found at radius r_f such that $M = M_\mathrm{i}(r_\mathrm{i}) = M_\mathrm{f}(r_\mathrm{f})$. The model is divided into three steps.

(1) Initially, the shells (and thus the halo) are in equilibrium. The total energy of a shell per unit mass is given by:

$$\boxed{E_\mathrm{i}(r_\mathrm{i}, p_\mathrm{i}) = U_\mathrm{i}(r_\mathrm{i}, p_\mathrm{i}) + K_\mathrm{i}(r_\mathrm{i}, p_\mathrm{i})} \tag{2.10}$$

where U_i and K_i are the gravitational potential and kinetic energy per unit mass, respectively, depending on the initial radius of the shell r_i and parameters of the initial mass profile. Since the halo is assumed to be in equilibrium, the kinetic energy is determined by the Jeans velocity dispersion (Eq. 2.9) derived in the previous section. We will elaborate on this and the expressions for U_i and K_i in the following sections.

(2) A mass m is instantaneously removed (or added, if $m > 0$) inside r_i. Because the mass variation occurs over a very short timescale compared to the dynamical timescale of the system (Förster Schreiber et al., 2019), the gravitational potential adjusts instantly to this mass variation while the velocities are frozen at their initial values (and the shells remain at radii r_i), leading to a transitional out-of-equilibrium state. The total energy per unit mass of a shell just after the mass variation is:

$$\boxed{E_\mathrm{t}(r_\mathrm{i}, p_\mathrm{i}) = U_\mathrm{t}(r_\mathrm{i}, p_\mathrm{i}) + K_\mathrm{i}(r_\mathrm{i}, p_\mathrm{i}) \quad \text{with} \quad U_\mathrm{t}(r_\mathrm{i}, p_\mathrm{i}) = U_\mathrm{i}(r_\mathrm{i}, p_\mathrm{i}) - \frac{Gm}{r_\mathrm{i}}} \tag{2.11}$$

where we assume that the mass flow is spherically symmetric and inside r_i. This assumption holds even if the removed (or added) mass is not point-like but has a mass profile $m(r)$, as long as the shell of interest is outside the main body of mass variations.

(3) The system is now out of equilibrium, the model assume it will relax at constant energy towards a new Jeans equilibrium, with the energy given by:

$$\boxed{E_\mathrm{f}(r_\mathrm{f}, p_\mathrm{f}) = U_\mathrm{f}(r_\mathrm{f}, p_\mathrm{f}) + K_\mathrm{f}(r_\mathrm{f}, p_\mathrm{f}, m) \quad \text{with} \quad U_\mathrm{f}(r_\mathrm{f}, p_\mathrm{f}) = U_\mathrm{f}(r_\mathrm{f}, p_\mathrm{f}) - \frac{Gm}{r_\mathrm{f}}.} \tag{2.12}$$

It is this relaxation that is responsible for the creation of the core in the density profile. The conservation of energy in the shells during the relaxation phase is a strong assumption of the model, which is not entirely justified since there is diffusion and not all orbits are circular. This assumption is partially justified a posteriori by the success of the model. Shell crossing might challenge this assumption, as we will see in the following sections. Figure (2.2) summarizes these three steps.

R

The kinetic energy $K_{\rm f}(r_{\rm f}, p_{\rm f}, m)$ accounts for the mass variation otherwise we would end up with the trivial solution $r_{\rm i} = r_{\rm f}$ and $p_{\rm i} = p_{\rm f}$.

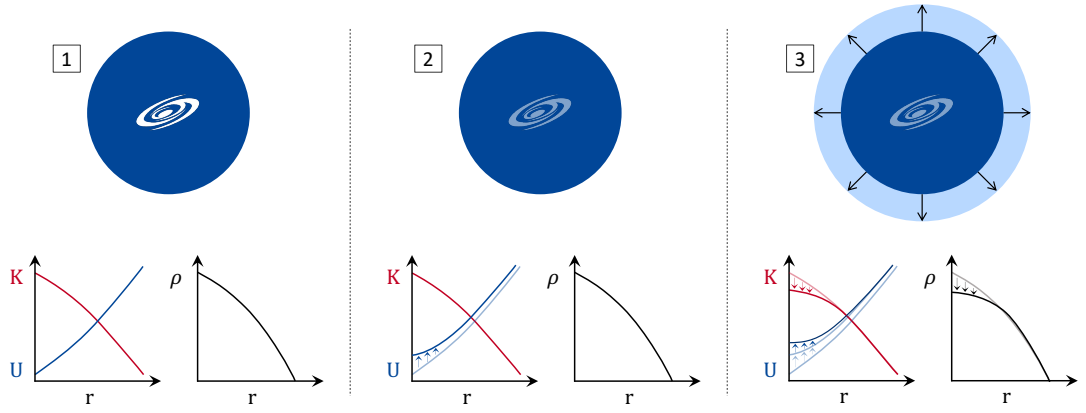

Figure 2.2: CuspCore model. (1) The dark matter halo is initially in equilibrium with the baryonic matter at the center. (2) Following a sudden change in mass, the gravitational potential adjusts instantaneously while the velocities remain fixed at their initial values. (3) The halo then relaxes at constant energy towards a new Jeans equilibrium. This relaxation process creates a core in the density profile.

2.2.3 Parameterization of the density profile

To describe how environmental effects lead to changes in the dark matter distribution from cusps to cores, Dekel et al. (2017) proposed a parameterization of the Zhao profile (Eq. 1.21) with $\alpha = 0.5$ the intermediate shape parameter and $\beta = 3.5$ the external asymptotic slope:

$$\rho(r) = \rho_0 \left(\frac{r}{r_{\rm s}}\right)^{-\gamma} \left[1 + \left(\frac{r}{r_{\rm s}}\right)^{1/2}\right]^{2(\gamma-3.5)} . \tag{2.13}$$

This profile has the advantage of a free inner slope γ and provides analytic expressions for the gravitational potential, velocity dispersion, mass, and circular velocity profiles. Dekel et al. (2017) and Freundlich et al. (2020b) showed that this functional form provides excellent fits for halos in simulations with and without baryons, ranging from sharp central cusps to flat cores. The parameterization with $\alpha = 0.5$ and $\beta = 3.5$ in particular fits the simulated profiles at least as well as the NFW profile but better accounts for cores. For a given halo mass (which sets ρ_0), this profile has two free parameters: γ, the inner slope, and $c = r_{200}/r_{\rm s}$. Consequently, the gravitational potential $U(r, p)$ and the kinetic energy $K(r, p)$ will also depend on these free parameters, with $p = (\gamma, c)$ in equations (2.10), (2.11) and (2.12) from the previous section.

2.2.4 Gravitational potential and kinetic energy of a shell

What remains now is to determine the analytical formulas for the gravitational potential and the kinetic energy per unit mass.

Gravitational potential. Following Freundlich et al. (2020a), the gravitational potential is equal to the negative of the energy required to extract a unit mass from r to infinity:

$$U(r) = \int_r^{+\infty} F(y)dy = -\int_r^{R_t} \frac{G\,M(y)}{y^2}dy - \frac{G\,M_t}{R_t} \tag{2.14}$$

where R_t is the truncation radius of the halo. We will identify it with the virial radius, implying that $R_t = r_{\rm vir} = r_{200}$ and $M_t = M_{\rm vir} = M_{200}$. By integrating by parts, equation (2.14) becomes:

$$U(r) = -\frac{G\,M(r)}{r} - G\int_r^{r_{200}} \frac{1}{y}\frac{dM}{dy}dy = -\frac{G\,M(r)}{r} - \int_r^{r_{200}} 4\pi y G\rho(y)dy \tag{2.15}$$

The first term represents the contribution of the shells inside r, while the second term accounts for the contribution of the shells outside r. For the density profile (2.13), Freundlich et al. (2020a) derived an analytical expression for the potential, given by:

$$U(r,\gamma,c) = -V_{\rm vir}^2\left(1 + 2c\mu\left[\frac{\chi_{\rm vir}^{2(2-\gamma)} - \chi^{2(2-\gamma)}}{2(2-\gamma)} - \frac{\chi_{\rm vir}^{2(2-\gamma)+1} - \chi^{2(2-\gamma)+1}}{2(2-\gamma)+1}\right]\right) \tag{2.16}$$

where $\gamma \neq 2$ or $5/2$ and :
- $c = r_{\rm vir}/r_{\rm s}$,
- $\mu = c^{\gamma-3}(1+c^{\alpha})^{\frac{\beta-\gamma}{\alpha}}$,
- $\chi = x^{1/2}/(1+x^{1/2})$ with $x = r/r_{\rm s}$,
- $\chi_{\rm vir} = \chi(c)$
- $V_{\rm vir} = G\,M_{\rm vir}/R_{\rm vir}$.

Kinetic energy. For an infinitesimal mass shell $\mathrm{d}M$ between r and $r+\mathrm{d}r$, the local kinetic energy tensor per unit mass is given by:

$$K_{jk} \equiv \frac{1}{2}\overline{v_j v_k}. \tag{2.17}$$

We take its trace to obtain the local kinetic energy per unit mass:

$$\begin{aligned} K &\equiv \frac{1}{2}\sum_i \overline{v_i^2} \\ &= \frac{1}{2}\left(\overline{v_r^2} + \overline{v_\theta^2} + \overline{v_\phi^2}\right) \\ &= \frac{(3-2\beta)}{2}\,\overline{v_r^2} \end{aligned} \tag{2.18}$$

where we used the expression for the β anisotropy parameter (2.8). Using the notation $\overline{v_r^2} \equiv \sigma_r^2$ for the radial velocity dispersion given by equation (2.9), we obtain:

$$K(r) = \frac{(3-2\beta)}{2}\sigma_r^2(r). \tag{2.19}$$

If we now consider the isotropic case ($\beta = 0$) and replace $\rho(r)$ with the analytical expression of the Dekel-Zhao profile (2.13), we also obtain an analytical expression for the local kinetic energy per unit mass (cf. Freundlich et al., 2020a):

$$K(r,\gamma,c) = c\mu\frac{G\,M_{\rm vir}}{R_{\rm vir}}\frac{(3-\gamma)\rho_0}{\rho(r)}\left[\mathcal{B}(4-4\gamma,9,\zeta)\right]_\chi^1 \tag{2.20}$$

where $\mathcal{B}(a,b,x) = \int_0^x t^{a-1}(1-t)^{b-1}dt$ is the incomplete beta function, and the brackets refer to the difference of the bracketed function between 1 and χ, i.e., $[f(\zeta)]_\chi^1 \equiv f(1) - f(\chi)$ for any function f.

2.2.5 Procedure

The CuspCore model can make predictions for the evolution of a dark matter halo subjected to sudden mass changes. In practice, the initial halo is fitted using the Dekel-Zhao profile, which enables the retrieval of the initial parameters $p_{\rm i} = (\gamma_{\rm i}, c_{\rm i})$ and the calculation of the gravitational potential, kinetic energy, and thus the initial energy of the halo using equation (2.10). For a chosen mass variation, the transitional energy is calculated using equation (2.11). The model is based on the assumption of relaxation at constant energy. The goal is then to find $E_{\rm f}(r_{\rm f}, p_{\rm f})$ that closely matches $E_{\rm t}(r_{\rm i}, p_{\rm i})$, ensuring energy conservation. This requires solving a two-parameter optimization problem to identify the final parameters $p_{\rm f} = (\gamma_{\rm f}, c_{\rm f})$ that minimize the difference $E_{\rm f}(r_{\rm f}, p_{\rm f}) - E_{\rm t}(r_{\rm i}, p_{\rm i})$ using the least squares method. These parameters will provide the final density profile of the halo after relaxation.

2.3 Simulations

We now need a way to test the theoretical predictions of the CuspCore model. Astrophysics is a unique science in that the Universe is not a replicable and fully observable object of study. We cannot conduct laboratory experiments on the Universe, so other methods had to be developed to adopt a proactive approach rather than merely relying on the glimpses the Universe is willing to reveal. Galaxies are vast assemblies of masses interacting through gravity. By leveraging our understanding of gravitational laws, we can simulate the movement of these masses and replicate the behavior of astrophysical systems. The algorithms that calculate gravitational interactions between multiple bodies are known as N-body codes. These codes work by first taking the initial positions and velocities of all the bodies. Then, they compute the gravitational force

on each body resulting from its interactions with all others. Using these forces, the bodies' positions and velocities are updated incrementally over small time steps. This process is repeated iteratively for the number of time steps required to cover the desired simulation timescale [3] .

2.3.1 N-body simulations

At each time step, the code must calculate the gravitational force on a mass (or 'particle') i resulting from interactions with other masses $j \neq i$. In the Newtonian formalism, this force is expressed as:

$$\mathbf{F}_i = \sum_{j \neq i} G m_j \frac{\mathbf{r}_j - \mathbf{r}_i}{|\mathbf{r}_j - \mathbf{r}_i|^3} \tag{2.21}$$

with m being the mass and $\mathbf{r}$ the position vector of the mass. This approach requires calculating $N-1$ distances per particle at each time step. Since there are N particles, this results in a total of $\frac{1}{2}N(N-1)$ distances to evaluate, with the division by two coming from the fact that each distance can be used twice ($i \to j$ and $j \to i$). The complexity is therefore $\mathcal{O}(N^2)$, and for a very large number of particles, which is typically the case for a galaxy where $N \sim 10^{10}$, the computation time can quickly escalate, even with modern and high-performance computing hardware. Therefore, efficient strategies had to be developed to make it feasible to simulate the Universe.

Tree-code Tree codes reduce the complexity from $\mathcal{O}(N^2)$ to $\mathcal{O}(N \log N)$ (Barnes & Hut, 1986). To achieve this, the simulation volume is recursively subdivided into 8 octants until each octant, called a cell or node, contains a maximum of N_{crit} particles. This hierarchical tree structure is called an octree. When calculating the gravitational force on a specific particle, particles from nearby cells are considered individually whereas particles in distant cells are approximated either as a single large particle at the cell's center of mass or as a low-order multipole expansion. Figure 2.3 illustrates this structure in 2D.

Softening Despite this technique that reduces complexity and saves computation time, galactic systems are still too ambitious for our current computational power. Another simplification is to reduce the mass resolution of the simulation. Instead of simulating particles with realistic stellar masses, around $M \sim 1, M_\odot$, we simulate 'super-particles' with higher masses. This way, for the same galactic mass, fewer particles need to be simulated, reducing the number of distance calculations between particles.

[3] While this discussion focuses on simulations of point masses influenced solely by gravity, it is worth noting that simulating gas dynamics requires hydrodynamical simulations. We should also mention that more complex codes exist that incorporate other forces, such as electromagnetic interactions, as well as additional galactic physical processes like feedback and radiation.

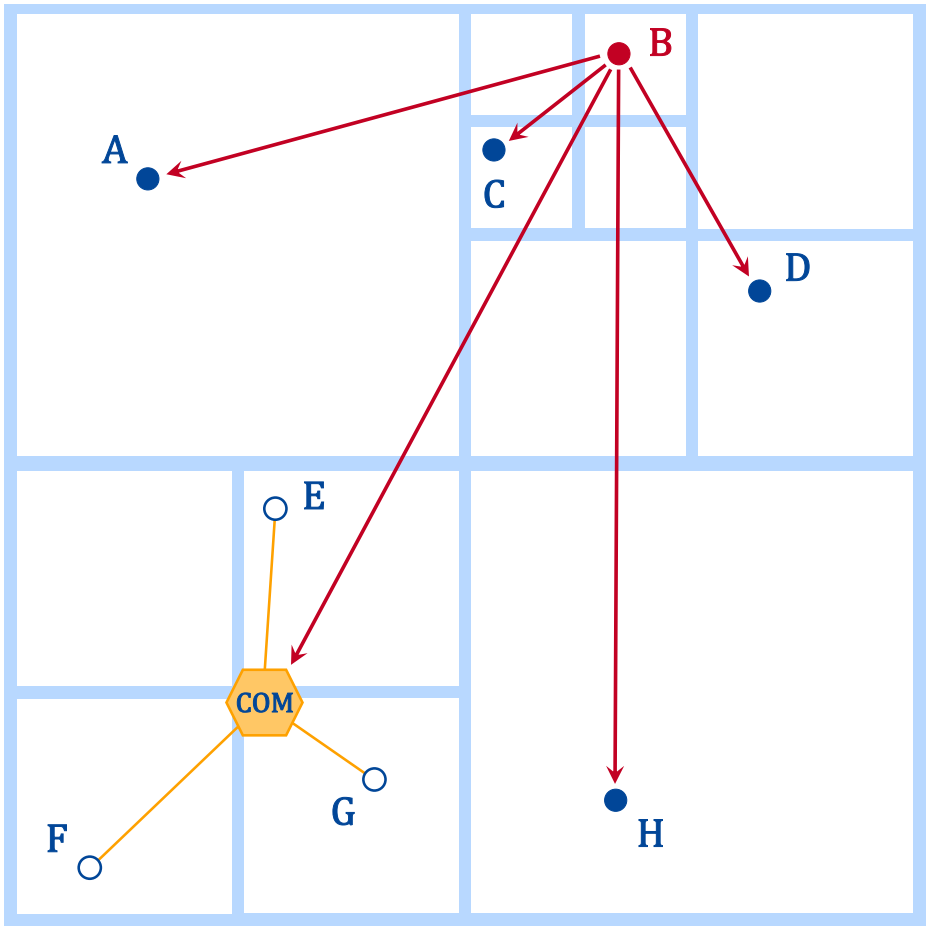

Figure 2.3: Barnes-Hut tree. When calculating the gravitational force on a specific particle (in this case, particle B), particles from nearby cells are considered individually whereas particles in distant cells (E, F and G here) are approximated either as a single large particle at the cell's center of mass or as a low-order multipole expansion.

The downside of this simplification is the introduction of an increased 'granularity,' which can lead to non-physical behaviors. Granularity is an artifact of sampling the density distribution, giving more importance to collisions in an intrinsically smooth (collisionless) physical system. To address this issue, softening is introduced to smooth out the overly coarse mass sampling and prevent divergences in the force when two particles are too close. This is achieved by replacing equation (2.21) with:

$$\mathbf{F}_i = \sum_{j \neq i} G m_j \; S_F(|\mathbf{r}_j - \mathbf{r}_i|) \frac{\mathbf{r}_j - \mathbf{r}_i}{|\mathbf{r}_j - \mathbf{r}_i|} \tag{2.22}$$

where we introduce the function $S_F(\mathbf{r})$, the force softening kernel. This function replaces the $\mathbf{r}^{-2}$ term in equation (2.21), where $\mathbf{r} = |\mathbf{r}_j - \mathbf{r}_i|$. $S_F(\mathbf{r})$ is a function that approximates $\mathbf{r}^{-2}$ for $\mathbf{r}$ larger than a certain length ε, known as the softening length,

and smoothly approaches zero for small values of $\mathbf{r}$, preventing divergences during close encounters. The challenge lies in finding a softening length that is not too large, to avoid significant bias in the physical laws, and not too small, to prevent non-physical behaviors in the simulation (we will discuss this point in more detail in Section 2.3.2).

2.3.2 Our setup

To test the predictions of the CuspCore model presented in Section 2.2.2, we use galaxy-scale N-body simulations. For this purpose, we employ the GYRFALCON code (Dehnen, 2000, 2002), an optimized tree code with a complexity of $\mathcal{O}(N)$, which is significantly faster than traditional tree codes with a complexity of $\mathcal{O}(N \log N)$ [4] . We simulate a live NFW dark matter halo in initial equilibrium with a central baryonic potential:

$$\Phi_{\rm bar}(r) = -\frac{G\, m_{\rm bar}}{\sqrt{r^2 + a^2}}. \tag{2.23}$$

We choose a Plummer potential, where $m_{\rm bar}$ is the baryonic mass at the center of the halo and a its characteristic radius. Initially, we approximate the baryonic mass as point-like by selecting a small value for the characteristic radius, $a = 0.01$ kpc. The halo is initially in equilibrium with the central baryonic potential. At $t = 0$ Gyr, we vary $m_{\rm bar}$ to observe the dynamical response of the dark matter halo. We will then compare its relaxed density profile to that predicted by the CuspCore model.

Study Object. Simulations indicate that core formation is very efficient in the mass regime of dwarf galaxies, with a sweet spot around $M_{\rm vir} \sim 10^{11} M_\odot$ (Chan et al., 2015; Tollet et al., 2016; Freundlich et al., 2020b). Figure 2.4 shows the inner slope of the Dekel-Zhao profile as a function of stellar mass $M_\star$, halo mass $M_{\rm vir}$, and the stellar-to-halo mass ratio $M_\star/M_{\rm vir}$. The inner slope is fitted from data derived by Freundlich et al. (2020b) from NIHAO simulations using their functional form (Eq. 45 of Freundlich et al., 2020b). A favorable mass range for the creation of density cores is observed for $M_{\rm vir}$ between $10^{10.5}$ and $10^{11.5}$. Therefore, we select a dark matter halo with $M_{\rm vir} = 10^{11} M_\odot$. This corresponds to a stellar mass of $M_\star \sim 5 \times 10^8 M_\odot$ according to the stellar-to-halo mass relation (Fig. 1.6) and the ratio, $M_\star/M_{\rm vir} = 0.5\%$, is also a good value for core creation (Di Cintio et al., 2014). However, to maximize core creation according to Fig. 2.4, we choose a baryonic mass of $m_{\rm bar} = 2 \times 10^8 M_\odot$. The mass parameters of our study object are indicated in Fig. 2.4. The virial radius of the

[4] The code achieves this efficiency by combining the Barnes-Hut tree structure with a Fast Multipole Method (Greengard & Rokhlin, 1987) to calculate mutual cell-cell interactions, where both cells act as source and sink simultaneously. The decision to split or execute a cell-cell interaction is made using an improved mass-dependent tolerance parameter.

halo is $r_{\rm vir} = 100$ kpc, while its scale radius is $r_{\rm s} = 6.7$ kpc, giving a concentration $c = 15$.

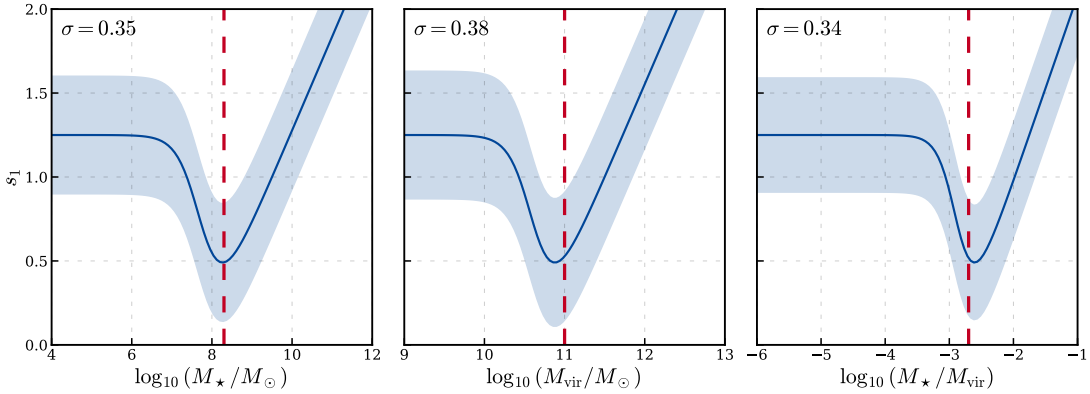

Figure 2.4: Inner slope s_1 of the Dekel-Zhao profile as a function of stellar mass $M_\star$, halo mass $M_{\rm vir}$, and stellar-to-halo mass ratio $M_\star/M_{\rm vir}$. The inner slope is fitted from data derived from NIHAO simulations using the functional form of Freundlich et al. (2020b). The best-fit curve is shown in blue, with parameters available in Table 1 of Freundlich et al. (2020b). σ is the standard deviation of the residuals. A favorable region for core creation ($s_1 \to 0$) is observed between $10^7 < M_\star/M_\odot < 10^{10}$ and $10^{10.5} < M_{\rm vir}/M_\odot < 10^{11.5}$. It is worth noting that s_1 measures the inner logarithmic slope at the resolution limit in the NIHAO simulations, i.e., at $r = 0.01\, r_{\rm vir}$, and thus slightly differs from the parameter γ in equation (2.13). The red vertical lines indicate the values for our study halo.

Softening kernel. We chose a softening kernel that replaces point masses with spheres of density:

$$\rho(r) \propto \left(1 + \left(\frac{r}{\varepsilon}\right)^2\right)^{-7/2} \tag{2.24}$$

with ε being the softening length. The advantage of this kernel is that it is continuous in all its derivatives and converges more rapidly to the Newtonian force at $r \gg \varepsilon$ than the classic Plummer kernel, resulting in less force bias (Dehnen, 2001).

Softening length. Selecting the appropriate softening length is crucial: a value too large introduces a significant bias in the gravitational force calculation (systematic error), while a value too small makes the simulation susceptible to random fluctuations in the gravitational force due to the mass distribution discretization (variance error). The optimal softening length lies between these two extremes and is typically comparable to the average distance between particles. In the central 5 kpc of our dark matter halo, the region of interest for core creation, this distance is $\overline{d} = 0.09$ kpc. However, to ensure accurate evaluation of the halo density up to $r = 0.1$ kpc from the center, we opt for a smaller softening length. To minimize the softening effects at $r = 0.1$ kpc (close to

$\overline{d} = 0.09$ kpc), we reduce this value by a factor of ten, resulting in $\epsilon = 0.01$ kpc (see Errani & Navarro, 2021, for example, which observe numerical deviation at the center when $r < 8\,\Delta x$, with Δx being their simulation resolution, equivalent to our softening length). With this choice, $r_{\rm min} > 10\,\epsilon$, where $r_{\rm min}$ is the smallest radius at which we will evaluate the central density. Figure 2.5 shows the density profile of the dark matter halo after 3 Gyr of evolution for various softening lengths. An excessively large softening length lowers the central density of the halo. We confirm convergence towards the theoretical density profile as ϵ decreases.

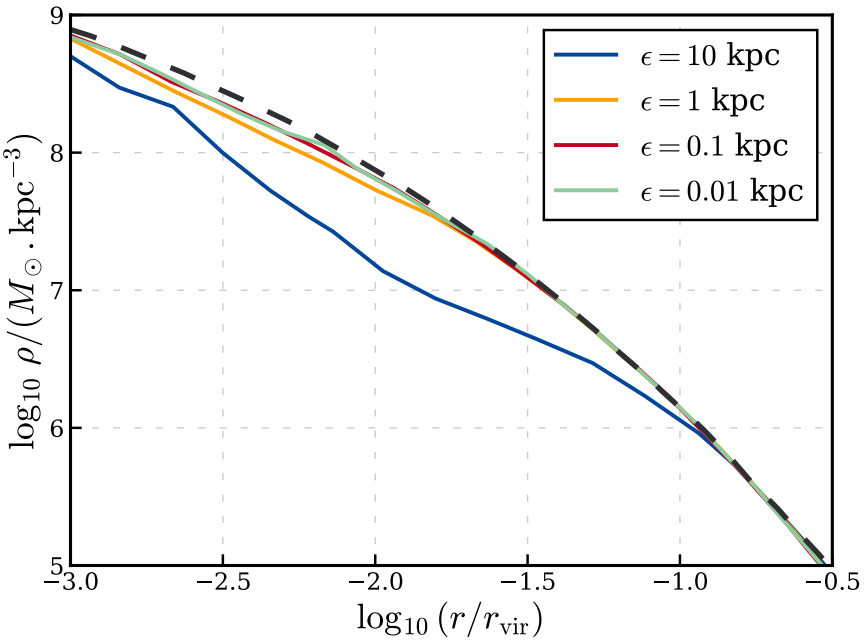

Figure 2.5: Convergence test of the softening length. The figure shows the density profile of the dark matter halo after 3 Gyr of evolution for different values of the softening length. An excessively large softening length lowers the central density of the halo due to the introduction of a bias in the gravitational force calculation. It convergences towards the theoretical density profile, shown by the dashed black line, when ϵ decreases.

Time step. The choice of the time step τ is made through the parameter $k_{\rm max}$ such that:

$$\tau = \frac{1}{2^{k_{\rm max}}}. \tag{2.25}$$

The time step should be a fraction of the typical time for a particle's trajectory to change significantly. As a rough estimate, we should have:

$$\tau \leq \frac{\lambda \epsilon}{v_{\rm typ}} \tag{2.26}$$

where $v_{\rm typ}$ is the typical velocity of the particles and λ is the accuracy parameter, which we set to 0.2. In the central 10 kpc of our halo, the typical velocity is close to 55 kpc/Gyr.

According to Eq. (2.26), this gives a time step condition of $\tau \leq 3.63 \times 10^{-5}$Gyr. Therefore, we choose $k_{\max} = 15$, which gives a time step of $\tau = 3.05 \times 10^{-5}$Gyr. Figure 2.6 shows the density profile of the dark matter halo after 3 Gyr of evolution for different values of $k_{\max}$. An excessively small value for this parameter creates an artificial density core at the halo's center. We confirm convergence towards the theoretical density profile as $k_{\max}$ increases.

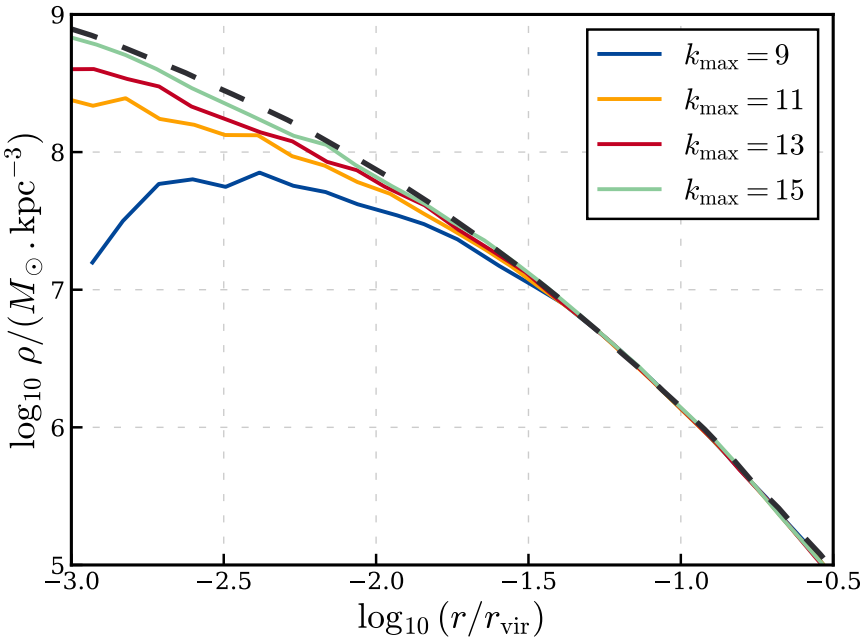

Figure 2.6: Time step convergence test. The figure shows the density profile of the dark matter halo after 3 Gyr of evolution for different values of $k_{\max}$. An excessively small value for $k_{\max}$ leads to the formation of an artificial core. It convergences towards the theoretical density profile, shown by the dashed black line, when $k_{\max}$ increases.

Other integration parameters. Regarding the tolerance parameter that determines the separation beyond which the interaction between two cells is approximated, GYRFALCON uses an improved mass-dependent tolerance parameter $\theta(M)$, which itself depends on a new tolerance parameter θ_0. We keep the default value $\theta_0 = 0.6$, which is a suitable choice for the simulation of spherical systems. We also keep the default maximum number of particles per cell at $N_{\mathrm{crit}} = 6$.

Number of particles and halo partition. Our focus is on the central few kiloparsecs of the halo, where we aim to maximize particle numbers to minimize statistical fluctuations in density. In contrast, the outer regions of the halo do not require the same precision. To optimize computational resources, we partition the halo into two populations with different mass resolutions. The inner region, within $r_{\mathrm{cut}} = 5$ kpc, is more

finely resolved, comprising of $N \simeq 6 \times 10^5$ particles, each with a mass of $M_{\rm p} = 10^4\,M_\odot$. Beyond $r_{\rm cut}$, the outer region contains $N \simeq 9 \times 10^4$ particles, each with a mass of $M_{\rm p} = 10^6\,M_\odot$. We performed tests to verify minimal mixing between the two populations due to mass segregation. After 3 Gyr of evolution, the central kiloparsec still retains 94% of the better-resolved particles.

2.4 Successes and failures of the CuspCore model

2.4.1 Single episode of mass flow

Figure 2.7 shows the evolution of the inner part of the dark matter halo following baryonic mass variations of 50% ($\eta = 0.5$), 75% ($\eta = 0.75$), and 100% ($\eta = 1$), characterized by the parameter η of the fractional mass change, defined as $\eta \equiv 1 - m_{\rm bar,f}/m_{\rm bar,i}$, where $m_{\rm bar,f}$ and $m_{\rm bar,i}$ are the final and initial baryonic masses, respectively. In each case, a lowering of the density profile at the halo's center, i.e., the creation of a core, is observed. Each time, the theoretical prediction of the CuspCore model is in very good agreement with the fit to the simulation data. In the three cases presented in Fig. 2.7, $m_{\rm bar}/M_{\rm vir} = 0.002$. We have observed that for large mass variations, $\eta > 0.35$, the ratio of baryonic-to-virial mass significantly affects the accuracy of the model's prediction. When $\eta > 0.35$ and $m_{\rm bar}/M_{\rm vir} \lesssim 0.001$, the model tends to underestimate core creation. Conversely, when $\eta > 0.35$ and $m_{\rm bar}/M_{\rm vir} \gtrsim 0.003$, the model overestimates core creation. Figure 2.8 illustrates these two cases where the model fails to predict the simulation behavior.

2.4.2 Multiple episodes of mass flow

We also tested the model's predictions in a scenario involving multiple episodes of baryonic mass variation. Here, we alternated between several episodes of outflows, presumed to be due to feedback, and inflows representing gas accretion at the center. Each episode involves the same mass variation. Figure 2.9 shows the evolution of the inner part of the dark matter halo following successive episodes. The left panel illustrates the first three episodes of mass variation: the initial outflow, followed by an inflow, and then the second outflow. As the episodes progress, the model increasingly deviates from the simulation, with significant divergence occurring from the second outflow onward. In the right panel, only the even-numbered episodes are shown, representing the moments when the halo has reaccreted the initial baryonic mass at its center. Despite the presence of the same amount of baryonic matter at the center, the density profile progressively lowers with each pair of episodes. This phenomenon is due to the asymmetry between outflow and inflow processes. While an adiabatic process would

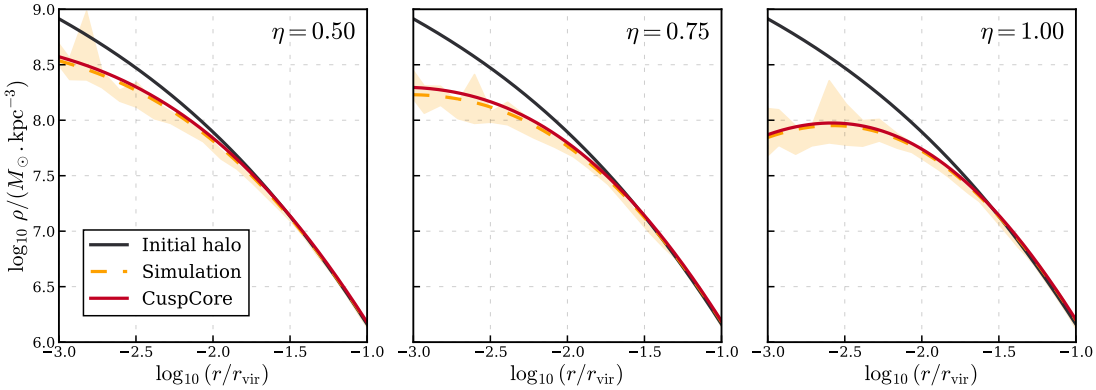

Figure 2.7: Successes of the CuspCore model. The figure shows the evolution of the inner part of the dark matter density profile after the first 3 Gyr. The initial profile is in black. The yellow area represents the final profile from the simulation, including the Poisson noise. The orange dashed curve is the fit of these data with the Dekel-Zhao profile (Eq. 2.13). The red curve is the theoretical prediction of the CuspCore model. The left panel shows a 50% variation in baryonic mass, the middle panel 75%, and the right panel 100%. The model accurately predicts the evolution of the dark matter halo in all three cases.

return the density profile to its initial state after an outflow followed by an inflow of the same mass, the impulsive nature [5] of feedback processes irreversibly transfers energy to the dark matter. To visualize this, consider a dark matter particle at a radius $r_{\rm i}$ near the galactic center. After the reduction of the central baryonic mass, the centripetal force decreases, causing the particle to move to a larger radius $r_{\rm f}$. If the same mass is later reaccreted at the center, the force exerted on the particle will be weaker due to its greater distance from the center, given that gravitational force scales with $1/r^2$ and $r_{\rm f} > r_{\rm i}$. Consequently, the particle will move back towards the center, but the force is insufficient to return it to $r_{\rm i}$. Repeating this process creates a significant core, varying a smaller amount of baryonic mass compared to what we discussed in the previous section, which would be unfeasible in a single ejection episode driven by supernovae.

The left panel of Fig. 2.10 shows the magnitude of the core creation as a function of the number of episodes. Core creation is measured using the ratio $r^{\rm f}_{1\%}/r^{\rm i}_{1\%}$ of the final to initial radius enclosing 1% of the virial mass of the halo. An increase in this ratio above 1 indicates an expansion of the halo's central region, signifying core creation. We conducted five different cases with varying numbers of episodes: $N = 4, 6, 8, 10$, and 12. In each case, the final central baryonic mass equals the initial baryonic mass, situating us after the re-accretion of the expelled matter. It is observed that $r^{\rm f}_{1\%}/r^{\rm i}_{1\%}$ increases with the number of episodes, indicating stronger core creation. The halo relaxes in just

[5] The ejection velocity of the matter is much higher than the local circular velocity.

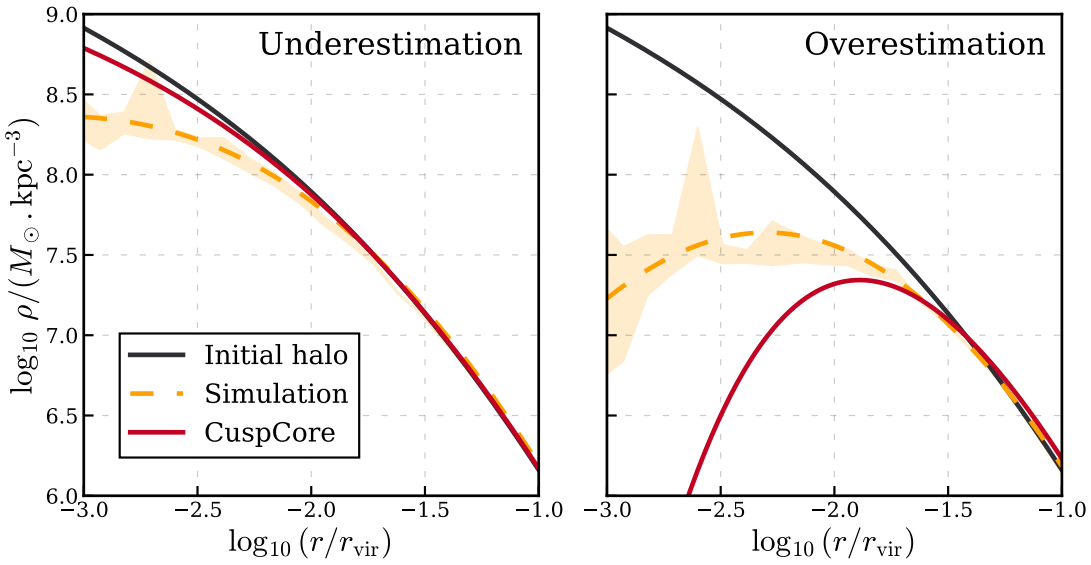

Figure 2.8: Failures of the CuspCore model. The figure shows the evolution of the inner part of the dark matter density profile after the first 3 Gyr. The initial profile is in black. The yellow area represents the final profile from the simulation, including the Poisson noise. The orange dashed curve is the fit of these data with the Dekel-Zhao profile (Eq. 2.13). The red curve is the theoretical prediction of the CuspCore model. In both panels, the halo responds to a 100% variation in baryonic mass. In the left panel, the total baryonic mass is such that $m_{\mathrm{bar}}/M_{\mathrm{vir}} \lesssim 0.001$. In this case, the model underestimates the core creation. In the right panel, the total baryonic mass is such that $m_{\mathrm{bar}}/M_{\mathrm{vir}} \gtrsim 0.003$. In this case, the model overestimates the core creation.

under 1 Gyr, so we spaced the flow episodes by 1 Gyr. This means that simulations with a larger N correspond to longer integration times. The region between 10 and 12 episodes is hatched because, in hindsight, we found that numerical scattering effects begin to appear over these time periods. The right panel of Fig. 2.10 illustrates the most extreme case of a 12 Gyr simulation without baryonic mass removal, showing a significant artificial lowering of density. For all five cases, we ran five simulations, and the scatter in the left panel corresponds to the standard deviation of the five $r^{\mathrm{f}}_{1\%}/r^{\mathrm{i}}_{1\%}$ values obtained for each case.

The fact that multiple episodes can effectively create a density core with potentially smaller mass variations suggests that it would be interesting to study the limit where N is very large and η is small. In this scenario the halo experiences a large number of small mass fluctuations, thus approaching the theoretical model developed by El-Zant et al. (2016), for example, where core creation arises from stochastic density fluctuations in the gas distribution. This situation closely resembles the reality of feedback in dwarf galaxies, i.e., multiple supernova explosions expelling smaller quantities of gas that are

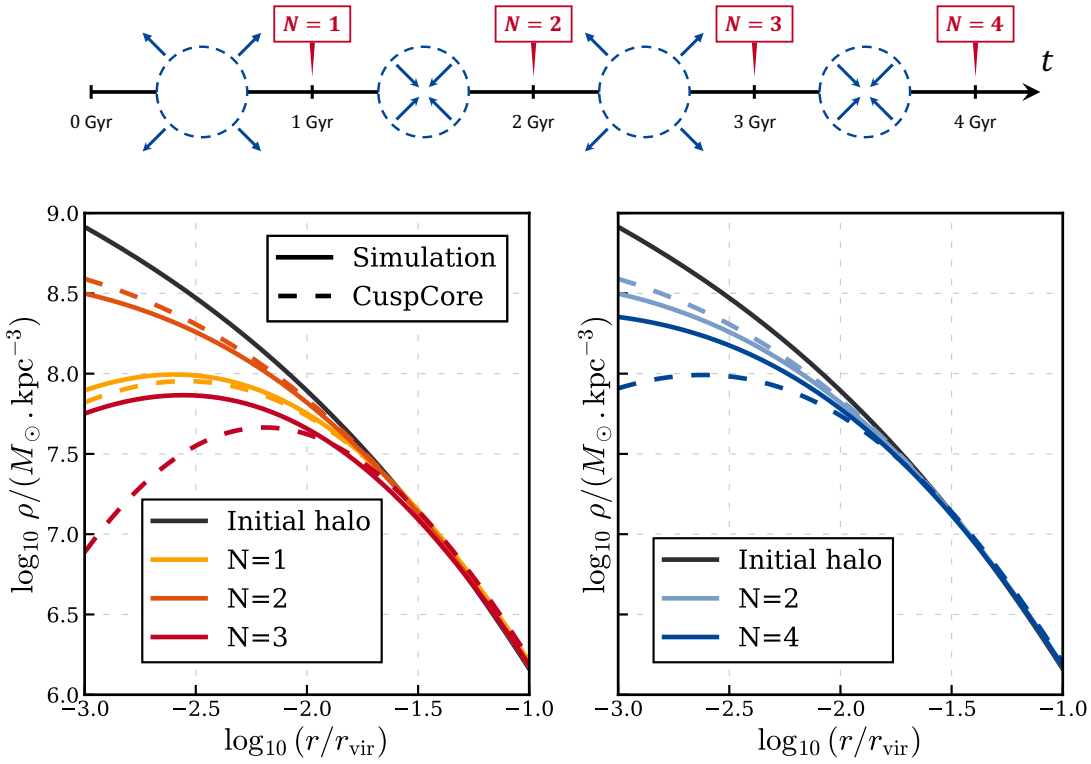

Figure 2.9: Multiple episodes of mass flow. The diagram at the top of the figure is a timeline of the mass flow events. At $t = 0$ Gyr, baryonic mass is removed, causing the halo to expand until $t = 1$ Gyr when the mass is re-added to the center. The halo then contracts until $t = 2$ Gyr when the mass is removed again, and so on. In the lower part of the figure, the two plots show the evolution of the inner part of the dark matter density profile after the flow episodes N indicated in the top diagram. In both panels, the initial profile is shown in black. The solid lines are fits to the simulation data using the Dekel-Zhao functional form (Eq. 2.13), and the dashed lines are predictions from the CuspCore model. The halo responds to a 100% variation in baryonic mass, and the total baryonic mass is such that $m_{\rm bar}/M_{\rm vir} = 0.002$. The left panel shows the density profiles after the first three flow episodes. It is observed that as N increases, the model diverges from the simulation. The right panel shows only the density profiles for the even-numbered N episodes, i.e., the moments when the central baryonic mass is the same as at the beginning of the simulation. Despite the presence of the same amount of baryonic matter at the halo's center, the density profile decreases. The impulsive nature of feedback processes assumed in the CuspCore model irreversibly transfers energy to the dark matter, creating a core in the density profile independent of the amount of central baryonic mass.

subsequently reaccreted at the center in a repeated manner.

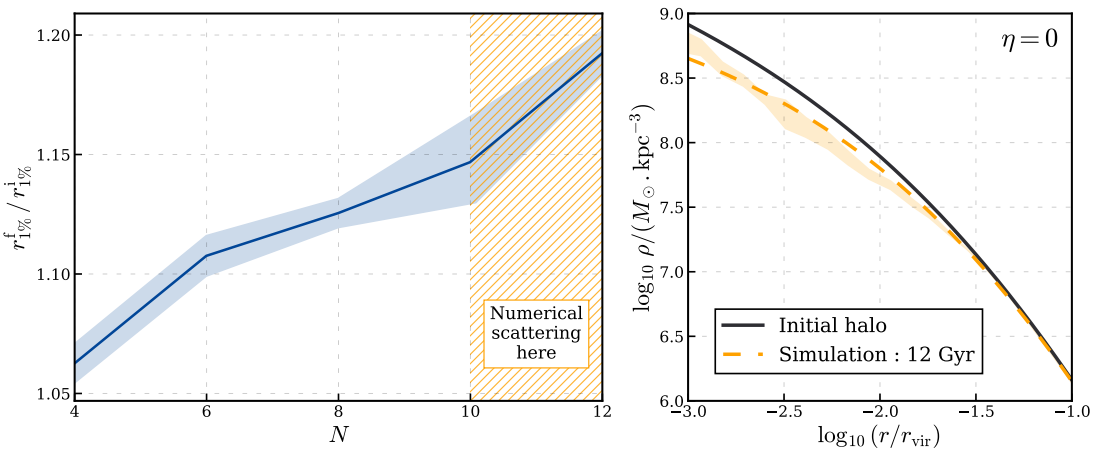

Figure 2.10: Left Panel: Magnitude of the core creation as a function of the number of alternating mass flows. Core creation is measured using the ratio $r^{\rm f}_{1\%}/r^{\rm i}_{1\%}$ of the final to initial radius enclosing 1% of the virial mass of the halo. We simulated the cases with $N = 4, 6, 8, 10$, and 12 even-numbered episodes, i.e., the moments when the central baryonic mass is the same as the initial mass. For each case, we conducted 5 simulations, and the scatter corresponds to the standard deviation of the 5 values of $r^{\rm f}_{1\%}/r^{\rm i}_{1\%}$ obtained. The increase in this ratio with N indicates that core creation becomes more significant as the number of flow episodes increases. The region where $N > 10$ is hatched to indicate the presence of numerical scattering. An example of the effect of this scattering is shown in the right panel, where the artificial lowering of the density profile is observed when the simulation time is too long, despite the baryonic mass remaining constant.

2.4.3 The CuspCore II model

The limitations of the CuspCore model that we have highlighted can be attributed to the simplifying assumptions underlying the model. The reasoning presented in Section 2.2.2 is valid under the assumption that there is no shell crossing, which allows us to assume that the energy of each shell is conserved during the system's relaxation. In other words, r_i and r_f refer to the same Lagrangian shell. When shell crossing occurs, we assume that the energy equality still holds but for shells encompassing the same mass before and after relaxation, even if they do not represent the same Lagrangian shell. This strong assumption of the model is not formally justified. The reality is more complex and for epicyclic orbits the energy change depends on the orbital phase as it is a function of the radius at the time of the potential variation. Thus, particles on the same initial orbit, and therefore with the same energy, can experience different energy gains depending on their phase. This is an energy diffusion process.

Such tests of the CuspCore model were carried out more systematically using a

setup close to the one I developed by Zhaozhou Li (Hebrew University of Jerusalem). Identifying the flaws of the model, as presented here, enabled Zhaozhou Li to generalize the model. Both the tests and the generalization of the model are presented in Li et al. (2023). The new CuspCore II model treats the relaxation process self-consistently. It traces the diffusion of orbital energy by iteratively updating the phase-space distribution function during relaxation. The new version of the model reproduces the simulated dark matter profiles with approximately 10% accuracy or better, outperforming the CuspCore model and providing more accurate predictions even in extreme cases of significant mass variation.

2.5 Dynamical buoyancy and core stalling

Limitation of Chandrasekhar's formalism. The presence of a core in the density profile has significant consequences on the orbital dynamics of objects within the galaxy. In Section 1.4.2, we discussed dynamical friction, which describes the loss of momentum and kinetic energy of a massive body moving through a field of lighter particles due to gravitational interactions. Chandrasekhar's description, as presented in Eq. 1.28, works well in simple cases to describe the orbits of satellites in spherical galaxies (and non-spherical ones if we account for velocity anisotropy corrections) with general background distributions (Binney, 1977; White, 1983; Bontekoe & van Albada, 1987; Zaritsky & White, 1988; Weinberg, 1989; Cora et al., 1997; Peñarrubia et al., 2004). However, it is based on strong assumptions. Firstly, it assumes the background is infinite, homogeneous, and isotropic. Secondly, it neglects the self-gravity of the medium, including the self-gravity of the wake and the medium's response to the perturbation caused by the perturber. Lastly, this description assumes that stars pass by the massive object M in Keplerian hyperbolae (cf. Sect. A.1), while orbits in the combined gravitational fields of M and the galaxy are more complex.

This description is therefore not perfect and shows several shortcomings. For instance, being local (proportional to the local density), it suggests that a perturber orbiting outside a galaxy (or halo) of finite extent would not feel any drag force, which is not what is observed in simulations (see Lin & Tremaine, 1983). Later, Tremaine & Weinberg (1984) formulated a perturbative theory of dynamical friction, providing a global rather than local understanding of the phenomenon through resonances. In this framework, the decay of the perturber's orbit is due to interactions between the latter and resonant background orbits, resulting in a net retarding torque called LBK torque (after Lynden-Bell & Kalnajs, 1972). This explanation naturally resolves the locality problem mentioned above.

Dynamical friction in density cores. Another problem is that the simplifications we mentioned earlier are particularly problematic when the perturber is near the galactic center, where the integrated galactic mass is comparable to the perturber's mass. More recently, other deviations from Chandrasekhar's formulation have been observed, particularly in density cores. Core stalling, i.e., the cessation of dynamical friction in a constant density core (Read et al., 2006; Inoue, 2011; Petts et al., 2015), and dynamical buoyancy, i.e., the outward push of a perturber initially placed near the center of a cored density profile (see Cole et al., 2012), have been observed in simulations and are not accounted for by Chandrasekhar's formulation. To tackle this issue, using a slightly different approach with the collisionless Boltzmann equation to compute the perturbed distribution function of field particles, Kaur & Sridhar (2018) found the net torque and showed that when the perturber enters a core region, important resonances are suppressed, decreasing the strength of the torque and stopping dynamical friction. This provides an explanation for core stalling in terms of resonances. They also found that the stalling radius $r_{\rm cs}$ is directly related to the mass of the perturber through:

$$\Omega_{\rm p}(r_{\rm cs}) = \Omega_{\rm b} \quad \text{with} \quad \Omega_{\rm p}(r) = \sqrt{G\frac{M_{\rm b}(<r) + M_{\rm p}}{r^3}}, \tag{2.27}$$

where $\Omega_{\rm p}$ is the perturber's orbital frequency, $\Omega_{\rm b}$ the orbital frequency of stars at the very center of the cored potential and $M_{\rm b}(<r)$ the enclosed mass of the background density.

Recently, Banik & van den Bosch (2021) extended the work of Tremaine & Weinberg (1984) and Kaur & Sridhar (2018) by relaxing two underlying assumptions: the secular approximation, which implies that the perturber evolves over a timescale much longer than the system's dynamical time, and the adiabatic approximation, which assumes that the perturber is introduced into the system over a long timescale.

By relaxing these two assumptions, they derived an expression for a generalized LBK torque which has contributions from both resonant and non-resonant orbits. In the adiabatic limit, which assumes a slow growth of the perturber potential, they recovered the LBK torque with contributions solely from pure resonances. Conversely, in the limit of an instantaneous introduction of the perturber (as typically done in idealized numerical simulations), the result is a time-dependent torque with contributions from both near-resonant and purely resonant orbits. This torque can be retarding, causing the slowing down of the perturber and thus the phenomenon of dynamical friction [6] , but it can also flip sign, making it enhancing and causing dynamical buoyancy. Core stalling is simply a migration trap that occurs at a radius balancing these two phenomena.

[6] They also recover the "super-Chandrasekhar" phase observed in Zelnikov & Kuskov (2016).

Figure 2.11 shows the radius of a perturber plunging into a density core as a function of time. With the theoretical model of Banik & van den Bosch (2021), it is observed that if the perturber initially has an orbital radius larger than the core stalling radius, it will plunge towards the center at a slightly slower rate than predicted by Chandrasekhar, then undergo a super-Chandrasekhar phase during which it falls at an accelerated rate (Read et al., 2006; Zelnikov & Kuskov, 2016). This enhancement occurs only in the core region of the galaxy. Finally, after this phase, it reaches the stalling radius and becomes trapped in this equilibrium zone between friction and buoyancy. Conversely, if the perturber initially has an orbital radius smaller than the core stalling radius, it will be pushed towards the latter by dynamical buoyancy and will also end up in this equilibrium. We note that the theoretical core stalling radius from Kaur & Sridhar (2018) is slightly different from that of Banik & van den Bosch (2021). In the following, we will use the definition by Kaur & Sridhar (2018), as it is simpler to implement.

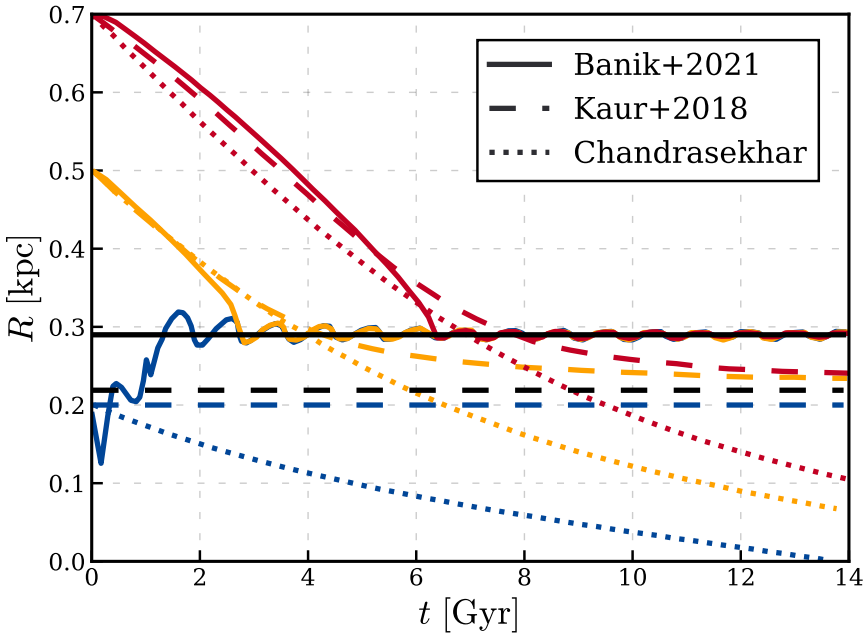

Figure 2.11: Orbital decay of a perturber in an isochrone potential for various initial radii. The dotted lines represent the results from Chandrasekhar's formalism. The dashed lines show the results from Kaur & Sridhar (2018) with the LBK torque, and the solid lines depict the results from the generalized LBK torque obtained by Banik & van den Bosch (2021). Each color corresponds to a different initial radius. The horizontal black lines represent the theoretical core stalling radii from the two formalisms. We observe that they differ slightly; in the following, we will use the definition by Kaur & Sridhar (2018), as it is simpler to implement. This figure is a simplified version of Fig. 4 from Banik & van den Bosch (2021).

To determine if we can achieve core stalling and to test the analytical formula for the core stalling radius given by Kaur & Sridhar (2018) in Eq. (2.27), we conducted a test simulation of a black hole on an epicyclic orbit within a cored potential. We used the BONSAI tree code, a GPU-based code that is faster than GYRFALCON, which operates on a single processor. For the simulation parameters, we followed those of Read et al. (2006) to see if we could obtain similar results. Thus, we have a black hole with a mass $M_{\rm BH} = 2 \times 10^5\, M_\odot$, initially located at $r = 1.069$ kpc from the center of a halo distributed according to a Zhao profile (cf. Eq. 1.21) with $\rho_0 = 9.93 \times 10^7 M_\odot.\mathrm{kpc}^{-3}$ (corresponding to a virial mass $M_{\rm vir} = 2 \times 10^9\, M_\odot$) and parameters $\alpha = 1.5$, $\beta = 3$, and $\gamma = 0$. The scale radius is $r_{\rm s} = 0.91$ kpc, and the concentration is $c = 40$. We simulated a total of $N = 10^7$ particles.

Figure 2.12 shows the radius of the black hole as a function of time. We observe the stalling phenomenon starting at around 9 Gyr of evolution, when the radius stabilizes. We also indicated on this figure the theoretical core stalling radius given by Eq. (2.27). This radius accurately describes the final position of the black hole. The black hole's stalling occurs around the core radius $r_{\rm core} \sim 200$ pc, similar to the results of Read et al. (2006). However, the stalling happens slightly later, which is due to the fact that the black hole is not entirely in equilibrium at the beginning of the simulation, explaining the initial jump in radius. Therefore, it starts from a slightly higher radius and takes longer to reach the core.

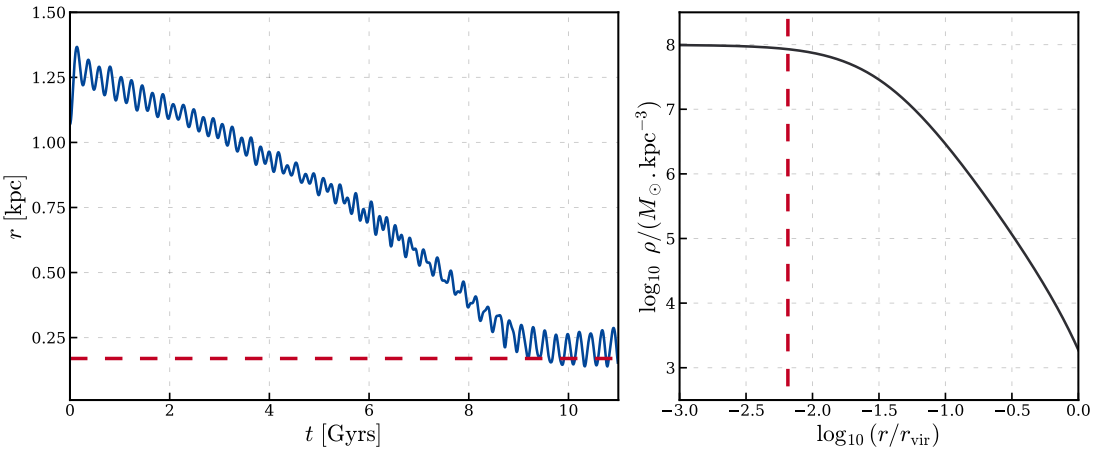

Figure 2.12: Core stalling in simulation. Left panel: Orbital radius of a black hole in a slightly elliptical orbit as a function of time. The red dashed line indicates the position of the theoretical core stalling radius given by Eq. (2.27). As the black hole approaches the density core, its radius stops decreasing and stabilizes at the core stalling radius. Right panel: Background density profile. The red dashed line indicates the theoretical core stalling radius.

As we have seen, the presence of a harmonic core changes the dynamics of perturbers and gives rise to various effects not accounted for by the classical description of dynamical friction. On the other hand, several observations point to the presence of cores approximately 1 kpc in size at the centers of dark matter halos across all scales, from dwarf galaxies to the most massive galaxies (see Binney & Evans, 2001; Borriello & Salucci, 2001; de Blok et al., 2001). If massive black holes become offset due to core stalling or long infall times, the question arises whether they can merge outside the galactic center. This is the question we will address in the following chapters of this manuscript.

2.6 Summary of Chapter 2

This chapter focuses on understanding the interplay between dark matter and baryonic matter within the centers of galaxies. It explores the discrepancy in the distribution of dark matter between the theoretical predictions of the ΛCDM model and observations.

Cusp-Core Discrepancy. The ΛCDM model predicts that dark matter governs large-scale structures, with baryons becoming significant later. Simulations based solely on dark matter show a density cusp at the center of halos. However, observations, particularly of dwarf galaxies, reveal flat density cores instead. This inconsistency, known as the cusp-core discrepancy, challenges the ΛCDM model. Two approaches have been proposed to address this discrepancy: one modifies the cold dark matter model, while the other retains it and emphasizes the interaction between baryonic and dark matter. In this chapter, we focused on the latter, presenting the CuspCore model, which explains core formation through feedback processes.

The CuspCore Model. Feedback processes, such as stellar winds and supernova explosions, can create potential fluctuations that drive dark matter particles away from the center, forming a core. Hydrodynamical simulations support this, but often rely on ad hoc parameters. We introduced the CuspCore model, which explains core formation through feedback-induced potential fluctuations. The model outlines a three-step process: initial equilibrium, instantaneous mass variation, and subsequent relaxation. The relaxation, assumed to occur at constant energy, leads to a new equilibrium state featuring a density core.

Tests with N-body simulations. Simulations are crucial for testing theoretical models, given the non-replicable nature of the universe. In this chapter, we tested the predictions of the CuspCore model using N-body simulations at the galactic scale. We described the setup for N-body simulations, including techniques like tree-code and softening to manage computational complexity.

Single epsiode. These simulations highlighted the successes and failures of the Cus-

pCore model. They revealed that the CuspCore model accurately predicts core formation in many scenarios (see Fig. 2.7) but fails under certain conditions, such as extreme mass variations. We found that for large mass variations (greater than 35%), the ratio of baryonic-to-virial mass significantly affects the accuracy of the model's prediction. In these cases, when $m_{\rm bar}/M_{\rm vir} \lesssim 0.001$, the model tends to underestimate core creation. Conversely, when $m_{\rm bar}/M_{\rm vir} \gtrsim 0.003$, the model overestimates core creation (see Fig. 2.8).

Multiple episodes. Multiple episodes of baryonic mass variation are also explored. In a scenario of alternating outflows and inflows, the model has significant difficulty predicting the behavior of the simulations starting from the second outflow (see Fig. 2.9). However, the simulations demonstrate the cumulative effect of repeated fluctuations in creating cores (see Fig. 2.9 and 2.10). The effectiveness of multiple episodes in creating a density core with smaller mass variations suggests studying the limit where the number of episodes is very large and the mass variation is small. This scenario, resembling feedback in dwarf galaxies, aligns with the theoretical model where core creation arises from stochastic density fluctuations in the gas distribution (El-Zant et al., 2016).

Caveat and improvements. The model's failures can be attributed to its strong assumptions, such as the conservation of energy during the relaxation phase and the disregard for orbital eccentricity, which induces an energy diffusion process. Acknowledging these limitations of the original CuspCore model led to its generalization: the CuspCore II model (Li et al., 2023). This new version self-consistently traces the diffusion of orbital energy, providing more accurate predictions even in extreme scenarios.

The consequences of a density core. To conclude this chapter, we discussed the impact of a density core on orbital dynamics. The presence of cores gives rise to new phenomena such as dynamical buoyancy and core stalling, which prevent perturbers like massive black holes from falling to the center of galaxies. This partly motivates the exploration of scenarios involving the mergers of massive black holes outside of galactic centers, which will be the focus of the upcoming chapters.

3 Off-center mergers and black hole influence in cored profiles

Overview

In this chapter, we present the standard scenario of massive black hole mergers in galactic centers. Then, after providing the motivation for our work, we propose an off-center merger scenario for black holes. We study the structure of the Lagrange points for the case of a cored dwarf galaxy and calculate the radius of influence of a black hole in this context. Finally, we define a capture criterion. Subsections 3.2, 3.3, and 3.4 are detailed versions of Sections 1, 2.4, and 2.5 of François et al. (2024), adapted to fit the manuscript. A summary of the chapter is available in Section 3.5.

3.1 Standard scenario of massive black hole mergers: the reign of dynamical friction

Observations indicate the presence of massive black holes (MBHs) in galaxies ranging from dwarfs to ellipticals, and even potentially in globular clusters [1] (see Section 1.4.3). Major galaxy mergers, accretion events, and the in-spiraling of globular clusters can result in multiple black holes (BHs) within the same galaxy (see Schweizer et al., 2018; Nguyen et al., 2019; Kollatschny et al., 2020; Shen et al., 2021; Stemo et al., 2021; Voggel et al., 2022; Pechetti et al., 2022). Subsequently, several physical processes come into play to bring MBHs from several kpcs away to form a binary and potentially merge.

[1] Although a clear consensus has not yet been established.

This process can roughly be divided into three stages (Begelman et al., 1980).

From kiloparsec to parsec. A typical galaxy has an effective radius [2] ranging from about a kiloparsec in dwarf galaxies to several tens of kiloparsecs in elliptical galaxies. In hopes of merging BHs within these galaxies, a physical process is needed to bring them from these distances down to a few parsecs. This role is fulfilled by dynamical friction. As a BH moves through a galaxy, it transfers part of its kinetic energy to stars and/or gas, loses angular momentum, and spirals towards the galaxy's center (see Section 1.4.2). Figure 3.1 shows the time required for a supermassive black hole (SMBH) on a circular orbit within the disk of our Milky Way to fall to the center due to dynamical friction. This was calculated using equations (A.71) and (A.72). It shows that a SMBH, originating several kiloparsecs away, can effectively reach the galactic center within the span of a Hubble time. In scenarios where multiple MBHs exist within the same galaxy, this process creates a focal point in phase space, enabling MBHs to converge within the galaxy.

Three-body scattering. When two MBHs of masses M_1 and M_2 converge at the galactic center and achieve a negative binding energy, they form a bound pair. In the center-of-mass frame, this energy is expressed by [3] :

$$E_\mathrm{b} = -\frac{G M_1 M_2}{2\, d_\mathrm{rel}}, \tag{3.1}$$

with $\mu = M_1 M_2/(M_1 + M_2)$ the reduced mass, G the gravitational constant, d_rel the relative distance between the two BHs and v_rel their relative velocity. Following this, the binary enters a second phase where it loses energy and angular momentum, tightening through three-body interactions with nearby stars. When a star approaches the BH pair, it gravitationally interacts and can be ejected from the three-body system with increased kinetic energy, which tightens the binary (Saslaw et al., 1974). During this interaction, the change in the binary's energy is given by:

$$\Delta E = \mathrm{C}\frac{2\, m_\star}{M_1 + M_2}\, E_\mathrm{b} \simeq -m_\star \frac{G\mu}{d_\mathrm{rel}}, \tag{3.2}$$

where $m_\star$ is the mass of the star and C is a non-trivial function of the encounter parameters. For the second equality, we used equation (3.1) and set $\mathrm{C} = 1$ since Monte Carlo experiments have shown that C is typically of the order of unity (Hills, 1983; Sesana et al., 2006).

The binary tightens when the star is ejected from the system, that is, if its velocity exceeds the escape velocity, which, to first order, equals the stars' velocity dispersion σ.

[2] The radius within which half of the galaxy's total light is emitted.

[3] This expression does not account for the external tidal field.

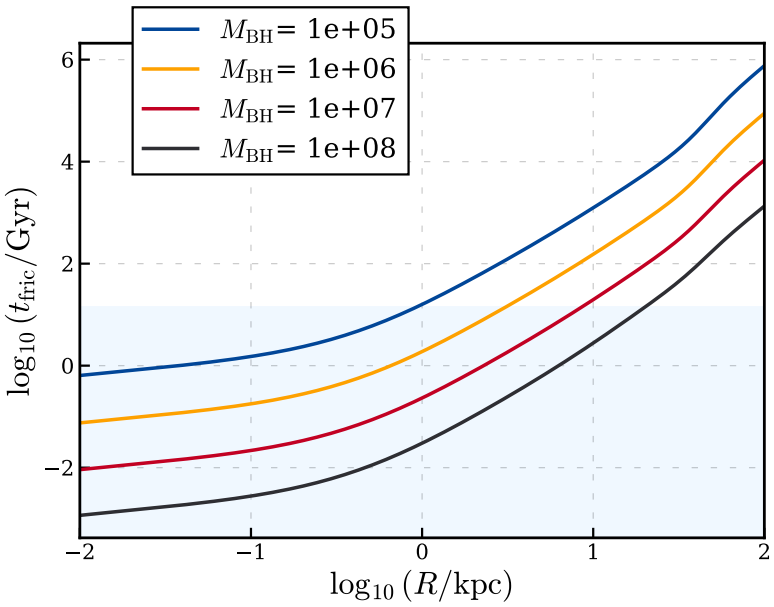

Figure 3.1: Time required to reach the Milky Way galactic centre due to dynamical friction as a function of the initial orbital radius R. Different colors indicate BHs of varying masses. The BH is assumed to be in a circular orbit within the disk plane. The Milky Way's potential is modeled with a thin and a thick stellar disk, a gas disk, a stellar bulge, and a dark matter halo. The parameters are from (McMillan, 2017). For the velocity dispersions of the thin disk, thick disk, gas disk, bulge, and halo, values of $43, 85, 10, 100, 200$ km.s^{-1} are adopted respectively (Bensby & Feltzing, 2006; Kalberla & Kerp, 2009; Rich et al., 2007; Battaglia et al., 2005). We assume an isotropic dark matter halo and use the radial dispersion from (Battaglia et al., 2005). The blue region represents times shorter than the age of the Universe.

We have:

$$-\Delta E > \frac{1}{2} m_\star \sigma^2 \quad \Leftrightarrow \quad d_{\rm rel} < r_h \equiv \frac{2\,G\mu}{\sigma^2} \tag{3.3}$$

where r_h is the hardening radius. To get an idea of the magnitudes involved, consider our Milky Way ($\sigma_{\rm MW} \sim 200$ km.s^{-1}) and suppose it harbors a second SMBH of the same mass as Sagittarius A* [4] ($M_{\rm Sgr} = 4.1 \times 10^6\, M_\odot$). In this case, stellar scattering becomes efficient when the binary has a separation of $d_{\rm rel} = r_h = 0.5$ pc.

However, this process is constrained by the number of stars that are available to interact with the binary. If there are insufficient encounters, the binary stalls, this is known as the "final parsec problem" (Milosavljević & Merritt, 2003). For a star to be ejected by the binary, it must have sufficiently low angular momentum to pass close to the galactic center, and there is a limited number of stars that meet this criterion.

[4] The BH at the center of our Galaxy.

This is particularly true in galaxies with strong symmetry, such as spherical or disk galaxies, where angular momentum conservation along the axis of rotation limits the number of stars that can pass close to the center [5] . Therefore, a process is needed to refill low angular momentum stars within a Hubble time to allow the BHs to merge. Several models have been proposed to solve this "loss cone refilling problem," but there are still many uncertainties. Negative gas torques were initially suggested as a potential solution, however, recent simulations indicate that AGN winds create a feedback cavity, effectively stripping the binary and halting the orbital decay process (del Valle & Volonteri, 2018). Another possibility is the presence of a third MBH, which could increase the binary's eccentricity through the Kozai mechanism (Blaes et al., 2002) or extract energy via gravitational slingshot (Valtonen et al., 1994).

Relativistic regime. If there are sufficient stars to facilitate energy loss through three-body scattering, the binary can reduce its separation to a point where gravitational radiation becomes a dominant factor. While gravitational waves are emitted in principle at all separations, the energy loss is significantly more efficient when the binary is closely bound. Let's calculate this critical separation, assuming the orbits are circular. Under this assumption, the system decays within a finite time, $t_{\rm GW}$, given by (see Peters, 1964, Eq. 5.10, and note that this formula is valid only at the 2.5 post-Newtonian correction level):

$$t_{\rm GW} = \frac{5\,c^5\,r^4}{256\,G^3\,M_1 M_2 (M_1+M_2)}, \tag{3.4}$$

where c is the speed of light. The separation required for the merger to occur within a Hubble time ($t_{\rm GW} = t_{\rm hubble} \sim 14$ Gyr) is therefore:

$$r_{\rm GW} = \left(\frac{256\,G^3\,M_1 M_2 (M_1+M_2)}{5\,c^5}\, t_{\rm hubble} \right)^{1/4}. \tag{3.5}$$

Taking our previous example of a Sagittarius A* binary at the center of our Milky Way, we calculate the separation at which gravitational waves significantly influence the merger to be $r_{\rm GW} = 0.001$ pc.

The three previous stages constitute the conventional framework for the merger of MBHs through the assembly of galaxies, they are depicted in the top panel of Fig. 3.2.

[5] The lack of angular momentum conservation in triaxial galaxies allows for phylocentric orbits that can feed the binary by passing through the center. However, the rate of replenishing stars via phylocentric orbits is significantly lower than the full loss-cone rate (Vasiliev et al., 2014).

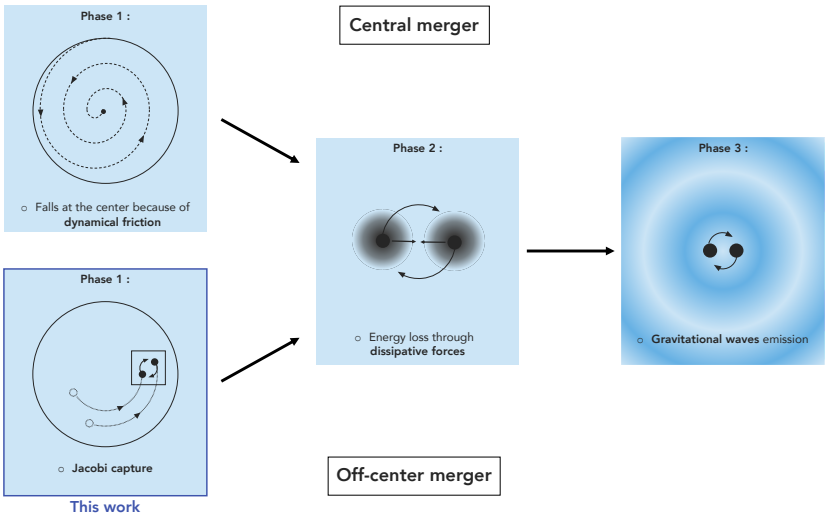

Figure 3.2: Central versus off-center BH merger scenarios. Top row: classical massive BH merger scenario in the galactic center. Phase 1: the massive BHs lose angular momentum through dynamical friction with the galaxy and halo, which causes them to sink toward the center. Phase 2: once both BHs have reached the center, they may form a bound pair and continue to lose energy via dissipative forces. Phase 3: the binary eventually enters the relativistic regime and loses energy through gravitational waves emission, allowing the two BHs to merge. Bottom row: proposed scenario for an off-center merger. Phase 1: the BHs are on off-center orbits e.g., as a result of long dynamical time for their radius to decrease through dynamical friction or core stalling acting against dynamical friction. If both BHs are sufficiently close energetically, they may form an off-center bound pair through Jacobi capture. This is the scenario explored in this thesis.

3.2 Off-center scenario of massive black hole mergers: the counterattack of long fall time and core stalling

The merging scenario relies mainly on dynamical friction to bring BHs together at the center. However, calculating the time it takes for intermediate-mass black holes (IMBHs) to reach the center of a dwarf galaxy reveals that it can significantly exceed the age of the Universe. Figure 3.3, analogous to Figure 3.1, displays this for IMBHs within a dark matter halo of a spheroidal dwarf galaxy. We used here the halo from Chapter 2 modeled by a Zhao profile (Eq. 1.21) with $\alpha = 1$ and $\beta = 3$ representing the outer and transitional slopes of the density profile. The figure shows the infall time for two different inner slopes: $\gamma = 0$, representing a core, and $\gamma = 1$, representing a cusp. The virial mass is still $M_{\rm vir} = 10^{11} M_\odot$, the virial radius is $r_{200} = 100$ kpc, and the scale radius is $r_{\rm s} = 6.7$ kpc, giving a concentration of 15.

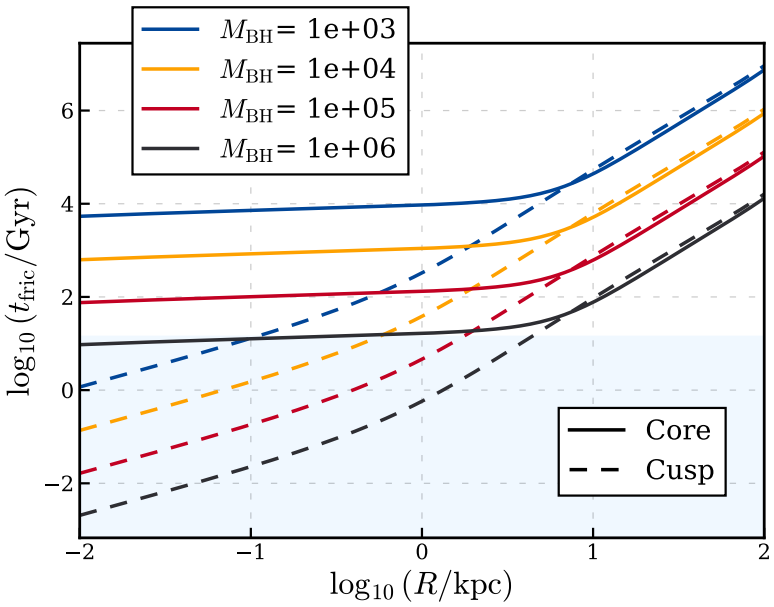

Figure 3.3: Time required to reach the galactic centre due to dynamical friction as a function of initial orbital radius R. Different colors indicate BHs of varying masses. The BH is assumed to be on a circular orbit. The potential is that of a spheroidal dwarf galaxy dark matter halo, described by an (α, β, γ) density profile (Hernquist, 1990; Zhao, 1996). Two internal slopes are used: $\gamma = 0$ (core) and $\gamma = 1$ (cusp). A velocity dispersion value of 20 km.s^{-1} has been used. The blue region represents times shorter than the age of the Universe. It is observed that in the case of a cored density profile, IMBHs do not have sufficient time to reach the center via dynamical friction.

It is observed that in the case of a cored density profile, IMBHs ($10^3 - 10^6 M_\odot$) predominantly do not have sufficient time to reach the center due to dynamical friction. As a consequence, BHs are left on off-center orbits, with their guiding radius reducing only very slightly over 14 Gyr. According to simulations and observations, it is estimated that half of the IMBHs are off-center in dwarf galaxies (see Bellovary et al., 2019; Pfister et al., 2019; Reines et al., 2020; Bellovary et al., 2021). Furthermore, their electromagnetic detection is highly challenging due to their low accretion luminosities, and their dynamical detection is equally problematic as they have a very small impact on the dynamics of the stars within their sphere of influence.

In certain instances, however, the long infall time argument alone does not provide a satisfactory explanation for the existence of off-center objects, such as in the case of the Fornax dwarf galaxy. This galaxy harbors five globular clusters orbiting at approximately 1 kpc from its center (Mackey & Gilmore, 2003), and based on conventional assumptions, these clusters should have migrated from their current locations within a few billion years (see Goerdt et al., 2006, though this picture has been challenged, given

the modeling freedom of the initial GC formation radius, and uncertainties arising from projection effects, see e.g., Borukhovetskaya et al. 2022). As we saw in Section 2.5, this is in part due to dynamical processes which cannot be modeled using Chandrasekhar dynamical friction alone: numerical simulations have revealed instances of core stalling, where the perturber's fall comes to a halt (see Read et al., 2006; Inoue, 2011; Petts et al., 2015), as well as the occurrence of an outward push, or dynamical buoyancy (see Cole et al., 2012). These phenomena are observed in constant-density cores (as those observed at the center of dark matter halos in low-mass galaxies, see Binney & Evans, 2001; Borriello & Salucci, 2001; de Blok et al., 2001), and are not accounted for in Chandrasekhar's description.

3.3 Off-center mergers as a 3-body problem

In light of these cases where IMBHs are found off-center, either because their infall time greatly exceeds the dynamical time of the system or because it is halted due to the presence of a constant density core, the question arises whether a IMBH merger is possible outside the galactic center. Indeed, the aforementioned three-phase scenario must be revised. Firstly, there is no guarantee that the BHs may get sufficiently close in phase space to form a binary, as opposed to the classical case where the galactic center acts as an attractor, allowing an agglomeration at a single point. In this context, specific phase-space conditions must be met for them to form bound configurations away from the center.

We propose a new scenario for off-center mergers of MBHs, starting with a gravitational capture [6] . During this phase, the two BHs meet a suitable configuration where their gravitational attraction becomes comparable to the force generated by the galaxy. They bond, outside the center, for a certain period of time and produce several close encounters. This scenario may be modeled, as a first approximation, as a circular-restricted three-body problem. This is a variation of the three-body problem in which two very light objects orbit around a much more massive body. This problem, known as Hill's problem, has been extensively studied to describe the movements of satellites around a planet (Petit & Henon, 1986; Henon & Petit, 1986; Petit & Hénon, 1990) as well as gravitational wave capture of stellar-mass BHs around a supermassive BH (Boekholt et al., 2023; Li et al., 2022). The principal distinctions in our case lies in the fact that a galaxy is an extended massive body rather than point-like, so the mass of the central body depends on the orbital radius of the BHs and the shape of the potential is different, featuring a density core at the center.

Then, it has been observed that dissipative forces play a crucial role in the hardening of the binary (e.g., Fabian et al., 1975; Goldreich et al., 2002). In Li et al. (2022);

[6] In this manuscript, we will use the terms gravitational capture, Jacobi capture, or simply capture.

Boekholt et al. (2023) this energy dissipation is facilitated by the emission of gravitational waves, while in Tagawa et al. (2018, 2020); Li et al. (2022); Rowan et al. (2023); DeLaurentiis et al. (2023), it is dynamical friction with the surrounding gas that tightens the binary. We anticipate a similar behavior for the case of two IMBHs: the bound stellar populations that typically surround them can generate dynamical friction on the other BH, eventually leading to the last step of the classical scenario (see bottom panel in Fig. 3.2).

3.3.1 Classical Keplerian case & distant tide approximation

In the following chapters of this manuscript, we focus on the first step of the off-center merger scenario, i.e. the Jacobi capture. In order to label captures, it is important to have a quantity that allows us to evaluate the gravitational influence of a BH orbiting within a dwarf galaxy. In this section and the subsequent ones, we will calculate this quantity and discuss its limitations within the scope of our study. This will be useful for defining a capture criterion in Section 3.4.

The volume of influence, also known as the Hill volume, defines a spatial domain surrounding the BH where its gravitational influence dominates. Traditionally, this volume is approximated as a sphere, characterized by the Hill radius (or radius of influence). In the classical restricted three-body problem, this radius is derived by determining the distance between the body of interest and the Lagrange point L1, situated along the line connecting the two massive bodies, between them (cf. Fig. 3.4).

Consider the simple case of a BH with mass m on a circular orbit around a point mass M, as described in Binney & Tremaine (2008) Sect. 8.3.1. We orient the coordinate system so that m and M are at $\mathbf{r}_m = [M, R/(M+m), 0, 0]$ and $\mathbf{r}_M = [-m, R/(M+m), 0, 0]$, respectively, and the angular speed is $\Omega = (0, 0, \Omega)$, with

$$\Omega = \sqrt{\frac{G(M+m)}{R}}, \tag{3.6}$$

where R is the relative distance between the two masses. According to its definition, the Hill radius, $r_{\rm H}$, satisfies:

$$\left.\frac{\partial \Phi_{\rm eff}}{\partial x}\right|_{(x_{\rm m}-r_{\rm H},0,0)} = 0, \tag{3.7}$$

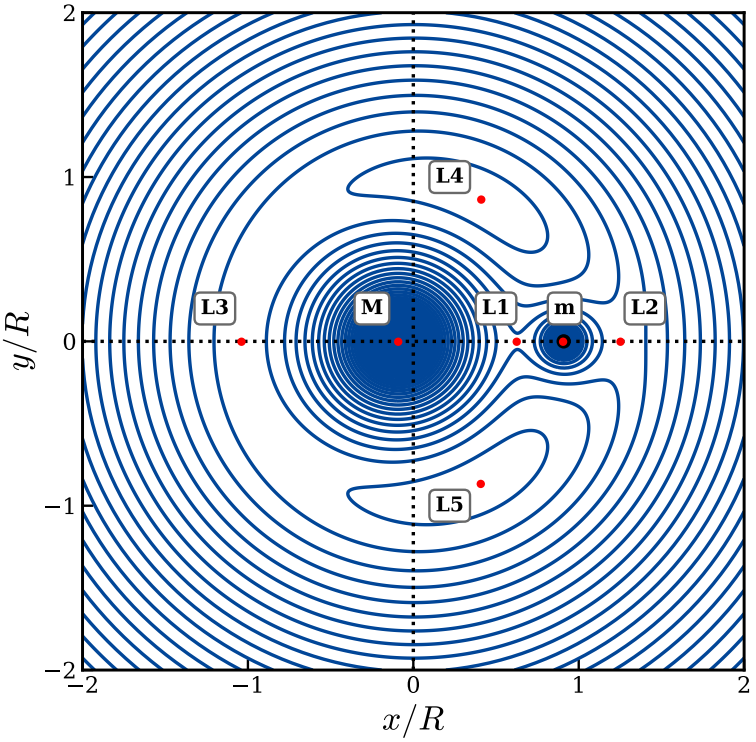

Figure 3.4: Effective potential of the two masses system M and m, plotted in the reference frame rotating at the angular frequency of the BH orbit in the (x, y) plane. The coordinates $(x, y) = (0, 0)$ denote the center of mass of the two masses. The Lagrange points, along with the positions of the masses are highlighted in red.

with the potential given by [7] :

$$\begin{aligned}\Phi_{\rm eff}(\mathbf{r}) &= \Phi_M(\mathbf{r}) + \Phi_m(\mathbf{r}) - \frac{1}{2}|\mathbf{\Omega} \times \mathbf{r}|^2 \\ &= -G\left[\frac{M}{|\mathbf{r}-\mathbf{r_M}|} - \frac{m}{|\mathbf{r}-\mathbf{r_m}|} + \frac{M+m}{2R^3}(x^2+y^2)\right].\end{aligned} \tag{3.8}$$

Thus, we have

$$\frac{1}{G}\left.\frac{\partial \Phi_{\rm eff}}{\partial x}\right|_{(x_{\rm m}-r_{\rm H},0,0)} = \frac{M}{(R-R_{\rm H})^2} - \frac{m}{R_{\rm H}^2} - \frac{M+m}{R^3}\left(\frac{MR}{M+m} - R_{\rm H}\right). \tag{3.9}$$

Under the distant-tide approximation, assuming a Hill radius much smaller than the distance between the masses ($R_{\rm H} \ll R$) and a significant mass hierarchy ($m \ll M$), the expression simplifies to

$$\frac{M}{(R-R_{\rm H})^2} = \frac{M}{R^2}\left(1 - \frac{R_{\rm H}}{R}\right)^{-2} \simeq \frac{M}{R^2}\left(1 + \frac{2\,R_{\rm H}}{R}\right) \tag{3.10}$$

and

$$\frac{M+m}{R^3}\,R_{\rm H} \simeq \frac{M}{R^3}\,R_{\rm H} \tag{3.11}$$

[7] In the case of a circular orbit.

which finally gives for equation (3.7):

$$\frac{3MR_{\rm H}}{R^3} - \frac{m}{R_{\rm H}^2} = 0 \quad \Leftrightarrow \quad \boxed{R_{\rm H} = \left(\frac{m}{3M}\right)^{1/3} R}. \tag{3.12}$$

It is worth noting that if we had chosen to define the Hill radius as the distance between the BH and the Lagrange point L2, the equation (3.9) would be replaced by

$$\frac{1}{G}\frac{\partial \Phi_{\rm eff}}{\partial x}\bigg|_{(x_{\rm m}+r_{\rm H},0,0)} = \frac{M}{(R+R_{\rm H})^2} + \frac{m}{R_{\rm H}^2} - \frac{M+m}{R^3}\left(\frac{MR}{M+m} + R_{\rm H}\right), \tag{3.13}$$

which, after simplification, yields the same expression for the radius of influence. Therefore, the distant tide approximation imposes a symmetry of the Lagrange points L1 and L2 on either side of the BH.

3.3.2 Lagrange points in a cored profiles

To address the extended galactic case, using the previous analytical expression for the Hill radius, which involves replacing M by $M_{\rm b}(< R)$ the enclosed mass of our background density at the radius of the BH, is not desirable. Complications arise due to several reasons: (*i*) our investigation deviates from previous assumptions, particularly when we examine the dynamics of BHs in close proximity to the center ($R_H \sim R$), where the galaxy's integrated mass is comparable in order to that of the BH ($M_{\rm b}(< R) \sim M_{\rm BH}$); (*ii*) in density profiles featuring a central core, distinct Lagrange point structures emerge, differing from those observed in the Keplerian case (Banik & van den Bosch, 2022); (*iii*) the density profile employed lacks an analytical formula for the potential. For these reasons, we have conducted numerical computations to determine the Lagrange points and the radius of influence.

Figure 3.5 shows the effective potential of the galaxy-BH system, plotted in the reference frame rotating with the BH. Each row in Fig. 3.5 corresponds to a distinct position of the BH within the core. The left-hand column is computed for the cored galactic potential, while the right-hand column corresponds to the Keplerian case, where we approximate the galaxy as a point mass equal to the enclosed galactic mass up to the BH orbit. Near the galactic center, the topology of the effective potential in the (α, β, γ) case differs from the Keplerian case. As the BH approaches the center and reaches a critical radius $R_{\rm crit}$, a bifurcation occurs and the Lagrange points L1, L3 and L0 merge into a single point. In the last two rows of Fig. 3.5, we observe the scenario where the BH's radius exceeds this critical value, resulting in the same number of Lagrange points as in the Keplerian case, albeit at different positions. Conversely, the first row illustrates the case where the BH's radius is smaller than the critical value, leading to

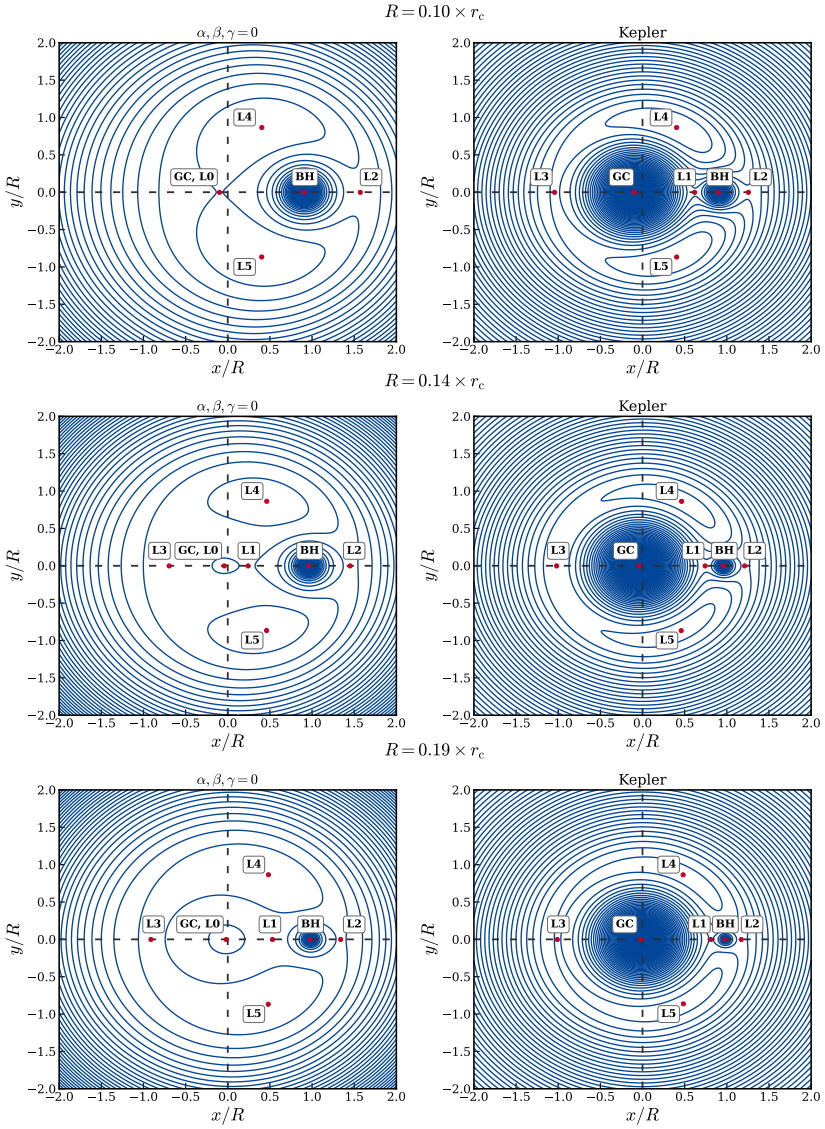

Figure 3.5: Effective potential of the galaxy-BH system plotted in the reference frame rotating at the angular frequency of the BH orbit in the (x, y) plane. The coordinates $(x, y) = (0, 0)$ denote the center of mass, calculated for the sum of the BH mass and the mass of the host galaxy integrated up to the BH orbit. Hence the galactic center is shifted significantly from $(0, 0)$ in some cases. The Lagrange points, along with the positions of the black hole (denoted BH) and galactic center (denoted GC), are highlighted in red. $R = f \times r_c$ is the orbital radius of the BH, where f is a dimensionless factor and r_c represents the core radius of the potential, defined by its inflection point. We observe distinct differences in the topology of the effective potential, as well as in the positioning and number of Lagrange points, between the cored galactic potential (on the left) and the Keplerian case (on the right) where we approximate the galaxy as a point mass equal to the enclosed galactic mass up to the BH orbit.

the merging of Lagrange points L1, L3, and L0 [8] . As the BH's orbital radius increases, the galactic potential gradually approaches the Keplerian model.

3.3.3 Black hole's influence radius in a cored profile

Figure 3.6 shows the Hill radius as a function of the BH orbital radius. It is computed in two ways, by taking the distance between the BH and the L1 Lagrange point and the distance between the BH and L2. Four background potentials are considered : a Keplerian potential and three (α, β, γ) profiles with different inner density slopes.

First, we observe that the distance between the BH and L1 matches that between the BH and L2 around and beyond the core radius. However, this symmetry does not persist within the core. Here, the distant-tide approximation, which enforces precise L1/L2 symmetry by eliminating asymmetry terms in the calculations, breaks down. The exception is the NFW profile ($\gamma = 1$), where symmetry holds across all radii.

In our study profile with a core ($\gamma = 0$), we discern a discontinuity in the BH-L1 distance at a specific radius, indicative of the earlier mentioned bifurcation. Beyond this critical radius, the L1 Lagrange point lies between the BH and the galactic center. However, as the BH's orbital radius diminishes, the L1 point converges toward the galactic center. Below the critical radius, the distance between the BH and the galactic center is measured, accounting for the linearity of the curve.

The Keplerian profile closely aligns with the Hill radius predicted by the distant-tide approximation formula, maintaining this consistency even within the core despite L1/L2 asymmetry. It is only in very close proximity to the center that significant divergence occurs. In contrast, the extended profiles (α, β, γ) exhibit clear discrepancies with the distant-tide approximation, particularly within the core, notably for inner slopes $\gamma = 0$ and $\gamma = 1$. Within our study profile ($\gamma = 0$), we see a difference of a factor of 2 between the distant-tide approximation's analytical formula and the precise computation. This discrepancy, coupled with the distinct shape of the Hill radius curve compared to the Keplerian case, suggests that the galaxy cannot be adequately treated as a radius-dependent point mass. Moreover, the disparities among the three extended density profiles highlight the significant dependence of the Hill radius in our study area on the inner density slope. Consequently, we anticipate an equally pronounced sensitivity of the capture process to this parameter.

Figure 3.7 shows the Hill radius as a function of the BH mass. Two background

[8] A detailed investigation is warranted to confirm whether this convergence indeed represents a single point or falls below our resolution limit. This aspect will be addressed in future research endeavors.

potentials are considered : a Keplerian potential and the cored Zhao profile with $\alpha = 1$, $\beta = 3$ and $\gamma = 0$. The Hill radius increases with the mass of the BH. As the BH mass increases, the BH-L1 and BH-L2 distances diverge. This occurs because the approximation $M_{\rm BH} \ll M_{\rm b}(< R)$ no longer holds, resulting in asymmetrical Lagrange points around the BH.

Figure 3.5 and 3.6 show that the dynamics and likelihood of Jacobi captures are significantly influenced by the galactic context. Firstly, the zone of influence of BHs is different from the Keplerian case, and secondly, the altered topology of the effective potential gives rise to novel types of BH orbits, including Pacman orbits (see Fig. 4.20), which are pivotal for core stalling (Banik & van den Bosch, 2022).

3.4 Capture criterion

We aim to contextualize Jacobi captures within an observable framework to evaluate the likelihood of forming and detecting off-center BH binaries. To achieve this, we conduct simulations spanning a timeframe of 14 Gyr. Consequently, some captures may be truncated by halting the simulation, while others that are theoretically feasible may not have sufficient time to occur. For instance, when the orbital radii of BHs are extremely close, the time required to catch-up their phase difference may exceed 14 Gyr. Likewise, in order to deduce a probability from initial conditions, we incorporate conditions that lead to capture at $t = 0$ Gyr. These cases are indeed conditions allowing BH binding off-center, and due to the ergodic nature of this study, any stretch of 14 Gyr should be equivalent to another. Put differently, a time shift in the simulation range would interchange some initial (happening at $t = 0$ Gyr) and dynamical (happening at $t > 0$ Gyr) captures. Lastly, although we simulate 14 Gyr of evolution during which an initial condition can result in several captures, we solely focus on the first, as higher-order effects can significantly influence the sequence of events in reality (such as dynamical friction and post-Newtonian corrections).

To determine a capture, two conditions must be met. First, the binding energy between the BHs must be negative. This is given by

$$E_{\rm b} = \frac{1}{2}\mu\, v_{\rm rel}^2 - \frac{GM_1M_2}{d_{\rm rel}}, \tag{3.14}$$

with $\mu = M_1M_2/(M_1 + M_2)$ the reduced mass, G the gravitational constant, $d_{\rm rel}$ the relative distance between the two BHs and $v_{\rm rel}$ their relative velocity. Note that this expression does not take into account the external tidal field. Secondly, during the period of negative binding energy, the distance between the BHs must fall below the

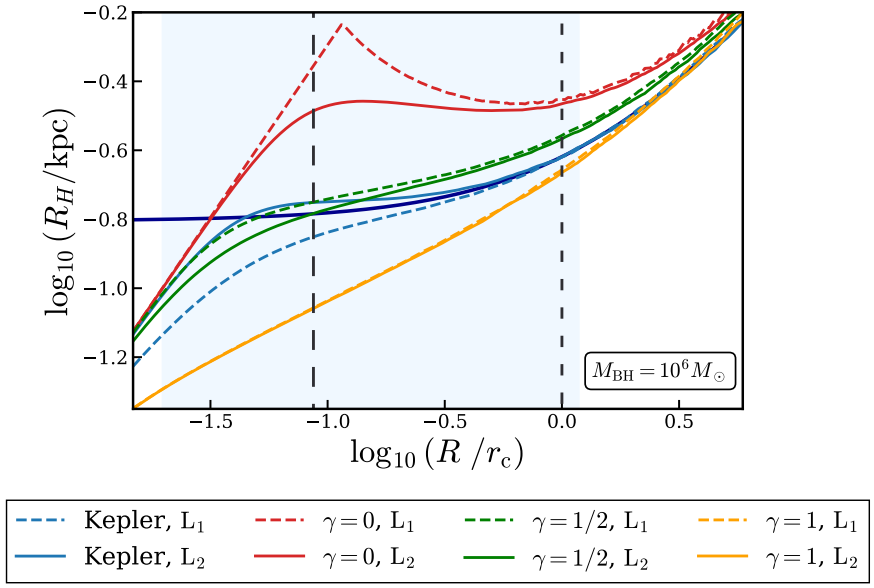

Figure 3.6: Hill radius ($R_{\rm H}$) as a function of the BH orbital radius R in units of the core radius for a mass $M_{\rm BH} = 10^6 M_\odot$. The Hill radius is computed as the BH-L1 distance (dashed lines) and the BH-L2 length (solid lines). Four background potentials were considered : a Keplerian potential (shown as light-blue lines); and three α, β, γ profiles with $\alpha = 1$, $\beta = 3$ and inner slopes $\gamma = 0$ (red), 1/2 (green) and 1 (yellow) respectively. The thick dark blue solid line is for the distant-tide approximation, which goes to a constant value as $R \to 0$. On the figure, the shaded area denotes the scope of this study. The core stalling radius and galactic core radius are indicated by vertical lines. The separation of the dashed and solid lines indicates an asymmetry between L1 and L2 on either side of the BH when entering the core region. Note that for the case of an NFW profile ($\gamma = 1$, yellow) the L1 and L2 solutions very nearly overlap inside the core. The discontinuity of the dashed red line shows a bifurcation of the Lagrange points in the core profile. It is striking that the Keplerian potential remains close to the distant-tide approximation well inside the core of the galaxy, before diverging significantly at $\log\ R/r_{\rm c} \lesssim -1.3$. By comparison, extended profiles may show differences with this approximation exceeding a factor 2 anywhere inside the core for $\gamma = 0$ (red).

binary Hill radius. This radius is defined as the average distance between BH-L1 (or BH-L0 if L1 no longer exists) and BH-L2 for a total mass $M_{\rm tot} = M_1 + M_2$ located at $\tilde{r} = (M_1 \times r_1 + M_2 \times r_2)/(M_1 + M_2)$. This additional condition prevents mislabeling due to coincidental alignment of velocity vectors, which could lead to a negative energy reading. It is important to bear in mind that classical two-body dynamics do not allow for gravitational capture, as BHs get accelerated upon approach due to energy conservation. However, in the three-body system, the presence of a third body enables the binding energy to dip below zero and later return to positive values, allowing for unbinding (Petit & Henon, 1986; Renaud et al., 2011; Peñarrubia, 2023). The time spent in this sub-zero state, during which the BHs can revolve around each other a few times,

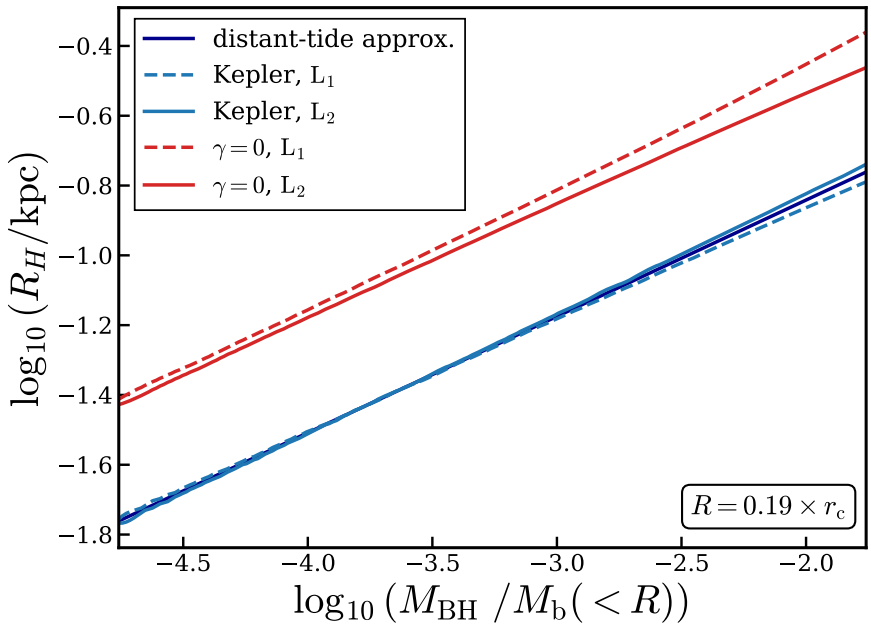

Figure 3.7: Hill radius ($R_{\rm H}$) as a function of the black hole (BH) mass $M_{\rm BH}$, divided by the enclosed galactic mass at the BH radius $M_{\rm b}(< R)$. The BH is placed at a radius $R = 0.19 \times r_{\rm c}$ where $r_{\rm c}$ represents the core radius of the potential, defined by its inflection point. The Hill radius is computed as the BH-L1 distance (dashed lines) and the BH-L2 length (solid lines). Two background potentials are considered : a Keplerian potential (shown as light-blue lines); and the α, β, γ profile with inner slopes $\gamma = 0$ (red). The dark blue line is the distant-tide approximation. The x-axis covers the mass range studied in this manuscript, i.e., $M_{\rm BH} \in [10^3 - 10^6] M_\odot$. The separation of the dashed and solid lines indicates an asymmetry between L1 and L2 on either side of the BH when the distant-tide approximation breaks down ($M_{\rm b}(< R) \sim M_{\rm BH}$).

is challenging to predict due to the chaotic nature of the three-body problem, occurring over a broad range of timescales. However, dissipative forces like dynamical friction, three-body scattering or post-Newtonian corrections can enhance temporary captures when considered (Samsing et al., 2018b; Li et al., 2022; Boekholt et al., 2023; Rowan et al., 2023; DeLaurentiis et al., 2023). Consequently, since our focus in this study is on Jacobi captures, our aim is to identify sub-zero crossings independently of their duration.

Although flybys with a single close encounter are traditionally distinguished from captures with more than one close encounter, we opt to label both scenarios as captures: (i) unlike other distance-based criteria (Boekholt et al., 2023), Eq. (3.14) is more stringent as it incorporates a velocity condition for BHs. This refinement ensures that the surviving flybys consist of BHs close in energy and with mean eccentricities below 1 (see Fig. 4.15). Consequently, we anticipate that these flybys may be more easily stabilized in the future (for a comparison with another, less restrictive criterion yielding

numerous hyperbolic flybys, refer to Section 4.6); (*ii*) it is conceivable that even a single close encounter could lead to eventual stabilization, especially when dissipative forces, such as those arising from the post-Newtonian corrections, play a significant role at the pericenter of eccentric binaries (cf. Fig. 4.15). The question of the conditions necessary for stabilization remains a subject for future investigation.

Figure 3.8 illustrates six instances of Jacobi captures characterized by varying numbers of close encounters. The top row displays the relative coordinates between the BHs during these captures, with the reference frame centered on the most massive BH and rotating with it. The binary Hill radius is depicted by the dotted circle. The bottom row shows the binding energy and the relative distance between the BHs.

3.5 Summary of Chapter 3

This chapter investigates the influence of massive black hole in off-center regions of cored galaxies. It starts with an overview of the standard scenario for massive black hole mergers at galactic centers and introduces a new scenario of off-center mergers as a possible alternative.

Off-Center Scenario for Black Hole Mergers. The standard picture of massive black hole mergers involves a three-phase process starting by their infall towards the galaxy center due to dynamical friction. However, in the case of intermediate-mass black holes in dwarf galaxies, the time required for them to reach the center can exceed the age of the Universe. Additionally, the presence of a constant-density cores allow black holes to settle on stable off-center orbits due to core stalling. In this chapter, we proposed a new scenario for off-center intermediate-mass black hole mergers, initiated by gravitational capture. This process can be approximated as a circular-restricted three-body problem, where the dynamics are influenced by the extended mass distribution of the galaxy, especially in the presence of a central core.

Structure of Lagrange Points in Cored Profiles. First, we studied the structure of Lagrange points in a cored galaxy potential, showing how the topology of the effective potential differs from the classical Keplerian case. Near the galactic center, a bifurcation occurs, and the merging of Lagrange points can significantly affect the dynamics of black holes, altering their zones of influence and the likelihood of gravitational capture.

Radius of Influence and Capture Criterion. Next, we calculated the influence radius of the black holes and showed that, within our study area, it is approximately twice the value given by the distant-tide approximation. In the core, the influence radius depends on the inner slope of the density profile and cannot be approximated using the Keplerian potential typically used in the literature. We defined a binding criterion based

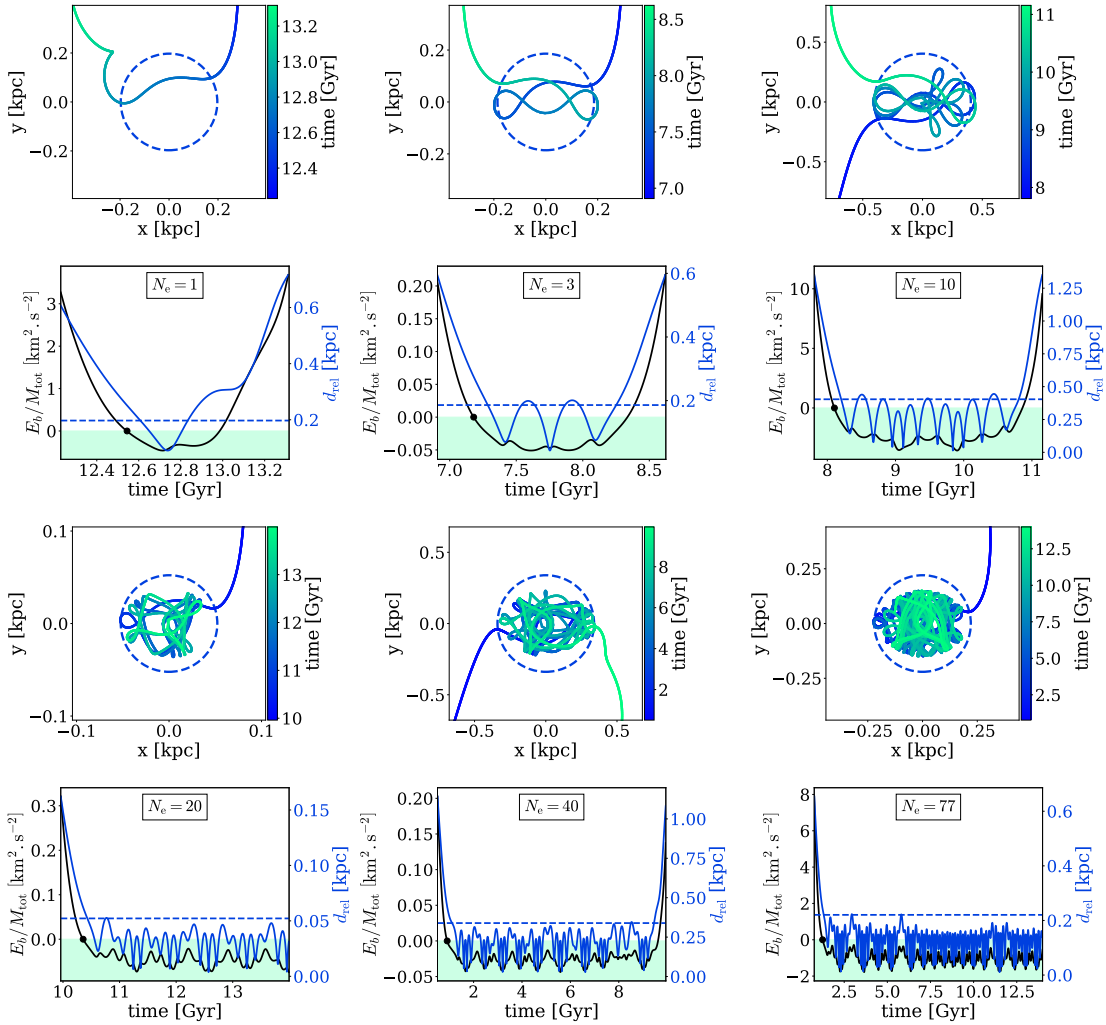

Figure 3.8: Examples of Jacobi captures with different numbers of close encounters between BHs. Top row: relative coordinates between BHs during Jacobi captures. The reference frame is centered on the most massive BH and rotates with it. The binary Hill radius is marked by the dotted circle. Bottom row: the black line represents the binding energy (E_b) per unit mass of the binary ($M_{tot} = M_1 + M_2$), with negative values shown in the colored area. The black marker indicates the point when the energy becomes negative. The blue curve represents the relative distance (d_{rel}) between the BHs. The binary Hill radius is indicated by a dashed blue line. The number of close encounters, N_e, is given in the box. To contextualize captures within observational framework, we extend our simulations over a period of 14 Gyr. Consequently, we observe instances where captures are halted prematurely, as illustrated by cases with $N_e = 20$ and $N_e = 77$. Additionally, we retain flybys due to our energy-based criterion, which is more stringent compared to distance-based criteria. This ensures that surviving flybys comprise BHs with similar energy levels, potentially facilitating stabilization through dissipative forces.

on two requirements: (1) the binding energy between the black holes must be negative, and (2) the distance between the black holes must fall within the binary Hill radius during the period of negative binding energy. The chapter concludes with examples of gravitational captures, illustrating the complex dynamics involved in off-center mergers and setting the stage for further exploration of this alternative scenario in the next chapter.

4 Simulating gravitational captures in dwarf galaxies

Overview

To study Jacobi captures of intermediate-mass black hole within a galactic context, we designed and ran numerical experiments. After presenting our setup, we will examine the sensitivity of captures to initial conditions. We will introduce the different types of captures, their probabilities based on initial conditions, and their properties. Additionally, we will discuss resonances. Finally, we will compare these results with those obtained using an alternative capture criterion, allowing us to discuss the challenge of choosing a perfect criterion for this problem. This chapter is a detailed version of subsections 2.1, 2.2, 3.1, and A of François et al. (2024), adapted to fit the manuscript. A summary of the chapter is available in Section 4.7.

4.1 Simulation setup, a tricky problem for the N-body

In this study, we aim to explore the influence of different initial properties of black holes (BHs) on the occurrence of a Jacobi capture. We also aim to provide physical insights on the capture process itself, occurring off-center in an extended galactic potential. As a consequence, we are reduced to a number of simplifying assumptions. Because we want to sample a large parameter space of initial BH masses and kinematics, we cannot afford to simulate the host galaxy as a live N-body component. Indeed, the problem we are considering requires high computational accuracy along two lines. First, we need to resolve the dynamics of the BH binary, implying a high time resolution of the integration. Second, an extreme number of galactic particles is required to resolve

processes such as dynamical friction [1] . As a workaround, we consider the galaxy as a background static potential, in a simplified setup that enables us to execute thousands of simulations within a reasonable timeframe [2] .

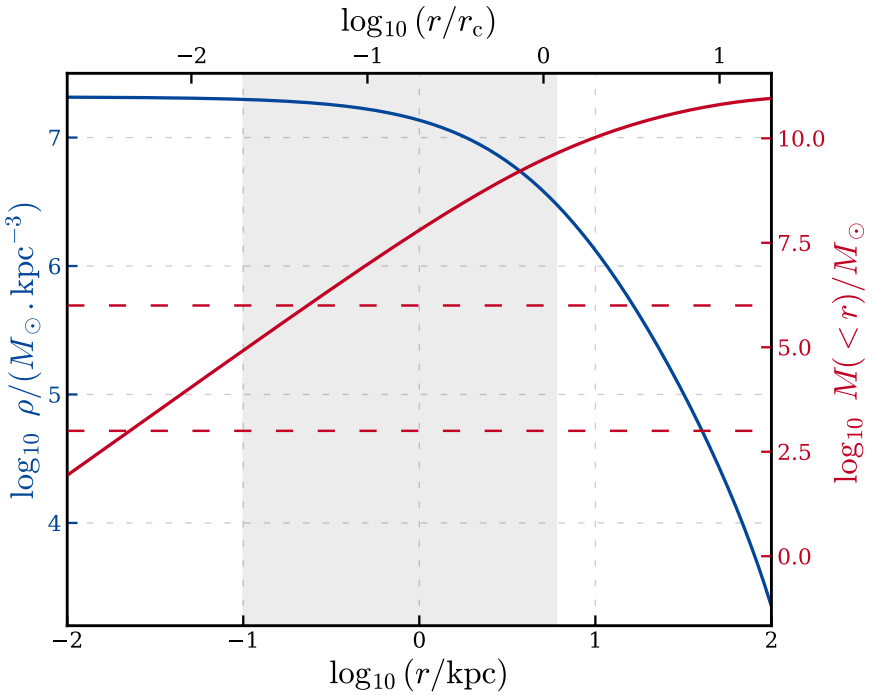

Figure 4.1: Density profile and integrated mass profile of the dark matter halo (background potential). The two horizontal lines represent the limits of the mass range we consider for the BHs. The shaded area denotes the scope of this study, and the x-axis at the top of the figure is expressed in units of the core radius of the potential r_c, defined by its inflection point.

We integrate the orbits of two BHs in an external gravitational potential representing the dark matter halo of a dwarf galaxy. Simulations made use of the REBOUND N-body code (Rein & Liu, 2012). The simulations were integrated using IAS15, a 15th order Gauss-Radau integrator (Rein & Spiegel, 2015). This integrator incorporates a step-size control mechanism to automatically select an optimal timestep and is adept at handling close encounters and orbits with high eccentricity. With systematic errors

[1] We simulate intermediate-mass black holes of $10^3 - 10^6 M_\odot$ in a dark matter halo of $10^{11} M_\odot$. In order to resolve dynamical friction, a mass ratio of $\sim 1/1000$ is required between the galactic particles and the BHs. Consequently, the mass of the galactic particles must not exceed $1\,M_\odot$. We therefore need to simulate 10^{11} particles which is well outside the technical capabilities at our disposal in terms of memory and computing time.

[2] This setup does not account for dynamical friction. However, as discussed in Section 3.2, the infall time of the intermediate-mass black hole in the galaxy under study is much longer than the age of the Universe.

maintained well below machine precision, IAS15 demonstrates adherence to Brouwer's law, where energy errors exhibit random walk behavior.

We choose a dwarf galaxy halo as various studies indicate that this type of galaxy hosts a substantial population of off-center BHs (Bellovary et al., 2019, 2021). Furthermore, in the standard ΛCDM paradigm dwarf galaxies are dominated by dark matter, hence we can initially approximate them by considering only their halo. We consider a galaxy with a $10^{11} M_\odot$ cored dark matter halo with a virial radius $r_{200} = 100$ kpc (this corresponds to a stellar mass of $\sim 10^8 M_\odot$). This halo mass range is expected to develop cored profiles more efficiently (see Tollet et al., 2016; Freundlich et al., 2020b, and Fig. 2.4). The dark matter component of our dwarf galaxy model is described by a cored (α, β, γ) density profile (Hernquist, 1990; Zhao, 1996)

$$\rho = \rho_0 \left(\frac{r}{a}\right)^{-\gamma} \left[1 + \left(\frac{r}{a}\right)^{\alpha}\right]^{\frac{\gamma-\beta}{\alpha}}, \tag{4.1}$$

with $\alpha = 1$, $\beta = 3$ and $\gamma = 0$ respectively the outer, transitional and inner slope of the density profile. The scale radius is $a = 6.7$ kpc. The density profile as well as the integrated mass profile are depicted in Fig. 4.1.

4.1.1 Toy model

We adopt a simplified model where the two BHs are on circular orbits in the same plane. This configuration closely resembles Hill's problem (Petit & Henon, 1986; Henon & Petit, 1986; Petit & Hénon, 1990; Boekholt et al., 2023). However, our massive body is extended rather than point-like, so its mass depends on the orbital radius of the BHs, and the potential shape differs, featuring a density core at the center. If our BHs are close to the center (which is the case for core stalling), the mass of the central body is comparable to the mass of the BHs. When the proximity of the two BHs leads to gravitational forces comparable to those exerted by the galaxy, temporary captures occur. These are known as Jacobi captures and are marked by multiple close encounters between BHs.

Our aim is to probe the phase space of the initial conditions to determine the percentage of cases in which the BHs produce a Jacobi capture. A priori, we have 14 parameters to describe an initial configuration: 6 phase space coordinates per BH $(r, v_r, \theta, v_\theta, \varphi, v_\varphi)$ and the mass of each object (M_1 and M_2). We decide to simplify the problem by considering the 2D case of two BHs orbiting in the same plane, which reduces our number of parameters to 10. We place the BHs on circular orbits in the $\theta = \pi/2$ plane which fixes v_r and v_φ once the position is known. Finally, we do not need each BH's phase (φ_1 and φ_2) but only the phase difference $\Delta\varphi$ because of cylindrical symmetry. We thus end up with five initial parameters: $r_1, r_2, \Delta\varphi_\mathrm{i}, M_1$ and M_2. However, it is more

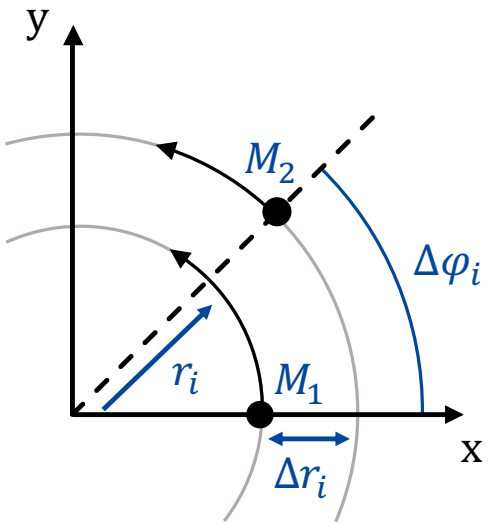

Figure 4.2: Parameters of an initial configuration, r_i the initial radius of the inner BH, Δr_i the radial separation between BHs, $\Delta\varphi_i$ the phase difference and M_1, M_2 the two masses.

Table 4.1: Parameter ranges for the five-parameter case. For a definition of the parameters in use, see Fig. 4.2

	Minimum value	Maximum value	Number of values	Spacing
$M_1/M_\odot$	10^3	10^6	8	Log
$M_2/M_\odot$	10^3	10^6	8	Log
r_i/kpc	0.1	6	14	Log
Δr_i/kpc	0.08	1.2	30	Log
$\Delta\varphi_i$	0	2π	9	Lin

convenient to use $r_\mathrm{i}, \Delta r_\mathrm{i}, \Delta\varphi_\mathrm{i}, M_1$ and M_2 with r_i the initial radius of the inner BH and Δr_i the initial radial separation between the two BHs (these parameters are shown in Fig. 4.2). Without loss of generality we impose that M_1 is always the inner BH (this means that Δr_i is always positive). We quantify the effect of the initial parameters on Jacobi capture and the percentage of cases in which such an event occurs. Parameter ranges are summarized in Table 4.1.

4.2 Chaos

To underscore the chaotic behavior of Jacobi captures in this context, we choose a specific capture as a point of reference and examine how small changes in initial conditions affect the number of close encounters between the BHs. In the left-hand panel of Fig. 4.3, this reference capture is shown, characterized by 5 close encounters (N_e) between the BHs. We set the initial conditions $(M_1, M_2, r_\mathrm{i}, \Delta r_\mathrm{i}, \Delta\varphi_\mathrm{i})$ for this capture and conducted two refined simulations: one varying (M_1, M_2) more finely and

another varying the radial parameters $(r_\mathrm{i}, \Delta r_\mathrm{i})$. For both sets of parameters, we sampled 400 linearly distributed values, varying them by plus or minus 1% relative to the original initial conditions. The central and right-hand panels of Fig. 4.3 present the number of close encounters between the BHs for each case. In these regions of phase space, the number of close encounters fluctuates between 5 to 33 for the central panel and 2 to 34 for the right-hand panel. The upper limits are due to the fixed integration time, truncating the captures beyond 14 Gyr. The significant irregularities in the count of close encounters when both pairs of parameters are varied illustrate the high sensitivity to initial conditions. In the central panel, the patterns of irregularity align along lines. In reality, these lines depend on a combination of the reduced mass and the total mass through the binding energy. However, in the case we are considering, where $M_1 \simeq M_2$, they can be approximated by $M_1 + M_2 \sim C$, with C being a constant.

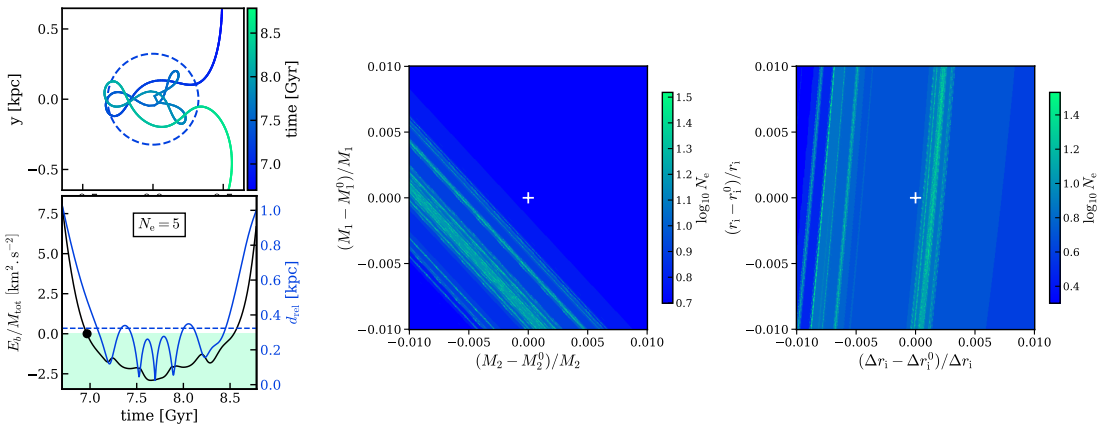

Figure 4.3: Influence of the initial conditions on the number of close encounters (N_e). Left panel: Reference Jacobi capture ($M_1^0 = 3.7276 \times 10^5\ M_\odot$, $M_2^0 = 3.7276 \times 10^5\ M_\odot$, $r_\mathrm{i}^0 = 6.000$ kpc, $\Delta r_\mathrm{i}^0 = 0.6242$ kpc, $\Delta\varphi_\mathrm{i}^0 = 3.4907$, with significant figures up to the resolution of the central and right panels). The top panel shows the relative coordinates between the BHs during the capture. The reference frame is centered on the most massive BH and rotates with it. The binary Hill radius is indicated by the dotted circle. In the bottom row, the black line represents the binding energy (E_b) per unit mass of the binary ($M_\mathrm{tot} = M_1 + M_2$), with negative values depicted in the colored area. The black marker indicates the point at which the energy becomes negative. The blue curve represents the relative distance (d_rel) between the BHs. The binary Hill radius is shown by a dashed blue line. The reference capture involves 5 close encounters between the BHs. Central panel: N_e variations as a function of initial conditions (M_1, M_2). The (M_1, M_2) values are distributed plus or minus 1% around the initial condition of the reference capture, denoted as (M_1^0, M_2^0). Right panel: N_e variations as a function of initial conditions $(r_\mathrm{i}, \Delta r_\mathrm{i})$. The $(r_\mathrm{i}, \Delta r_\mathrm{i})$ values are distributed plus or minus 1% around the initial condition of the reference capture, denoted as $(r_\mathrm{i}^0, \Delta r_\mathrm{i}^0)$. The reference capture is located at $(0, 0)$ in each panel. The strong variations of N_e with initial conditions is suggestive of chaotic motion.

4.3 Mapping the initial conditions for Jacobi captures

4.3.1 General statistics and 1:1 resonances

We integrated $8 \times 8 \times 14 \times 30 \times 9 = 241\,920$ initial configurations (cf. Table 4.1) over 14 Gyr. We find a capture in 7.1% of cases, of which 26.2% are flybys.

Even though we do not focus on what happens after the first capture, as collective effects and relativistic corrections are expected to significantly alter the dynamics, it is interesting to note that 39.3% of flybys result in subsequent captures. Figures 4.4 and 4.5 show examples of these cases. Figure 4.4 illustrates cases of 1:1 resonances, with an example of a horseshoe orbit shown on the left. In a horseshoe orbit, two objects share a similar average orbital radius but periodically swap their positions relative to each other. This swap is mediated by their gravitational interactions, which cause exchanges of angular momentum. As the objects approach each other, their mutual gravitational attraction causes one to accelerate (moving to a slightly higher orbit) and the other to decelerate (moving to a slightly lower orbit). Over long timescales, the average distance of both objects from the central body remains the same, meaning they complete their orbits in the same amount of time on average. This is why the system is considered to be in a 1:1 resonance, even though the instantaneous periods can differ slightly. The existence of a central core within the density profile facilitates the emergence of a novel orbital type known as Pacman orbits (Banik & van den Bosch, 2022). An example of this orbital type is shown in the central panel of Fig. 4.4. These orbits play a key role in the phenomenon of dynamical buoyancy within cores, which drives perturbers outward to an equilibrium radius with the dynamical friction, ultimately resulting in core stalling. During capture events, BHs experience these unique dynamics. Finally, the right panel of Fig. 4.4 illustrates a chimera orbit, where a Pacman orbit transitions into a horseshoe orbit. Figure 4.5 presents cases of stabilized horseshoe orbits. Initially, these cases are horseshoe flybys during a first close encounter, which then stabilize into more stable captures during a second encounter several Gyr later. Examples of more stable Jacobi captures, featuring various numbers of close encounters, are also presented in Fig. 3.8.

The captures can be further categorized into two distinct types: those formed at the beginning of the simulations (t=0 Gyr, hereafter referred to as initial captures), comprising 66.3% of the total captures, and those emerging during the integration at later times (t>0 Gyr, hereafter referred to as dynamical captures), making up the remaining 33.7% of the captures. It is essential to bear in mind that in the following sections our focus is on the initial conditions that initiate the capture process i.e., the transition

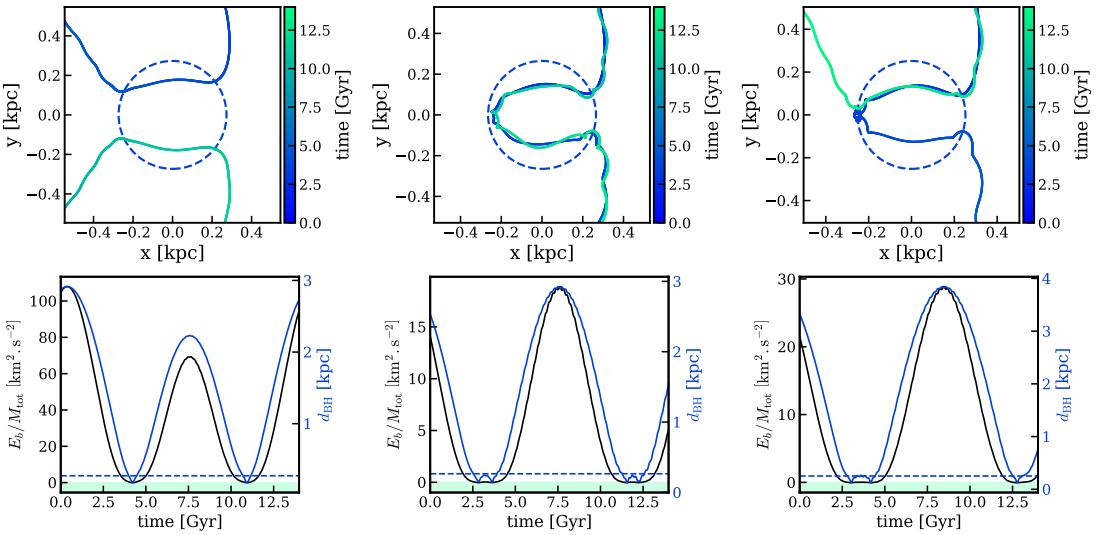

Figure 4.4: Examples of 1:1 resonances. Top row: relative coordinates between BHs during Jacobi captures. The reference frame is centered on the most massive BH and rotates with it. The binary Hill radius is marked by the dotted circle. Bottom row: the black line represents the binding energy (E_b) per unit mass of the binary ($M_\mathrm{tot} = M_1 + M_2$), with negative values shown in the colored area. The blue curve represents the relative distance (d_rel) between the BHs. The binary Hill radius is indicated by a dashed blue line. Left column: Horseshoe orbit. Central column: Pacman orbit. Right column: Chimera orbit.

from two separate two-body problems to a three-body problem. Consequently, the results presented here are not subject to chaos. We examine the initiation of the process rather than the subsequent three-body interaction (such as capture duration or number of close encounters) which typically exhibit chaotic behavior (cf. Section 4.2).

4.3.2 Initial captures

Initial captures are traditionally not considered in the study of Jacobi captures (Petit & Henon, 1986; Henon & Petit, 1986; Petit & Hénon, 1990; Boekholt et al., 2023), despite their crucial role in understanding this process. To fully comprehend the capture phenomenon, they should not be disregarded for three reasons: (*i*) These captures facilitate off-centered binding between BHs, which cannot be overlooked when performing statistical analyses on the initial conditions leading to off-center captures. Additionally, due to the ergodic nature of the problem, some initial captures and dynamical captures are interchangeable with a time shift in the simulation; (*ii*) as we will see, some initial captures are actually permanent captures –bound throughout the entire simulation– that appear to conspire with all temporary captures to account for the theoretical statistics related to the capture process (Peñarrubia et al., 2024); (*iii*) the formation mechanisms

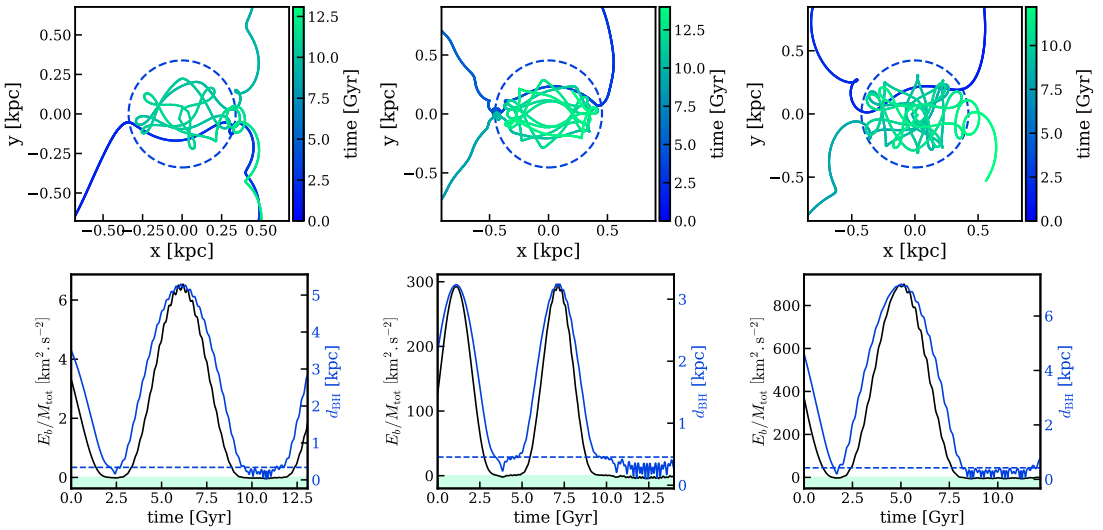

Figure 4.5: Examples of stabilized horseshoe. Top row: relative coordinates between BHs during Jacobi captures. The reference frame is centered on the most massive BH and rotates with it. The binary Hill radius is marked by the dotted circle. Bottom row: the black line represents the binding energy (E_b) per unit mass of the binary ($M_\mathrm{tot} = M_1 + M_2$), with negative values shown in the colored area. The blue curve represents the relative distance (d_rel) between the BHs. The binary Hill radius is indicated by a dashed blue line.

for BHs can include bound or nearly bound compact remnants, so quick captures may reflect a correlation in phase space that corresponds to this. Therefore, it is essential not to exclude them from consideration.

When examining initial captures more closely, we distinguish two different behaviors. Some of these captures become unbound during the simulation, and may even lead to subsequent captures. Figure 4.6 shows three examples of such cases. Another portion of initial captures remains bound throughout the entire simulation and exhibits a high degree of regularity. We will refer to these as permanent captures, meaning they stay bound for the entire 14 Gyr simulated period. Figure 4.7 illustrates examples of these cases. The stability of these perturber-phylic captures is remarkable, given the chaotic nature of the three-body problem. There is a striking difference between these highly regular captures and the more chaotic initial captures shown in Figure 4.6. Permanent captures occur only at $t = 0$ Gyr, but Peñarrubia et al. (2024) have shown that in cases where the masses vary over time, they can occur spontaneously and randomly during the simulation, which is particularly interesting in the case of accreting BHs. This study also indicates that there seems to be an underlying connection between permanent and temporary captures, working together to preserve a constant phase-space density. It suggests that both populations are intrinsically linked. The question remains whether

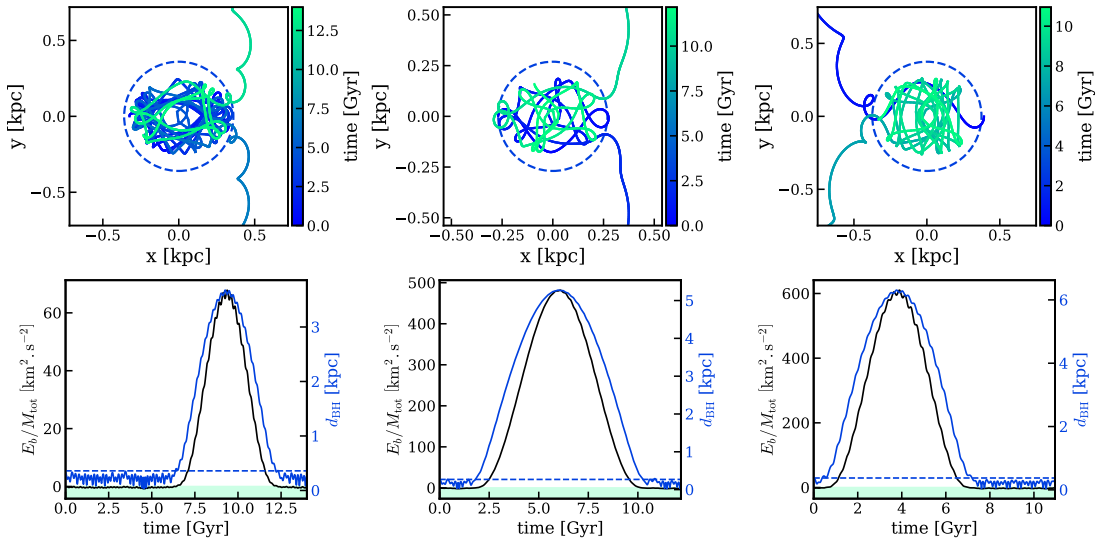

Figure 4.6: Examples of initial captures that become unbound and subsequently lead to a second capture during the simulation.

these are unstable captures with a characteristic instability time much longer than the 14 Gyr simulated, or if allowing initial captures grants access to a non-zero measure phase space region that results in regular periodic captures. This question remains unanswered, but it is an exciting prospect for future exploration.

In the bottom right panel of Fig. 4.7, we notice a case where the capture remains regular despite the separation between the BHs being greater than the Hill radius of the binary. This echoes the study by Johnston et al. (1999), which found a population of extra-tidal stars bound to a cluster but outside its radius of influence. The inverse has also been observed, where unbound stars (with energy above the escape energy) remain indefinitely within the cluster's radius of influence (see Fukushige & Heggie, 2000). In the bottom left panel of Fig. 4.7, we observe a case where a regular capture appears to be perturbed but then regains its regularity.

Figure 4.8 shows the percentage of initial captures in the space of different parameter pairs, marginalized over the others. The right-hand panels show this percentage in $(M_1, \Delta r_\mathrm{i})$ space (top) and in $(M_2, \Delta r_\mathrm{i})$ space (bottom). In both panels, the proportion of captures increases as the radial separation between the BHs decreases and their masses increase. These conditions elevate the potential term of the binding energy (see Eq. 3.14), consequently reducing the binding energy of the binary. Beyond a certain threshold of radial separation, captures cease to occur. This limit does not precisely match the maximum binary Hill radius (for the parameter range explored in this study, $\log R_\mathrm{H}^\mathrm{max} = -0.35$), as the definition of the Hill radius accounts for the centrifugal force,

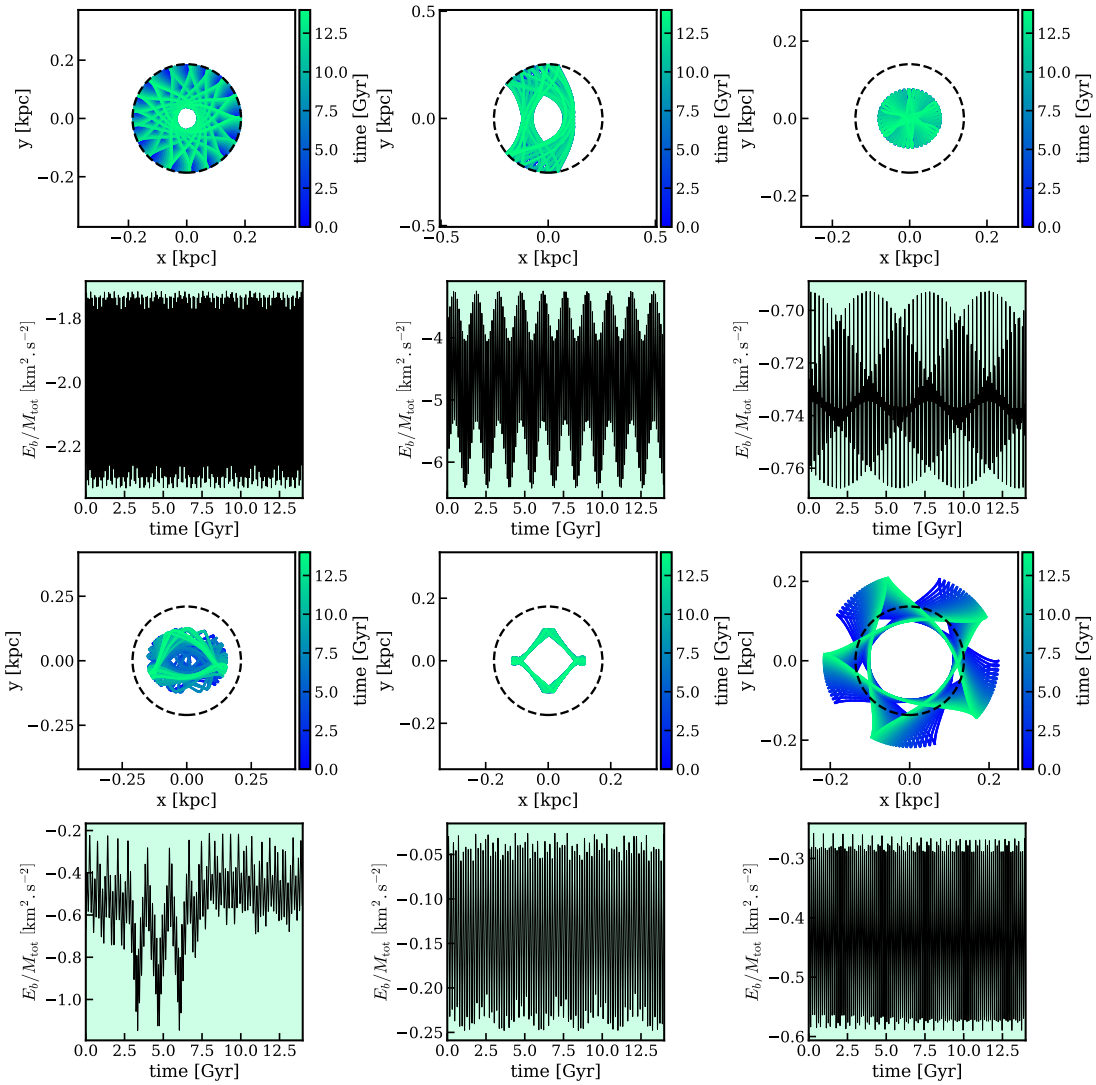

Figure 4.7: Examples of permanent initial captures.

which we ignore in our energy-based criterion. Nevertheless, the maximum radial separation allowing initial capture is rather close to $R_{\rm H}^{\rm max}$.

The top left panel of Fig. 4.8 shows the percentage of initial captures as a function of $(M_1, r_{\rm i})$, while the lower left panel shows it as a function of $(M_2, r_{\rm i})$. Regarding the $r_{\rm i}$ dependence, we observe a sharp increase in the percentage of capture at low radii ($\log r_{\rm i}/{\rm kpc} < -0.4$) for higher masses, which then stabilizes for higher radii. The constant part at higher radii is attributed to the nearly constant Hill radius within this range (refer to Fig. 3.6 for the case of a $10^6 M_\odot$ BH). At small radii, marginalization increases the probability of capture. In this region, there are more values of $\Delta\varphi_{\rm i}$ that allow the BHs to remain within their sphere of influence, despite its decrease. As

illustrated in Fig. 4.9, which shows the percentage of captures as a function of the initial radius of the inner BH and the initial phase difference between the BHs, we note that when the BHs are closer to the center (low r_i), there are more phase differences that allow a bond at $t = 0$ Gyr. Back to Fig. 4.8, the captures at high masses and small radii correspond to cases where the BHs are initially outside the binary Hill's radius (which is smaller at low radii) but with negative binding energy. Their labeling is sensitive to the capture criterion used (whether pseudo-forces related to rotation are considered or not). We will discuss this point in more detail in Section 4.6.

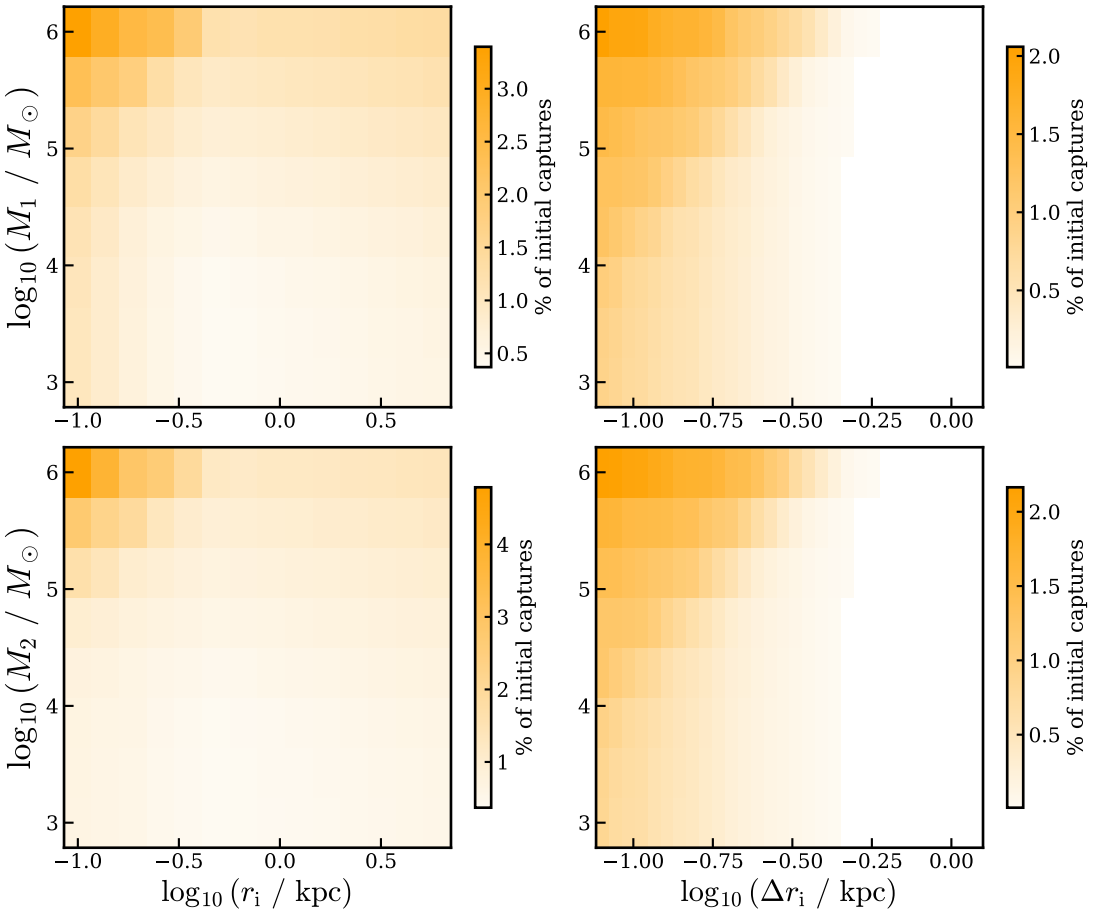

Figure 4.8: Percentage of initial captures as a function of different parameter pairs, marginalising each time over the three others. Top-left panel: as a function of the mass of the inner BH (M_1) and its initial radius (r_i); bottom-left panel: as a function of the mass of the outer BH (M_2) and r_i; top-right panel: as a function of M_1 and the initial radial separation between the BHs (Δr_i); bottom-right panel: as a function of M_2 and Δr_i.

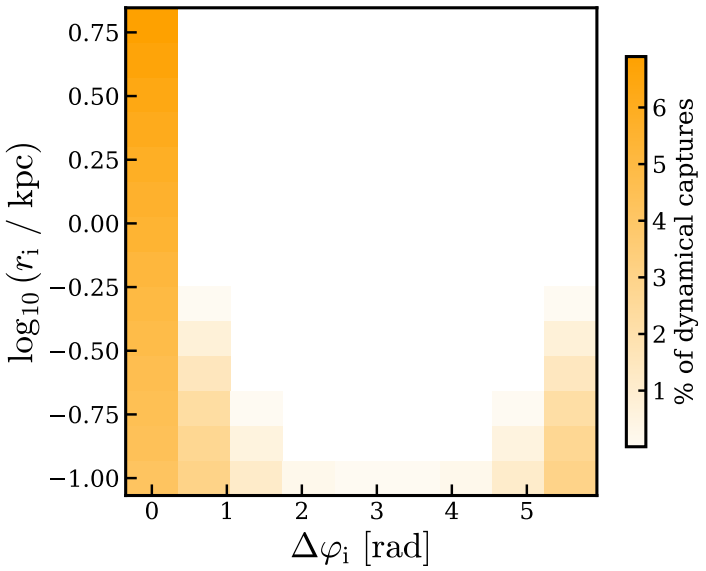

Figure 4.9: Percentage of initial captures as a function of the initial radius of the inner BH (r_i) and the initial phase difference between BHs ($\Delta\varphi_\mathrm{i}$).

4.3.3 Dynamical captures

Examples of dynamical captures are shown in Fig. 3.8. Figure 4.10 shows the percentage of dynamical captures (i.e., happening at t>0 Gyr) as a function of (M_1, M_2). The percentage of captures increases as the mass of the two BHs increases, and we notice that the percentage is higher when the mass of the outer BH is greater than the mass of the inner one ($M_2 > M_1$). This is of particular interest within the context of core stalling, which predicts a larger stalling radius for more massive BHs (cf. Eq. 5.2). This outcome can be attributed to the interaction between BHs, which imparts eccentricity to the initially circular orbits over time. This eccentricity gain depends on the BH mass: when one BH is much more massive, it remains nearly circular while the lighter one becomes eccentric. Consequently, if the more massive BH is positioned closer to the center, the lighter one will approach it more centrally, resulting in higher kinetic energy and a more challenging capture. On the contrary, when the more massive BH occupies the outer position, the lighter BH approaches it at a larger radius, resulting in reduced kinetic energy and thus facilitating the capture process. In Fig. 4.10, we also overplotted contour lines representing the average time it took for the capture to occur since the start of the simulation. The average capture time shows an increase as the total BH mass diminishes.

Figure 4.11 represents the percentage of captures as a function of $(r_\mathrm{i}, \Delta r_\mathrm{i})$, when we fix the masses M_1, M_2 and marginalize over $\Delta\varphi_\mathrm{i}$ only. We show the results for two

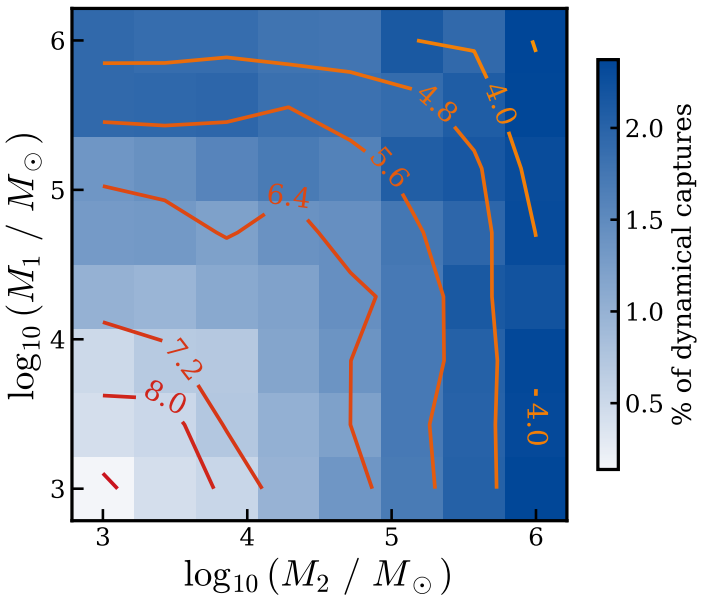

Figure 4.10: Percentage of dynamical captures as a function of inner (M_1) and outer (M_2) BH mass. The contour lines represent the average time it took for the capture to occur since the start of the simulation, measured in Gyr. The percentage of captures increases as the mass of the two BHs increases, and the mass of the outer BH is greater than the mass of the inner one ($M_2 > M_1$).

different pairs of masses, on the left-hand panel $\log(M_{\rm tot}/M_\odot) = 4.8$ and on the right panel $\log(M_{\rm tot}/M_\odot) = 6.1$. Yellow areas represent initial captures and blue areas dynamical captures. Note the presence of blue bands that shift to the right ($\Delta r_{\rm i}$ larger) as the total mass increases. To the left of these bands ($\Delta r_{\rm i}$ smaller), we notice the presence of initial captures on a shallow yellow background. The plot can be divided into three regions: to the left, within, and to the right of the bands.

To the right of the band ($\Delta r_{\rm i}$ larger), there is no capture: the BHs are too distant initially to reach a configuration where their gravitational attraction is comparable to the force generated by the external potential. To the left of the band ($\Delta r_{\rm i}$ smaller), captures occur at t=0 (in yellow). Indeed, two possible scenarios arise: (*i*) captures form at t=0 if BHs have a sufficiently low initial phase shift $\Delta\varphi_{\rm i}$, (*ii*) the initial phase shift is too large for an initial capture, and $\Delta r_{\rm i}$ is too small to allow phase catch-up within the simulation timeframe [3] . Also note the darker yellow area in the lower left of the right panel of Fig. 4.11. In this region the BHs are positioned very near the galactic center ($r_{\rm i}$ small) and are in close radial proximity to each other. Under these conditions, the shorter distances for the same angular separation allow for more flexibility in terms of

[3] When $\Delta r_{\rm i}$ is small, the BHs share similar orbital frequencies, so their phase difference evolves slowly.

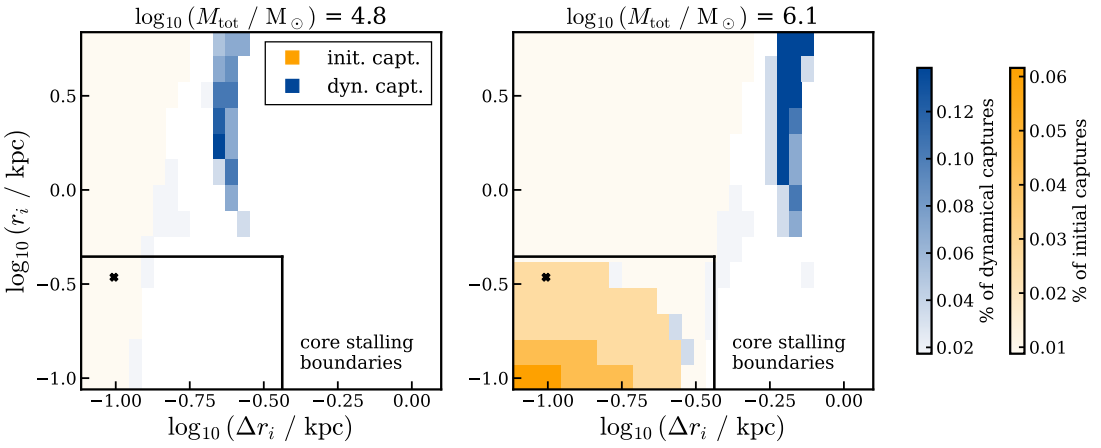

Figure 4.11: Percentage of captures as a function of initial inner BH radius (r_i) and initial radial separation (Δr_i) for two mass pairs. In the left panel, $\log(M_1/M_\odot) = 3.9$ and $\log(M_2/M_\odot) = 4.7$, in the right panel, $\log(M_1/M_\odot) = 5.6$ and $\log(M_2/M_\odot) = 6$. Red areas represent initial captures while blue areas dynamical captures. The black lines indicate the limits within which core stalling can position our BHs, given the mass range studied. The black crosses indicate where core stalling would position the BHs in each case.

the initial phase shifts that result in Jacobi capture. In other words, when r_i decreases larger initial phase shifts can lead to a capture, which explains the increased capture percentage (cf. Fig. 4.9).

Figure 4.12 shows the percentage of dynamical captures as a function of the initial radius of the inner BH (r_i) and the initial phase difference between the BHs ($\Delta\varphi_\mathrm{i}$). We observe the presence of a clump of dynamical captures when the initial phase difference is zero ($\Delta\varphi_\mathrm{i} = 0$) for certain values of r_i. These dynamical captures are, in fact, borderline cases where the BHs are within the binary's sphere of influence at $t = 0$ Gyr, but their relative velocity is slightly too high for the binding energy to be negative. After a few time steps, this condition changes, and they become bound. These cases highlight the limitations of the binding criterion and the difficulty in establishing a perfect criterion. Another criterion based solely on the binary's radius of influence would label these bindings as initial, for example (cf. Section 4.6).

4.4 Lindblad resonance

As discussed in Section 4.3.1, we have identified the presence of 1:1 resonances. It is worthwhile to investigate whether other types of resonances exist within our system. Two objects in orbit at radii r_1 and r_2 are in resonance when their relative frequencies

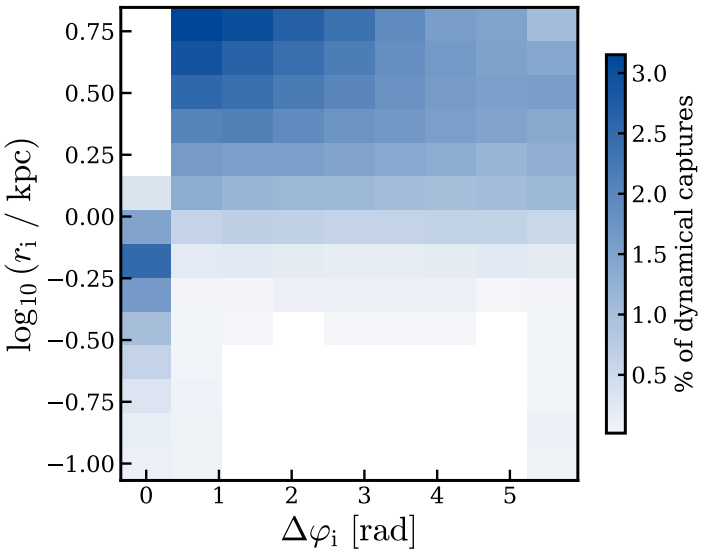

Figure 4.12: Percentage of dynamical captures as a function of initial inner BH radius (r_i) and initial phase difference between BHs ($\Delta\varphi_\mathrm{i}$).

are commensurate, meaning that

$$\mathbf{n} \cdot (\mathbf{\Omega}_1 - \mathbf{\Omega}_2) = 0 \tag{4.2}$$

with $\mathbf{\Omega}_1 = \mathbf{\Omega}(r_1)$ and $\mathbf{\Omega}_2 = \mathbf{\Omega}(r_2)$ being the frequency vectors of the two objects and $\mathbf{n}$ a vector of integer values such that $\mathbf{n} \neq \mathbf{0}$. In the case of two coplanar BHs, $\mathbf{\Omega} = (\Omega, \kappa)$ with Ω the circular frequency and κ the epicycle frequency given by:

$$\begin{aligned} \Omega(r) &\equiv \frac{v_\mathrm{c}}{r} = \left(\frac{G\,M_\mathrm{b}(<r)}{r^3}\right)^{1/2} \\ \kappa(r_\mathrm{g}) &= \left(r\frac{\mathrm{d}\Omega^2}{\mathrm{d}r} + 4\Omega^2\right)^{1/2}_{r_\mathrm{g}} \end{aligned} \tag{4.3}$$

with v_c the circular velocity (cf. Eq. 1.14) and r_g the guiding radius of the orbit [4] . The equation (4.2) is written as follows:

$$\begin{aligned} & n_1 \cdot (\Omega_1 - \Omega_2) + n_2 \cdot (\kappa_1 - \kappa_2) = 0 \\ \Leftrightarrow\quad & \Omega_1 + \frac{n_2}{n_1}\,\kappa_1 = \Omega_2 + \frac{n_2}{n_1}\,\kappa_2 \\ \Leftrightarrow\quad & \Omega_1 + n\,\kappa_1 = \Omega_2 + n\,\kappa_2 \\ \text{or}\quad & \Omega(r_1) + n\,\kappa(r_1) = \Omega(r_2) + n\,\kappa(r_2) \end{aligned} \tag{4.4}$$

[4] Radius that minimizes the effective potential energy and for which the circular orbit would have the same angular momentum as the given orbit.

where (n_1, n_2) are the components of $\mathbf{n}$ and $n = n_2/n_1$. If $n_2 = 0$, it results in the corotation resonance $\Omega_1 = \Omega_2$, and when $(n_1, n_2) = (m, \mp 1)$, the Lindblad resonances [5] $m(\Omega_1 - \Omega_2) = \pm(\kappa_1 - \kappa_2)$ arise. Figure 4.13 shows $\Omega(r) + n\,\kappa(r)$ for different values of n in our density profile (cf. Eq. 1.21). The only non-monotonic curve in the displayed radial range, which allows for a solution to equation (4.4) other than the trivial solution $r_1 = r_2$, is the inner Lindblad resonance ($n = -1/2$). We have plotted this resonance in Fig. 4.14. It can be seen that every radius within our study area resonates with another radius outside our study area, indicating that we are too close to the galactic center for inner Lindblad resonances to play a major role.

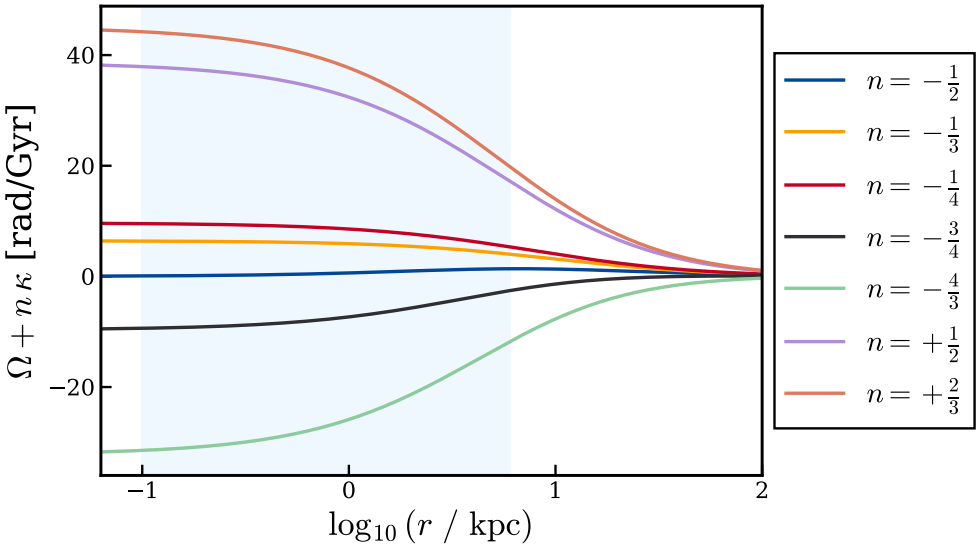

Figure 4.13: Behavior of $\Omega + n\,\kappa$ for our background potential.

4.5 Binary eccentricity during Jacobi captures

The histogram in the left panel of Fig. 4.15 displays the mean eccentricity of the binary during captures. Jacobi captures tend to result in rather eccentric binaries, a factor that can aid in stabilization through energy dissipation caused by dissipative forces. Post-Newtonian corrections can particularly influence highly eccentric orbits, especially at the pericenter (Samsing et al., 2018b). Notably, our criterion ensures that the mean eccentricity during captures remains below 1. On the right panel of Fig. 4.15, the standard deviation of eccentricity during captures is depicted. These variations may permit a very high eccentricity during the capture, despite a lower mean eccentricity.

[5] For the case of a single object $(\Omega_1, \kappa_1) = (\Omega_0, \kappa_0)$ in resonance with a bar $(\Omega_2, \kappa_2) = (\Omega_\mathrm{b}, 0)$, we have: $m\,(\Omega_0 - \Omega_\mathrm{b}) = \pm\kappa_0$.

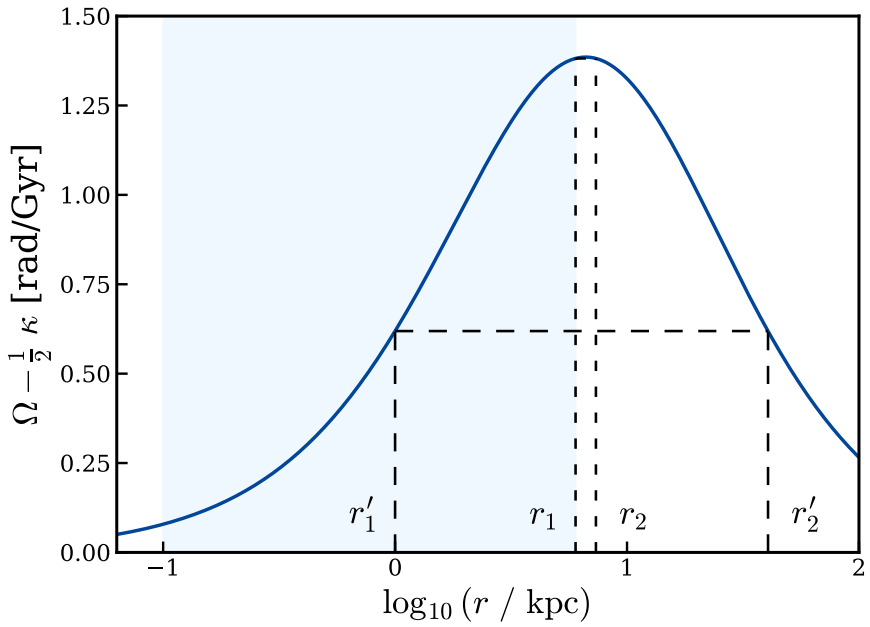

Figure 4.14: Inner Lindblad resonance for our background potential. The light blue area represents our study zone. We have plotted two examples of radii r_1 and r_1' that resonate with r_2 and r_2', respectively. It is noteworthy that even r_1, the largest radius within our study zone, resonates with r_2 located outside the study zone. Therefore, inner Lindblad resonances do not play a major role within our study area.

4.6 Alternative capture criterion

In this section, we revisit some of the findings using an alternative capture criterion based solely on the radius of influence (i.e., only on the effective potential). Here, we define BHs as captured when their separation is less than the Hill radius of the binary. When the separation between the BHs is smaller than the binary Hill radius, the potential generated by the BHs competes with that of the galaxy, resulting in a significant perturbation of the BH trajectories. Therefore, it is natural to consider that this criterion alone may suffice to define a capture. We examine here the differences that this approach entails.

Applying this new criterion to the general five-parameter case, we find captures in 16.4% of the simulated instances. This is more than double the 7.1% obtained with the energy criterion. There are 5.4% initial captures (compared to 4.7% with the energy criterion) and 11.0% dynamical captures (compared to 2.4%). We observe a significant increase in the number of dynamical captures.

Figure 4.16 serves as the counterpart to Fig. 4.8, depicting the percentage of initial

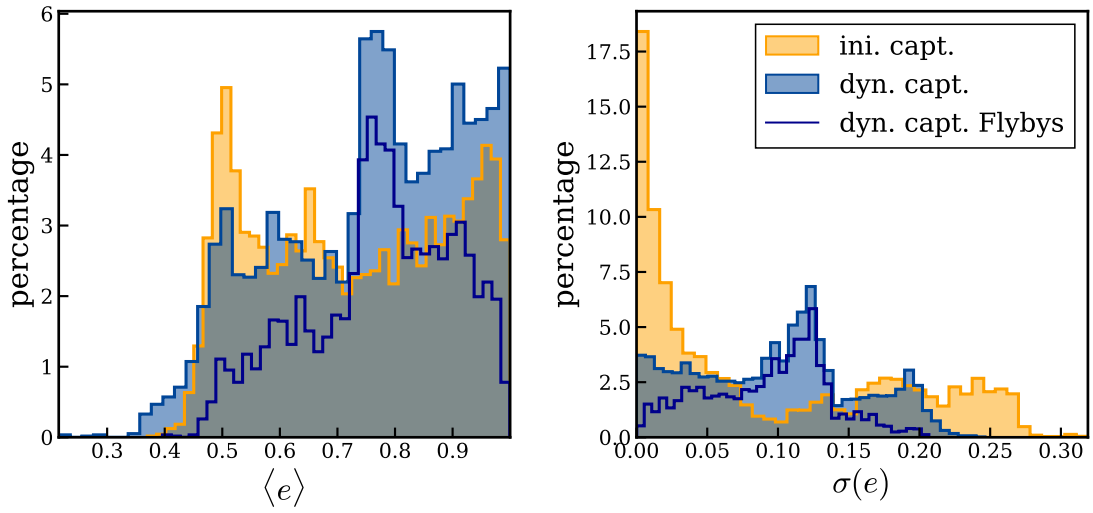

Figure 4.15: Eccentricity during Jacobi captures. Left panel: histogram in percent of the mean eccentricity of the binary during captures (initial captures in yellow and dynamical captures in blue). The dark blue line represents only dynamical captures with a single close encounter (i.e., flybys). Jacobi captures produce rather eccentric binaries. A significant proportion are in the very high eccentricity range ($e \gtrsim 0.9$), for which Post-Newtonian corrections can be significant at the pericenter. Right panel: percentage histogram of standard deviation of eccentricity during captures. These variations may permit a very high eccentricity during the capture, despite the lower mean eccentricity.

captures across various parameter pairs, marginalized over the remaining three. In the top-left panel, the percentage of captures with respect to r_i closely mirrors the Hill radius curve depicted in Figure 3.6, albeit with a leftward shift as the BH mass decreases. The white area in the top-left corner of Fig. 4.16 appears dark on the figure 4.8 due to cases where the BHs initially maintain a relative distance slightly larger than the Hill radius but have a negative binding energy. It is important to note that the potential term in our energy-based criterion differs from the effective potential used to calculate the Lagrange points and the Hill radius. Consequently, it is possible for the BHs to have a separation greater than the Hill radius (according to the effective potential), yet if their relative velocity is sufficiently low, the sum of the kinetic term and the potential term (non-effective potential this time) results in a negative binding energy. In these cases they are energetically close and plunge into the Hill sphere after a few time steps. Under the distance criterion they are classified as dynamical captures, while the energy-based criterion categorizes them as initial captures. This can be verified in Fig. 4.17. It shows the dynamical captures based on the distance criterion for the parameter pair (M_1, r_i). We observe a higher probability area in the top-left corner (low r_i and high M_1), which corresponds to the white area of missing captures in Fig. 4.16.

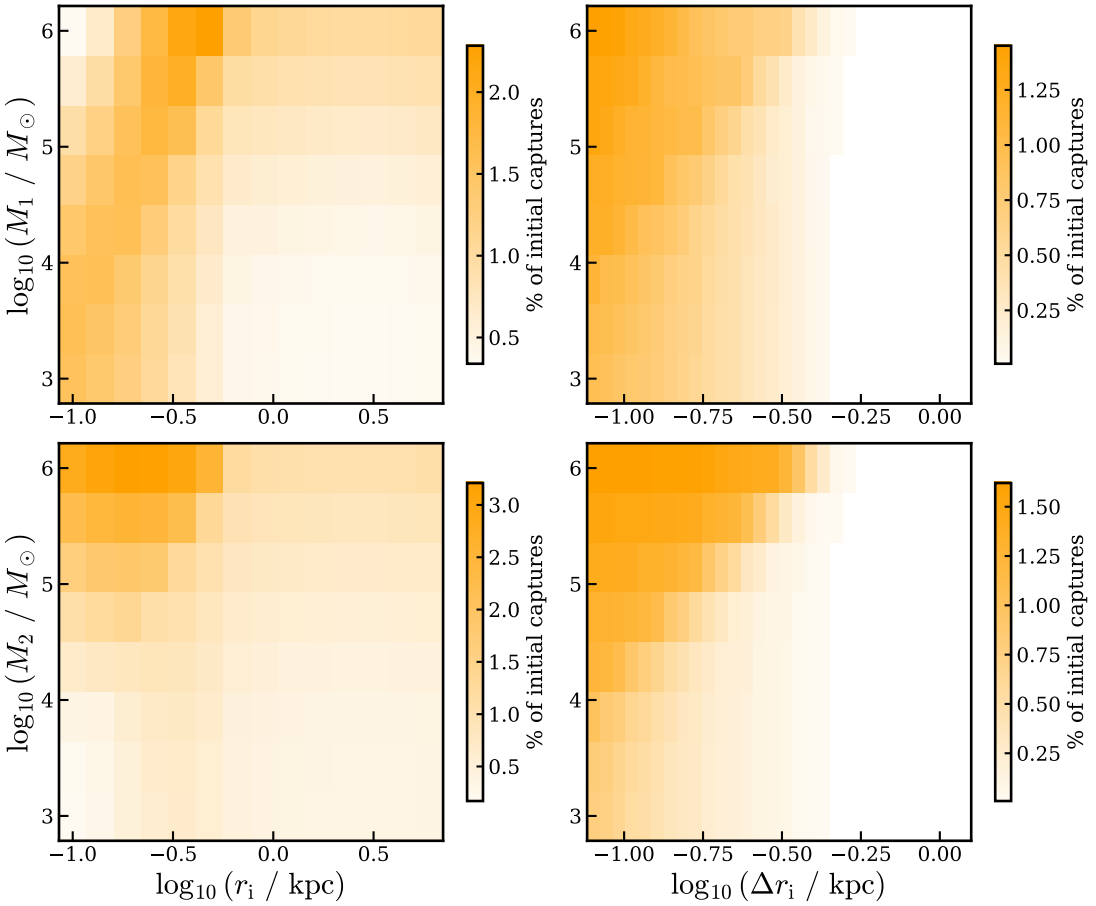

Figure 4.16: Percentage of initial captures as a function of different parameter pairs, marginalising each time over the three others. Top-left panel: as a function of the mass of the inner BH (M_1) and its initial radius (r_i); bottom-left panel: as a function of the mass of the outer BH (M_2) and r_i; top-right panel: as a function of M_1 and the initial radial separation between the BHs (Δr_i); bottom-right panel: as a function of M_2 and Δr_i. This figure is analogous to Fig. 4.8 with a different capture criterion. BHs are considered bound if their relative distance falls below the binary's Hill radius.

Figure 4.18 serves as the counterpart to Fig. 4.11, depicting the percentage of dynamical captures relative to the initial radius of the inner BH (r_i) and the initial radial separation between the BHs (Δr_i). Comparing it with Figure 4.11, we observe that the dynamical binding bands extend further down in r_i. To understand the nature of these dynamical captures introduced by the alternative criterion, we can turn to Fig. 4.19, mirroring Figure 4.15. The histogram of mean eccentricities during captures on the left-hand panel extends beyond 1. Consequently, these newly added dynamical captures are mostly hyperbolic flybys close to the galactic center.

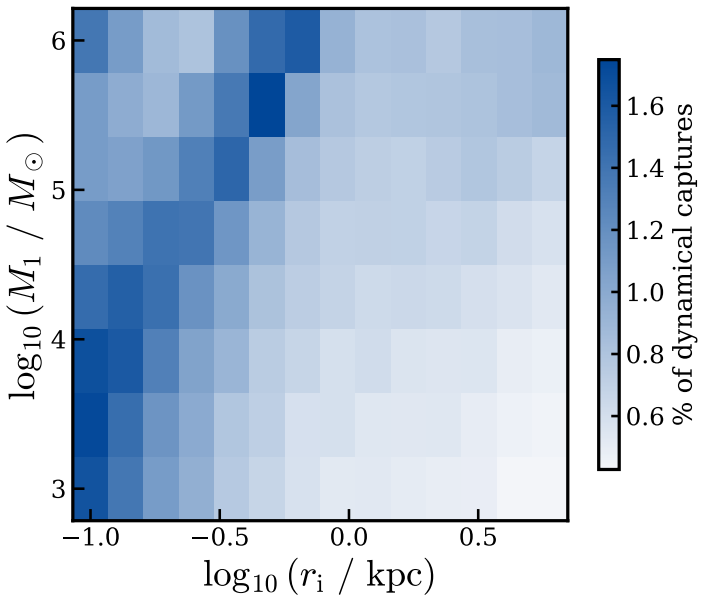

Figure 4.17: Percentage of dynamical captures as a function of the mass of the inner BH (M_1) and its initial radius (r_i), marginalising over the other parameters. BHs are considered bound if their relative distance falls below the binary's Hill radius.

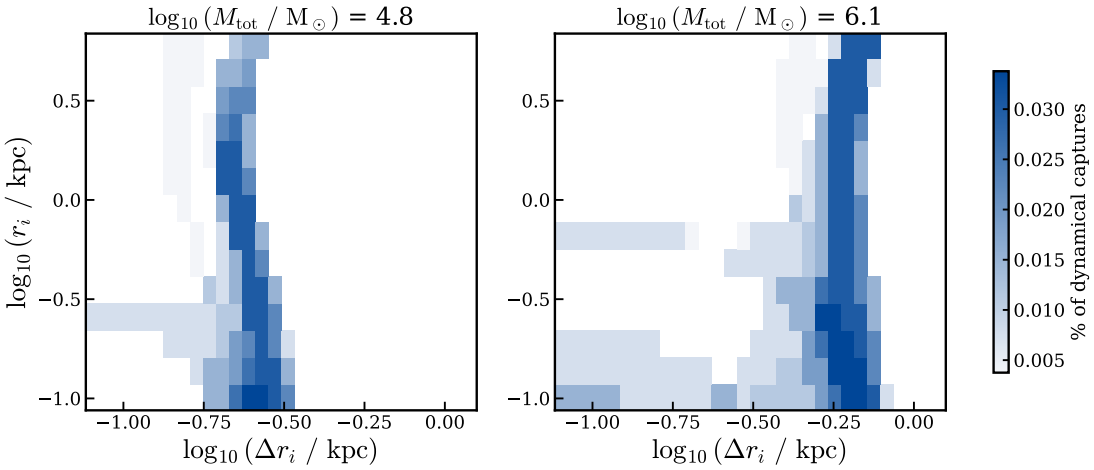

Figure 4.18: Percentage of dynamical captures as a function of initial inner BH radius (r_i) and initial radial separation (Δr_i) for two mass pairs. In the left panel, $\log(M_1/M_\odot) = 3.9$ and $\log(M_2/M_\odot) = 4.7$, in the right panel, $\log(M_1/M_\odot) = 5.6$ and $\log(M_2/M_\odot) = 6$. This figure is analogous to Fig. 4.11 with a different capture criterion. BHs are considered bound if their relative distance falls below the binary's Hill radius. We observe that the binding bands of dynamical captures extend closer to the galactic center. The majority of these captures involve hyperbolic flybys, indicating that the BHs involved have high relative velocities.

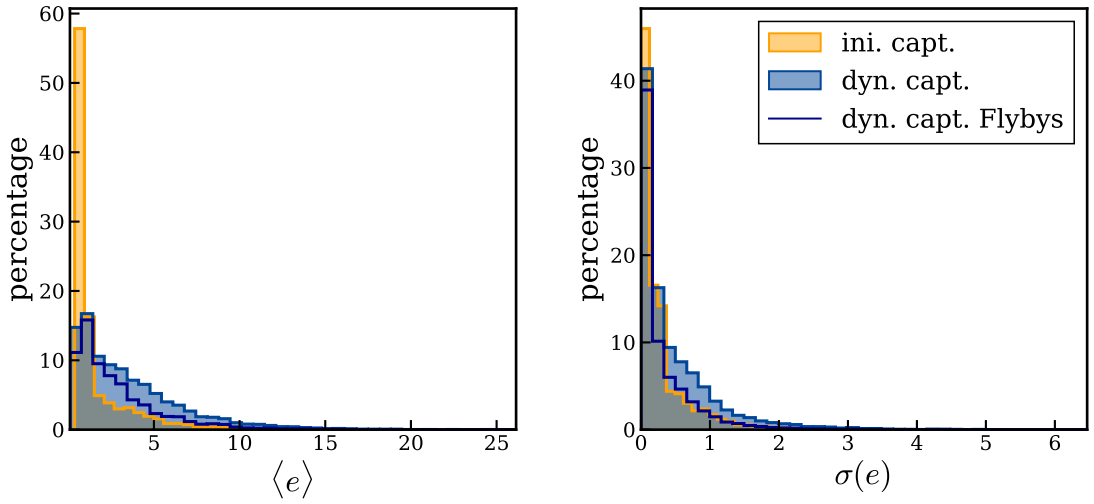

Figure 4.19: Eccentricity during Jacobi captures. Left panel: histogram in percent of the mean eccentricity of the binary during captures (initial captures in red and dynamical captures in blue). The dark blue line represents only dynamical captures with a single close encounter (i.e., flybys). Right panel: percentage histogram of standard deviation of eccentricity during captures. This figure is analogous to Fig. 4.15 with a different capture criterion. BHs are considered bound if their relative distance falls below the binary's Hill radius. Note that the alternative criterion adds captures for which the mean eccentricity is greater than 1.

4.6.1 Pacman orbit and number of close encounters

Figure 4.20 illustrates another example of a Pacman capture. This example serves as a perfect illustration of how the labeling of the number of close encounters between BHs depends, in some borderline cases like this one, on the criterion used to label a capture. In the right panel of Fig. 4.20, the binding energy and relative distance between the BHs during the capture are depicted. With the energy-based capture criterion (Eq. 3.14), we would label two captures with a single close encounter, as the energy returns to positive values between the encounters. However, if we utilize the alternative criterion presented in this section (where BHs are labeled as captured when the relative distance is less than the binary Hill radius), we would label only a single capture with two close encounters. This case underscores the complexity of selecting an appropriate capture criterion, as finding a perfect one remains a challenging task.

4.7 Summary of Chapter 4

This chapter explores the phenomenon of gravitational capture of intermediate-mass black holes within the context of dwarf galaxies. The aim is to develop an intuition for this initial stage of the off-center merger scenario, where black holes bind outside the

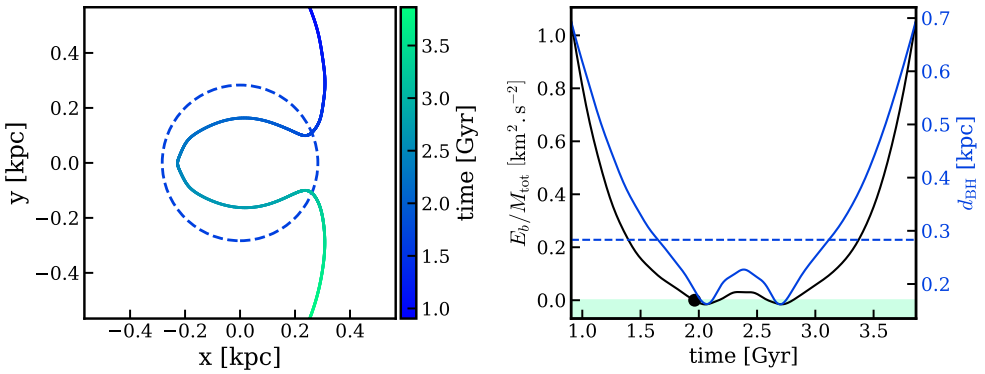

Figure 4.20: Example of Pacman capture. Top row: relative coordinates between BHs during the Jacobi capture. The reference frame is centered on the most massive BH and rotates with it. The binary Hill radius is marked by the dotted circle. Bottom row: the black line represents the binding energy (E_b) per unit mass of the binary ($M_\mathrm{tot} = M_1 + M_2$), with negative values shown in the colored area. The black marker indicates the point when the energy becomes negative. The blue curve represents the relative distance (d_rel) between the BHs. The binary Hill radius is indicated by a dashed blue line.

galactic center and undergo several close encounters.

Simulation Setup. In order to isolate the capture step and conduct thousands of simulations efficiently, we performed idealized simulations of two point-like black holes in a smooth background gravitational potential. We considered black holes with masses ranging from 10^3 to $10^6\,M_\odot$ within a cored dark matter halo of $10^{11}\,M_\odot$ (same galaxy as previous chapters). We considered five initial parameters: initial radius of the inner black hole (r_i), radial separation between black holes (Δr_i), phase difference ($\Delta\varphi_\mathrm{i}$), and the masses (M_1 and M_2). We varied them to analyze which initial configurations allow gravitational capture to occur within a Hubble time. This approach pinpoints regions in phase space where captures are most likely, paving the way for a comprehensive investigation of the subsequent merger stages through N-body simulations.

Chaos in captures. Jacobi captures exhibit chaotic behavior, indicated by their high sensitivity to initial conditions. Small variations in initial parameters can lead to significant changes in the number of close encounters between black holes (Fig. 4.3).

Mapping initial conditions. We integrated 241 920 initial configurations (see Table 4.1) over 14 Gyr, finding that 7.1% resulted in captures. Captures can be classified into initial captures (66.3%), formed at the start of the simulation, and dynamical captures (33.7%) that occur during the integration at later times. Initial captures include both temporary (Fig. 4.6) and permanent captures which remain bound throughout the simulation, exhibiting remarkable stability despite the chaotic nature of the three-body problem (Fig. 4.7). Dynamical captures are favored when the mass of the outer black

hole exceeds that of the inner one (Fig. 4.10), which is of particular interest within the context of core stalling. We found capture bands in Δr_i, i.e., a range of radial separation values leading to capture (Fig. 4.11). The capture band moves to higher Δr_i as the binary mass increases. To the right of the band (Δr_i larger), the black holes are too far away from each other to produce a capture. To the left of the band (Δr_i smaller), dynamical capture is infeasible due to the impossibility of phase catch-up within a Hubble time.

Eccentricity of captures. Jacobi captures generally result in highly eccentric binaries (Fig. 4.15), which can facilitate stabilization through energy dissipation from Post-Newtonian corrections at the pericenter (Samsing et al., 2018b).

Alternative capture criterion. We explored an alternative capture criterion based solely on the radius of influence, defining captures when black holes are within the binary Hill radius. This criterion results in a higher percentage of captures (16.4%) compared to the energy-based criterion (7.1%). While this alternative criterion is useful for understanding the behavior of certain captures, it is less desirable than the energy criterion. The additional captures it introduces are mostly hyperbolic flybys, which are unlikely to lead to mergers due to the high relative velocity between black holes. Choosing the appropriate capture criterion is challenging and can lead to contradictions in borderline cases. This is evident in the example of Pacman captures (Fig. 4.20). These near-resonant captures emerge due to the presence of the density core and perfectly illustrate a limiting case where the number of close encounters between black holes depends on the criterion used.

Caveat. The primary goal of our work is to gain a better qualitative understanding of Jacobi capture on a case-by-case basis. On the way, we had to make two key assumptions that need to be addressed in future studies: we restricted the problem to specific initial orbits and assumed a static galactic potential. **The first assumption** concerns the geometry of black hole orbits, as we considered only coplanar black holes. While orbits could be randomly oriented in general, coplanar orbits may artificially increase the probability of Jacobi capture since black holes are, on average, closer both spatially and in velocity. However, in scenarios where off-center black holes originate from accretion events, they are expected to exhibit spatial correlations that favor coplanar orbits. Additionally, we assumed initially circular orbits, which is realistic given that dynamical friction tends to circularize a black hole's orbit over time. Finally, we assumed all orbits revolve in the same direction, effectively doubling the probability of capture. This effect could be mitigated by the correlated origin of accreted black holes. **The second assumption** of a static galactic potential is also noteworthy. In some cases, the galaxy's reflex response may significantly affect the dynamics, particularly for stalling black holes, where the very definition of stalling implies that the galaxy is responding. This background motion may induce complex changes in the dynamics, even for a single black

hole orbiting a galaxy, and even more so for two black holes. Dynamical friction and buoyancy exerted on each individual black hole could couple, in a way that would modify the stalling radii of each black hole, or suppress the stalling process altogether. A more detailed treatment using live N-body simulations is required to assess the influence of galactic response on Jacobi capture.

Capture probability | 5

Overview

The previous chapter provides valuable insights into the impact of various parameters on Jacobi captures. In this chapter, our objective is to reduce the number of free parameters by making two assumptions concerning the origin and decentering of black holes. This allows us to calculate a probability of capture. This chapter is a detailed version of subsection 3.2 of François et al. (2024), adapted to fit the manuscript. A summary of the chapter is available in Section 5.3.

5.1 Bound black holes from the core stalling radii

The general five-parameter case helps us emphasize the influence of masses and kinematics on Jacobi captures. Yet, to derive a probability of capture, we must delve deeper into a physically motivated parameter space with a reduced number of degrees of freedom. To achieve this, we conduct a second simulation, assuming that black holes (BHs) are off-center at their core stalling radius. This fixes the radii once the masses are defined, effectively reducing the number of free parameters to three. The stalling radius $r_{\rm cs}$ is directly related to the mass of the BH through (see Kaur & Sridhar, 2018)

$$\Omega_{\rm p}(r_{\rm cs}) = \Omega_{\rm b} \quad \text{with} \quad \Omega_{\rm p}(r) = \sqrt{G\frac{M_{\rm b}(<r) + M_{\rm p}}{r^3}}, \tag{5.1}$$

where $\Omega_{\rm p}$ is the BH's orbital frequency, $\Omega_{\rm b}$ the orbital frequency of stars at the very center of the cored potential and $M_{\rm b}(<r)$ the enclosed mass of our background density. Numerical integration of Eq. 5.1 leads to a near-power solution which we find is accurately recovered from

$$\frac{r_{\rm cs}}{\rm kpc} \simeq A\left(\frac{M}{M_\odot}\right)^{1/4} \tag{5.2}$$

Table 5.1: Parameter ranges for the three-parameter case.

	Minimum value	Maximum value	Number of values	Spacing
$M_1/M_\odot$	10^3	10^6	20	Log
$M_2/M_\odot$	10^3	10^6	20	Log
$\Delta\varphi_i$	$2\pi/1000$	2π	400	Lin

with $A \simeq 1/80$ a dimensionless constant. We note that $r_{\rm cs}$ increases with the mass of the perturber, which is in agreement with Read et al. (2006). We end up with only three parameters: M_1, M_2 and $\Delta\varphi_i$ (the parameter ranges used are summarized in Table 5.1). We can impose $M_2 \geq M_1$ without loss of generality, ensuring that M_1 consistently represents the inner BH, as in the previous section. Not imposing this condition would mean simulating all possible cases twice, merely swapping the BH labels. This approach would yield mass-symmetric outcomes, offering limited insights into the impact of BH positioning on captures. Thus, we consider a total of 84 000 initial configurations, 11 712 of which show a Jacobi capture, corresponding to 13.9% of cases. There is an increase in the percentage of captures, meaning that core stalling allows BHs to be placed on radii that favor capture.

The left panel of Fig. 5.1 shows the percentage of captures as a function of the mass of the inner (M_1) and outer (M_2) BH. The upper left region of the figure is left empty because of the condition $M_2 \geq M_1$, guaranteeing that BH2 consistently holds the outer position. The right-hand panel depicts the percentage of captures as a function of the initial phase difference $\Delta\varphi_i$. The left panel reveals a higher percentage of captures when both M_1 and M_2 exhibit higher values, and when the mass gap between BHs is modest. The right-hand panel illustrates that captures predominantly occur with small initial phase difference ($\Delta\varphi_i$ close to 0).

Core stalling positions the BHs on very similar radii, as can be seen in Fig. 4.11, where the black lines indicate the boundaries within which core stalling operates for the studied mass range of $10^3 - 10^6\,M_\odot$. This region is in the regime of small radial separation discussed in Section 4.3.3. In that region, the vast majority of captures (95.4%) occur initially, when the BHs are sufficiently close in both initial radius and initial phase shift. Furthermore, to understand why there is a higher percentage of capture when masses are high, we can once again refer to Fig. 4.11. In each panel, the black cross indicates the positioning of BHs by core stalling. Notably, in the right-hand panel with higher masses, this cross falls within a darker region. This zone shifts from left to right as the mass of the BHs increases. In the right panel of Fig. 5.1, captures are observed at

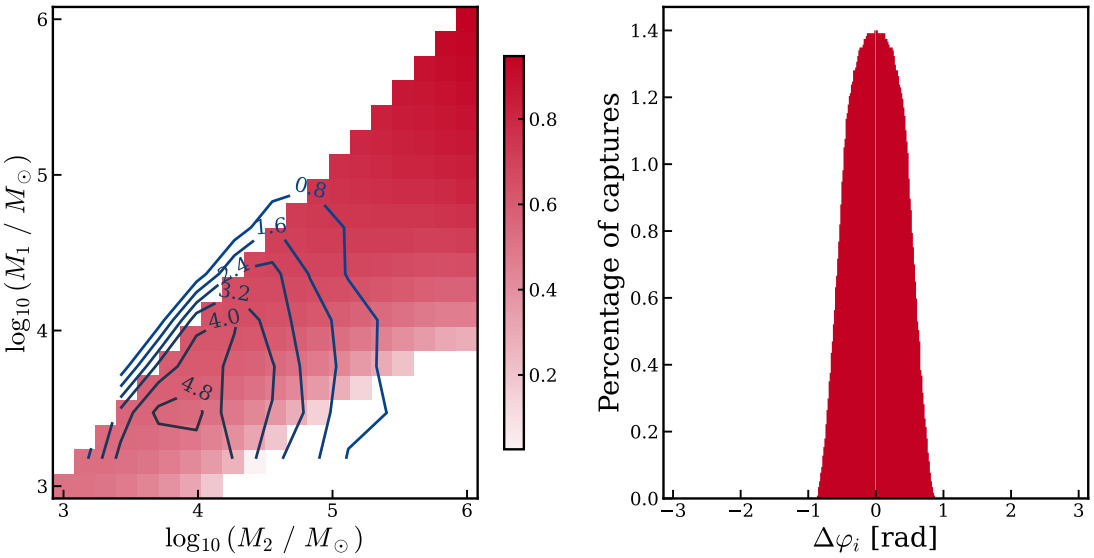

Figure 5.1: Percentage of captures in the three-parameter case. Left panel: as a function of inner (M_1) and outer (M_2) BH mass when positioned on their core stalling radius. The contour lines depict the probability (in percentage) of obtaining a mass pair (derived from a Monte Carlo sampling using SatGen, see Section 5.2). Right panel: as a function of the initial phase difference.

low angular separations, as we simulate 14 Gyr of evolution to evaluate captures within a Hubble time. When the angular separation is too large, BHs are unable to catch up with their phase delay within the given timeframe.

5.2 Black holes from a cosmological sequence of mergers

It is possible to reduce further the parameter set by employing a statistical sampling approach for the BH masses, based on a cosmological model. This fixes M_1 and M_2 and leaves a single parameter $\Delta\varphi_\mathrm{i}$ assumed to be uniform, allowing the derivation of a probability of capture. The selection of BH masses hinges on the assumption that they originate from the nuclei of two galaxies that underwent major mergers, ultimately forming our target galaxy for study. We also assume that within these nuclei, the BHs were accreting matter from the galaxy, which makes it possible to correlate their mass with that of their host galaxy.

First, we used dark matter merger trees obtained within the Semi-Analytic Satellite Generator (SatGen) introduced by Jiang et al. (2021). These merger trees are generated using an algorithm (Parkinson et al., 2008) based on the extended Press-Schechter formalism (Lacey & Cole, 1993). We generated 4 000 such merger trees for the target

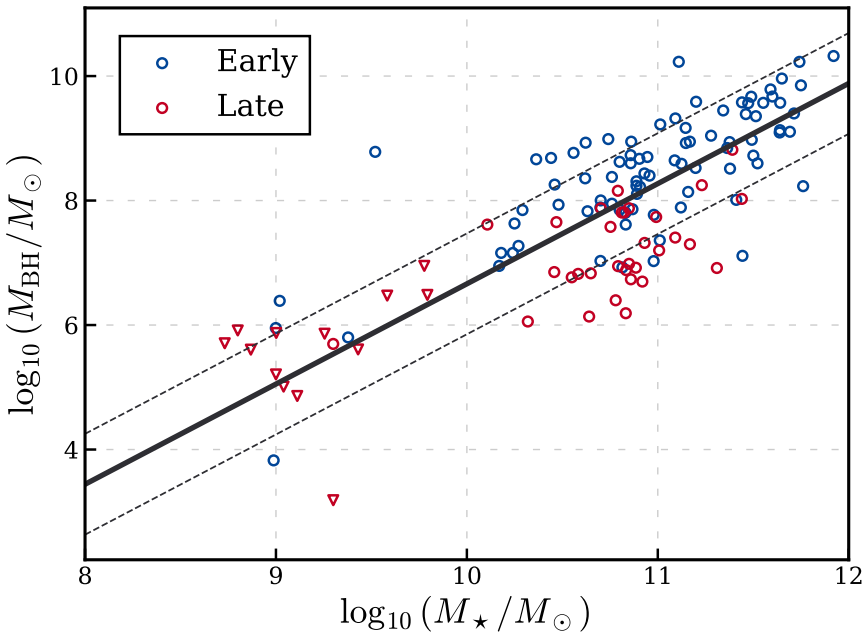

Figure 5.2: Scaling relation between black hole mass and stellar mass. The $M_{\rm BH} - M_\star$ relation is represented by the thick solid black line: $\log(M_{\rm BH}/{\rm M}_\odot) = \alpha + \beta \log(M_\star/M_0)$, with $M_0 = 3 \times 10^{10} M_\odot$, $\alpha = 7.43 \pm 0.09$, $\beta = 1.61 \pm 0.12$. The gray dashed lines denote the intrinsic scatter of the relation $\epsilon = 0.81 \pm 0.06$. The fit and data are from Greene et al. (2020). Blue markers represent early-type galaxies and red markers late-type galaxies. Upper limits are shown as open triangles.

halo of mass $M = 10^{11} M_\odot$ at z=0, and assess the associated stellar masses of the two progenitors according to the stellar-to-halo mass relation of Behroozi et al. (2013), see Fig. 1.6. Given the 0.16 dex scatter of the relation, we drew 10 realizations of the stellar mass per halo mass, following a lognormal distribution. In the context of accreting BH, mass accumulation is tied to the stellar mass. We assumed that the BH masses follow the $M_{BH} - M_\star$ relation of Greene et al. (2020) [1] :

$$\log(M_{\rm BH}/{\rm M}_\odot) = \alpha + \beta \log(M_\star/M_0) \pm \epsilon \tag{5.3}$$

with $M_0 = 3 \times 10^{10} M_\odot$, $\alpha = 7.43$, $\beta = 1.61$ and $\epsilon = 0.81$ the intrinsic scatter. This relationship is plotted in Fig. 5.2. We drew a series of 10 BH masses per stellar mass assuming again a lognormal distribution given the scatter of the relation. Following a selection process that involves filtering major mergers [2] , requiring progenitors' halo mass ratio to be above 1/3, we end up with 4 367 pairs of BH masses (M_1, M_2). A

[1] Low-mass galaxies pose challenges as they lack $\sigma_\star$ measurements and have diminished bulge fractions (MacArthur et al., 2003b). Consequently, Greene et al. (2020) revisited the $M_{\rm BH} - M_\star$ correlation, focusing on dynamical studies involving BHs with $M_{\rm BH} < 10^6 M_\odot$.

[2] For BHs to accrete and for us to apply the $M_{\rm BH} - M_\star$ relation, they must be sufficiently massive. Minor mergers involve less massive galaxies, where the $M_{\rm BH} - M_\star$ relation no longer holds.

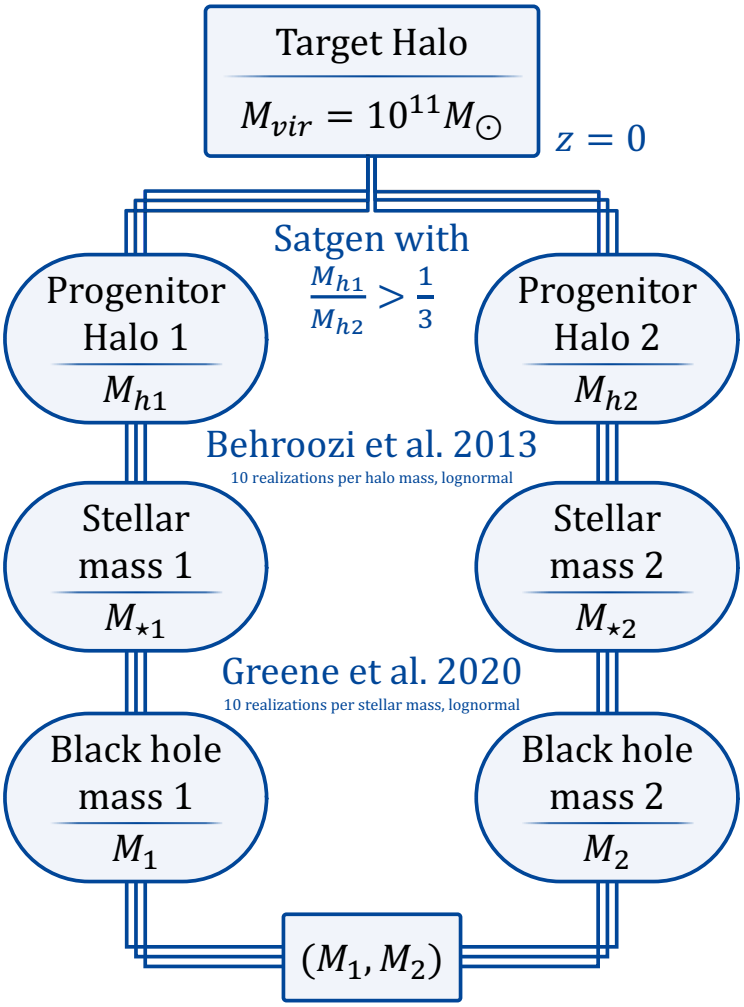

Figure 5.3: Diagram summarizing the procedure for obtaining the black hole mass pair.

diagram summarizing our procedure is shown in Fig. 5.3 and a visualization of the (M_1, M_2) distribution is plotted in Fig. 5.4 and is also reported as contour lines in Fig. 5.1. We then convolved the merger probability (Figure 5.1) with the mass distribution derived from the semi-analytic model (Figure 5.4). For each pair of masses (M_1, M_2) generated by the Monte Carlo algorithm, we calculated the capture proportion using our results from Section 5.1 as

$$p_i(M_1, M_2) = \frac{n(\text{bound} \mid M_1, M_2)}{n(\text{tot} \mid M_1, M_2)} \tag{5.4}$$

with $p_i(M_1, M_2)$ the capture proportion for a given pair of masses, $n(\text{bound}|M_1, M_2)$ the number of captures for the pair of masses (M_1, M_2) and $n(\text{tot}|M_1, M_2)$ the total number

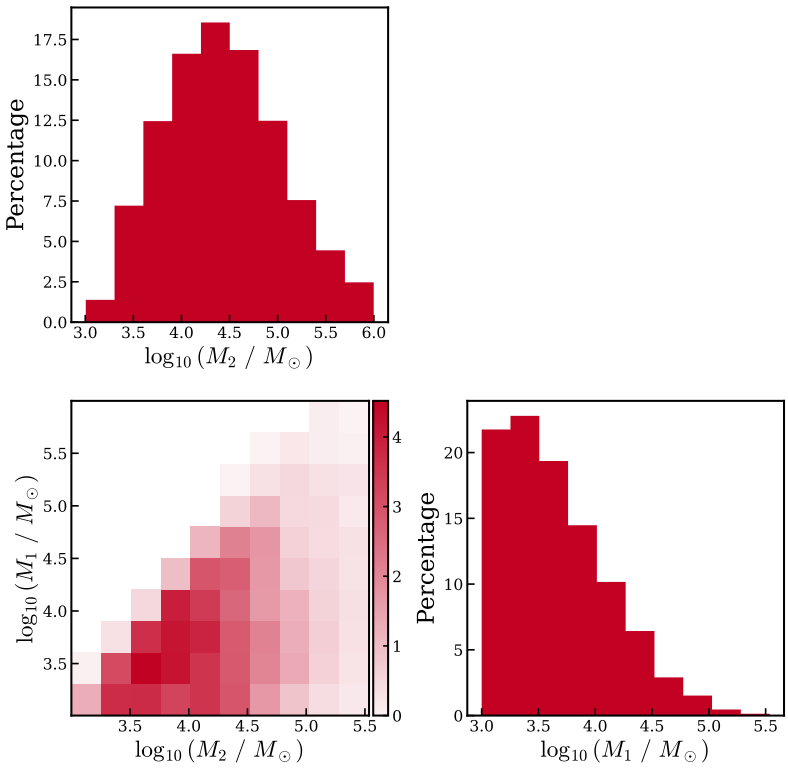

Figure 5.4: Monte Carlo sampling of BH mass using SatGen.

of simulations conducted for this pair of masses. The distribution of p_i is plotted in Fig. 5.5. The median value is indicated in the blue box. The positive (negative) uncertainty is derived from the difference between the median and the third (first) quartile. We finally estimate the total probability by taking the average value of this distribution:

$$p_{\rm tot} = \frac{1}{N} \sum_{i=1}^{N} p_i \tag{5.5}$$

where the sum relates to the cases generated by SatGen, N being the number of BH pairs generated. We obtain: $p_{\rm tot} = 13.2\%$. This result, which is not negligible, carries significant implications for the assembly of BH masses, especially if these captures can be sustained over time through dissipative forces. Further investigations into the effectiveness of these forces, particularly within stripped nuclei or globular clusters, are warranted.

5.3 Summary of Chapter 5

This chapter aims to determine the probability of gravitational captures by reducing the number of free parameters. To reach this goal, we made assumptions about the

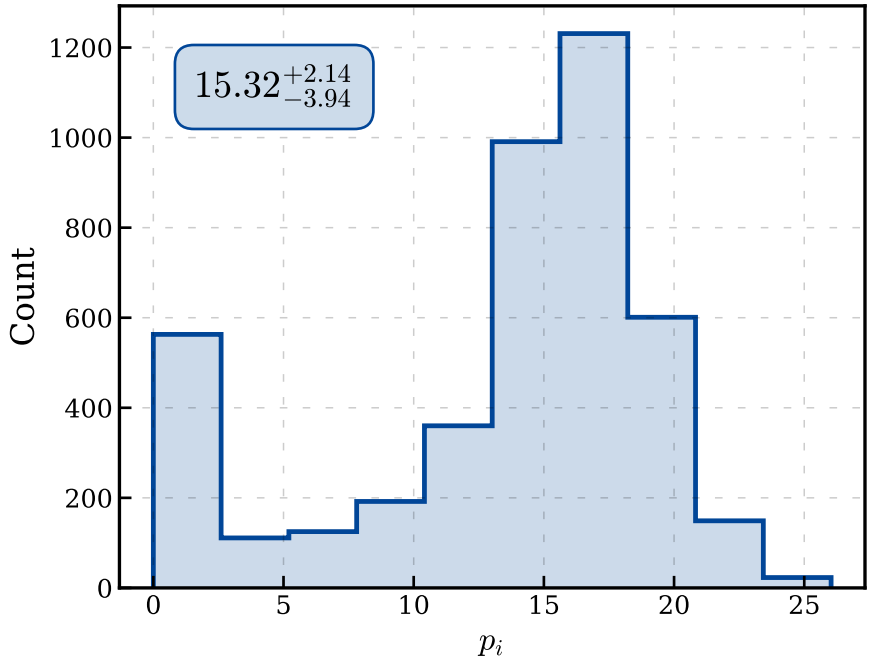

Figure 5.5: Distribution of $p_i(M_1, M_2)$ values. The median value is indicated in the blue box. The positive (negative) uncertainty is derived from the difference between the median and the third (first) quartile.

origin of the black holes and the nature of their shift from the center.

Bound black holes from the core stalling radii. First, we assumed black holes are off-center at their core stalling radius, which allows us to fix the radii of the black holes based on their mass. We ran 84 000 simulations with the three remaining free parameters (masses of the black holes M_1 and M_2 and the initial phase difference $\Delta\varphi_\mathrm{i}$, see Table 5.1). Of these, 11 712 show a Jacobi capture, corresponding to 13.9% of cases. The increase in the capture percentage compared to the five-parameters case (7.1%) suggests that core stalling positions black holes at radii that favor capture. Given the mass range under study, core stalling positions the black holes within a regime characterized by close radial separations. In this context, the vast majority of captures (95.4%) occur initially, if the black holes are sufficiently close. This condition necessitates M_1 and M_2 to be close, corresponding to a small radial separation and a low initial phase shift $\Delta\varphi_\mathrm{i}$ (Fig. 5.1).

Black holes from a cosmological sequence of mergers. Our second assumption is that these black holes originate from the central regions of two galaxies that underwent a major merger, ultimately forming our target galaxy for study. This enabled to recover a statistical distribution of black hole masses, employing a Monte Carlo sampling algorithm to construct merger trees and using scaling relations between stellar

and black hole masses (Fig. 5.4). By doing this, we obtained a probability of capture of 13.2%.

Caveat. We selected the black hole masses from a semi-analytical model, which is contingent upon the assumption that they are remnants of central black holes from past major mergers. The application of a correlation between stellar mass and black hole mass hinges on the assumption of black hole accretion of galactic matter. For scenarios involving wandering black holes situated outside the galactic center, refraining from accretion, reference to Fig. 5.1 is required on a case-by-case basis for each black hole mass pair.

Conclusion | 6

6.1 Overall summary

If I had to encapsulate the essence of this thesis in one compelling sentence, it would be: "What occurs when the most elusive type of black hole encounters the most enigmatic type of galaxy in the Universe?". Although this statement is somewhat sensational, it highlights the two key protagonists of this study. First, there are dwarf galaxies, enigmatic due to their very low luminosity, making them difficult to observe beyond the local universe, and their low mass, complicating their simulation on cosmological scales (see Section 1.3). Dwarf galaxies are a remarkable playground for testing our theories and exploring new physics. They have unique properties such as their high dark matter fraction and are a possible point of divergence between theories and observations. The presence of density cores in their centers, in contradiction with ΛCDM dark matter only simulations, is a perfect example. The second main character in this story is intermediate-mass black holes (IMBHs). Although their existence is crucial for understanding the mass assembly of black holes (BHs), their detection is still debated, especially in the low mass regime and there is considerable uncertainty surrounding their formation (see Section 1.4.3). This thesis explores the dynamics of IMBHs within cored dwarf galaxies.

First of all, in Chapter 2, we addressed the cusp-core discrepancy, a significant issue in cosmology where the ΛCDM model suggests a central density cusp in dark matter halos, while observations, especially of dwarf galaxies, show flat cores. Using N-body simulations, we showed that feedback processes could explain this discrepancy within the framework of the ΛCDM model. Stellar winds and supernova explosions create potential fluctuations that drive dark matter from the center, forming a core. Additionally, we showed that the repetition of outflow / inflow episodes of baryonic matter can create cores even if the final central mass returns to its initial value. This process could be highly effective in forming cores and is particularly interesting to study within the limit of a very large number of small variations, thereby approximating the behavior of feedback in dwarf galaxies.

Orbital dynamics are also unique in cored dwarf galaxies. A massive black hole (MBH) orbiting in a galaxy is assumed to fall to the center due to dynamical friction, which causes it to lose kinetic energy. While a supermassive black hole (SMBH) falls to the center of a Milky Way-type galaxy within a few billion years, the infall time of an IMBH within a dwarf galaxy can far exceed the age of the Universe. Furthermore, in a cored profile, the fall towards the galactic center is halted as it enters the core, a phenomenon known as core stalling. Due to prolonged dynamical friction timescales and core stalling in cored dark matter halos, a significant population of off-center wandering IMBHs is expected in dwarf galaxies. In this thesis, we investigated the possibility of such BHs binding outside the galactic center.

In Chapter 3, we proposed a novel scenario for off-center MBH mergers. We showed that the Lagrangian points and the zone of influence of a BH binary in a cored profile differ significantly from those in a Keplerian case or an NFW profile (with a cusp). In Chapter 4, we focused on the initial stage of off-center IMBH mergers: gravitational capture. Using idealized simulations, we examined the conditions under which two IMBHs can capture each other in a cored dark matter halo. Our study shows that these captures are chaotic, with small variations in initial conditions leading to vastly different outcomes, typically resulting in highly eccentric binaries. By mapping the initial conditions that lead to captures, we identified regions in phase space where captures are most likely. This analysis not only develops an understanding of the capture process but also paves the way for a comprehensive investigation of the subsequent merger stages through N-body simulations. Finally, in Chapter 5, we estimated the probability of gravitational captures by simplifying the number of free parameters. Assuming that BHs are off-center at their core stalling radii and originate from the central regions of galaxies that underwent major mergers, we found a capture probability of 13.2%.

6.2 Implications

In recent years, IMBHs have been successfully detected outside the centers of dwarf galaxies (Reines et al., 2020), as well as single relic nuclear clusters at kiloparsecs from the center of the galaxy have been confirmed (Seth et al., 2014; Ahn et al., 2018). Simulations and model predictions suggest that these relics of accretion events should be extremely common (Tremmel et al., 2018; Voggel et al., 2019), and mergers are thought to be a driving force behind the M-σ relation (Volonteri & Natarajan, 2009). In this thesis, we investigated whether and under what circumstances two IMBHs can become bound while outside the center of a galaxy. We find that such captures do occur at substantial fractions in our simplified simulations. Our capture probability of 13.2% is based on strong assumptions, and it is likely that this figure may decrease when these assumptions are relaxed. However, even a small fraction of this percentage

remains noteworthy, especially since cosmological simulations predict not just two off-center BHs, as we studied, but rather an entire population of wandering IMBHs in dwarf galaxies (Pfister et al., 2019; Bellovary et al., 2019, 2021). Therefore, even a lower probability could have significant implications for BH mass assembly and the expected gravitational wave signals.

This study is particularly timely, given the advent of detectors with unprecedented sensitivity that have recently been launched or are expected in the coming years. The first major breakthrough is the James Webb Space Telescope (JWST), launched on December 25, 2021 (Menzel et al., 2023; Rigby et al., 2023). JWST can observe in the infrared, reducing contamination from dust and offering greater sensitivity than its predecessor, the Hubble Space Telescope. This has enabled high-redshift observations that provide key insights into the formation and evolution of massive BHs. Early observations have already re-confirmed the presence of SMBHs at high redshift (Furtak et al., 2024), making it crucial to refine our models to explain how such massive BHs could form so early in the universe's history.

Off-center IMBHs are very challenging to observe due to their position, in a low-density environment, and their low mass (they minimally perturb surrounding stars and have little to no accretion activity). If this hidden off-center population of BHs merge repeatedly before reaching the center they would increase their mass with smaller merging events and be more massive once they reach the center of the main galaxy. Furthermore, as the probability of capture increases with BH mass, off-center mergers could further enhance the likelihood of additional off-center mergers by leaving behind a more massive merger product. The existence of off-center BH mergers also implies that three massive BHs simultaneously descending toward the galaxy's center becomes more rare. When this does occur, it causes an unstable three-body system, which can lead to the ejection of one BH. However, if two of the three BHs merge during their inspiral path, only two BHs reach the center, enabling a more stable situation and thus a more likely subsequent merger that yields a more massive BH than in the previous scenario. The history of BH mergers being altered by the possibility of off-center mergers, this will modify the emission rate of gravitational waves at a given frequency. This is particularly significant as the upcoming gravitational wave detector, LISA (Laser Interferometer Space Antenna; Amaro-Seoane et al., 2017), will offer to detect mergers of more massive BHs such as IMBHs.

Dwarf galaxies being the most common type of galaxy in the Universe, off-center mergers could have a major impact on the assembly of BH mass and gravitational wave emission. Moreover, dwarf galaxies can be accreted by more massive galaxies, meaning that events within dwarfs will have long-term consequences for more massive galaxies as well.

6.3 Outlook

6.3.1 The role of dissipative forces

As this type of merger can have major implications but has not been explored much in the literature, it is crucial to improve upon our idealized simulations. First, our study of gravitational captures does not account for the energy loss of BHs due to dissipative processes. This energy loss primarily arises from three sources:

1. Typically, BHs are surrounded by nuclear star clusters (Seth et al., 2008), and as they approach each other, they lose energy due to dynamical friction with the surrounding clusters.

2. The BH binary can also interact with nearby stars, ejecting them through three-body interactions, which tightens the binary.

3. Relativistic energy losses can be significant, especially at pericenter in highly eccentric binaries, which is typically the case during captures, as we have observed.

While gravitational captures are temporary, it has been observed that dissipative forces play a crucial role in the hardening of the binary (Fabian et al., 1975; Goldreich et al., 2002; Samsing et al., 2018b; Tagawa et al., 2018, 2020; Li et al., 2022; Boekholt et al., 2023; Rowan et al., 2023; DeLaurentiis et al., 2023). The next step is therefore to determine whether this inclusion can help maintain our gravitational captures over time and tighten the binary (as can be seen in the right panel of Fig. 6.1).

I have recently begun exploring this question. To do so, I set up initial conditions that present a gravitational capture in the idealized case without dissipation. I then replace the individual BHs with BH-star cluster systems, where the stars are distributed according to a King profile (King, 1966), ensuring that the total mass remains unchanged. My initial tests with GyrfalcON, the N-body code presented in Chapter 2, revealed that this code, being designed for collisionless systems, is not well-suited for simulating star clusters. The high central density of the clusters requires a drastic reduction in the time step, resulting in very long integration times. Consequently, I have recently installed the KETJU code (Mannerkoski et al., 2023).

This code integrates several crucial features: direct interactions in the vicinity of BHs, feedback mechanisms, post-Newtonian corrections, and even a tool for predicting gravitational wave signals. Beyond resolving the dynamics of stars near the center, this code will also allow for the incorporation of relativistic corrections. The aim now is to explore the following questions: can all captures be stabilized, or only those featuring a minimum number of close encounters? How is the stability influenced by the density profile of stars bound to the BHs? Additionally, is dissipation through three-body

interactions effective in this context? Do these dissipations allow the transition to the relativistic regime?

To address these questions, I will continue the work I began with GYRFALCON, initially focusing on the energy loss due to interactions with the star clusters. Specifically, I will investigate how stabilization depends on (*i*) the properties of the idealized capture and (*ii*) the various parameters of the clusters' density profiles. If the transition to the relativistic regime is possible at this stage, the next goal will be to integrate post-Newtonian corrections to resolve the final stages of the merger and predict the gravitational wave signals expected from these events.

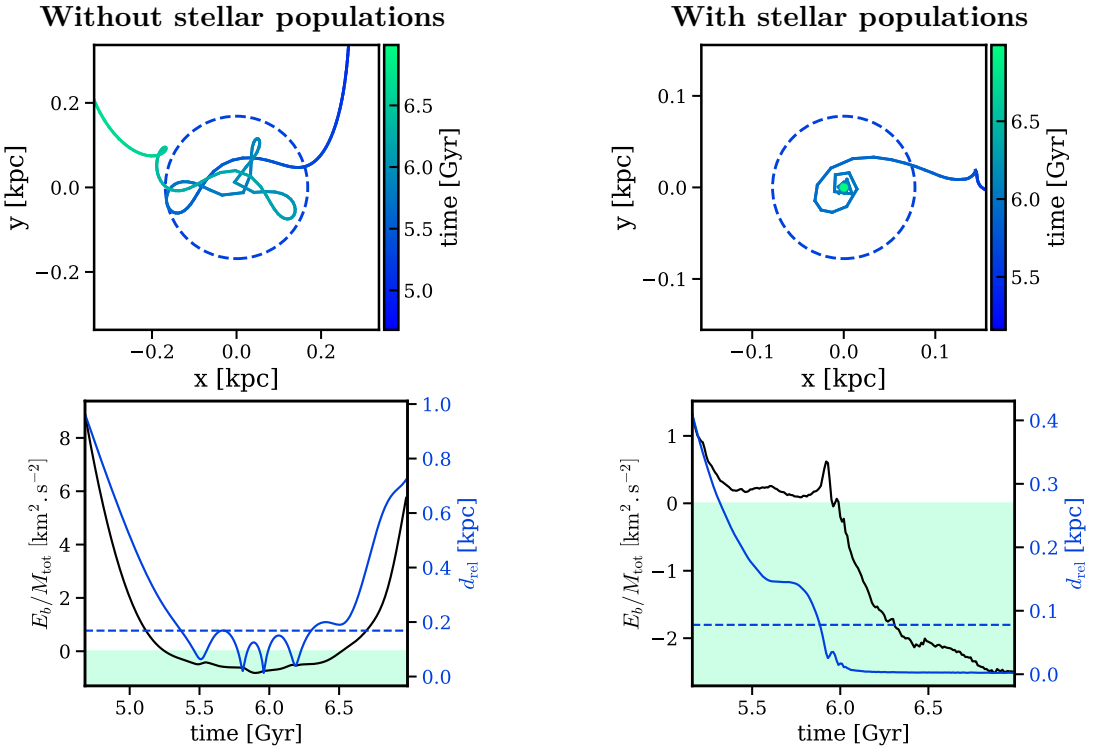

Figure 6.1: Stabilization of a Jacobi capture in the presence of stellar populations around the black holes (right panel) compared to the case without such stellar populations (left panel). The top row shows BH trajectory in the center of mass frame of the binary, the color gradient indicates the time. The bottom row shows the binding energy and the BHs separation as a function of time. In both cases, the initial conditions, total mass, and integrator are the same. ⚠ The right case was obtained with GYRFALCON but should be considered as a proof of concept. Using a more appropriate code is advisable for drawing physical conclusions. Here, each cluster consists of $N = 4 \times 10^4$ stars with a mass of $M_\star \sim 1\,M_\odot$, distributed according to a King profile with $W_0 = 5$ and a scale radius $a = 10$ pc. The black hole accounts for 10% of the total mass.

6.3.2 Globular cluster mergers

Most globular clusters exhibit multiple stellar populations, the origin of which remains uncertain, possibly resulting from secondary star formation. However, this mechanism falls short in explaining the observed significant spread in iron content. Bekki & Tsujimoto (2016) and Gavagnin et al. (2016) propose a solution involving the merger of two globular clusters with slightly different formation times ($\sim$ 300 Myr). According to their hypotheses, such mergers are predominantly feasible within the halo or nucleus of dwarf galaxies due to their shallower gravitational potentials. Subsequently, these dwarf galaxies, along with their pristine or merged globular clusters, are accreted by the Milky Way. To test this hypothesis, it is crucial to investigate the likelihood of mergers between globular clusters in dwarf galaxies. My results on Jacobi captures are transferable to this problem, since any merger outside the galactic center, including for globular clusters, begins with this physical process. In cases where a capture occurs, one can replace the BHs with a sets of N particles distributed according to stellar density profiles (King 1966 or Varri & Bertin 2012) to assess if interactions between stellar populations through N-body simulations can lead to capture stabilization and, consequently, the merger of globular clusters.

6.3.3 Capture rate for gravitational wave prediction

So far, I tackled Jacobi captures primarily from a kinematic perspective. While this approach provides insights into the phenomenon and helps develop an intuitive understanding of BH motion, it necessitates certain orbit-related assumptions. To achieve greater generality and take into account the distribution of wandering BHs in the galaxy, I propose to adopt a statistical approach, following Peñarrubia (2023). This new perspective involves treating an off-center BH as a reference point, referred to as RBH, and assessing the likelihood of its interactions with a population of other off-center BHs as it moves through the galaxy. The process will consist of two key steps. First, I will use cosmological hydrodynamical simulations (in the same spirit as what was done in Bellovary et al., 2019, 2021) to obtain a density profile of wandering BHs $\rho(r)$. Then I will use it to calculate the theoretical fraction of off-center BH with negative binding energy within RBH's sphere of influence. Second, as RBH moves through the galaxy, I will estimate the number of BHs entering its sphere of influence during a given time interval, using Poisson statistics. Putting these two elements together, I will obtain an off-center BH-BH capture rate, a valuable tool in the long run for making predictions about the emission of gravitational waves and the mass growth of BHs through repeated off-center mergers.

6.3.4 Influence of the galactic response on Jacobi captures

For the captures we have simulated near the galactic center, where the galaxy's integrated mass is comparable to that of the BHs, the galaxy must be treated with live particles. It would be interesting to explore the effect of the core's response on Jacobi captures. To do this, one could select initial conditions that present a capture and replace the external potential with a live halo. This question is closely linked to the study of core stalling in the presence of two perturbers (in this case, two BHs). This is a non-trivial problem, and it is unclear how core stalling is affected by the presence of a second BH.

My initial intuition is that in the case of two BHs with similar masses, $M_1 \simeq M_2$, the presence of the second BH could prevent the emergence of the orbits responsible for buoyancy and core stalling. However, if the BHs are out of phase, positioned on opposite sides of the galactic center, a quadrupolar mode might preserve the regularity necessary for such orbits to emerge. In the scenario of two BHs with a significant mass hierarchy, $M_1 \gg M_2$, the lighter BH could be perceived as a minor perturbation, and stalling might persist. In this case, it would be interesting to study a situation where a massive BH (say $M_1 \sim 10^6\,M_\odot$) stalls while several less massive BHs ($M_2 \sim 10^2 - 10^3\,M_\odot$) are present. The massive BH at its core stalling radius could capture these smaller BHs, potentially merge with them, and thus increase its mass. As its mass increases, it would move farther from the galactic center because its theoretical core stalling radius is larger.

6.3.5 Fractal structure

In Section 4.2, we showed that captures exhibit chaotic behavior with respect to the four parameters M_1, M_2, r_i, and Δr_i. When plotting the number of close encounters as a function of one of these parameters, such as Δr_i, we obtain irregularities in the form of peaks, as shown in Fig. 6.2. In the Keplerian case (with a central point mass instead of the galaxy), these irregularity peaks have been shown to exhibit a self-similar fractal structure that can be described by a generalised Cantor set with a dimension of approximately 0.4 (Boekholt et al., 2023). It would be interesting to investigate whether this fractal structure persists in the case of an extended central potential. Additionally, examining how the fractal dimension varies with the potential parameters, such as the inner slope of the density profile, would also be of great interest.

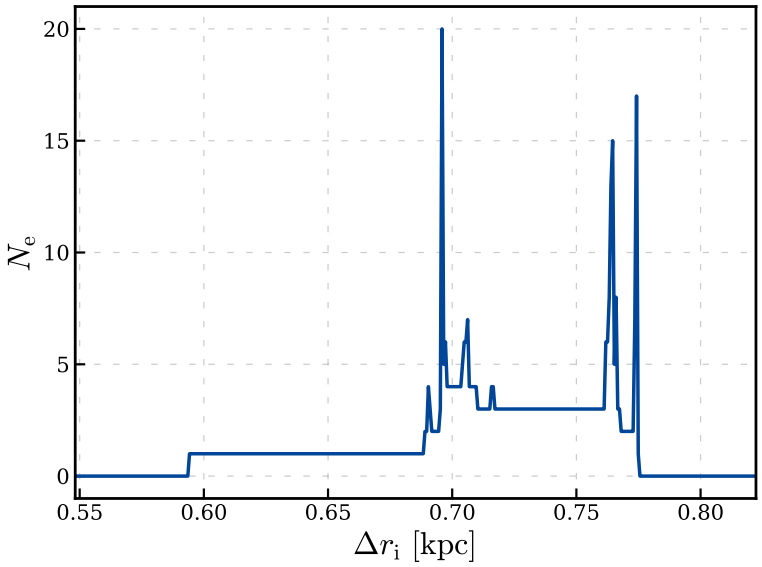

Figure 6.2: Number of close encounters N_e between BHs during capture as a function of their initial radial separation Δr_i.

French summary / Résumé en français

7

7.1 Résumé détaillé

Si je devais résumer l'essence de cette thèse en une phrase accrocheuse, ce serait : "Que se passe-t-il lorsque le type de trou noir le plus insaisissable rencontre le type de galaxie le plus énigmatique de l'Univers ?". Bien que cette affirmation soit quelque peu sensationnelle, elle met en lumière les protagonistes clés de cette étude. Premièrement, il y a les galaxies naines, énigmatiques en raison de leur très faible luminosité, qui les rend difficiles à observer au-delà de l'univers local, et de leur faible masse, ce qui complique leur simulation à des échelles cosmologiques (voir Section 1.3). Les galaxies naines constituent un terrain de jeu remarquable pour tester nos théories et explorer de nouvelles physiques. Elles ont des propriétés uniques, comme leur forte fraction de matière noire, et représentent un point de divergence possible entre théories et observations. La présence de coeurs de densité en leur centre, en contradiction avec les simulations de matière noire seules du modèle ΛCDM, en est un exemple parfait. Les autres personnages principaux de cette histoire sont les trous noirs de masse intermédiaire. Bien que leur existence soit cruciale pour comprendre l'assemblage de la masse des trous noirs, leur détection fait encore débat, en particulier dans le régime des faibles masses, et il existe une grande incertitude concernant leur formation (voir Section 1.4.3). Cette thèse explore la dynamique des trous noirs de masse intermédiaire au sein des galaxies naines à coeur.

7.1.1 Chapitre 2

Tout d'abord, au chapitre 2, nous avons exploré la divergence cusp-core, un problème majeur en cosmologie où la densité des halos de matière noire dans le cadre du modèle ΛCDM ne reproduit pas certaines observations. Ce chapitre examine l'interaction entre la matière noire et la matière baryonique au sein des centres de galaxies afin de mieux comprendre et potentiellement résoudre cette divergence.

Divergence cusp-core. Le modèle ΛCDM prédit que la matière noire domine les grandes structures de l'Univers, tandis que la matière baryonique devient significative plus tard. Les simulations basées uniquement sur la matière noire montrent une divergence de la densité au centre des halos. Cependant, les observations, en particulier celles des galaxies naines, révèlent des coeurs de densité plats. Cette incohérence, connue sous le nom de divergence cusp-core, remet en question le modèle ΛCDM. Deux approches ont été proposées pour résoudre cette divergence : l'une modifie le modèle de matière noire froide, tandis que l'autre le conserve et met l'accent sur l'interaction entre la matière baryonique et la matière noire. Dans ce chapitre, nous nous sommes concentrés sur la seconde, en présentant le modèle CuspCore, qui explique la formation des coeurs par des processus de rétroaction.

Le modèle CuspCore. Les processus de rétroaction, tels que les vents stellaires et les explosions de supernova, peuvent créer des fluctuations de potentiel qui repoussent les particules de matière noire du centre, formant ainsi un coeur. Les simulations hydrodynamiques soutiennent cette idée, mais reposent souvent sur des paramètres ad hoc. Nous avons introduit le modèle CuspCore, qui explique la formation des coeurs par des variations du potentiel induites par la rétroaction. Le modèle décrit un processus en trois étapes : l'équilibre initial, une variation instantanée de masse, et une relaxation ultérieure. La relaxation, supposée se produire à énergie constante, conduit à un nouvel état d'équilibre caractérisé par un coeur de densité.

Tests avec des simulations N-corps. Les simulations sont essentielles pour tester les modèles théoriques, compte tenu de la nature non réplicable de l'Univers. Dans ce chapitre, nous avons testé les prédictions du modèle CuspCore à l'aide de simulations N-corps à l'échelle galactique. Nous avons introduit les concepts fondamentaux des simulations N-corps utilisant un code en arborescence, en détaillant les techniques d'optimisation comme le lissage, ainsi que les paramètres spécifiques employés dans nos simulations.

Épisode unique. Ces simulations ont mis en évidence les succès et les échecs du modèle CuspCore. Elles ont révélé que le modèle prédit avec précision la formation de coeurs dans de nombreux scénarios (voir Fig. 2.7) mais échoue dans certaines conditions, comme lors de variations de masse extrêmes. Nous avons constaté que pour de grandes variations de la masse baryonique (supérieures à 35%), le rapport de la masse baryonique ($m_{\rm bar}$) à la masse de viriel ($M_{\rm vir}$) affecte considérablement la précision de la prédiction du modèle. Dans ces cas, lorsque $m_{\rm bar}/M_{\rm vir} \lesssim 0.001$, le modèle a tendance à sous-estimer la création de coeurs. À l'inverse, lorsque $m_{\rm bar}/M_{\rm vir} \gtrsim 0.003$, le modèle surestime la création de coeurs (voir Fig. 2.8).

Épisodes multiples. Des épisodes multiples de variation de masse baryonique ont également été explorés. Dans un scénario d'alternance entre expulsions et accrétion, le

modèle a des difficultés importantes à prédire le comportement des simulations à partir de la deuxième expulsion (voir Fig. 2.9). Cependant, les simulations montrent l'effet cumulatif des fluctuations répétées dans la création de coeurs (voir Fig. 2.9 et 2.10). L'efficacité des épisodes multiples dans la création d'un coeur de densité avec de plus petites variations de masse suggère d'étudier la limite où le nombre d'épisodes est très grand et la variation de masse est faible. Ce scénario, plus fidèle au réel comportement de la rétroaction dans les galaxies naines, est en accord avec des modèles théoriques où la création de coeurs résulte de fluctuations stochastiques de densité dans la distribution de gaz (El-Zant et al., 2016).

Limites et améliorations. Les échecs du modèle peuvent être attribués à ses hypothèses fortes, telles que la conservation de l'énergie pendant la phase de relaxation et la négligence de l'excentricité des orbites, ce qui induit un processus de diffusion de l'énergie. La reconnaissance de ces limites du modèle CuspCore original a conduit à sa généralisation : le modèle CuspCore II (Li et al., 2023). Cette nouvelle version suit de manière auto-cohérente la diffusion de l'énergie orbitale, fournissant des prédictions plus précises même dans les cas extrêmes de variation de masse.

Les conséquences d'un coeur de densité. Pour conclure ce chapitre, nous avons discuté de l'impact d'un coeur de densité sur la dynamique orbitale. La présence de coeurs donne lieu à de nouveaux phénomènes tels que la flottabilité dynamique et le core stalling, qui empêchent les perturbateurs comme les trous noirs massifs de tomber au centre des galaxies. Cela motive en partie l'exploration d'un scénario impliquant des fusions de trous noirs massifs en dehors des centres galactiques, qui fera l'objet des chapitres suivants.

7.1.2 Chapitre 3

Au Chapitre 3, nous avons étudié l'influence des trous noirs massifs à l'extérieur du centre des galaxies naines à coeur. Nous avons commencé par un aperçu du scénario standard des fusions de trous noirs massifs au centre des galaxies et nous avons ensuite introduit un nouveau scénario de fusion en dehors du centre comme alternative possible.

Scénario de fusion excentrée de trous noirs. Le scénario standard des fusions de trous noirs massifs implique un processus en trois phases commençant par leur chute vers le centre de la galaxie sous l'effet de la friction dynamique. Cependant, dans le cas des trous noirs de masse intermédiaire dans les galaxies naines, le temps nécessaire pour atteindre le centre peut dépasser l'âge de l'Univers. De plus, la présence de coeurs de densité constante permet aux trous noirs de se stabiliser sur des orbites excentrées en raison du phénomène de core stalling. Dans ce chapitre, nous avons proposé un nouveau scénario de fusions de trous noirs de masse intermédiaire en dehors du centre, initié

par une capture gravitationnelle. Ce processus peut être approximé par un problème restreint à trois corps circulaire, où la dynamique est influencée par la distribution de masse étendue de la galaxie, en particulier en présence d'un coeur central.

Structure des points de Lagrange dans les profils à coeur. Tout d'abord, nous avons étudié la structure des points de Lagrange dans un potentiel de galaxie à coeur, montrant comment la topologie du potentiel effectif diffère du cas képlérien classique. Près du centre galactique, une bifurcation se produit et la fusion des points de Lagrange peut affecter de manière significative la dynamique des trous noirs, modifiant leurs zones d'influence et la probabilité de capture gravitationnelle.

Rayon d'influence et critère de capture. Ensuite, nous avons calculé le rayon d'influence des trous noirs et montré que, dans notre zone d'étude, il est environ deux fois plus grand que la valeur donnée par l'approximation des marées lointaines. Dans le coeur, le rayon d'influence dépend de la pente interne du profil de densité et ne peut pas être approximé à l'aide du potentiel képlérien typiquement utilisé dans la littérature. Nous avons défini un critère de liaison basé sur deux conditions : (1) l'énergie de liaison entre les trous noirs doit être négative, et (2) la distance entre les trous noirs doit devenir inférieure au rayon de Hill de la binaire pendant la période d'énergie de liaison négative. Le chapitre se termine par des exemples de captures gravitationnelles, illustrant la dynamique complexe des fusions excentrées et ouvrant la voie à une exploration plus approfondie de ce scénario alternatif dans le chapitre suivant.

7.1.3 Chapitre 4

Au Chapitre 4, nous nous sommes concentrés sur la première étape d'une fusion excentrée de trous noirs de masse intermédiaire : la capture gravitationnelle. L'objectif est de développer une intuition de ce processus à l'échelle galactique, où les trous noirs se lient en dehors du centre et subissent plusieurs rencontres proches.

Configuration des simulations. Afin d'isoler l'étape de capture et d'explorer efficacement des centaines de milliers de conditions initiales, nous avons effectué des simulations idéalisées de deux trous noirs ponctuels dans un potentiel gravitationnel lisse. Nous avons considéré des trous noirs de masses allant de 10^3 à $10^6\,M_\odot$ dans un halo de matière noire à coeur de $10^{11}\,M_\odot$ (la même galaxie que dans les chapitres précédents). Nous avons pris en compte cinq paramètres initiaux : le rayon initial du trou noir intérieur (r_i), la séparation radiale entre les trous noirs (Δr_i), la différence de phase ($\Delta\varphi_\mathrm{i}$) et les masses des trous noirs (M_1 et M_2). Nous les avons variés pour analyser quelles configurations initiales permettent une capture gravitationnelle dans un temps de Hubble. Cette approche permet d'identifier les régions dans l'espace des phases où les captures sont plus probables, ouvrant ainsi la voie à une enquête approfondie des

étapes de fusion suivantes grâce aux simulations N-corps.

Chaoticité des captures. Les captures de Jacobi présentent un comportement chaotique, comme en témoigne leur grande sensibilité aux conditions initiales. De légères variations de ceux-ci peuvent entraîner des changements significatifs dans le comportement, notamment dans le nombre de rencontres proches entre les trous noirs (Fig. 4.3).

Cartographie des conditions initiales. Nous avons intégré 241 920 configurations initiales (voir Table 4.1) sur 14 milliards d'années, et constaté que $7,1\%$ d'entre elles aboutissent à des captures. Les captures peuvent être classées en deux sous-catégories : les captures initiales ($66,3\%$), formées au début de la simulation, et les captures dynamiques ($33,7\%$) qui se produisent plus tard lors de l'intégration. Les captures initiales comprennent à la fois des captures temporaires (Fig. 4.6) et permanentes, qui restent liées tout au long de la simulation et montrent une stabilité remarquable malgré la nature chaotique du problème à trois corps (Fig. 4.7). Les captures dynamiques sont favorisées lorsque la masse du trou noir extérieur dépasse celle du trou noir intérieur (Fig. 4.10), ce qui est particulièrement intéressant dans le contexte du core stalling. Nous avons identifié des bandes de capture en $\Delta r_{\rm i}$, c'est-à-dire une gamme de valeurs de séparation radiale menant à une capture (Fig. 4.11). La bande de capture se déplace vers des valeurs plus élevées de $\Delta r_{\rm i}$ à mesure que la masse de la binaire augmente. À droite de la bande ($\Delta r_{\rm i}$ plus grand), les trous noirs sont trop éloignés l'un de l'autre pour produire une capture. À gauche de la bande ($\Delta r_{\rm i}$ plus petit), la capture dynamique est impossible en raison de l'impossibilité de rattraper le retard de phase en un temps de Hubble.

Excentricité des captures. Les captures de Jacobi aboutissent généralement à des binaires très excentriques (Fig. 4.15), ce qui peut faciliter leur stabilisation par dissipation d'énergie due aux corrections post-newtoniennes au péricentre (Samsing et al., 2018b). Ce résultat présente également un intérêt particulier dans le contexte des ondes gravitationnelles, dont la fréquence est influencée par l'excentricité des binaires.

Critère de capture alternatif. Nous avons exploré un critère de capture alternatif basé uniquement sur le rayon d'influence, définissant les captures lorsque les trous noirs se trouvent à l'intérieur du rayon de Hill de la binaire. Ce critère conduit à un pourcentage de captures plus élevé ($16,4\%$) par rapport au critère basé sur l'énergie ($7,1\%$). Bien que le critère alternatif soit utile pour comprendre le comportement de certaines captures, il est moins souhaitable que le critère énergétique. Les captures supplémentaires qu'il introduit sont principalement des flybys hyperboliques, qui sont peu susceptibles de mener à des fusions en raison de la grande vitesse relative entre les trous noirs. Le choix du critère de capture approprié est complexe et peut entraîner des contradictions dans les cas limites. Cela se manifeste clairement dans l'exemple des captures Pacman (Fig. 4.20). Ces captures quasi-résonnantes émergent en raison de la présence du coeur de densité et illustrent parfaitement un cas limite où le nombre de

rencontres proches entre les trous noirs dépend du critère utilisé.

Limitations. Le principal objectif de notre travail est d'obtenir une meilleure compréhension qualitative des captures de Jacobi au cas par cas. En chemin, nous avons dû faire deux hypothèses clés qui devront être relachées dans de futures études : nous avons restreint le problème à des orbites initiales spécifiques et supposé un potentiel galactique statique. **La première hypothèse** concerne la géométrie des orbites des trous noirs, car nous n'avons considéré que des trous noirs coplanaires. Bien que les orbites puissent généralement être orientées de manière aléatoire, les orbites coplanaires peuvent augmenter artificiellement la probabilité de capture de Jacobi puisque les trous noirs sont, en moyenne, plus proches à la fois spatialement et en vitesse. Cependant, dans les scénarios où les trous noirs excentrés proviennent d'événements d'accrétion, ils devraient présenter des corrélations spatiales favorisant des orbites coplanaires. Nous avons également supposé des orbites initialement circulaires, ce qui est idéalisé mais raisonnable étant donné que la friction dynamique tend à circulariser l'orbite d'un trou noir au fil du temps. Enfin, nous avons supposé que toutes les orbites tournent dans la même direction, doublant effectivement la probabilité de capture. Cet effet pourrait être atténué par l'origine corrélée des trous noirs accrétés. **La deuxième hypothèse** d'un potentiel galactique statique est également notable. Dans certains cas, la réponse réflexe de la galaxie peut avoir un impact significatif sur la dynamique, en particulier pour les trous noirs en stalling, où la définition même du stalling implique que la galaxie réagit. Ce mouvement de fond peut induire des changements complexes dans la dynamique, même pour un seul trou noir en orbite autour d'une galaxie, et encore plus pour deux trous noirs. La friction dynamique et la flottabilité exercées sur chaque trou noir individuel pourraient se coupler, modifiant les rayons de stalling de chaque trou noir ou supprimant complètement le processus de stalling. Un traitement plus détaillé utilisant des simulations N-corps en direct est nécessaire pour évaluer l'influence de la réponse galactique sur les captures de Jacobi.

7.1.4 Chapitre 5

Enfin, au Chapitre 5, nous avons estimé la probabilité de captures gravitationnelles en réduisant le nombre de paramètres libres. Pour ce faire, nous avons fait des hypothèses sur l'origine des trous noirs et la nature de leur décalage par rapport au centre.

Trous noirs liés à partir des rayons de core stalling. Tout d'abord, nous avons supposé que les trous noirs sont excentrés à leur rayon de core stalling, ce qui nous permet de fixer les rayons des trous noirs en fonction de leur masse. Nous avons réalisé 84 000 simulations avec les trois paramètres libres restants (masses des trous noirs M_1 et M_2 et la différence de phase initiale $\Delta\varphi_{\rm i}$, voir Table 5.1). Parmi celles-ci, 11 712

montrent une capture de Jacobi, correspondant à $13,9\%$ des cas. L'augmentation du pourcentage de captures par rapport au cas à cinq paramètres ($7,1\%$) suggère que le core stalling positionne les trous noirs à des rayons favorables à la capture. Étant donné l'intervalle de masse étudié, le core stalling place les trous noirs dans un régime caractérisé par des séparations radiales rapprochées. Dans ce contexte, la grande majorité des captures ($95,4\%$) se produisent initialement, si les trous noirs sont suffisamment proches. Cette condition nécessite que M_1 et M_2 soient proches, ce qui correspond à une petite séparation radiale et à un faible décalage de phase initiale $\Delta\varphi_{\rm i}$ (Fig. 5.1).

Trous noirs issus d'une séquence cosmologique de fusions. Notre seconde hypothèse est que ces trous noirs proviennent des régions centrales de deux galaxies ayant subi une fusion majeure, formant ainsi notre galaxie d'étude. Cela nous a permis de retrouver une distribution statistique des masses des trous noirs, en utilisant un algorithme d'échantillonnage Monte Carlo pour construire des arbres de fusion et en utilisant des relations d'échelle entre les masses stellaires et les masses des trous noirs (Fig. 5.4). De cette façon, nous avons obtenu une probabilité de capture de $13,2\%$.

Limitation. Nous avons sélectionné les masses des trous noirs à partir d'un modèle semi-analytique, qui repose sur l'hypothèse qu'ils sont les résidus de trous noirs centraux provenant de fusions majeures passées. L'application d'une corrélation entre la masse stellaire et la masse du trou noir dépend de l'hypothèse d'accrétion de matière galactique par les trous noirs. Pour des scénarios impliquant des trous noirs errants situés en dehors du centre galactique, sans accrétion, il faut se référer à la Fig. 5.1 au cas par cas pour chaque paire de masses de trous noirs.

7.2 Implications

Au cours des dernières années, des trous noirs de masse intermédiaire ont été détectés avec succès en dehors des centres de galaxies naines (Reines et al., 2020), et des amas nucléaires reliques isolés à plusieurs kiloparsecs du centre des galaxies ont également été confirmés (Seth et al., 2014; Ahn et al., 2018). Les simulations et les modèles prédisent que ces reliques d'événements d'accrétion devraient être extrêmement courantes (Tremmel et al., 2018; Voggel et al., 2019), et les fusions sont considérées comme une force motrice derrière la relation M-σ (Volonteri & Natarajan, 2009). Dans cette thèse, nous avons étudié si, et dans quelles circonstances, deux trous noirs de masse intermédiaire peuvent devenir liés alors qu'ils sont situés en dehors du centre d'une galaxie. Nos résultats montrent que de telles captures se produisent couramment dans nos simulations simplifiées. Notre probabilité de capture de $13,2\%$ est basée sur des hypothèses fortes, et il est probable que cette valeur diminue lorsque ces hypothèses sont relâchées. Cependant, même une fraction réduite de ce pourcentage reste notable, d'autant plus que les simulations cosmologiques prédisent non pas seulement deux trous noirs décen-

trés, comme nous les avons étudiés, mais une population entière de trous noirs de masse intermédiaire errants dans les galaxies naines (Pfister et al., 2019; Bellovary et al., 2019, 2021). Par conséquent, même une probabilité plus faible pourrait avoir des implications significatives sur l'assemblage de la masse des trous noirs et les signaux attendus d'ondes gravitationnelles.

Cette étude est particulièrement pertinente dans le contexte de l'arrivée de détecteurs d'une sensibilité sans précédent, récemment lancés ou prévus dans les années à venir. Le premier jalon important est la mise en service du télescope spatial James Webb (JWST), lancé le 25 décembre 2021 (Menzel et al., 2023; Rigby et al., 2023). Le JWST peut observer dans l'infrarouge, réduisant ainsi la contamination par la poussière et offrant une sensibilité accrue par rapport à son prédécesseur, le télescope spatial Hubble. Cela a permis des observations à haut redshift qui fournissent des informations clés sur la formation et l'évolution des trous noirs massifs. Les premières observations ont déjà reconfirmé la présence de trous noirs supermassifs à haut redshift (Furtak et al., 2024), soulignant l'importance de raffiner nos modèles pour expliquer comment de tels trous noirs massifs ont pu se former si tôt dans l'histoire de l'univers.

Les trous noirs intermédiaires décentrés sont très difficiles à observer en raison de leur position, dans un environnement de faible densité, et de leur faible masse (ils perturbent peu les étoiles environnantes et ont peu ou pas d'activité d'accrétion). Si cette population cachée de trous noirs décentrés fusionne de manière répétée avant d'atteindre le centre, ils augmenteraient leur masse avec des événements de fusion plus petits et seraient plus massifs une fois arrivés au centre de la galaxie principale. De plus, comme la probabilité de capture augmente avec la masse des trous noirs, les fusions décentrées pourraient encore augmenter la probabilité d'autres fusions décentrées en laissant derrière elles un produit de fusion plus massif. L'existence de fusions de trous noirs décentrés implique également que la situation où trois trous noirs massifs descendent simultanément vers le centre de la galaxie devient plus rare. Lorsque cela se produit, il en résulte un système instable à trois corps, qui peut entraîner l'éjection d'un trou noir. Cependant, si deux des trois trous noirs fusionnent au cours de leur chutte vers le centre, seuls deux d'entre eux parviennent à cette région centrale, permettant une situation plus stable et une fusion ultérieure plus probable qui produit un trou noir plus massif que dans le scénario précédent. L'histoire des fusions de trous noirs étant modifiée par la possibilité de fusions décentrées, cela modifiera le taux d'émission d'ondes gravitationnelles à une fréquence donnée. Cela est particulièrement important car le futur détecteur d'ondes gravitationnelles, LISA (Laser Interferometer Space Antenna; Amaro-Seoane et al., 2017), offrira la possibilité de détecter des fusions de trous noirs plus massifs, tels que les trous noirs de masse intermédiaire.

Les galaxies naines étant le type de galaxie le plus courant dans l'Univers, les fusions décentrées pourraient avoir un impact majeur sur l'assemblage de la masse des

trous noirs et l'émission d'ondes gravitationnelles. De plus, les galaxies naines peuvent être accrétées par des galaxies plus massives, ce qui signifie que les événements qui se produisent dans ces systèmes auront des conséquences à long terme pour les galaxies plus massives.

7.3 Perspectives

7.3.1 Le rôle des forces dissipatives

Comme ce type de fusion peut avoir des implications majeures mais a été peu exploré dans la littérature, il est crucial d'améliorer nos simulations idéalisées. Tout d'abord, notre étude des captures gravitationnelles ne tient pas compte de la perte d'énergie des trous noirs due aux processus dissipatifs. Cette perte d'énergie provient principalement de trois sources :

1. En général, les trous noirs sont entourés de amas d'étoiles (Seth et al., 2008), et à mesure qu'ils se rapprochent, ils perdent de l'énergie en raison de la friction dynamique avec les amas environnants.

2. La binaire de trous noirs peut également interagir avec des étoiles proches, les éjectant par interaction à trois corps, ce qui resserre la binaire.

3. Les pertes d'énergie relativistes peuvent être significatives, notamment au péricentre dans les binaires très excentriques, ce qui est généralement le cas lors des captures, comme nous l'avons observé.

Bien que les captures gravitationnelles soient temporaires, il a été observé que les forces dissipatives jouent un rôle crucial dans le resserrement de la binaire (Fabian et al., 1975; Goldreich et al., 2002; Samsing et al., 2018b; Tagawa et al., 2018, 2020; Li et al., 2022; Boekholt et al., 2023; Rowan et al., 2023; DeLaurentiis et al., 2023). L'étape suivante consiste donc à déterminer si cette inclusion peut aider à maintenir nos captures gravitationnelles au fil du temps et à resserrer la binaire (comme on peut le voir dans le panneau de droite de la Fig. 6.1).

J'ai récemment commencé à explorer cette question. Pour ce faire, j'ai établi des conditions initiales présentant une capture gravitationnelle dans le cas idéalisé sans dissipation. J'ai ensuite remplacé les trous noirs individuels par des systèmes de trous noirs-amas d'étoiles, où les étoiles sont réparties selon un profil de King (King, 1966), en veillant à ce que la masse totale reste inchangée. Mes premiers tests avec Gyrfalcon, le code N-corps présenté au Chapitre 2, ont révélé que ce code, conçu pour des systèmes sans collisions, n'est pas bien adapté pour simuler les amas d'étoiles. Leur forte densité centrale nécessite une réduction drastique du pas de temps, ce qui entraîne des

temps d'intégration très longs. Par conséquent, j'ai récemment installé le code KETJU (Mannerkoski et al., 2023).

Ce code intègre plusieurs fonctionnalités cruciales : des interactions directes à proximité des trous noirs, des mécanismes de rétroaction, des corrections post-newtoniennes, et même un outil de prédiction des signaux d'ondes gravitationnelles. En plus de résoudre la dynamique des étoiles proches du centre des amas, ce code permettra également d'incorporer des corrections relativistes. L'objectif est maintenant d'explorer les questions suivantes : toutes les captures peuvent-elles être stabilisées, ou seulement celles présentant un nombre minimum de rencontres proches ? Comment la stabilité des captures est-elle influencée par le profil de densité des étoiles liées aux trous noirs ? De plus, la dissipation par interactions à trois corps est-elle efficace dans ce contexte ? Ces dissipations permettent-elles le passage au régime relativiste ?

7.3.2 Fusions d'amas globulaires

La plupart des amas globulaires présentent plusieurs populations stellaires, dont l'origine reste incertaine, résultant possiblement d'une formation secondaire d'étoiles. Cependant, ce mécanisme ne suffit pas à expliquer l'importante dispersion observée dans la teneur en fer. Bekki & Tsujimoto (2016) et Gavagnin et al. (2016) proposent une solution impliquant la fusion de deux amas globulaires ayant des temps de formation légèrement différents ($\sim$ 300 Myr). Selon leurs hypothèses, de telles fusions sont principalement réalisables au sein du halo ou du noyau des galaxies naines en raison de leur potentiel gravitationnel plus faible. Par la suite, ces galaxies naines, avec leurs amas globulaires intacts ou fusionnés, sont accrétées par la Voie lactée. Pour tester cette hypothèse, il est crucial d'examiner la probabilité de fusions entre amas globulaires dans les galaxies naines. Mes résultats sur les captures de Jacobi sont transférables à ce problème, car toute fusion en dehors du centre galactique, y compris pour les amas globulaires, commence par ce processus physique. Dans les cas où une capture se produit, on peut remplacer les trous noirs par un ensemble de N particules distribuées selon des profils de densité stellaire (King 1966 ou Varri & Bertin 2012) pour évaluer si les interactions entre populations stellaires, par le biais de simulations N-corps, peuvent conduire à la stabilisation de la capture et, par conséquent, à la fusion des amas globulaires.

7.3.3 Taux de capture pour la prédiction des ondes gravitationnelles

Jusqu'à présent, j'ai abordé les captures de Jacobi principalement sous un angle cinématique. Bien que cette approche aide à développer une compréhension intuitive du mouvement des trous noirs, elle nécessite certaines hypothèses liées aux orbites. Pour atteindre une plus grande généralité et tenir compte de la distribution des trous

noirs errants dans la galaxie, je propose d'adopter une approche statistique, en suivant Peñarrubia (2023). Cette nouvelle perspective consiste à traiter un trou noir décentré comme un point de référence, appelé RBH, et à évaluer la probabilité de ses interactions avec une population d'autres trous noirs décentrés au fur et à mesure de son déplacement dans la galaxie. Le processus se composera de deux étapes clés. Tout d'abord, j'utiliserai des simulations hydrodynamiques cosmologiques (dans le même esprit que ce qui a été fait dans Bellovary et al., 2019, 2021) pour obtenir un profil de densité des trous noirs errants $\rho(r)$. Ensuite, j'utiliserai ce profil pour calculer la fraction théorique de trous noirs décentrés ayant une énergie de liaison négative à l'intérieur de la sphère d'influence de RBH. À mesure que RBH se déplace dans la galaxie, j'estimerai le nombre de trous noirs entrant dans sa sphère d'influence pendant un intervalle de temps donné, en utilisant la statistique de Poisson. En combinant ces deux éléments, j'obtiendrai un taux de capture de trous noirs décentrés, un outil précieux à long terme pour faire des prédictions sur l'émission d'ondes gravitationnelles et la croissance de masse des trous noirs par le biais de fusions répétées hors du centre.

7.3.4 Influence de la réponse galactique sur les captures de Jacobi

Pour les captures simulées près du centre galactique, où la masse intégrée est comparable à celle des trous noirs, il est nécessaire de traiter la galaxie avec des particules vivantes. Il serait intéressant d'explorer l'effet de la réponse du coeur sur les captures de Jacobi. Pour ce faire, on pourrait sélectionner des conditions initiales qui présentent une capture et remplacer le potentiel externe par un halo vivant. Cette question est étroitement liée à l'étude du core stalling en présence de deux perturbateurs (dans ce cas, deux trous noirs). Il s'agit d'un problème non trivial, et l'impact de la présence d'un second trou noir sur le core stalling reste incertain.

Mon intuition initiale est que, dans le cas de deux trous noirs de masses similaires, $M_1 \simeq M_2$, la présence du second trou noir pourrait empêcher l'émergence des orbites responsables de la flottabilité dynamique et du core stalling. Cependant, si les trous noirs sont déphasés, positionnés de part et d'autre du centre galactique, un mode quadripolaire pourrait préserver la régularité nécessaire à l'émergence de telles orbites. Dans le scénario de deux trous noirs avec une hiérarchie de masses significative, $M_1 \gg M_2$, le trou noir plus léger pourrait être perçu comme une perturbation mineure, et le stalling pourrait persister. Dans ce cas, il serait intéressant d'étudier une situation où un trou noir massif (disons $M_1 \sim 10^6\, M_\odot$) stall tandis que plusieurs trous noirs moins massifs ($M_2 \sim 10^2 - 10^3\, M_\odot$) sont présents. Le trou noir massif à son rayon de core stalling pourrait capturer ces petits trous noirs, fusionner potentiellement avec eux, et ainsi augmenter sa masse. À mesure que sa masse augmente, il s'éloignerait du centre galactique car son rayon théorique de stalling est plus grand.

7.3.5 Structure fractale

Dans la Section 4.2, nous avons montré que les captures présentent un comportement chaotique par rapport aux quatre paramètres M_1, M_2, r_i, et Δr_i. Lorsqu'on trace le nombre de rencontres proches en fonction de l'un de ces paramètres, Δr_i par exemple, on obtient des irrégularités sous forme de pics, comme montré dans la Fig. 6.2. Dans le cas képlérien (avec une masse ponctuelle centrale à la place de la galaxie), il a été montré que ces pics d'irrégularités présentent une structure fractale auto-similaire qui peut être décrite par un ensemble de Cantor généralisé avec une dimension d'environ 0.4 (Boekholt et al., 2023). Il serait intéressant d'examiner si cette structure fractale persiste dans le cas d'un potentiel central étendu. Il serait également pertinent d'étudier comment la dimension fractale évolue en fonction des paramètres du potentiel, tels que la pente interne du profil de densité.

Appendices

Derivation of dynamical friction

A

In this section, we derive the analytical expression for dynamical friction. We consider a black hole with mass M navigating through a sea of stars with mass m. In subsection A.1, we first calculate the black hole's velocity perturbation caused by a single encounter with a star in the galaxy (based on the derivation provided in Binney & Tremaine, 2008). Then, in subsection A.2, we integrate over all the stars in the galaxy to calculate the total contribution from all encounters. Finally, in subsection A.3, we calculate the friction time, i.e. the time required for the black hole to fall to the center of a galaxy.

A.1 Single encounter

A.1.1 Equation of motion

We begin by considering the perturbation induced by a star of mass m when a black hole of mass M passes nearby. In the inertial frame of reference, let $(\mathbf{r}_M, \mathbf{v}_M)$ denote the position and velocity vectors of the black hole, and $(\mathbf{r}_m, \mathbf{v}_m)$ denote the position and velocity vectors of the star. To make the equations of motion more manageable, we switch to a coordinate system that uses the relative position and velocity between the two objects $(\mathbf{r}, \dot{\mathbf{r}} = \mathbf{v})$, along with the position and velocity of the center of mass $(\mathbf{R}, \dot{\mathbf{R}} = \mathbf{V})$ as shown in Fig. A.1.

So we have:

$$\begin{aligned} \mathbf{r} &= \mathbf{r}_m - \mathbf{r}_M, \qquad & \mathbf{R} &= M \cdot \mathbf{r}_M + m \cdot \mathbf{r}_m, \\ \dot{\mathbf{r}} &= \dot{\mathbf{r}}_m - \dot{\mathbf{r}}_M, \qquad & \dot{\mathbf{R}} &= M \cdot \dot{\mathbf{r}}_M + m \cdot \dot{\mathbf{r}}_m, \end{aligned} \tag{A.1}$$

and the relative positions in terms of the center of mass are:

$$\begin{aligned} \mathbf{r}'_M &= -\frac{m}{M+m}\mathbf{r} \\ \mathbf{r}'_m &= \frac{M}{M+m}\mathbf{r}. \end{aligned} \tag{A.2}$$

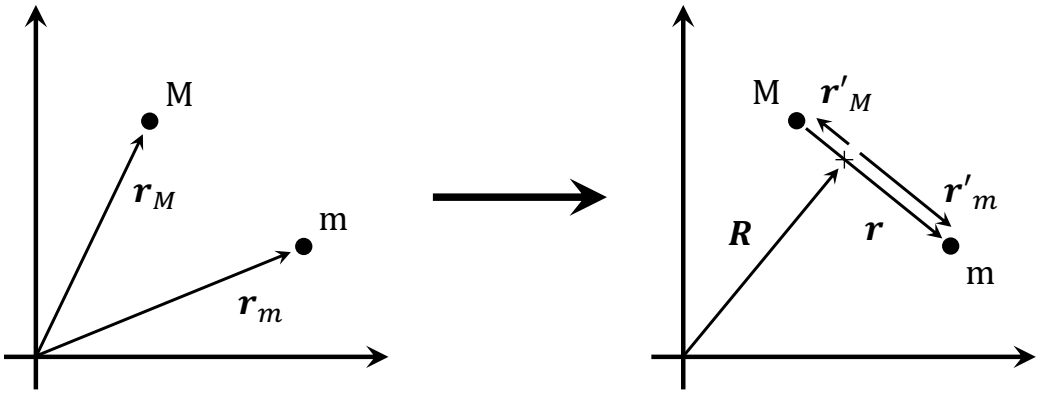

Figure A.1: Coordinate system change. On the left, the two objects are described in the inertial coordinate system. On the right, the center of mass position $\mathbf{R}$ and the relative position between the objects $\mathbf{r}$ are used.

The Lagrangian of the system is:

$$\mathcal{L} = \frac{1}{2} M \dot{\mathbf{r}}_M^2 + \frac{1}{2} m \dot{\mathbf{r}}_m^2 - \Phi(r) \quad \text{with} \quad \Phi(r) = -\frac{GMm}{r} \tag{A.3}$$

this becomes:

$$\begin{aligned}
\mathcal{L} &= \frac{1}{2}(M+m)\dot{\mathbf{R}}^2 + \frac{1}{2} M \dot{\mathbf{r}}_M'^2 + \frac{1}{2} m \dot{\mathbf{r}}_m'^2 - \Phi(r) \\
&= \frac{1}{2}(M+m)\dot{\mathbf{R}}^2 + \frac{1}{2} M \left(-\frac{m}{M+m}\dot{\mathbf{r}}\right)^2 + \frac{1}{2} m \left(\frac{M}{M+m}\dot{\mathbf{r}}\right)^2 - \Phi(r) \\
&= \frac{1}{2}(M+m)\dot{\mathbf{R}}^2 + \frac{1}{2}\frac{Mm}{M+m}\dot{\mathbf{r}}^2 - \Phi(r) \\
&= \frac{1}{2}(M+m)\dot{\mathbf{R}}^2 + \frac{1}{2}\mu\,\dot{\mathbf{r}}^2 - \Phi(r) \quad \text{with} \quad \mu = \frac{Mm}{M+m},
\end{aligned} \tag{A.4}$$

assuming the system is isolated, with no external forces acting on the masses, and using μ as the reduced mass. The Lagrange equation

$$\frac{d}{dt}\left(\frac{\partial \mathcal{L}}{\partial \dot{\mathbf{R}}}\right) - \frac{\partial \mathcal{L}}{\partial \mathbf{R}} = \mathbf{0} \tag{A.5}$$

becomes

$$\frac{d\,\dot{\mathbf{R}}}{dt} = \mathbf{0} \quad \Leftrightarrow \quad M\frac{d\,\dot{\mathbf{r}}_M}{dt} + m\frac{d\,\dot{\mathbf{r}}_m}{dt} = \mathbf{0} \tag{A.6}$$

which is the equation for the conservation of momentum. It can be rewritten as:

$$\begin{aligned}
&\frac{d\,\dot{\mathbf{r}}_M}{dt} = -\frac{m}{M}\frac{d\,\dot{\mathbf{r}}_m}{dt} = -\frac{m}{M}\frac{d}{dt}(\dot{\mathbf{r}} + \dot{\mathbf{r}}_M) \\
&\Leftrightarrow \quad \frac{M+m}{M}\frac{d\,\dot{\mathbf{r}}_M}{dt} = -\frac{m}{M}\frac{d\,\dot{\mathbf{r}}}{dt} \quad \Leftrightarrow \quad \boxed{\frac{d\,\dot{\mathbf{r}}_M}{dt} = -\frac{m}{M+m}\frac{d\,\dot{\mathbf{r}}}{dt}}.
\end{aligned} \tag{A.7}$$

We can now calculate the change in relative velocity caused by the encounter and determine the change in the black hole's velocity using equation (A.7). By applying the Lagrange equation to $\mathbf{r}$:

$$\frac{d}{dt}\left(\frac{\partial \mathcal{L}}{\partial \dot{\mathbf{r}}}\right) - \frac{\partial \mathcal{L}}{\partial \mathbf{r}} = \mathbf{0} \tag{A.8}$$

we have the equation of motion for a particle with mass μ orbiting at a distance r from a mass $M + m$:

$$\mu \ddot{\mathbf{r}} = -\frac{GMm}{r^2}\,\mathbf{e}_r. \tag{A.9}$$

It is more insightful to project the Lagrange equations onto polar coordinates $\mathbf{r} = (r, \psi)$:

$$\begin{aligned} \frac{d}{dt}\left(\frac{\partial \mathcal{L}}{\partial \dot{r}}\right) - \frac{\partial \mathcal{L}}{\partial r} &= 0 \\ \frac{d}{dt}\left(\frac{\partial \mathcal{L}}{\partial \dot{\psi}}\right) - \frac{\partial \mathcal{L}}{\partial \psi} &= 0. \end{aligned} \tag{A.10}$$

Using the Lagrangian [1] in polar coordinates

$$\mathcal{L} = \frac{1}{2}\mu\left[\dot{r}^2 + r^2\dot{\psi}^2\right] - \Phi(r) \tag{A.11}$$

the equation for ψ gives

$$\frac{d}{dt}\left(r^2\dot{\psi}\right) = 0 \quad \Leftrightarrow \quad \boxed{\frac{dL}{dt} = 0 \quad \text{with} \quad L = r^2\dot{\psi}} \tag{A.12}$$

where L is the angular momentum, a conserved quantity for central force problems. The equation for r is given by:

$$\begin{aligned} \mu\left(\ddot{r} - r\dot{\psi}^2\right) &= -\frac{d\Phi}{dr} \\ \Leftrightarrow \ddot{r} &= -\frac{1}{\mu}\frac{d\Phi}{dr} + \frac{L^2}{r^3}. \end{aligned} \tag{A.13}$$

Next, we note that

$$L = r^2\,\frac{d\psi}{dt} \quad \Leftrightarrow \quad \frac{d\psi}{dt} = \frac{L}{r^2} \tag{A.14}$$

thus:

$$\frac{d}{dt} = \frac{d}{d\psi}\frac{d\psi}{dt} = \frac{L}{r^2}\frac{d}{d\psi} \tag{A.15}$$

which gives:

$$\frac{dr}{dt} = \frac{L}{r^2}\frac{dr}{d\psi} \tag{A.16}$$

and thus:

$$\ddot{r} = \frac{d}{dt}\left(\frac{dr}{dt}\right) = \frac{L}{r^2}\frac{d}{d\psi}\left(\frac{L}{r^2}\frac{dr}{d\psi}\right) = \frac{L^2}{r^2}\frac{d}{d\psi}\left(\frac{1}{r^2}\frac{dr}{d\psi}\right). \tag{A.17}$$

[1] We have omitted the part involving $\mathbf{R}$ as it does not contribute.

Equation (A.13) becomes:

$$\begin{aligned} &\frac{L^2}{r^2}\frac{d}{d\psi}\left(\frac{1}{r^2}\frac{dr}{d\psi}\right) - \frac{L^2}{r^3} = -\frac{1}{\mu}\frac{d\Phi}{dr} \\ \Leftrightarrow \quad &\frac{d}{d\psi}\left(\frac{1}{r^2}\frac{dr}{d\psi}\right) - \frac{1}{r} = -\frac{r^2}{\mu L^2}\frac{d\Phi}{dr}. \end{aligned} \tag{A.18}$$

If we now set $u = 1/r$, the first term becomes:

$$\frac{d}{d\psi}\left[u^2\frac{d}{d\psi}\left(\frac{1}{u}\right)\right] = -\frac{d}{d\psi}\left(\frac{du}{d\psi}\right) = -\frac{d^2u}{d\psi^2} \tag{A.19}$$

and the equation simplifies to:

$$\frac{d^2u}{d\psi^2} + u = \frac{1}{\mu L^2 u^2}\frac{d\Phi(1/u)}{dr}. \tag{A.20}$$

For a Keplerian potential:

$$\Phi = -\frac{GMm}{r} \quad \text{hence} \quad \frac{d\Phi}{dr} = \frac{GMm}{r^2} = GMmu^2. \tag{A.21}$$

The equation becomes:

$$\frac{d^2u}{d\psi^2} + u = \frac{G(M+m)}{L^2} \tag{A.22}$$

which has the following solution:

$$\boxed{u(\psi) = \mathrm{C}\,\cos(\psi - \psi_0) + \frac{G(M+m)}{L^2}} \tag{A.23}$$

where C and ψ_0 are determined by the initial conditions.

A.1.2 Velocity perturbation

With this information, we are now equipped to determine the velocity perturbation resulting from a hyperbolic encounter.

Let $\mathbf{v}_0 = \mathbf{v}(t \to -\infty)$ be the initial relative velocity vector and b the impact parameter (see Fig. A.2). We then have [2]

$$L = b\,v_0 \tag{A.24}$$

and according to Eq. (A.23),

$$\frac{1}{r} = \mathrm{C}\,\cos(\psi - \psi_0) + \frac{G(M+m)}{b^2\,v_0^2}. \tag{A.25}$$

[2] The cross product eliminates the component of the position vector parallel to $\mathbf{v}_0$, leaving only the perpendicular component b.

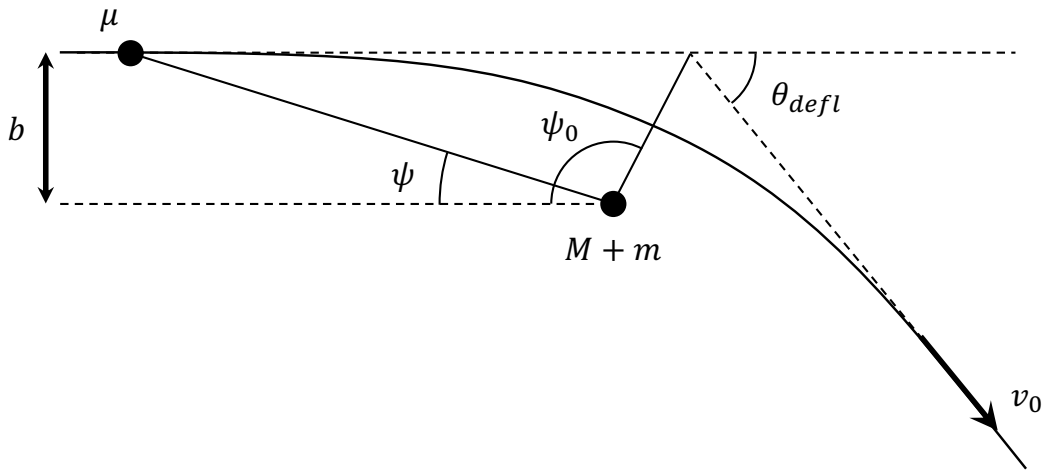

Figure A.2: Trajectory of a reduced mass throughout a hyperbolic encounter.

Now, let's take the derivative of equation (A.25):

$$\begin{aligned} &\frac{d}{dt}\left(\frac{1}{r}\right) = -\mathrm{C}\,\sin(\psi-\psi_0)\,\dot{\psi} \\ \Leftrightarrow \quad &\dot{r} = \mathrm{C}\,\underbrace{r^2\dot{\psi}}_{L=\mathrm{Cst}}\,\sin(\psi-\psi_0) = \mathrm{C}\,b\,v_0\sin(\psi-\psi_0). \end{aligned} \tag{A.26}$$

Defining the direction $\psi = 0$ to point towards μ as t approaches negative infinity, we evaluate equation (A.26) at $t \to -\infty$. We can replace $\dot{r}(t \to -\infty) \to -v_0$ and $\psi(t \to -\infty) \to 0$ and we obtain:

$$-v_0 = \mathrm{C}\,b\,v_0\sin(-\psi_0) \quad \Leftrightarrow \quad \mathrm{C} = -\frac{1}{b\,\sin(-\psi_0)}. \tag{A.27}$$

If we now evaluate equation (A.25) at $t \to -\infty$, we obtain:

$$0 = \mathrm{C}\cos(-\psi_0) + \frac{G(M+m)}{b^2\,v_0^2} \tag{A.28}$$

by substituting C, we get:

$$\tan(\psi_0) = -\frac{b\,v_0^2}{G(M+m)}. \tag{A.29}$$

Noting from (A.25) and (A.26) that $\psi = \psi_0$ corresponds to the closest approach, making the orbit symmetric about this angle, the deflection angle is [3]

$$\theta_{\mathrm{defl}} = 2\,\psi_0 - \pi. \tag{A.30}$$

We can now calculate the velocity deviations caused by the encounter:

$$|\Delta v_\perp| = v_0\,\sin(\theta_{\mathrm{defl}}) = v_0\,\sin(2\,\psi_0 - \pi) = -v_0\,\sin(2\,\psi_0) \tag{A.31}$$

[3] To convince oneself, consider the case of an almost negligible deflection, which would give $\theta_{\mathrm{defl}} \sim 0$ and $2\,\psi_0 \sim \pi$.

bearing in mind that [4]

$$\sin(2x) = 2\,\sin(x)\,\cos(x) = \frac{2\,\tan(x)}{1+\tan^2(x)} \tag{A.32}$$

we get

$$\sin(\theta_{\rm defl}) = -\sin(2\,\psi_0) = -\frac{2\,\tan(\psi_0)}{1+\tan^2(\psi_0)}. \tag{A.33}$$

If $\psi_0 = \pi$ i.e. $\theta_{\rm defl} = \pi$:

$$\tan(\psi_0) = 0 \quad \Leftrightarrow \quad b = \boxed{\frac{G(M+m)}{v_0^2} \equiv b_{90}} \tag{A.34}$$

this gives

$$\tan(\psi_0) = -\frac{b}{b_{90}} \tag{A.35}$$

and finally

$$\boxed{|\Delta v_\perp| = \frac{2\,v_0\,(b/b_{90})}{1+b^2/b_{90}^2}}. \tag{A.36}$$

On the other hand,

$$|\Delta v_\parallel| = v_0\,[1-\cos(\theta_{\rm defl})] = v_0\,[1+\cos(2\,\psi_0)] \tag{A.37}$$

using the fact that

$$\begin{aligned} &\tan^2(x) = \frac{1-\cos(2x)}{1+\cos(2x)} \\ \Leftrightarrow\ &\tan^2(x) + \cos(2x)\tan^2(x) = 1-\cos(2x) \\ \Leftrightarrow\ &\tan^2(x) - 1 = -\cos(2x)\left[\tan^2(x)+1\right] \\ \Leftrightarrow\ &\cos(2x) = -\frac{\tan^2(x)-1}{\tan^2(x)+1} \end{aligned} \tag{A.38}$$

we finally get for the parallel perturbation:

$$|\Delta v_\parallel| = v_0\left[1-\frac{\tan^2(x)-1}{\tan^2(x)+1}\right] = 2\,v_0\left[\tan^2(x)+1\right]^{-1} \tag{A.39}$$

or

$$\boxed{|\Delta v_\parallel| = \frac{2\,v_0}{1+b^2/b_{90}^2}}. \tag{A.40}$$

Finally, converting back to the original coordinate system using equation (A.7), we get:

$$\boxed{\begin{aligned} |\Delta v_{M\perp}| &= \frac{2\,m\,v_0}{M+m}\,\frac{b/b_{90}}{1+b^2/b_{90}^2} \qquad (A.41)\\ |\Delta v_{M\parallel}| &= \frac{2\,m\,v_0}{M+m}\,\frac{1}{1+b^2/b_{90}^2} \qquad (A.42) \end{aligned}}$$

These are the parallel and perpendicular velocity perturbations caused by an encounter (b, v_0) on the black hole of mass M by a star of mass m.

[4] $\sin(a)\,\cos(b) = \frac{1}{2}\,[\sin(a+b)+\sin(a-b)]$

A.2 Sea of stars

We now need to integrate over the impact parameters (b) and velocities (v_0) to obtain the total perturbation caused by a galaxy. The sum of the perpendicular perturbations ($\Delta v_{M\perp}$) is zero because encounters are stochastic processes, resulting in equal perturbations in both directions. However, the mean squared perturbation is not zero:

$$\langle \Delta v_{M\perp}^2 \rangle = \int_{6D} |\Delta v_{M\perp}|^2 \, f(\mathbf{x},\mathbf{v}) d^3x \, d^3v \tag{A.43}$$

This calculation provides a more precise analog to equation (1.8) that can be used to calculate the relaxation time more accurately.

The tangential velocity perturbations do not cancel out, and we can calculate the acceleration produced on the black hole by the cumulative encounters:

$$\frac{d\mathbf{v}_M}{dt} = \int_{5D} |\Delta v_{M\parallel}| \, f(\mathbf{x},\mathbf{v}_m) \, \mathbf{v}_0 \, d^2x \, d^3v_m \tag{A.44}$$

where $f(\mathbf{x},\mathbf{v}_m)\,\mathbf{v}_0\,d^2x\,d^3v_m$ is an encounter rate because the left-hand side represents a change in velocity. If we make the following assumptions:

- **Assumption 1:** The medium is homogeneous [5] .
- **Assumption 2:** The velocities are Maxwellian distributed [6] .

We have

$$f(\mathbf{x},\mathbf{v}_m) = \frac{n_0}{(2\pi\sigma^2)^{3/2}} \exp\left(-\frac{v_m^2}{2\sigma^2}\right) = f(\mathbf{v}_m) \quad \text{with} \quad n_0 = \frac{\rho_0}{m} \tag{A.45}$$

where σ is the velocity dispersion, n_0 is the number density and ρ_0 is the density of stars (assumed homogeneous). Thanks to these two assumptions, we can rewrite equation (A.44):

$$\frac{d\mathbf{v}_M}{dt} = \int_{5D} |\Delta v_{M\parallel}| \, f(\mathbf{v}_m) \, \mathbf{v}_0 \, 2\pi \, b \, db \, d^3v_m. \tag{A.46}$$

First, we integrate over the impact parameters to obtain $\frac{d\mathbf{v}_M}{dt}\Big|_{\mathbf{v}_m}$ and then we integrate over the velocities $\frac{d\mathbf{v}_M}{dt} = \int_{\mathbf{v}_m} \frac{d\mathbf{v}_M}{dt}\Big|_{\mathbf{v}_m}$.

[5] Implications of homogeneity:

- $f(\mathbf{x},\mathbf{v}) = n_0\, f(\mathbf{v})$ where n_0 and ρ_0 are constants.

[6] Implications of velocity distribution:

- $f(\mathbf{v}) = \frac{1}{(2\pi\sigma^2)^{3/2}} \exp\left(-\frac{v^2}{2\sigma^2}\right) = \prod_{i=1}^{3} \frac{1}{(2\pi\sigma^2)^{1/2}} \exp\left(-\frac{v_i^2}{2\sigma^2}\right) = \prod_{i=1}^{3} f(v_i)$
- $f_x(v_x) = f_y(v_y) = f_z(v_z) = f(v_i)\,\forall\, i$
- $\langle \mathbf{v} \rangle = \int \mathbf{v} f(\mathbf{v}) d\mathbf{v} = \mathbf{0} \quad \Rightarrow \quad \sigma = \sqrt{\langle v^2 \rangle - \langle v \rangle^2} = \sqrt{\langle v^2 \rangle}$
- $f_n(v) = 4\pi\, v^2 f(v)$, with $f_n(v)$ the probability density of the velocity norm and $f(\mathbf{v}) = f(v)$ the probability density of having a velocity vector, dependent only on the norm. We could write $f(\mathbf{v}_m) = f(v_m)$ but we keep the vector notation to avoid confusion with $f_n(v_m)$ the probability density of the velocity norm.

A.2.1 Integration over Impact Parameters

We have:

$$\left.\frac{d\mathbf{v}_M}{dt}\right|_{\mathbf{v}_m} = \frac{4\pi\, m\, v_0}{M+m}\, f(\mathbf{v}_m)\, \mathbf{v}_0\, d^3v_m \underbrace{\int_0^{b_{\max}} \left[1 + \frac{b^2 v_0^4}{G^2(M+m)^2}\right]^{-1} b\, db.}_{\text{Int.I}} \tag{A.47}$$

We set:

$$x = \frac{b^2 v_0^4}{G^2(M+m)^2} \;\Rightarrow\; b = \frac{G(M+m)}{v_0^2} x^{1/2} \;\Rightarrow\; db = \frac{G(M+m)}{2\, v_0^2} x^{-1/2}\, dx \tag{A.48}$$

and we recall that:

$$b_{90} \equiv \frac{G(M+m)}{v_0^2} \;\Rightarrow\; x = \frac{b^2}{b_{90}^2}, \tag{A.49}$$

The minimum and maximum integration bounds become 0 and $b_{\max}^2/b_{90}^2$, respectively. We denote:

$$\boxed{\Lambda \equiv \frac{b_{\max}}{b_{90}} = \frac{b_{\max}\, v_0^2}{G(M+m)}} \tag{A.50}$$

and (Int.I) becomes

$$\begin{aligned} \text{Int.I} &= \int_0^{\Lambda^2} [1+x]^{-1} \cdot \frac{G(M+m)}{v_0^2} x^{1/2} \cdot \frac{G(M+m)}{2\, v_0^2} x^{-1/2}\, dx \\ &= \frac{G^2(M+m)^2}{2\, v_0^4} \int_0^{\Lambda^2} [1+x]^{-1}\, dx \\ &= \frac{G^2(M+m)^2}{2\, v_0^4} \left[\ln(1+b)\right]_0^{\Lambda^2} \\ &= \frac{G^2(M+m)^2}{2\, v_0^4} \ln\left(1+\Lambda^2\right) \end{aligned} \tag{A.51}$$

Thus, equation (A.47) becomes:

$$\begin{aligned} \left.\frac{d\mathbf{v}_M}{dt}\right|_{\mathbf{v}_m} &= \frac{4\pi\, m\, v_0}{M+m}\, f(\mathbf{v}_m)\, \mathbf{v}_0\, d^3v_m \times \text{Int.I} \\ &= \frac{4\pi\, m\, v_0}{M+m}\, f(\mathbf{v}_m)\, \mathbf{v}_0\, d^3v_m\, \frac{G^2(M+m)^2}{2\, v_0^4} \ln\left(1+\Lambda^2\right) \\ &= 2\pi G^2 m(M+m) \ln\left(1+\Lambda^2\right) f(\mathbf{v}_m)\, \frac{\mathbf{v}_0}{v_0^3}\, d^3v_m \end{aligned} \tag{A.52}$$

A.2.2 Integration over Velocities

Now, we will integrate $\left.\frac{d\mathbf{v}_M}{dt}\right|_{\mathbf{v}_m}$ over the velocities. First, we need to express $\mathbf{v}_0$ in terms of $\mathbf{v}_M$ and $\mathbf{v}_m$.

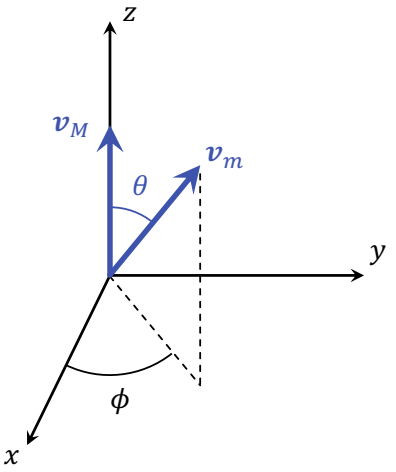

Figure A.3: Coordinate system for velocity vectors.

$$\mathbf{v}_M = v_M \begin{pmatrix} 0 \\ 0 \\ 1 \end{pmatrix}, \ \mathbf{v}_m = v_m \begin{pmatrix} \sin\theta\cos\phi \\ \sin\theta\sin\phi \\ \cos\theta \end{pmatrix}, \ \mathbf{v}_0 = \mathbf{v}_m - \mathbf{v}_M = \begin{pmatrix} v_m \sin\theta\cos\phi \\ v_m \sin\theta\sin\phi \\ v_m\cos\theta - v_M \end{pmatrix}$$

Thus,

$$\begin{aligned} |\mathbf{v}_m - \mathbf{v}_M| &= \sqrt{v_m^2\sin^2\theta\cos^2\phi + v_m^2\sin^2\theta\sin^2\phi + v_m^2\cos^2\theta + v_M^2 - 2v_m v_M\cos\theta} \\ &= \sqrt{v_m^2 + v_M^2 - 2v_m v_M\cos\theta} \\ &= v_M\left(1 + \frac{v_m^2}{v_M^2} - 2\frac{v_m}{v_M}\cos\theta\right)^{1/2}. \end{aligned} \tag{A.53}$$

We can now integrate over the velocities:

$$\begin{aligned} \frac{d\mathbf{v}_M}{dt} &= \int_{\mathbf{v}_m} \left.\frac{d\mathbf{v}_M}{dt}\right|_{\mathbf{v}_m} \\ &= \underbrace{2\pi G^2 m(M+m)\ln\left(1+\Lambda^2\right)}_{\chi} \iiint f(\mathbf{v}_m)\,\frac{\mathbf{v}_m - \mathbf{v}_M}{|\mathbf{v}_m - \mathbf{v}_M|^3}\,d^3v_m \\ &= \chi\cdot\iiint \frac{f(\mathbf{v}_m)}{v_M^3\left(1 + \frac{v_m^2}{v_M^2} - 2\frac{v_m}{v_M}\cos\theta\right)^{3/2}} \begin{pmatrix} v_m\sin\theta\cos\phi \\ v_m\sin\theta\sin\phi \\ v_m\cos\theta - v_M \end{pmatrix} v_m^2\,\sin\theta\,dv_m\,d\theta\,d\phi \end{aligned} \tag{A.54}$$

along the x-axis, the integral gives:

$$\iiint \frac{v_m^3\sin^2\theta\cos\phi\,f(\mathbf{v}_m)}{v_M^3\left(1 + \frac{v_m^2}{v_M^2} - 2\frac{v_m}{v_M}\cos\theta\right)^{3/2}}\,dv_m\,d\theta\,d\phi = 0 \quad \text{because} \quad \int_0^{2\pi}\cos\phi\,d\phi = 0 \tag{A.55}$$

similarly, along the y-axis:

$$\iiint \frac{v_m^3 \sin^2\theta \sin\phi\, f(\mathbf{v}_m)}{v_M^3 \left(1+\frac{v_m^2}{v_M^2}-2\frac{v_m}{v_M}\cos\theta\right)^{3/2}} dv_m\, d\theta\, d\phi = 0 \quad \text{because} \quad \int_0^{2\pi} \sin\phi\, d\phi = 0 \tag{A.56}$$

along the z-axis, we have:

$$\begin{aligned} &\iiint \frac{v_m^2 \sin\theta\, f(\mathbf{v}_m)}{v_M^3 \left(1+\frac{v_m^2}{v_M^2}-2\frac{v_m}{v_M}\cos\theta\right)^{3/2}} (v_m\cos\theta - v_M)\, dv_m\, d\theta\, d\phi \\ = \;& \frac{2\pi}{v_M^3} \iint \frac{v_m^2 \sin\theta\, f(\mathbf{v}_m)}{\left(1+\frac{v_m^2}{v_M^2}-2\frac{v_m}{v_M}\cos\theta\right)^{3/2}} (v_m\cos\theta - v_M)\, d\theta\, dv_m. \end{aligned} \tag{A.57}$$

We make a change of variable $t = \cos\theta \;\Rightarrow\; d\theta = -dt/\sin\theta$, the integral becomes:

$$\begin{aligned} &\int_0^{\pi} \frac{v_m^2 \sin\theta\, f(\mathbf{v}_m)}{\left(1+\frac{v_m^2}{v_M^2}-2\frac{v_m}{v_M}\cos\theta\right)^{3/2}} (v_m\cos\theta - v_M)\, d\theta \\ = \;& \int_{-1}^{1} \frac{v_m^2\, f(\mathbf{v}_m)}{\left(1+\frac{v_m^2}{v_M^2}-2\frac{v_m}{v_M}t\right)^{3/2}} (v_m t - v_M)\, dt \\ = \;& v_m^2\, f(\mathbf{v}_m) \left[\frac{v_m - v_M}{\sqrt{\frac{(v_m-v_M)^2}{v_M^2}}} - \frac{v_m + v_M}{\sqrt{\frac{(v_m+v_M)^2}{v_M^2}}}\right] \\ = \;& v_m^2\, f(\mathbf{v}_m) \left[|v_M|\frac{v_m - v_M}{|v_m - v_M|} - |v_M|\frac{v_m + v_M}{|v_m + v_M|}\right] \\ = \;& \begin{cases} -2\, v_m^2\, v_M\, f(\mathbf{v}_m) & \text{if } v_M > v_m, \\ 0 & \text{if } v_M < v_m. \end{cases} \end{aligned} \tag{A.58}$$

Thus, equation (A.54) becomes:

$$\begin{aligned} \frac{d\mathbf{v}_M}{dt} &= -8\pi^2 G^2 m(M+m) \ln\Big(1+\Lambda^2\Big) \frac{\mathbf{v}_M}{v_M^3} \int_0^{v_M} v_m^2\, f(\mathbf{v}_m) dv_m \\ &= -8\pi^2 G^2 m(M+m) \ln\Big(1+\Lambda^2\Big) \frac{\mathbf{v}_M}{v_M^3} \times \frac{n_0}{(2\pi\sigma^2)^{3/2}} \underbrace{\int_0^{v_M} v_m^2 \exp\left(-\frac{v_m^2}{2\sigma^2}\right) dv_m}_{\text{Int.II}}. \end{aligned} \tag{A.59}$$

It remains to calculate (Int.II). To do this, we integrate by parts: $\int u'v = [uv] - \int uv'$, with

- $u' = v_m \exp\left(-\frac{v_m^2}{2\sigma^2}\right) \Rightarrow u = \int v_m \exp\left(-\frac{v_m^2}{2\sigma^2}\right) dv_m$
$= -\sigma^2 \int \frac{d\exp\left(-\frac{v_m^2}{2\sigma^2}\right)}{dv_m} dv_m$
$= -\sigma^2 \exp\left(-\frac{v_m^2}{2\sigma^2}\right)$
- $v = v_m \Rightarrow v' = 1$

thus

$$\begin{aligned}\text{Int.II} &= \left[-\sigma^2 v_m \exp\left(-\frac{v_m^2}{2\sigma^2}\right)\right]_0^{v_M} + \int_0^{v_M} \sigma^2 \exp\left(-\frac{v_m^2}{2\sigma^2}\right) dv_m \\ &= -\sigma^2 v_M \exp\left(-\frac{v_M^2}{2\sigma^2}\right) + \underbrace{\sigma^2 \int_0^{v_M} \exp\left(-\frac{v_m^2}{2\sigma^2}\right) dv_m}_{\text{Int.III}}.\end{aligned} \tag{A.60}$$

To calculate (Int.III), we change variables: $t = \frac{v_m}{\sqrt{2}\sigma} \Rightarrow dv_m = \sqrt{2}\,\sigma\, dt$. The integral becomes:

$$\text{Int.III} = \sqrt{2}\,\sigma^3 \int_0^X \exp\left(-t^2\right) dt \equiv \sqrt{\frac{\pi}{2}}\,\sigma^3 \,\text{erf}(X) \quad \text{with} \quad \boxed{X \equiv \frac{v_M}{\sqrt{2}\,\sigma}} \tag{A.61}$$

and with $\text{erf}(x) = \frac{2}{\sqrt{\pi}} \int_0^x \exp(-t^2)\, dt$. Thus, we have:

$$\text{Int.II} = \int_0^{v_M} v_m^2 \exp\left(-\frac{v_m^2}{2\sigma^2}\right) dv_m = -\sqrt{2}\,\sigma^3\, X \exp\left(-X^2\right) + \sqrt{\frac{\pi}{2}}\,\sigma^3 \,\text{erf}(X). \tag{A.62}$$

Finally, we obtain:

$$\begin{aligned}\frac{d\mathbf{v}_M}{dt} &= -8\pi^2 G^2 m(M+m) \ln\left(1+\Lambda^2\right) \frac{\mathbf{v}_M}{v_M^3} \times \frac{n_0}{(2\pi\sigma^2)^{3/2}} \int_0^{v_M} v_m^2 \exp\left(-\frac{v_m^2}{2\sigma^2}\right) dv_m \\ &= -8\pi^2 G^2 m(M+m) \ln\left(1+\Lambda^2\right) \frac{n_0}{4\pi} \left[-\frac{2X}{\sqrt{\pi}} \exp\left(-X^2\right) + \text{erf}(X)\right] \frac{\mathbf{v}_M}{v_M^3}\end{aligned}$$

$$\boxed{\frac{d\mathbf{v}_M}{dt} = -2\pi\, G^2\, \rho_0\, (M+m) \ln\left(1+\Lambda^2\right) \left[-\frac{2X}{\sqrt{\pi}} \exp\left(-X^2\right) + \text{erf}(X)\right] \frac{\mathbf{v}_M}{v_M^3}} \tag{A.63}$$

This expression can be simplified by using two approximations:

- **Assumption 3:** $\Lambda \gg 1$, which is typically the case in our context [7] .

[7] We have: $\ln\left(1+\Lambda^2\right) = \ln\left(\Lambda^2[\frac{1}{\Lambda^2}+1]\right) = \ln\left(\Lambda^2\right) + \ln\left(1+\frac{1}{\Lambda^2}\right)$ and if $\Lambda \gg 1$ we can approximate: $\ln\left(\Lambda^2\right) + \ln\left(1+\frac{1}{\Lambda^2}\right) \simeq \ln\left(\Lambda^2\right) = 2\ln(\Lambda)$.

- **Assumption 4:** $M \gg m$, which is justified when studying the motion of an IMBH or SMBH ($M > 10^2\,M_\odot$) within a population of stars ($m \sim 1 - 10\,M_\odot$).

This gives

$$\boxed{\frac{d\mathbf{v}_M}{dt} = -4\pi\,G^2\,\rho_0\,M\ln(\Lambda)\,\left[-\frac{2X}{\sqrt{\pi}}\,\exp\Big(-X^2\Big) + \mathrm{erf}(X)\right]\,\frac{\mathbf{v}_M}{v_M^3}.} \tag{A.64}$$

From equations (A.63) or (A.64), we see that this force acting on the moving black hole in a sea of stars is collinear with and opposite to its velocity vector. Thus, it is a force that acts "against" the black hole, causing it to lose energy and angular momentum during its motion.

A.3 Friction time

Due to this frictional force, the black hole loses angular momentum and spirals towards the center of the galaxy. We can calculate the time required for a black hole initially positioned at a radius r_i to spiral to the center. Starting from:

$$\frac{d\mathbf{L}}{dt} = \frac{d(\mathbf{r}\times\mathbf{v})}{dt} = \frac{d\mathbf{r}}{dt}\times\mathbf{v} + \mathbf{r}\times\frac{d\mathbf{v}}{dt} = \mathbf{r}\times\frac{d\mathbf{v}}{dt} \tag{A.65}$$

with $\mathbf{L}$ as the angular momentum per unit mass of the black hole, and assuming:

- **Assumption 5:** The black hole is on a circular orbit [8] .

we can write on the one hand:

$$\frac{dL}{dt} = \frac{F}{M}\times r \tag{A.66}$$

[8] The only force not collinear with $\mathbf{r}$ is the frictional force, which is collinear with the velocity vector, itself perpendicular to the position vector during circular motion. In this context, we also have $L = r\,v_\mathrm{c}$ with v_c being the circular velocity.

with $F = M \times \frac{d\mathbf{v}_M}{dt}$ being the dynamical friction force. And on the other hand:

$$\begin{aligned}
\frac{dL}{dt} &= \frac{d(r\,v_\mathrm{c})}{dt} \\
&= r\frac{dv_\mathrm{c}(r)}{dt} + v_\mathrm{c}(r)\frac{dr}{dt} \\
&= r\frac{dv_\mathrm{c}(r)}{dr}\,\frac{dr}{dt} + v_\mathrm{c}(r)\frac{dr}{dt} \\
&= r\frac{d}{dr}\left(\frac{G\,M_\mathrm{tot}(r)}{r}\right)^{1/2}\,\frac{dr}{dt} + v_\mathrm{c}(r)\frac{dr}{dt} \\
&= \frac{dr}{dt}\left(r\frac{d}{dr}\left(\frac{G\,M_\mathrm{tot}(r)}{r}\right)^{1/2} + v_\mathrm{c}(r)\right) \\
&= \frac{dr}{dt}\left(\frac{r}{2}\left(\frac{GM_\mathrm{tot}(r)}{r}\right)^{-1/2}\,\frac{d}{dr}\left(\frac{G\,M_\mathrm{tot}(r)}{r}\right) + v_\mathrm{c}(r)\right) \\
&= \frac{dr}{dt}\left(\frac{Gr}{2}\left(\frac{r}{GM_\mathrm{tot}(r)}\right)^{1/2}\,\frac{d}{dr}\left(\frac{M_\mathrm{tot}(r)}{r}\right) + v_\mathrm{c}(r)\right) \\
&= \frac{dr}{dt}\left(\frac{G}{2r}\left(\frac{r}{GM_\mathrm{tot}(r)}\right)^{1/2}\left[r\frac{dM_\mathrm{tot}(r)}{dr} - M_\mathrm{tot}(r)\right] + v_\mathrm{c}(r)\right) \\
&= \frac{dr}{dt}\left(\frac{G}{2r\,v_\mathrm{c}(r)}\left[r\frac{dM_\mathrm{tot}(r)}{dr} - M_\mathrm{tot}(r)\right] + v_\mathrm{c}(r)\right)
\end{aligned} \tag{A.67}$$

where we used $v_\mathrm{c}(r) = \left(\frac{G\,M_\mathrm{tot}(r)}{r}\right)^{1/2}$ with $M_\mathrm{tot}(r)$ being the total mass (including all components) enclosed within the galaxy at radius r.

For a spherical matter distribution:

- **Assumption 6:** Spherically symmetric matter distribution.

then

$$\frac{dM_\mathrm{tot}(r)}{dr} = 4\pi\,r^2\,\rho_\mathrm{tot}(r) \tag{A.68}$$

and equation (A.67) becomes:

$$\frac{dL}{dt} = \frac{dr}{dt}\left(\frac{G}{2r\,v_\mathrm{c}(r)}\left[4\pi\,r^3\,\rho_\mathrm{tot}(r) - M_\mathrm{tot}(r)\right] + v_\mathrm{c}(r)\right). \tag{A.69}$$

By equating (A.66) and (A.69), we obtain:

$$\begin{aligned}
&\frac{F}{M}\times r = \frac{dr}{dt}\left(\frac{G}{2r\,v_\mathrm{c}(r)}\left[4\pi\,r^3\,\rho_\mathrm{tot}(r) - M_\mathrm{tot}(r)\right] + v_\mathrm{c}(r)\right) \\
\Leftrightarrow\quad &dt = \left(\frac{G}{2r\,v_\mathrm{c}(r)}\left[4\pi\,r^3\,\rho_\mathrm{tot}(r) - M_\mathrm{tot}(r)\right] + v_\mathrm{c}(r)\right)\frac{M}{r\times F}\,dr \\
\Leftrightarrow\quad &dt = -\frac{v_\mathrm{c}^2(r)\left(\frac{G}{2r\,v_\mathrm{c}(r)}\left[4\pi\,r^3\,\rho_\mathrm{tot}(r) - M_\mathrm{tot}(r)\right] + v_\mathrm{c}(r)\right)}{2\pi\,G^2\,\rho_0\,(M+m)\ln(1+\Lambda^2)\,\left[-\frac{2X}{\sqrt{\pi}}\,\exp(-X^2) + \mathrm{erf}(X)\right]\,r}\,dr
\end{aligned} \tag{A.70}$$

where we replaced v_M with v_c. We then have:

$$\boxed{t_\mathrm{fric} = -\int_0^{r_\mathrm{i}} \mathcal{I}(r)\, dr} \tag{A.71}$$

with

$$\boxed{\mathcal{I}(r) = -\frac{v_\mathrm{c}^2(r)\left(\frac{G}{2r\,v_\mathrm{c}(r)}\left[4\pi\, r^3\,\rho_\mathrm{tot}(r) - M_\mathrm{tot}(r)\right] + v_\mathrm{c}(r)\right)}{2\pi\, G^2\,\rho_0\,(M+m)\ln(1+\Lambda^2)\,\left[-\frac{2X}{\sqrt{\pi}}\,\exp(-X^2) + \mathrm{erf}(X)\right]\,r}} \tag{A.72}$$

or if we use expression (A.64):

$$\boxed{\mathcal{I}(r) = -\frac{v_\mathrm{c}^2(r)\left(\frac{G}{2r\,v_\mathrm{c}(r)}\left[4\pi\, r^3\,\rho_\mathrm{tot}(r) - M_\mathrm{tot}(r)\right] + v_\mathrm{c}(r)\right)}{4\pi\, G^2\,\rho_0\, M\ln(\Lambda)\,\left[-\frac{2X}{\sqrt{\pi}}\,\exp(-X^2) + \mathrm{erf}(X)\right]\,r}} \tag{A.73}$$

Jeans equation and dispersion

B

B.1 Derivation of the spherical Jeans equation

First, let's simplify the Jeans equation in spherical coordinates:

$$\frac{\partial f}{\partial t} + p_r \frac{\partial f}{\partial r} + \frac{p_\theta}{r^2}\frac{\partial f}{\partial \theta} + \frac{p_\phi}{r^2 \sin^2\theta}\frac{\partial f}{\partial \phi} - \left(\frac{\partial \Phi}{\partial r} - \frac{p_\theta^2}{r^3} - \frac{p_\phi^2}{r^3 \sin^2\theta}\right)\frac{\partial f}{\partial p_r} - \left(\frac{\partial \Phi}{\partial \theta} - \frac{p_\phi^2 \cos\theta}{r^2 \sin^3\theta}\right)\frac{\partial f}{\partial p_\theta} - \frac{\partial \Phi}{\partial \phi}\frac{\partial f}{\partial p_\phi} = 0.$$

by assuming that the system is spherically symmetric and time-independent, which allows us to ignore the terms $\partial\Phi/\partial\theta$, $\partial\Phi/\partial\phi$, $\partial f/\partial t$ and $\partial f/\partial\phi$. However, we retain the term $\partial f/\partial\theta$, as the dependence of f on v_ϕ will introduce terms that depend on θ [1] . After these simplifications, the equation becomes:

$$p_r \frac{\partial f}{\partial r} + \frac{p_\theta}{r^2}\frac{\partial f}{\partial \theta} - \left(\frac{\mathrm{d}\Phi}{\mathrm{d}r} - \frac{p_\theta^2}{r^3} - \frac{p_\phi^2}{r^3 \sin^2\theta}\right)\frac{\partial f}{\partial p_r} + \frac{p_\phi^2 \cos\theta}{r^2 \sin^3\theta}\frac{\partial f}{\partial p_\theta} = 0. \tag{B.1}$$

Recall that:

$$p_r = \dot{r} = v_r \quad ; \quad p_\theta = r^2\dot{\theta} = r v_\theta \quad ; \quad p_\phi = r^2 \sin^2\theta\ \dot{\phi} = r \sin\theta v_\phi \tag{B.2}$$

and

$$\int \mathrm{d}p_r \mathrm{d}p_\theta \mathrm{d}p_\phi\ f = r^2 \sin\theta \int \mathrm{d}v_r \mathrm{d}v_\theta \mathrm{d}v_\phi\ f = r^2 \sin\theta \nu \tag{B.3}$$

where in the last equality, we used:

$$\nu(\mathbf{x}) \equiv \int f(\mathbf{x}, \mathbf{v})\, \mathrm{d}^3\mathbf{v}.$$

[1] See equation (B.2): $v_\phi = p_\phi / r \sin\theta$.

We multiply equation (B.1) by $p_r \, \mathrm{d}p_r \mathrm{d}p_\theta \mathrm{d}p_\phi$ and integrate over the momenta:

$$\overbrace{\int p_r^2 \frac{\partial f}{\partial r} \mathrm{d}^3\mathbf{p}}^{①} + \overbrace{\int \frac{p_\theta p_r}{r^2} \frac{\partial f}{\partial \theta} \mathrm{d}^3\mathbf{p}}^{②} - \overbrace{\int \frac{\mathrm{d}\Phi}{\mathrm{d}r} \frac{\partial f}{\partial p_r} p_r \, \mathrm{d}^3\mathbf{p}}^{③} + \overbrace{\int \frac{p_\theta^2 p_r}{r^3} \frac{\partial f}{\partial p_r} \mathrm{d}^3\mathbf{p}}^{④} + \underbrace{\int \frac{p_\phi^2 p_r}{r^3 \sin^2\theta} \frac{\partial f}{\partial p_r} \mathrm{d}^3\mathbf{p}}_{⑤} + \underbrace{\int \frac{p_\phi^2 p_r \cos\theta}{r^2 \sin^3\theta} \frac{\partial f}{\partial p_\theta} \mathrm{d}^3\mathbf{p}}_{⑥} = 0.$$

$$① \int p_r^2 \frac{\partial f}{\partial r} \mathrm{d}^3\mathbf{p} = \frac{\partial}{\partial r} \int p_r^2 f \mathrm{d}^3\mathbf{p} = \frac{\partial}{\partial r} \int r^2 \sin\theta p_r^2 f \mathrm{d}^3\mathbf{v} = \frac{\partial}{\partial r} \left(r^2 \sin\theta \nu \overline{p_r^2} \right)$$

where the first equality is obtained because p_r does not depend on r, the second equality follows directly from equation (B.3), and the last equality holds because

$$\overline{p_r^2} = \int p_r^2 f_{\mathbf{x}}(\mathbf{v}) \mathrm{d}^3\mathbf{v} = \int p_r^2 \frac{f(\mathbf{x},\mathbf{v})}{\nu(\mathbf{x})} \mathrm{d}^3\mathbf{v} \quad \Rightarrow \quad \nu(\mathbf{x}) \overline{p_r^2} = \int p_r^2 f \mathrm{d}^3\mathbf{v}$$

in the same way:

$$② \int \frac{p_\theta p_r}{r^2} \frac{\partial f}{\partial \theta} \mathrm{d}^3\mathbf{p} = \frac{\partial}{\partial \theta} \int \frac{p_\theta p_r}{r^2} f \mathrm{d}^3\mathbf{p} = \frac{\partial}{\partial \theta} \int r^2 \sin\theta \frac{p_\theta p_r}{r^2} f \mathrm{d}^3\mathbf{v} = \frac{\partial}{\partial \theta} \left(\sin\theta \nu \overline{p_\theta p_r} \right).$$

For the third term, we have:

$$\begin{aligned} ③ \int \frac{\mathrm{d}\Phi}{\mathrm{d}r} \frac{\partial f}{\partial p_r} p_r \, \mathrm{d}^3\mathbf{p} &= \frac{\mathrm{d}\Phi}{\mathrm{d}r} \int \left(\frac{\partial (f p_r)}{\partial p_r} - f \frac{\partial p_r}{\partial p_r} \right) \mathrm{d}^3\mathbf{p} = \frac{\mathrm{d}\Phi}{\mathrm{d}r} \left(\int \nabla_{p_r} (f p_r) \, \mathrm{d}^3\mathbf{p} - \int f \, \mathrm{d}^3\mathbf{p} \right) \\ &= \frac{\mathrm{d}\Phi}{\mathrm{d}r} \left(\oint_S f p_r \, \mathbf{n} \cdot \mathbf{e}_{p_r} \mathrm{d}S - \int f \, \mathrm{d}^3\mathbf{p} \right) = -\frac{\mathrm{d}\Phi}{\mathrm{d}r} r^2 \sin\theta \nu. \end{aligned}$$

For the third equality, we used the divergence theorem:

$$\int_V \boldsymbol{\nabla} g \, \mathrm{d}V = \oint_S g \, \mathbf{n} \, \mathrm{d}S,$$

where $\mathbf{n}(x', g(x')) = 1/\sqrt{1 + |\nabla g(x')|^2}(-\nabla g(x'), 1)$. The surface integral is zero because f is zero for $|\mathbf{v}|$ tending to infinity, as the probability of finding a star with infinite velocity is zero regardless of its position.

$$\begin{aligned} ④ \int \frac{p_\theta^2 p_r}{r^3} \frac{\partial f}{\partial p_r} \mathrm{d}^3\mathbf{p} &= \int \frac{1}{r^3} \left(\frac{\partial (p_\theta^2 p_r f)}{\partial p_r} - \frac{\partial (p_\theta^2 p_r)}{\partial p_r} f \right) \mathrm{d}^3\mathbf{p} \\ &= \underbrace{\oint_{\mathbf{S}} \frac{1}{r^3} p_\theta^2 p_r f \, \mathbf{n} \cdot \mathbf{e}_{p_r} \mathrm{d}S}_{=0} - \int \frac{p_\theta^2}{r^3} f \, \mathrm{d}^3\mathbf{p} = -\frac{\overline{p_\theta^2}}{r^3} r^2 \sin\theta \nu \end{aligned}$$

in the same way:

$$\textcircled{5} \int \frac{p_\phi^2 p_r}{r^3 \sin^2\theta} \frac{\partial f}{\partial p_r} \mathrm{d}^3\mathbf{p} = \int \frac{1}{r^3 \sin^2\theta} \left(\frac{\partial (p_\phi^2 p_r f)}{\partial p_r} - \frac{\partial (p_\phi^2 p_r)}{\partial p_r} f \right) \mathrm{d}^3\mathbf{p}$$
$$= \underbrace{\oint_{\mathbf{S}} \frac{1}{r^3 \sin^2\theta} p_\phi^2 p_r f \ \mathbf{n} \cdot \mathbf{e}_{p_r} \mathrm{d}S}_{=0} - \int \frac{p_\phi^2}{r^3 \sin^2\theta} f \ \mathrm{d}^3\mathbf{p}$$
$$= -\frac{\overline{p_\phi^2}}{r^3 \sin^2\theta} r^2 \sin\theta \nu$$

and finally, for the last term:

$$\textcircled{6} \int \frac{p_\phi^2 p_r \cos\theta}{r^2 \sin^3\theta} \frac{\partial f}{\partial p_\theta} \mathrm{d}^3\mathbf{p} = \int \frac{\cos\theta}{r^2 \sin^3\theta} \left(\frac{\partial (p_\phi^2 p_r f)}{\partial p_\theta} - \frac{\partial (p_\phi^2 p_r)}{\partial p_\theta} f \right) \mathrm{d}^3\mathbf{p}$$
$$= \oint_{\mathbf{S}} \frac{\cos\theta}{r^2 \sin^3\theta} p_\phi^2 p_r f \ \mathbf{n} \cdot \mathbf{e}_{p_\theta} \mathrm{d}S = 0$$

Combining all the terms, we get:

$$\frac{\partial}{\partial r}(r^2 \sin\theta \nu \overline{p_r^2}) + \frac{\partial}{\partial \theta}(\sin\theta \nu \overline{p_r p_\theta}) + r^2 \sin\theta \nu \left(\frac{\mathrm{d}\Phi}{\mathrm{d}r} - \frac{\overline{p_\theta^2}}{r^3} - \frac{\overline{p_\phi^2}}{r^3 \sin^2\theta} \right) = 0 \tag{B.4}$$

In a static spherical system, $\overline{p_r p_\theta} = r\overline{v_r v_\theta}$ vanishes because the PDF is an even function of v_r [2] so

$$r\,\overline{v_r v_\theta} = r \int v_r v_\theta \, f_{\mathbf{x}}(\mathbf{v}) \mathrm{d}^3\mathbf{v} = r \int v_r v_\theta \frac{f(H, \mathbf{L})}{\nu(\mathbf{x})} \mathrm{d}^3\mathbf{v} = \frac{r}{\nu(\mathbf{x})} \int \overbrace{v_r}^{\text{odd}} v_\theta \underbrace{f(H, \mathbf{L})}_{\text{even}} \mathrm{d}^3\mathbf{v} = 0.$$

The second term of Eq. (B.4) disappears. We divide by $r^2 \sin\theta$ and use equations (B.2):

$$\frac{\mathrm{d}(\nu \overline{v_r^2})}{\mathrm{d}r} + \nu \left(\frac{\mathrm{d}\Phi}{\mathrm{d}r} + \frac{2\overline{v_r^2} - \overline{v_\theta^2} - \overline{v_\phi^2}}{r} \right) = 0. \tag{B.5}$$

Which can be rewritten as:

$$\boxed{\frac{\mathrm{d}(\nu \overline{v_r^2})}{\mathrm{d}r} + 2\frac{\beta}{r} \nu \overline{v_r^2} = -\nu \frac{\mathrm{d}\Phi}{\mathrm{d}r}} \tag{B.6}$$

with

$$\beta \equiv 1 - \frac{\overline{v_\theta^2} + \overline{v_\phi^2}}{2\overline{v_r^2}}$$

[2] This is due to Jeans' theorem, which states that any stationary solution of the collisionless Boltzmann equation depends on the phase space coordinates only through integrals of the motion of the potential, and any function of the integrals of motion provides a stationary solution to the collisionless Boltzmann equation. According to this theorem, the PDF can be written as $f(H, \mathbf{L})$, with H being the Hamiltonian and $\mathbf{L}$ the angular momentum of the system. Thus, it is an even function of v_r because H depends on v_r^2 (cf. Eq. 2.3) and $\mathbf{L}$ does not depend on $v_r /\!\!/ r$.

B.2 Jeans velocity dispersion

Now let's calculate the radial velocity dispersion of a dark matter halo assumed to be spherical and isotropic ($\beta = 0$). Eq. (B.6) becomes:

$$\frac{\mathrm{d}(\nu\overline{v_r^2})}{\mathrm{d}r} = -\nu\frac{\mathrm{d}\Phi}{\mathrm{d}r}. \tag{B.7}$$

We multiply by the total mass of the system to introduce the density (cf. Eq. 2.6):

$$\frac{\mathrm{d}(\rho\overline{v_r^2})}{\mathrm{d}r} = -\rho\frac{\mathrm{d}\Phi}{\mathrm{d}r},$$

We then integrate over the radii from r to $r_{\max}$, where $r_{\max}$ is the maximum radius of the halo, defined by cosmology. These integration bounds are chosen because we want the system to satisfie the boundary condition: $\lim_{r\to r_{\max}} \overline{v_r^2} = 0$. Thus, we have:

$$\int_r^{r_{\max}} \frac{\mathrm{d}(\rho\overline{v_r^2})}{\mathrm{d}r'}\mathrm{d}r' = -\int_r^{r_{\max}} \rho(r')\frac{\mathrm{d}\Phi}{\mathrm{d}r'}\mathrm{d}r' \quad\Longleftrightarrow\quad \left[\rho\overline{v_r^2}\right]_r^{r_{\max}} = -\int_r^{r_{max}} \rho(r')\frac{\mathrm{d}\Phi}{\mathrm{d}r'}\mathrm{d}r'$$

and according to the boundary condition:

$$\rho(r)\overline{v_r^2}(r) = \int_r^{r_{\max}} \rho(r')\frac{\mathrm{d}\Phi}{\mathrm{d}r'}\mathrm{d}r' \quad\Longleftrightarrow\quad \overline{v_r^2}(r) = \frac{1}{\rho(r)}\int_r^{r_{\max}} \rho(r')\frac{\mathrm{d}\Phi}{\mathrm{d}r'}\mathrm{d}r'.$$

In our case, $\Phi(r) = -Gm(r)/r$ with $m(r)$ the enclosed mass, we thus obtain the Jeans dispersion equation (2.9):

$$\boxed{\overline{v_r^2}(r) = \frac{1}{\rho(r)}\int_r^{r_{\max}} \rho(r')\frac{Gm(r')}{r'^2}\mathrm{d}r'.}$$

R

If we study a system composed of multiple populations (e.g., stars and dark matter), then ρ refers to the population for which we want to determine the dispersion, and $m(r)$ is the total enclosed mass (i.e., the sum of all populations).

Bibliography

Abbott, B. P., Abbott, R., Abbott, T. D., et al. 2016, PhRvL, 116, 061102, doi: 10.1103/PhysRevLett.116.061102

Abbott, R., Abbott, T. D., Abraham, S., et al. 2020, Phys. Rev. Lett., 125, 101102, doi: 10.1103/PhysRevLett.125.101102

Abbott, R., Abbott, T. D., Acernese, F., et al. 2023, Physical Review X, 13, 041039, doi: 10.1103/PhysRevX.13.041039

Abraham, R. G. 1998, arXiv e-prints, astro, doi: 10.48550/arXiv.astro-ph/9809131

Accadia, T., Acernese, F., Alshourbagy, M., et al. 2012, Journal of Instrumentation, 7, 3012, doi: 10.1088/1748-0221/7/03/P03012

Acernese, F., Agathos, M., Agatsuma, K., et al. 2015, Classical and Quantum Gravity, 32, 024001, doi: 10.1088/0264-9381/32/2/024001

Ahn, C. P., Seth, A. C., Cappellari, M., et al. 2018, ApJ, 858, 102, doi: 10.3847/1538-4357/aabc57

Alfaro-Cuello, M., Kacharov, N., Neumayer, N., et al. 2019, ApJ, 886, 57, doi: 10.3847/1538-4357/ab1b2c

Alpher, R. A., & Herman, R. 1948a, Nature, 162, 774, doi: 10.1038/162774b0

Alpher, R. A., & Herman, R. C. 1948b, Physical Review, 74, 1737, doi: 10.1103/PhysRev.74.1737

Amaro-Seoane, P., Audley, H., Babak, S., et al. 2017, arXiv e-prints, arXiv:1702.00786, doi: 10.48550/arXiv.1702.00786

Anglés-Alcázar, D., Özel, F., & Davé, R. 2013, ApJ, 770, 5, doi: 10.1088/0004-637X/770/1/5

Arora, N., Courteau, S., Macciò, A. V., et al. 2024, MNRAS, 529, 2047, doi: 10.1093/mnras/stae669

Arora, N., Fossati, M., Fontanot, F., Hirschmann, M., & Wilman, D. J. 2019, MNRAS, 489, 1606, doi: 10.1093/mnras/stz2266

Bañados, E., Decarli, R., Walter, F., et al. 2015, ApJL, 805, L8, doi: 10.1088/2041-8205/805/1/L8

Bañados, E., Venemans, B. P., Mazzucchelli, C., et al. 2018, Nature, 553, 473, doi: 10.1038/nature25180

Baldassare, V. F., Reines, A. E., Gallo, E., & Greene, J. E. 2015, ApJL, 809, L14, doi: 10.1088/2041-8205/809/1/L14

—. 2017, ApJ, 836, 20, doi: 10.3847/1538-4357/836/1/20

Baldry, I. K., Balogh, M. L., Bower, R. G., et al. 2006, MNRAS, 373, 469, doi: 10.1111/j.1365-2966.2006.11081.x

Banik, U., & van den Bosch, F. C. 2021, ApJ, 912, 43, doi: 10.3847/1538-4357/abeb6d

—. 2022, ApJ, 926, 215, doi: 10.3847/1538-4357/ac4242

Barnes, J., & Hut, P. 1986, Nature, 324, 446, doi: 10.1038/324446a0

Battaglia, G., Helmi, A., Morrison, H., et al. 2005, MNRAS, 364, 433, doi: 10.1111/j.1365-2966.2005.09367.x

Begelman, M. C., Blandford, R. D., & Rees, M. J. 1980, Nature, 287, 307, doi: 10.1038/287307a0

Behroozi, P. S., Conroy, C., & Wechsler, R. H. 2010, ApJ, 717, 379, doi: 10.1088/0004-637X/717/1/379

Behroozi, P. S., Wechsler, R. H., & Conroy, C. 2013, ApJ, 770, 57, doi: 10.1088/0004-637X/770/1/57

Bekki, K., & Tsujimoto, T. 2016, ApJ, 831, 70, doi: 10.3847/0004-637X/831/1/70

Bell, E. F., Zucker, D. B., Belokurov, V., et al. 2008, ApJ, 680, 295, doi: 10.1086/588032

Bellovary, J. M., Cleary, C. E., Munshi, F., et al. 2019, MNRAS, 482, 2913, doi: 10.1093/mnras/sty2842

Bellovary, J. M., Hayoune, S., Chafla, K., et al. 2021, MNRAS, 505, 5129, doi: 10.1093/mnras/stab1665

Bender, R., Surma, P., Doebereiner, S., Moellenhoff, C., & Madejsky, R. 1989, A&A, 217, 35

Bennett, C. L., Larson, D., Weiland, J. L., et al. 2013, ApJS, 208, 20, doi: 10.1088/0067-0049/208/2/20

Bensby, T., & Feltzing, S. 2006, MNRAS, 367, 1181, doi: 10.1111/j.1365-2966.2006.10037.x

Binney, J. 1977, MNRAS, 181, 735, doi: 10.1093/mnras/181.4.735

Binney, J., & Tremaine, S. 2008, Galactic Dynamics: Second Edition

Binney, J. J., & Evans, N. W. 2001, MNRAS, 327, L27, doi: 10.1046/j.1365-8711.2001.04968.x

Blaes, O., Lee, M. H., & Socrates, A. 2002, ApJ, 578, 775, doi: 10.1086/342655

Blumenthal, G. R., Faber, S. M., Primack, J. R., & Rees, M. J. 1984, Nature, 311, 517, doi: 10.1038/311517a0

Bode, P., Ostriker, J. P., & Turok, N. 2001, ApJ, 556, 93, doi: 10.1086/321541

Boekholt, T. C. N., Rowan, C., & Kocsis, B. 2023, MNRAS, 518, 5653, doi: 10.1093/mnras/stac3495

Bontekoe, T. R., & van Albada, T. S. 1987, MNRAS, 224, 349, doi: 10.1093/mnras/224.2.349

Borriello, A., & Salucci, P. 2001, MNRAS, 323, 285, doi: 10.1046/j.1365-8711.2001.04077.x

Borukhovetskaya, A., Errani, R., Navarro, J. F., Fattahi, A., & Santos-Santos, I. 2022, MNRAS, 509, 5330, doi: 10.1093/mnras/stab2912

Boselli, A., & Gavazzi, G. 2014, A&A Rv, 22, 74, doi: 10.1007/s00159-014-0074-y

Braun, R., Walterbos, R. A. M., & Kennicutt, Robert C., J. 1992, Nature, 360, 442, doi: 10.1038/360442a0

Burkert, A. 2000, ApJL, 534, L143, doi: 10.1086/312674

Burkert, A., & Tremaine, S. 2010, ApJ, 720, 516, doi: 10.1088/0004-637X/720/1/516

Buson, L. M., Sadler, E. M., Zeilinger, W. W., et al. 1993, A&A, 280, 409

Cann, J. M., Satyapal, S., Bohn, T., et al. 2020, ApJ, 895, 147, doi: 10.3847/1538-4357/ab8b64

Chan, T. K., Kereš, D., Oñorbe, J., et al. 2015, MNRAS, 454, 2981, doi: 10.1093/mnras/stv2165

Chandrasekhar, S. 1943, ApJ, 97, 255, doi: 10.1086/144517

Chugunov, I. V., Marchuk, A. A., Mosenkov, A. V., et al. 2024, MNRAS, 527, 9605, doi: 10.1093/mnras/stad3850

Cole, D. R., Dehnen, W., Read, J. I., & Wilkinson, M. I. 2012, MNRAS, 426, 601, doi: 10.1111/j.1365-2966.2012.21885.x

Cole, D. R., Dehnen, W., & Wilkinson, M. I. 2011, MNRAS, 416, 1118, doi: 10.1111/j.1365-2966.2011.19110.x

Colín, P., Avila-Reese, V., & Valenzuela, O. 2000, ApJ, 542, 622, doi: 10.1086/317057

Conroy, C., & Wechsler, R. H. 2009, ApJ, 696, 620, doi: 10.1088/0004-637X/696/1/620

Cora, S. A., Muzzio, J. C., & Vergne, M. M. 1997, MNRAS, 289, 253, doi: 10.1093/mnras/289.2.253

de Blok, W. J. G. 2010, Advances in Astronomy, 2010, 789293, doi: 10.1155/2010/789293

de Blok, W. J. G., McGaugh, S. S., Bosma, A., & Rubin, V. C. 2001, ApJL, 552, L23, doi: 10.1086/320262

de Blok, W. J. G., Walter, F., Brinks, E., et al. 2008, AJ, 136, 2648, doi: 10.1088/0004-6256/136/6/2648

de Jong, R. S. 1996, A&A, 313, 45, doi: 10.48550/arXiv.astro-ph/9601005

de Vaucouleurs, G. 1974, in The Formation and Dynamics of Galaxies, ed. J. R. Shakeshaft, Vol. 58, 1

Dehnen, W. 2000, ApJL, 536, L39, doi: 10.1086/312724

—. 2001, MNRAS, 324, 273, doi: 10.1046/j.1365-8711.2001.04237.x

—. 2002, Journal of Computational Physics, 179, 27, doi: 10.1006/jcph.2002.7026

Dekel, A., Ishai, G., Dutton, A. A., & Maccio, A. V. 2017, MNRAS, 468, 1005, doi: 10.1093/mnras/stx486

Dekel, A., & Silk, J. 1986, ApJ, 303, 39, doi: 10.1086/164050

del Valle, L., & Volonteri, M. 2018, MNRAS, 480, 439, doi: 10.1093/mnras/sty1815

DeLaurentiis, S., Epstein-Martin, M., & Haiman, Z. 2023, MNRAS, 523, 1126, doi: 10.1093/mnras/stad1412

Di Cintio, A., Brook, C. B., Macciò, A. V., et al. 2014, MNRAS, 437, 415, doi: 10.1093/mnras/stt1891

Dreyer, J. L. E. 1888, MmRAS, 49, 1

—. 1910, MmRAS, 59, 105

Dubinski, J., & Carlberg, R. G. 1991, ApJ, 378, 496, doi: 10.1086/170451

Dubois, Y., Beckmann, R., Bournaud, F., et al. 2021, A&A, 651, A109, doi: 10.1051/0004-6361/202039429

Dutton, A. A., Macciò, A. V., Dekel, A., et al. 2016, MNRAS, 461, 2658, doi: 10.1093/mnras/stw1537

El-Zant, A., Shlosman, I., & Hoffman, Y. 2001, ApJ, 560, 636, doi: 10.1086/322516

El-Zant, A. A., Freundlich, J., & Combes, F. 2016, MNRAS, 461, 1745, doi: 10.1093/mnras/stw1398

El-Zant, A. A., Hoffman, Y., Primack, J., Combes, F., & Shlosman, I. 2004, ApJL, 607, L75, doi: 10.1086/421938

Errani, R., & Navarro, J. F. 2021, MNRAS, 505, 18, doi: 10.1093/mnras/stab1215

Faber, S. M., & Gallagher, J. S. 1979, ARA&A, 17, 135, doi: 10.1146/annurev.aa.17.090179.001031

Faber, S. M., Tremaine, S., Ajhar, E. A., et al. 1997, AJ, 114, 1771, doi: 10.1086/118606

Fabian, A. C., Pringle, J. E., & Rees, M. J. 1975, MNRAS, 172, 15, doi: 10.1093/mnras/172.1.15P

Famaey, B., & McGaugh, S. S. 2012, Living Reviews in Relativity, 15, 10, doi: 10.12942/lrr-2012-10

Ferguson, A. M. N., Irwin, M. J., Ibata, R. A., Lewis, G. F., & Tanvir, N. R. 2002, AJ, 124, 1452, doi: 10.1086/342019

Ferrarese, L., & Merritt, D. 2000, ApJL, 539, L9, doi: 10.1086/312838

Förster Schreiber, N. M., Übler, H., Davies, R. L., et al. 2019, ApJ, 875, 21, doi: 10.3847/1538-4357/ab0ca2

Fossati, M., Wilman, D. J., Fontanot, F., et al. 2015, MNRAS, 446, 2582, doi: 10.1093/mnras/stu2255

François, T. L., Boily, C. M., Freundlich, J., Rozier, S., & Voggel, K. 2024, A&A, 687, A203, doi: 10.1051/0004-6361/202348591

Freundlich, J., Dekel, A., Jiang, F., et al. 2020a, MNRAS, 491, 4523, doi: 10.1093/mnras/stz3306

Freundlich, J., Jiang, F., Dekel, A., et al. 2020b, MNRAS, 499, 2912, doi: 10.1093/mnras/staa2790

Fried, J. W., & Illingworth, G. D. 1994, AJ, 107, 992, doi: 10.1086/116912

Frosst, M., Courteau, S., Arora, N., et al. 2022, MNRAS, 514, 3510, doi: 10.1093/mnras/stac1497

Fukushige, T., & Heggie, D. C. 2000, MNRAS, 318, 753, doi: 10.1046/j.1365-8711.2000.03811.x

Furtak, L. J., Labbé, I., Zitrin, A., et al. 2024, Nature, 628, 57, doi: 10.1038/s41586-024-07184-8

Gamow, G. 1948a, Nature, 162, 680, doi: 10.1038/162680a0

—. 1948b, Physical Review, 74, 505, doi: 10.1103/PhysRev.74.505.2

Gavagnin, E., Mapelli, M., & Lake, G. 2016, MNRAS, 461, 1276, doi: 10.1093/mnras/stw1397

Gebhardt, K., Bender, R., Bower, G., et al. 2000, ApJL, 539, L13, doi: 10.1086/312840

Gentile, G., Famaey, B., & de Blok, W. J. G. 2011, A&A, 527, A76, doi: 10.1051/0004-6361/201015283

Goerdt, T., Moore, B., Read, J. I., & Stadel, J. 2010, ApJ, 725, 1707, doi: 10.1088/0004-637X/725/2/1707

Goerdt, T., Moore, B., Read, J. I., Stadel, J., & Zemp, M. 2006, MNRAS, 368, 1073, doi: 10.1111/j.1365-2966.2006.10182.x

Goldreich, P., Lithwick, Y., & Sari, R. 2002, Nature, 420, 643, doi: 10.1038/nature01227

Goodman, J. 2000, NewA, 5, 103, doi: 10.1016/S1384-1076(00)00015-4

Governato, F., Brook, C., Mayer, L., et al. 2010, Nature, 463, 203, doi: 10.1038/nature08640

Governato, F., Zolotov, A., Pontzen, A., et al. 2012, MNRAS, 422, 1231, doi: 10.1111/j.1365-2966.2012.20696.x

Graham, A. W., & Driver, S. P. 2007, ApJ, 655, 77, doi: 10.1086/509758

Grebel, E. K., Gallagher, John S., I., & Harbeck, D. 2003, AJ, 125, 1926, doi: 10.1086/368363

Greene, J. E., Strader, J., & Ho, L. C. 2020, ARA&A, 58, 257, doi: 10.1146/annurev-astro-032620-021835

Greengard, L., & Rokhlin, V. 1987, Journal of Computational Physics, 73, 325, doi: 10.1016/0021-9991(87)90140-9

Grillmair, C. J. 2009, ApJ, 693, 1118, doi: 10.1088/0004-637X/693/2/1118

Gültekin, K., Richstone, D. O., Gebhardt, K., et al. 2009, ApJ, 698, 198, doi: 10.1088/0004-637X/698/1/198

Gunn, J. E., & Gott, J. Richard, I. 1972, ApJ, 176, 1, doi: 10.1086/151605

Häberle, M., Neumayer, N., Seth, A., et al. 2024, Nature, 631, 285, doi: 10.1038/s41586-024-07511-z

Haiman, Z., & Loeb, A. 2001, ApJ, 552, 459, doi: 10.1086/320586

Hannestad, S., & Scherrer, R. J. 2000, Phys. Rev. D, 62, 043522, doi: 10.1103/PhysRevD.62.043522

Häring, N., & Rix, H.-W. 2004, ApJL, 604, L89, doi: 10.1086/383567

Helmi, A., White, S. D. M., de Zeeuw, P. T., & Zhao, H. 1999, Nature, 402, 53, doi: 10.1038/46980

Henon, M., & Petit, J. M. 1986, Celestial Mechanics, 38, 67, doi: 10.1007/BF01234287

Hernquist, L. 1990, ApJ, 356, 359, doi: 10.1086/168845

Hills, J. G. 1983, AJ, 88, 1269, doi: 10.1086/113418

Hu, W., Barkana, R., & Gruzinov, A. 2000, Phys. Rev. Lett., 85, 1158, doi: 10.1103/PhysRevLett.85.1158

Hubble, E. 1929, Contributions from the Mount Wilson Observatory / Carnegie Institution of Washington, 376, 1

Hubble, E. P. 1926, ApJ, 64, 321, doi: 10.1086/143018

Ibata, R. A., Gilmore, G., & Irwin, M. J. 1994, Nature, 370, 194, doi: 10.1038/370194a0

Ibata, R. A., Malhan, K., & Martin, N. F. 2019, ApJ, 872, 152, doi: 10.3847/1538-4357/ab0080

Inoue, S. 2011, MNRAS, 416, 1181, doi: 10.1111/j.1365-2966.2011.19122.x

Jensen, J., Thomas, G., McConnachie, A. W., et al. 2021, MNRAS, 507, 1923, doi: 10.1093/mnras/stab2325

Jiang, F., Dekel, A., Freundlich, J., et al. 2021, MNRAS, 502, 621, doi: 10.1093/mnras/staa4034

Johnston, K. V., Sigurdsson, S., & Hernquist, L. 1999, MNRAS, 302, 771, doi: 10.1046/j.1365-8711.1999.02200.x

Kalberla, P. M. W., & Kerp, J. 2009, ARA&A, 47, 27, doi: 10.1146/annurev-astro-082708-101823

Kaur, K., & Sridhar, S. 2018, ApJ, 868, 134, doi: 10.3847/1538-4357/aaeacf

King, I. R. 1966, AJ, 71, 64, doi: 10.1086/109857

Kollatschny, W., Weilbacher, P. M., Ochmann, M. W., et al. 2020, A&A, 633, A79, doi: 10.1051/0004-6361/201936540

Kormendy, J., & Richstone, D. 1995, ARA&A, 33, 581, doi: 10.1146/annurev.aa.33.090195.003053

Lacey, C., & Cole, S. 1993, MNRAS, 262, 627, doi: 10.1093/mnras/262.3.627

Lanzoni, B., Mucciarelli, A., Origlia, L., et al. 2013, ApJ, 769, 107, doi: 10.1088/0004-637X/769/2/107

Leauthaud, A., George, M. R., Behroozi, P. S., et al. 2012, ApJ, 746, 95, doi: 10.1088/0004-637X/746/1/95

Li, J., Lai, D., & Rodet, L. 2022, ApJ, 934, 154, doi: 10.3847/1538-4357/ac7c0d

Li, Z., Dekel, A., Mandelker, N., Freundlich, J., & François, T. L. 2023, MNRAS, 518, 5356, doi: 10.1093/mnras/stac3233

LIGO Scientific Collaboration, Aasi, J., Abbott, B. P., et al. 2015, Classical and Quantum Gravity, 32, 074001, doi: 10.1088/0264-9381/32/7/074001

Lin, D. N. C., & Tremaine, S. 1983, ApJ, 264, 364, doi: 10.1086/160604

Lützgendorf, N., Kissler-Patig, M., Gebhardt, K., et al. 2013a, memsai, 84, 129, doi: 10.48550/arXiv.1301.2998

Lützgendorf, N., Kissler-Patig, M., Neumayer, N., et al. 2013b, A&A, 555, A26, doi: 10.1051/0004-6361/201321183

Lyke, B. W., Higley, A. N., McLane, J. N., et al. 2020, ApJS, 250, 8, doi: 10.3847/1538-4365/aba623

Lynden-Bell, D., & Kalnajs, A. J. 1972, MNRAS, 157, 1, doi: 10.1093/mnras/157.1.1

MacArthur, L. A., Courteau, S., & Holtzman, J. A. 2003a, in Revista Mexicana de Astronomia y Astrofisica Conference Series, Vol. 17, Revista Mexicana de Astronomia y Astrofisica Conference Series, ed. V. Avila-Reese, C. Firmani, C. S. Frenk, & C. Allen, 180–181

MacArthur, L. A., Courteau, S., & Holtzman, J. A. 2003b, ApJ, 582, 689, doi: 10.1086/344506

Macciò, A. V., Crespi, S., Blank, M., & Kang, X. 2020, MNRAS, 495, L46, doi: 10.1093/mnrasl/slaa058

Macciò, A. V., Paduroiu, S., Anderhalden, D., Schneider, A., & Moore, B. 2012, MNRAS, 424, 1105, doi: 10.1111/j.1365-2966.2012.21284.x

Mackey, A. D., & Gilmore, G. F. 2003, MNRAS, 345, 747, doi: 10.1046/j.1365-8711.2003.07001.x

Madau, P., Shen, S., & Governato, F. 2014, ApJL, 789, L17, doi: 10.1088/2041-8205/789/1/L17

Magorrian, J., Tremaine, S., Richstone, D., et al. 1998, AJ, 115, 2285, doi: 10.1086/300353

Malbon, R. K., Baugh, C. M., Frenk, C. S., & Lacey, C. G. 2007, MNRAS, 382, 1394, doi: 10.1111/j.1365-2966.2007.12317.x

Mannerkoski, M., Rawlings, A., Johansson, P. H., et al. 2023, MNRAS, 524, 4062, doi: 10.1093/mnras/stad2139

Marconi, A., & Hunt, L. K. 2003, ApJL, 589, L21, doi: 10.1086/375804

Marsh, D. J. E., & Silk, J. 2014, MNRAS, 437, 2652, doi: 10.1093/mnras/stt2079

Martizzi, D., Teyssier, R., & Moore, B. 2013, MNRAS, 432, 1947, doi: 10.1093/mnras/stt297

Mashchenko, S., Couchman, H. M. P., & Wadsley, J. 2006, Nature, 442, 539, doi: 10.1038/nature04944

Mashchenko, S., Wadsley, J., & Couchman, H. M. P. 2008, Science, 319, 174, doi: 10.1126/science.1148666

McConnachie, A. W. 2012, AJ, 144, 4, doi: 10.1088/0004-6256/144/1/4

McGaugh, S. S., & de Blok, W. J. G. 1997, ApJ, 481, 689, doi: 10.1086/304100

McGaugh, S. S., & Schombert, J. M. 2014, AJ, 148, 77, doi: 10.1088/0004-6256/148/5/77

McMillan, P. J. 2017, MNRAS, 465, 76, doi: 10.1093/mnras/stw2759

McNamara, B. J., Harrison, T. E., Baumgardt, H., & Khalaj, P. 2012, ApJ, 745, 175, doi: 10.1088/0004-637X/745/2/175

Menzel, M., Davis, M., Parrish, K., et al. 2023, PASP, 135, 058002, doi: 10.1088/1538-3873/acbb9f

Mestel, L. 1963, MNRAS, 126, 553, doi: 10.1093/mnras/126.6.553

Mezcua, M. 2017, International Journal of Modern Physics D, 26, 1730021, doi: 10.1142/S021827181730021X

Mezcua, M., Civano, F., Marchesi, S., et al. 2018, MNRAS, 478, 2576, doi: 10.1093/mnras/sty1163

Mezcua, M., & Lobanov, A. P. 2011, Astronomische Nachrichten, 332, 379, doi: 10.1002/asna.201011504

Mezcua, M., Suh, H., & Civano, F. 2019, MNRAS, 488, 685, doi: 10.1093/mnras/stz1760

Milgrom, M. 1983, ApJ, 270, 365, doi: 10.1086/161130

Miller, M. C., & Hamilton, D. P. 2002, MNRAS, 330, 232, doi: 10.1046/j.1365-8711.2002.05112.x

Milosavljević, M., & Merritt, D. 2003, ApJ, 596, 860, doi: 10.1086/378086

Mo, H., van den Bosch, F. C., & White, S. 2010, Galaxy Formation and Evolution

Moore, B. 1994, Nature, 370, 629, doi: 10.1038/370629a0

Mortlock, D. J., Warren, S. J., Venemans, B. P., et al. 2011, Nature, 474, 616, doi: 10.1038/nature10159

Moster, B. P., Naab, T., & White, S. D. M. 2013, MNRAS, 428, 3121, doi: 10.1093/mnras/sts261

Moster, B. P., Somerville, R. S., Maulbetsch, C., et al. 2010, ApJ, 710, 903, doi: 10.1088/0004-637X/710/2/903

Murali, C., & Dubinski, J. 1999, AJ, 118, 911, doi: 10.1086/300971

Navarro, J. F., Frenk, C. S., & White, S. D. M. 1995, MNRAS, 275, 720, doi: 10.1093/mnras/275.3.720

—. 1996, ApJ, 462, 563, doi: 10.1086/177173

Neumayer, N., Seth, A., & Böker, T. 2020, A&A Rv, 28, 4, doi: 10.1007/s00159-020-00125-0

Newman, A. B., Treu, T., Ellis, R. S., et al. 2013, ApJ, 765, 24, doi: 10.1088/0004-637X/765/1/24

Nguyen, D. D., Seth, A. C., Neumayer, N., et al. 2019, ApJ, 872, 104, doi: 10.3847/1538-4357/aafe7a

Nipoti, C., & Binney, J. 2015, MNRAS, 446, 1820, doi: 10.1093/mnras/stu2217

Noyola, E., Gebhardt, K., & Bergmann, M. 2008, in Dynamical Evolution of Dense Stellar Systems, ed. E. Vesperini, M. Giersz, & A. Sills, Vol. 246, 341–345, doi: 10.1017/S1743921308015895

Odenkirchen, M., Grebel, E. K., Dehnen, W., et al. 2002, in American Astronomical Society Meeting Abstracts, Vol. 200, American Astronomical Society Meeting Abstracts #200, 10.01

Odenkirchen, M., Grebel, E. K., Dehnen, W., et al. 2003, in Astronomical Society of the Pacific Conference Series, Vol. 296, New Horizons in Globular Cluster Astronomy, ed. G. Piotto, G. Meylan, S. G. Djorgovski, & M. Riello, 501, doi: 10.48550/arXiv.astro-ph/0209555

Oh, S.-H., de Blok, W. J. G., Brinks, E., Walter, F., & Kennicutt, Robert C., J. 2011, AJ, 141, 193, doi: 10.1088/0004-6256/141/6/193

Oh, S.-H., Hunter, D. A., Brinks, E., et al. 2015, AJ, 149, 180, doi: 10.1088/0004-6256/149/6/180

Oria, P.-A., Tenachi, W., Ibata, R., et al. 2022, ApJL, 936, L3, doi: 10.3847/2041-8213/ac86d3

Ostriker, E. C. 1999, ApJ, 513, 252, doi: 10.1086/306858

Pardo, K., Goulding, A. D., Greene, J. E., et al. 2016, ApJ, 831, 203, doi: 10.3847/0004-637X/831/2/203

Parkinson, H., Cole, S., & Helly, J. 2008, MNRAS, 383, 557, doi: 10.1111/j.1365-2966.2007.12517.x

Pasquali, A., van den Bosch, F. C., & Rix, H. W. 2007, ApJ, 664, 738, doi: 10.1086/518856

Peñarrubia, J. 2023, MNRAS, 519, 1955, doi: 10.1093/mnras/stac3642

Peñarrubia, J., Errani, R., Walker, M. G., Gieles, M., & Boekholt, T. C. N. 2024, arXiv e-prints, arXiv:2404.19069, doi: 10.48550/arXiv.2404.19069

Peñarrubia, J., Just, A., & Kroupa, P. 2004, MNRAS, 349, 747, doi: 10.1111/j.1365-2966.2004.07549.x

Peñarrubia, J., Navarro, J. F., & McConnachie, A. W. 2008, ApJ, 673, 226, doi: 10.1086/523686

Pechetti, R., Seth, A., Kamann, S., et al. 2022, ApJ, 924, 48, doi: 10.3847/1538-4357/ac339f

Peebles, P. J. E. 1980, in Physical Cosmology, ed. J. Audouze, R. Balian, & D. N. Schramm, 213

Peebles, P. J. E. 1982a, ApJ, 258, 415, doi: 10.1086/160094

—. 1982b, ApJL, 263, L1, doi: 10.1086/183911

—. 2000, ApJL, 534, L127, doi: 10.1086/312677

Peek, B. M. 1932, MNRAS, 92, 707, doi: 10.1093/mnras/92.7.707

Peirani, S., Dubois, Y., Volonteri, M., et al. 2017, MNRAS, 472, 2153, doi: 10.1093/mnras/stx2099

Peletier, R. F., Davies, R. L., Illingworth, G. D., Davis, L. E., & Cawson, M. 1990, AJ, 100, 1091, doi: 10.1086/115582

Penzias, A. A., & Wilson, R. W. 1965, ApJ, 142, 419, doi: 10.1086/148307

Peters, P. C. 1964, Physical Review, 136, 1224, doi: 10.1103/PhysRev.136.B1224

Petit, J. M., & Henon, M. 1986, icarus, 66, 536, doi: 10.1016/0019-1035(86)90089-8

Petit, J.-M., & Hénon, M. 1990, in Dynamics and Stochastic Processes Theory and Applications, ed. R. Lima, L. Streit, & R. Vilela Mendes, Vol. 355, 225–241, doi: 10.1007/3-540-52347-2_33

Petts, J. A., Gualandris, A., & Read, J. I. 2015, MNRAS, 454, 3778, doi: 10.1093/mnras/stv2235

Pfister, H., Volonteri, M., Dubois, Y., Dotti, M., & Colpi, M. 2019, MNRAS, 486, 101, doi: 10.1093/mnras/stz822

Pillepich, A., Nelson, D., Springel, V., et al. 2019, MNRAS, 490, 3196, doi: 10.1093/mnras/stz2338

Planck Collaboration, Aghanim, N., Akrami, Y., et al. 2020, A&A, 641, A6, doi: 10.1051/0004-6361/201833910

Planelles, S., Borgani, S., Fabjan, D., et al. 2014, MNRAS, 438, 195, doi: 10.1093/mnras/stt2141

Poggio, E., Drimmel, R., Cantat-Gaudin, T., et al. 2021, A&A, 651, A104, doi: 10.1051/0004-6361/202140687

Pontzen, A., & Governato, F. 2012, MNRAS, 421, 3464, doi: 10.1111/j.1365-2966.2012.20571.x

—. 2014, Nature, 506, 171, doi: 10.1038/nature12953

Portegies Zwart, S. F., Baumgardt, H., Hut, P., Makino, J., & McMillan, S. L. W. 2004, Nature, 428, 724, doi: 10.1038/nature02448

Read, J. I., & Gilmore, G. 2005, MNRAS, 356, 107, doi: 10.1111/j.1365-2966.2004.08424.x

Read, J. I., Goerdt, T., Moore, B., et al. 2006, MNRAS, 373, 1451, doi: 10.1111/j.1365-2966.2006.11022.x

Reid, M. J., Menten, K. M., Brunthaler, A., et al. 2019, ApJ, 885, 131, doi: 10.3847/1538-4357/ab4a11

Rein, H., & Liu, S. F. 2012, A&A, 537, A128, doi: 10.1051/0004-6361/201118085

Rein, H., & Spiegel, D. S. 2015, MNRAS, 446, 1424, doi: 10.1093/mnras/stu2164

Reines, A. E., Condon, J. J., Darling, J., & Greene, J. E. 2020, ApJ, 888, 36, doi: 10.3847/1538-4357/ab4999

Reines, A. E., Greene, J. E., & Geha, M. 2013, ApJ, 775, 116, doi: 10.1088/0004-637X/775/2/116

Renaud, F., Gieles, M., & Boily, C. M. 2011, MNRAS, 418, 759, doi: 10.1111/j.1365-2966.2011.19531.x

Rich, R. M., Reitzel, D. B., Howard, C. D., & Zhao, H. 2007, ApJL, 658, L29, doi: 10.1086/513509

Rigby, J., Perrin, M., McElwain, M., et al. 2023, PASP, 135, 048001, doi: 10.1088/1538-3873/acb293

Roberts, M. S., Hogg, D. E., Bregman, J. N., Forman, W. R., & Jones, C. 1991, ApJS, 75, 751, doi: 10.1086/191548

Romano-Díaz, E., Shlosman, I., Hoffman, Y., & Heller, C. 2008, ApJL, 685, L105, doi: 10.1086/592687

Rowan, C., Boekholt, T., Kocsis, B., & Haiman, Z. 2023, MNRAS, 524, 2770, doi: 10.1093/mnras/stad1926

Sadoun, R., & Colin, J. 2012, MNRAS, 426, L51, doi: 10.1111/j.1745-3933.2012.01321.x

Saifollahi, T. 2022, PhD thesis, University of Groningen, doi: 10.33612/diss.206448373

Sales, L. V., Wetzel, A., & Fattahi, A. 2022, Nature Astronomy, 6, 897, doi: 10.1038/s41550-022-01689-w

Samsing, J., D'Orazio, D. J., Askar, A., & Giersz, M. 2018a, arXiv e-prints, arXiv:1802.08654, doi: 10.48550/arXiv.1802.08654

Samsing, J., MacLeod, M., & Ramirez-Ruiz, E. 2014, ApJ, 784, 71, doi: 10.1088/0004-637X/784/1/71

—. 2018b, ApJ, 853, 140, doi: 10.3847/1538-4357/aaa715

Saslaw, W. C., Valtonen, M. J., & Aarseth, S. J. 1974, ApJ, 190, 253, doi: 10.1086/152870

Schweizer, F., Seitzer, P., Whitmore, B. C., Kelson, D. D., & Villanueva, E. V. 2018, ApJ, 853, 54, doi: 10.3847/1538-4357/aaa424

Secrest, N. J., Satyapal, S., Gliozzi, M., et al. 2015, ApJ, 798, 38, doi: 10.1088/0004-637X/798/1/38

Sesana, A., Haardt, F., & Madau, P. 2006, ApJ, 651, 392, doi: 10.1086/507596

Seth, A., Agüeros, M., Lee, D., & Basu-Zych, A. 2008, ApJ, 678, 116, doi: 10.1086/528955

Seth, A. C., van den Bosch, R., Mieske, S., et al. 2014, Nature, 513, 398, doi: 10.1038/nature13762

Shangguan, J., Ho, L. C., & Xie, Y. 2018, ApJ, 854, 158, doi: 10.3847/1538-4357/aaa9be

Shen, Y., Chen, Y.-C., Hwang, H.-C., et al. 2021, Nature Astronomy, 5, 569, doi: 10.1038/s41550-021-01323-1

Silk, J., & Mamon, G. A. 2012, Research in Astronomy and Astrophysics, 12, 917, doi: 10.1088/1674-4527/12/8/004

Silk, J., & Rees, M. J. 1998, A&A, 331, L1, doi: 10.48550/arXiv.astro-ph/9801013

Simon, J. D. 2019, ARA&A, 57, 375, doi: 10.1146/annurev-astro-091918-104453

Smoot, G. F., Bennett, C. L., Kogut, A., et al. 1992, ApJL, 396, L1, doi: 10.1086/186504

Spergel, D. N., & Steinhardt, P. J. 2000, PhRvL, 84, 3760, doi: 10.1103/PhysRevLett.84.3760

Springel, V., White, S. D. M., Jenkins, A., et al. 2005, Nature, 435, 629, doi: 10.1038/nature03597

Stemo, A., Comerford, J. M., Barrows, R. S., et al. 2021, ApJ, 923, 36, doi: 10.3847/1538-4357/ac0bbf

Tagawa, H., Haiman, Z., & Kocsis, B. 2020, ApJ, 898, 25, doi: 10.3847/1538-4357/ab9b8c

Tagawa, H., Saitoh, T. R., & Kocsis, B. 2018, PhRvL, 120, 261101, doi: 10.1103/PhysRevLett.120.261101

Temi, P., Brighenti, F., & Mathews, W. G. 2007, ApJ, 660, 1215, doi: 10.1086/513690

Tenachi, W., Oria, P.-A., Ibata, R., et al. 2022, ApJL, 935, L22, doi: 10.3847/2041-8213/ac874f

Teyssier, R., Pontzen, A., Dubois, Y., & Read, J. I. 2013, MNRAS, 429, 3068, doi: 10.1093/mnras/sts563

Tollet, E., Macciò, A. V., Dutton, A. A., et al. 2016, MNRAS, 456, 3542, doi: 10.1093/mnras/stv2856

Tonini, C., Lapi, A., & Salucci, P. 2006, ApJ, 649, 591, doi: 10.1086/506431

Tran, H. D., Tsvetanov, Z., Ford, H. C., et al. 2001, AJ, 121, 2928, doi: 10.1086/321072

Tremaine, S., & Weinberg, M. D. 1984, MNRAS, 209, 729, doi: 10.1093/mnras/209.4.729

Tremaine, S., Gebhardt, K., Bender, R., et al. 2002, ApJ, 574, 740, doi: 10.1086/341002

Tremmel, M., Governato, F., Volonteri, M., Pontzen, A., & Quinn, T. R. 2018, ApJL, 857, L22, doi: 10.3847/2041-8213/aabc0a

Tully, R. B. 1982, ApJ, 257, 389, doi: 10.1086/159999

Valtonen, M. J., Mikkola, S., Heinamaki, P., & Valtonen, H. 1994, ApJS, 95, 69, doi: 10.1086/192094

van den Bosch, R. C. E. 2016, ApJ, 831, 134, doi: 10.3847/0004-637X/831/2/134

van der Marel, R. P., & Anderson, J. 2010, ApJ, 710, 1063, doi: 10.1088/0004-637X/710/2/1063

van Dokkum, P. G., & Franx, M. 1995, AJ, 110, 2027, doi: 10.1086/117667

Varri, A. L., & Bertin, G. 2012, A&A, 540, A94, doi: 10.1051/0004-6361/201118300

Vasiliev, E., Antonini, F., & Merritt, D. 2014, ApJ, 785, 163, doi: 10.1088/0004-637X/785/2/163

Venemans, B. P., Findlay, J. R., Sutherland, W. J., et al. 2013, ApJ, 779, 24, doi: 10.1088/0004-637X/779/1/24

Venemans, B. P., Bañados, E., Decarli, R., et al. 2015, ApJL, 801, L11, doi: 10.1088/2041-8205/801/1/L11

Voggel, K. T., Seth, A. C., Baumgardt, H., et al. 2019, ApJ, 871, 159, doi: 10.3847/1538-4357/aaf735

—. 2022, A&A, 658, A152, doi: 10.1051/0004-6361/202140827

Volonteri, M., & Bellovary, J. 2012, Reports on Progress in Physics, 75, 124901, doi: 10.1088/0034-4885/75/12/124901

Volonteri, M., & Natarajan, P. 2009, MNRAS, 400, 1911, doi: 10.1111/j.1365-2966.2009.15577.x

Wang, F., Yang, J., Fan, X., et al. 2021, ApJL, 907, L1, doi: 10.3847/2041-8213/abd8c6

Waterval, S., Elgamal, S., Nori, M., et al. 2022, MNRAS, 514, 5307, doi: 10.1093/mnras/stac1191

Weinberg, M. D. 1989, MNRAS, 239, 549, doi: 10.1093/mnras/239.2.549

Welch, G. A., Sage, L. J., & Young, L. M. 2010, ApJ, 725, 100, doi: 10.1088/0004-637X/725/1/100

Wetzel, A. R., & White, M. 2010, MNRAS, 403, 1072, doi: 10.1111/j.1365-2966.2009.16191.x

White, S. D. M. 1983, ApJ, 274, 53, doi: 10.1086/161425

White, S. D. M., Huchra, J., Latham, D., & Davis, M. 1983, MNRAS, 203, 701, doi: 10.1093/mnras/203.3.701

White, S. D. M., & Rees, M. J. 1978, MNRAS, 183, 341, doi: 10.1093/mnras/183.3.341

Willott, C. J., McLure, R. J., & Jarvis, M. J. 2003, ApJL, 587, L15, doi: 10.1086/375126

Wilman, D. J., Zibetti, S., & Budavári, T. 2010, MNRAS, 406, 1701, doi: 10.1111/j.1365-2966.2010.16845.x

Yang, X., Mo, H. J., & van den Bosch, F. C. 2009, ApJ, 695, 900, doi: 10.1088/0004-637X/695/2/900

Yang, X., Mo, H. J., van den Bosch, F. C., Zhang, Y., & Han, J. 2012, ApJ, 752, 41, doi: 10.1088/0004-637X/752/1/41

Yanny, B., Newberg, H. J., Grebel, E. K., et al. 2003, ApJ, 588, 824, doi: 10.1086/374220

Yoachim, P., & Dalcanton, J. J. 2006, AJ, 131, 226, doi: 10.1086/497970

Young, J. S., & Scoville, N. Z. 1991, ARA&A, 29, 581, doi: 10.1146/annurev.aa.29.090191.003053

Zaritsky, D., & White, S. D. M. 1988, MNRAS, 235, 289, doi: 10.1093/mnras/235.1.289

Zaw, I., Rosenthal, M. J., Katkov, I. Y., et al. 2020, ApJ, 897, 111, doi: 10.3847/1538-4357/ab9944

Zeldovich, Y. B., & Sunyaev, R. A. 1969, Ap&SS, 4, 301, doi: 10.1007/BF00661821

Zelnikov, M. I., & Kuskov, D. S. 2016, MNRAS, 455, 3597, doi: 10.1093/mnras/stv2389

Zhao, H. 1996, MNRAS, 278, 488, doi: 10.1093/mnras/278.2.488

Zibetti, S., White, S. D. M., & Brinkmann, J. 2004, MNRAS, 347, 556, doi: 10.1111/j.1365-2966.2004.07235.x

Zolotov, A., Brooks, A. M., Willman, B., et al. 2012, ApJ, 761, 71, doi: 10.1088/0004-637X/761/1/71

Université de Strasbourg

Thibaut François

Observatoire astronomique de Strasbourg

Trous noirs massifs dans les galaxies naines : formation de binaires excentrées par capture gravitationnelle

Résumé

L'observation de trous noirs (TNs) supermassifs à haut redshift questionne notre compréhension de leur croissance. Le scénario standard de fusion des TNs massifs prévoit que ces derniers se retrouvent au centre galactique, amenés par la friction dynamique. Cependant, le temps nécessaire à un TN de masse intermédiaire pour atteindre le centre d'une galaxie naine typique est bien plus grand que l'âge de l'univers. De plus, les phénomènes de rétroaction peuvent abaisser la densité centrale de ces galaxies et créer un cœur, permettant le phénomène de core stalling, où les TNs restent sur des orbites stables excentrées.
Ainsi, la question se pose : ces TNs peuvent-ils fusionner à l'extérieur du centre galactique ? Cette thèse explore d'abord la formation de cœurs de densité dans les galaxies naines et propose un nouveau scénario de fusion excentrée des TNs massifs, initiée par une capture gravitationnelle. Nous découvrons que les captures permettent la formation de binaires dans 13% des cas dans notre configuration idéalisée. Ce résultat justifie une analyse approfondie des processus dissipatifs pour stabiliser ces captures, en particulier à la lumière des futurs observatoires comme LISA, qui détecteront les ondes gravitationnelles issues de telles fusions.

Mots-clés : astrophysique, dynamique galactique, galaxies naines, trous noirs, gravitation, simulations

Abstract

The observation of supermassive black holes (BHs) at high redshift challenges our understanding of their growth. The standard scenario of massive BH mergers relies on the fact that they settle at the galactic center due to dynamical friction. However, the time required for an intermediate-mass BH to reach the center of a typical dwarf galaxy far exceeds the age of the universe. Additionally, feedback processes can reduce the central density of these galaxies, creating a core and leading to core stalling, where BHs remain in stable, off-center orbits.
This raises the question : can these BHs merge outside the galactic center ? This thesis first examines the formation of density cores in dwarf galaxies and proposes a new scenario for off-center mergers of massive BHs, initiated by gravitational capture. We find that in our idealized setup, captures result in the formation of binaries in 13% of cases. This finding underscores the need for a detailed analysis of dissipative processes to stabilize these captures, especially given the upcoming capabilities of observatories like LISA, which are expected to detect gravitational waves from such mergers.

Keywords : astrophysics, galactic dynamics, dwarf galaxies, black holes, gravity, simulations